KU LEUVEN
ARENBERG DOCTORAL SCHOOL
Faculty of Engineering Science

CTU
Czech Technical
University in Prague
Faculty of Electrical Engineering
Department of Control Engineering

Dynamic Modeling of Macro-Fiber Composite Transducers integrated into Composite Structures

Doctor of Philosophy Dissertation

ZhongZhe DONG

October 2018

Czech Technical University in Prague
Faculty of Electrical Engineering
Departement of Control Engineering

Dynamic Modeling of Macro-Fiber Composite Transducers integrated into Composite Structures

by
ZhongZhe DONG

Presented to the faculty of Electrical Engineering
Czech Technical University in Prague,
in partial fulfillment of the requirements for the degree of
Doctoral of Philosophy

PhD program: Electrical Engineering and Information Technology
Branch of Study: Control Engineering and Robotics,
Supervisor CTU: prof. Ing. Michael Šebek, CSc.
Prague, October 2018

Dynamic Modeling of Macro-Fiber Composite Transducers integrated into Composite Structures

ZhongZhe DONG

Examination committee:
Prof. dr. ir. Y. Willems, chair (KUL)
Prof. dr. ir. W. Desmet, supervisor (KUL)
Prof. dr. ir. M. Šebek, supervisor (CTU)
Dr. ir. B. Pluymers, co-supervisor (KUL)
Dr. ir. C. Faria (Siemens PLM Software N.V.)
Dr. ir. M. Hromčík (CTU)
Prof. dr. ir. P. Sas (KUL)
Prof. dr. ir. K. Gryllias (KUL)
External jury member (External affiliation)

Dissertation presented in partial fulfillment of the requirements for the degree of:
- Doctor in Engineering Science (KU Leuven)
- Doctor in Electrical Engineering (Czech Technical University in Prague)

Copyright © 2018 ZhongZhe Dong
All rights reserved. No part of the publication may be reproduced in any form by print, photoprint, microfilm, electronic or any other means without written permission from the publisher.

Declaration

I hereby declare I have written this doctoral thesis independently and quoted all the sources of information used in accordance with methodological instructions on ethical principles for writing an academic dissertation.

In Prague, October 2018

ZhongZhe DONG

Preface

Foremost, I would like to thank prof. dr. ir. Wim Desmet, dr. ir. Bert Pluymers and prof. dr. ir Paul Sas from KU Leuven, dr. ir. Cassio Faria, prof. dr. ir. Herman Van Der Auweraer from Siemens Software Industry and prof. dr. ir. Michael Šebek, dr. ir. Martin Hromčík from Czech Technical University in Prague for their great guidance and support to my work. I appreciated their generous contributions of time, idea and patience through my PhD. I am grateful to have these people around me during my PhD. They gave me a lot of inspirations and put me on the right track when I got lost.

The European Commission is greatly appreciated for the financial support to ARRAYCON project. The project let me start not only my PhD but also my career at Leuven. Thanks for the great efforts from prof. dr. ir. Herman Van der Auweraer, prof. dr. ir. Wim Desmet, prof. dr. ir. Michael Sebek, dr. ir. Cassio Faria, dr. ir. Martin Hormcik, dr. ir. Kristian Hengster Movric and dr. ir. Bert Pluymers for precipitating the dual degree program between Czech Technical University and KU Leuven. It is an honor to be a PhD student at both great universities.

My PhD can be summarized to three stations: Siemens PLM Software, N.V., Czech Technical University in Prague, and KU Leuven in Belgium:

I started my career in Siemens at Leuven. Being an employee of this great company not only let me learn professional skills but also allowed me to understand different cultures. The RTD group in engineering service brought together people from different countries. I really enjoyed the open environment and the multi-cultures in this group. I would like to thank all the colleagues and friends in engineering service for their companions and help in my three years stay at Siemens. Thank Wenjun Guo, Dominiek Sacré, Cassio Faria, Xin Xin, Fabien Chauvicourt and all the other colleagues for their availabilities and technical support.

My PhD started at Czech Technical University in Prague. I spent memorable days in Prague. The food, the beer, the city, and of course the people there let me understand the unique Bohemia culture. I would like to thank all the colleagues in Prague for their support to my PhD too. Thank Petra Stehlikova, Stefan Knotek, Man Zhang and other friends for helping me during my secondments in Prague.

KU Leuven is the last stop of my PhD after the three years work at Siemens. People at KU Leuven are very enthusiastic and helpful. Thank Stijn Jonckheere, Xiang Xie, Hendrik Devriendt, Dionysios Panagiotopoulos, Shoufeng Yang, Jun Qian, Yansong Guo, Guanghai Fei, Liang Fang, Xu Huang, Yang Zhou, Junyu Qi, Chenyu Liu, Cheng Guo and the other friends that I met there for their helps and friendship.

Finally, I must give my deepest gratitude to my parents, to my sister and her family. Their love has continuously encouraged and supported me not only during my PhD but also over the more than ten years of journey in Europe.

ZhongZhe Dong
April 2018

Abstract

Composite structures have been already widely applied in engineering. Laminated composites using isotropic or anisotropic layers provide numerous options for designing lightweight structural components, that have high static stiffness and excellent impact resistance for automotive and aerospace products. However, lightweight structures can be susceptible to external disturbances due to the mass reduction and light damping in many cases. As a result, unwanted vibrations and noise can easily occur on these structures. Smart structures that use multifunctional materials as actuators/sensors spurred considerable research, aiming at reducing the noise and vibrations. Macro-fiber composite (MFC) piezoelectric transducers are an attractive choice in engineering because of their flexibility, reliability, and high-performance comparing to other types of transducers. Comprehensive design of composite structures with integrated MFC transducers is essential for appropriate deploying control systems in noise and vibrations control. Finite Element Modeling (FEM) methods are commonly used for modeling piezoelectric systems such kind of model always needs to be reduced for dynamic applications. For example, MFC transducers can be used in vibro-acoustic systems for noise and vibrations control. Reducing the piezoelectric vibro-acoustic system model can be challenging because the controller design and real-time simulations require stable low-order models. Conventional model order reduction techniques, such as the Krylov subspace projection and the balanced truncation, project the system model into an equivalent vector space. Many important physical parameters are not preserved by the reduced-order model. As a result, it is also challenging to determine the optimal placement and piezoelectric fibrous orientation of MFC transducers on a host structure with the consideration of their mechanical influences. There is no practical approach yet for these purposes in the literature. In this dissertation, laminated composite plates with spatially distributed rectangular MFC transducers are studied. Equivalent Substructure Modeling (ESM) approach is developed to generate stable structure-preserving low-order system models of piezoelectric composite structures. We proposed equivalent forces as a new solution to characterize the inverse piezoelectric effect of the integrated transducer. The corresponding direct piezoelectric effect is also derived. The analytical piezoelectric couplings are introduced into an equivalent substructuring process for modeling piezoelectric systems. Experiments verified the validation of the ESM approach. Two kinds of study cases are given to demonstrate the odds of the ESM approach for evaluating the placement and piezoelectric fibrous orientation of a MFC transducer on a non-homogeneous composite plate. The vibro-acoustic study of composite plates with integrated MFC transducer is carried out. The ESM approach is used to generate a low-order stable model, and validated by experimental data. The piezoelectric reciprocal relations in a vibro-acoustic field are defined. The work enables MFC transducers to expand their application in vibro-acoustics.

Keywords: Macro-fiber composite, composite structures, stable low-order modeling, structure-preserving, dynamic applications

Abstrakt

Kompozitní struktury byly již široce používány ve strojírenství. Laminované kompozity používající izotropní nebo anizotropní vrstvy poskytují řadu možností navrhování lehkých konstrukčních prvků, které mají vysokou statickou tuhost a vynikající odolnost proti nárazům pro automobilový a letecký průmysl. Lehké konstrukce však mohou být v mnoha případech náchylné k vnějším poruchám způsobeným redukcí hmotnosti a lehkým tlumením. V důsledku toho mohou na těchto strukturách snadno dojít k nechtěným vibracím a šumu. Inteligentní struktury, které používají multifunkční materiály jako akční členy / senzory, podnítily značný výzkum zaměřený na snížení hluku a vibrací. Kombinované piezoelektrické měniče makro-vláken (MFC) jsou atraktivní volbou ve strojírenství díky své flexibilitě, spolehlivosti a vysokému výkonu v porovnání s jinými typy převodníků. Komplexní návrh kompozitních konstrukcí s integrovanými převodníky MFC je nezbytný pro správné nasazení řídicích systémů při řízení hluku a vibrací. Metody modelování konečných prvků (FEM) se běžně používají pro modelování piezoelektrických systémů, protože tento typ modelu je vždy nutné pro dynamické aplikace snížit. Například měniče MFC mohou být použity ve vibroakustických systémech pro řízení hluku a vibrací. Snížení piezoelektrického modelu vibro-akustického systému může být náročné, protože návrh regulátoru a simulace v reálném čase vyžadují stabilní modely s nízkým pořadím. Techniky konvenčního snižování pořadí modelů, jako je Krylovova podprostorová projekce a vyvážené zkrácení, navrhují systémový model do ekvivalentního vektorového prostoru. Mnoho důležitých fyzických parametrů není zachováno modelem s redukovaným uspořádáním. V důsledku toho je rovněž náročné stanovit optimální umístění a piezoelektrickou vláknitou orientaci snímačů MFC na hostitelské struktuře s ohledem na jejich mechanické vlivy. Pro tyto účely zatím v literatuře neexistuje žádný praktický přístup. V této disertační práci jsou studovány vrstvené kompozitní desky s prostorově rozloženými obdélníkovými MFC převodníky. Ekvivalentní modelování substrukturálního modelu (ESM) je vyvinuta tak, aby generovala stabilní strukturálně chránící systémové modely piezoelektrických kompozitních struktur. Navrhli jsme ekvivalentní síly jako nové řešení charakterizující inverzní piezoelektrický efekt integrovaného převodníku. Rovněž je odvozen odpovídající přímý piezoelektrický efekt. Analytické piezoelektrické spojky jsou zavedeny do ekvivalentního substrukturního procesu pro modelování piezoelektrických systémů. Pokusy ověřily validaci přístupu ESM. Dva druhy studijních případů jsou uvedeny, aby prokázaly šanci přístupu ESM k vyhodnocení umístění a piezoelektrické vláknité orientace snímače MFC na nehomogenní kompozitní desce. Probíhá vibro-akustická studie kompozitních desek s integrovaným převodníkem MFC. Přístup ESM se používá k vytvoření stabilního modelu s nízkou objednávkou a ověřován experimentálními údaji. Jsou definovány piezoelektrické vzájemné vztahy ve vibroakustickém poli. Práce umožňuje převodníkům MFC rozšířit jejich aplikaci v oblasti vibroakustiky.

Klíčová slova: Makro-vláknové kompozity, kompozitní struktury, stabilní modelování s nízkou objednávkou, strukturně chránící, dynamické aplikace

Beknopte samenvatting

Composietstructuren zijn al op grote schaal toegepast in engineering. Gelamineerde composieten met isotrope of anisotrope lagen bieden talloze opties voor het ontwerpen van lichtgewicht structurele componenten, die een hoge statische stijfheid en uitstekende slagvastheid hebben voor auto- en ruimtevaartproducten. Lichtgewicht constructies kunnen echter gevoelig zijn voor externe verstoringen als gevolg van de massareductie en lichtdemping in veel gevallen. Dientengevolge kunnen ongewenste trillingen en ruis gemakkelijk optreden op deze structuren. Slimme constructies die multifunctionele materialen gebruiken als actuatoren / sensoren, spoorden aanzienlijk onderzoek aan, gericht op het verminderen van het lawaai en de trillingen. Macro-vezel composiet (MFC) piëzo-elektrische transducers zijn een aantrekkelijke keuze in engineering vanwege hun flexibiliteit, betrouwbaarheid en hoge prestaties in vergelijking met andere typen transducers. Een uitgebreid ontwerp van composietstructuren met geïntegreerde MFC-transducers is essentieel voor geschikte besturingssystemen voor bediening van geluid en trillingen. Finite Element Modeling (FEM) -methoden worden vaak gebruikt voor het modelleren van piëzo-elektrische systemen, dit soort modellen moet altijd worden verlaagd voor dynamische toepassing. MFC-transducers kunnen bijvoorbeeld worden gebruikt in vibro-akoestische systemen voor controle van ruis en trillingen. Het reduceren van het piëzo-elektrische vibro-akoestische systeemmodel kan een uitdaging zijn omdat het ontwerp van de controller en real-time simulaties stabiele lage-orde modellen vereisen. Conventionele technieken voor modelreductie, zoals de Krylov-subruimteprojectie en de gebalanceerde truncatie, projecteren het systeemmodel in een equivalente vectorruimte. Veel belangrijke fysieke parameters worden niet bewaard door het gereduceerde bestelmodel. Dientengevolge is het ook een uitdaging om de optimale plaatsing en piëzo-elektrische vezeloriëntatie van MFC-transducenten op een gastheerstructuur te bepalen met inachtneming van hun mechanische invloeden. Er is nog geen praktische benadering voor deze doeleinden in de literatuur. In dit proefschrift worden gelamineerde composietplaten met ruimtelijk verdeelde rechthoekige MFC-transducers bestudeerd. Equivalent Substructure

Modeling (ESM) -aanpak is ontwikkeld om stabiele structuurbehoudende systeemmodellen van lage orde van piëzo-elektrische composietstructuren te genereren. We hebben equivalente krachten voorgesteld als een nieuwe oplossing om het inverse piëzo-elektrische effect van de geïntegreerde transducer te karakteriseren. Het overeenkomstige directe piëzo-elektrische effect wordt ook afgeleid. De analytische piëzo-elektrische koppelingen worden geïntroduceerd in een equivalent substructureringsproces voor het modelleren van piëzo-elektrische systemen. Experimenten hebben de validatie van de ESM-aanpak geverifieerd. Er worden twee soorten studiecasussen gegeven om de kansen van de ESM-benadering aan te tonen voor het evalueren van de plaatsing en piëzo-elektrische vezeloriëntatie van een MFC-transducer op een niet-homogene composietplaat. De vibro-akoestische studie van composietplaten met geïntegreerde MFC-transducer wordt uitgevoerd. De ESM-benadering wordt gebruikt om een stabiel model van lage orde te genereren en gevalideerd door experimentele gegevens. De piëzo-elektrische wederkerige relaties in een vibro-akoestisch veld zijn gedefinieerd. Het werk stelt MFC-transducers in staat hun toepassing in vibro-akoestiek uit te breiden.

Trefwoorden: Macro-vezel composiet, composiet structuren, stabiele modellering van lage orde, structuur-behoudende, dynamische toepassingen

List of Abbreviations

AFC: Active Fiber Composite

Dof: Degree of Freedom

EFM: Equivalent Force Modeling

ESM: Equivalent Substructure Modeling

FEM: Finite Element Method

FOSD: First Order Shear Deformation

FRF: Frequency Response Function

MAC: Modal Assurance Criterion

MFC: Macro Fiber Composite

RPT: Refined Plate Theory

List of Symbols

a: Length of a rectangular MFC transducer

b: Width of a rectangular MFC transducer

$[d]$: Piezoelectric strain constant matrix

d_{ij}: Piezoelectric strain constants before electrode's transform

d_{ij}^{*}: Piezoelectric strain constants after electrode's transform

$[e]$: Piezoelectric stress constant matrix

e_{ij}: Piezoelectric stress constants before electrode's transform

e_{ij}^{*}: Piezoelectric stress constants after electrode's transform

$\bar{e}_{ij}$: Generalized piezoelectric stress constants of MFC transducer

f_{xx},f_{yy},f_{zz}: Equivalent forces in x, y and z directions

$[g]$: Piezoelectric constant matrix relating the applied stress to the resultant electric field in a piezoelectric material

$[h]$: Piezoelectric constant matrix relating the applied strain to the resultant electric field in a piezoelectric material

$h_{_E}$: Electrode distance

j: complex unit

m_{ij}: Equivalent bending moment

$\vec{n}$: Normal vector

$\boldsymbol{p}$: Acoustic pressure

q_i: Nodal displacement in FEM

$[s^E]$: Compliance matrix of piezoelectric material defined for a constant electric field

$[s^D]$: Compliance matrix of piezoelectric material defined for a constant electric displacement

t: Time variable

t_a: Thickness of adhesive layer

t_f: Thickness of the active layer in MFC transducers

t_s: Thickness of a plate

t_p: Thickness of a MFC transducer

$\boldsymbol{u}$: generalized displacement in FEM

$u_\bullet$: Displacement in x direction of a plate for $\bullet$

$v_\bullet$: Displacement in y direction of a plate for $\bullet$

$w_\bullet$: Displacement in z direction of a plate for $\bullet$

$\boldsymbol{u}_r$: Remained Dofs in numerical models

$\boldsymbol{u}_d$: Removed Dofs in numerical models

w_f: Finger width of the interdigitated electrodes on a MFC transducer

z_p: Thickness-wise integration of MFC transducer on a host structure

z_s: Thickness-wise position of MFC transducer on a host structure

$A_{ij}^\bullet$: Membrane rigidity of a plate for $\bullet$

$B_{ij}^\bullet$: Membrane-bending coupling rigidity of a plate for $\bullet$

B_b: Elemental interpolation function of bending strain field

B_i^b: Nodal interpolation function of bending strain in FEM

B_i^e Nodal interpolation function of electromechanical coupling in FEM

B_m: Elemental interpolation function of membrane strain field

B_i^m: Nodal interpolation function of membrane strain in FEM

$\boldsymbol{C}$: Damping matrix

C_p Capacitance of a MFC transducer

$\boldsymbol{C}_r$: Reduced-order damping matrix

$\{D\}$: Electrical displacment tensor

D^*, and D_s^*: Equivalent mechanical constant matrix of a laminate composite plate

$D_{ij}^{\bullet}$: Bending rigidity components for $\bullet$

$\{E\}$: Electric field tensor

$\boldsymbol{F_a}$: Acoustic excitation

F_a: Amplitude of acoustic excitation

$\boldsymbol{F_s}$: Mechanical excitation

F_s: Amplitude of mechanical excitation

G_{ij}: Shear modulus

$\boldsymbol{G_p}$: A generalized term

H: The Heaviside function

$\boldsymbol{K}_{\bullet}$: Stiffness matrix for $\bullet$

$\widetilde{\boldsymbol{K}}$: Stiffness matrix of a substructure

$\overline{\boldsymbol{K}}$: Low-order stiffness matrix of a substructure

$\boldsymbol{K}_c$: Structural-acoustic stiffness coupling matrix

$\boldsymbol{K}_{Ag}$: Augmented stiffness matrix

K_{ij} Electromechanical coupling coefficient

L Inductance

$\boldsymbol{L}_{\bullet}$ Localization matrix for $\bullet$

$\boldsymbol{M}_{\bullet}$: Mass matrix for $\bullet$

$\widetilde{\boldsymbol{M}}$: Mass matrix of a substructure

$\overline{\boldsymbol{M}}$: Low-order mass matrix of a substructure

$\boldsymbol{M}_c$: Structural-acoustic mass coupling matrix

$M_{xx}^{\bullet}$, $M_{yy}^{\bullet}$, $M_{xy}^{\bullet}$: Bending moments in x, y and xy directions for $\bullet$

N: Elemental interpolation function of displacement field

N_i: Nodal interpolation function of transverse displacement in FEM

$N_\bullet$: Resultant force for $\bullet$.

$[Q^E]$: Elastic matrix of a piezoelectric material defined for a constant electric field

$[Q^D]$: Elastic matrix of a piezoelectric material defined for a constant electric displacement

$Q_{ij}^\bullet$: Elastic components of a composite layer in material coordinates for $\bullet$

$\bar{Q}_{ij}$: Elastic components of a composite layer in structural coordinates

Q_{yz}, Q_{zx}: Transverse shear loads

$\dot{\boldsymbol{Q}}$: volume velocity source

Q: Amplitude of volume velocity source

$\boldsymbol{R}^{(\bullet)}$: Dynamic condensation transformation matrix for $\bullet$

R: Resistance

$\{S\}$: Strain tensor

$\{T\}$: Stress tensor

$\boldsymbol{T}$: Model order reduction transformation matrix

$T_\bullet^*$: Kinetic energy for $\bullet$

$U_\bullet^*$: Stored energy/potential energy for $\bullet$

V: Voltage

V_{in}: Operational voltage

V_{out}: Generated voltage

W^*: External work

Y_{ij}: Young's modulus

Z_e: Impedance of external electric circuit

Z_s: Thickness-wise dimension of a plate

Z_p: Thickness-wise dimension of a MFC transducer

$\boldsymbol{Z}_\bullet$: Elementary thickness-wise integration of mass matrix for $\bullet$ in FEM

$\alpha_\bullet$: Equivalent force correction factor for $\bullet$

$\alpha_{_P}$: Direct piezoelectric effect correction factor

$\alpha_{_E}$: Inverse piezoelectric effect correction factor of MFC-d33 transducers for the operational electric field

β^T: Free dielectric impermeability matirx at a constant stress

$[\epsilon^\bullet]$: Dielectric constant matrix of a piezoelectric material for $\bullet$

δ: The Dirac-delta function

$\boldsymbol{\varepsilon}_\bullet^{\boldsymbol{m}}$: Slope on a plate for $\bullet$

$\boldsymbol{\kappa}_\bullet^{\boldsymbol{b}}$: Curvature on a plate for $\bullet$

θ: Radial angle

ν_{ij}: Poisson ratio

ξ: Critical damping ratio

λ, η Proportional damping coefficients

$\rho_\bullet$: Mass density for $\bullet$

τ_{ij}: Transverse shear loads

ϕ: Electric DOF

ω: Angular frequency

ΔT^*: Kinetic energy variation

ΔW^*: External work variation

ΔU^*: Stored energy variation

Δx, Δy: Spacing of finite difference interval in x and y directions

ΔS: Strain variation

Δu: Variation of u

Δv: Variation of v

Δw: Variation of w

$\Gamma_\bullet$: Area for $\bullet$

$\boldsymbol{\Theta}$: Electromechanical coupling matrix

$\widetilde{\boldsymbol{\Theta}}$: Electromechanical coupling matrix on a substructure

$\overline{\boldsymbol{\Theta}}$: Electromechanical coupling matrix on a low-order substructure

$\boldsymbol{L}_f$: Mechanical force input localization matrix

$\boldsymbol{L}_{\dot{u}}$: Transverse velocity output localization matrix

$\Lambda_x^p \Lambda_y^p$: Spatial distribution of a MFC transducer

Contents

Abstract iii

Abstrakt v

Beknopte samenvatting vii

List of Abbreviations ix

List of Symbols xi

Contents xvii

List of Figures xxiii

List of Tables xxxi

1 Introduction 1

- 1.1 Research context and motivation 1
- 1.2 Research objectives 3
- 1.3 Research approach 4
- 1.4 Contributions and achievements 5
- 1.5 Outline of the dissertation 6

2 State-of-the-art on dynamic modeling of MFC transducers 9

2.1 Piezoelectricity 9

2.2 Advances of piezoelectric transducers 12

2.3 Application of piezoelectric transducers for noise and vibration control 17

2.4 Application of piezoelectric transducers for energy harvesting . 20

2.5 Nonlinearity of piezoelectric materials 23

2.6 Modeling of MFC transducers integrated into a thin host structure 26

2.6.1 Modeling hypothesis 26

2.6.2 Material characterization of MFC transducers 29

2.6.3 Analytical modeling approaches 30

2.6.4 Numerical modeling approaches 32

2.7 Concluding remarks 35

3 Basic concept of equivalent dynamic modeling 37

3.1 Constitutive relations 38

3.1.1 Constitutive relations of laminated plate 38

3.1.2 Piezoelectric constitutive relations of MFC transducers . . 41

3.1.3 Transverse shear forces 45

3.2 Generalized Hamilton's principle 46

3.2.1 Potential energy and its variation 47

3.2.2 Kinetic energy and its variation 49

3.2.3 Work due to external loads and its variation 49

3.2.4 Governing equations and boundary constraints of the transducer 50

3.3 Inverse piezoelectric effect characterization using equivalent forces 52

3.3.1 Equivalent membrane forces 52

3.3.2 Equivalent bending forces 53

3.3.3 Accuracy analysis of the inverse piezoelectric coupling . 57

3.4 Assessments of different equivalent loads 59

3.5 Direct piezoelectric effect characterization using electric boundary conditions 61

3.6 Concluding remarks 64

4 Equivalent dynamic modeling of MFC transducers integrated into composite plates 65

4.1 Equivalent Force Modeling approach 66

4.2 Equivalent Substructure Modeling approach 70

4.3 Modeling sensitivity analysis 72

4.3.1 Cantilever laminated plate with integrated MFC transducers 73

4.3.2 Sensitivity analysis on the size of MFC transducers . . . 74

4.3.3 Sensitivity analysis on the piezoelectric fibrous orientation of MFC transducers 76

4.3.4 Verification of ESM approach 78

4.4 Limitations of the proposed methods 81

4.5 Concluding remarks 81

5 Structural dynamic validation of equivalent modeling approaches 83

5.1 Experimental testing of a laminated plate with integrated MFC transducers 83

5.1.1 Laminated composite plate 84

5.1.2 MFC-d33 transducers 85

5.1.3 Experimental analysis 88

5.2 Equivalent modeling of composite plate with integrated MFC transducers 91

5.3 Validations of EFM and ESM models 93

5.3.1 Modal validation 93

5.3.2 Dynamic response validation 95
5.4 Piezoelectric reciprocal relation 103
5.5 Dynamic application of ESM approach 106
5.5.1 Energy harvesting 106
5.5.2 Piezoelectric shunt damping 107
5.6 Concluding remarks 113

6 Vibro-acoustic study on MFC transducers 115

6.1 Reciprocal relations of a piezoelectric vibro-acoustic system . . 116
6.2 Equivalent substructure modeling of the piezoelectric vibro-acoustic system 120
6.2.1 FEM modeling in Comsol 120
6.2.2 ESM approach 123
6.3 Validation of ESM model 125
6.3.1 Frequency response validations 127
6.3.2 Stability verification of ESM model 130
6.4 Reciprocal relations verification 131
6.4.1 Verification in the frequency domain 131
6.4.2 Verification in the time domain 134
6.5 Concluding remarks 135

7 Conclusions and Perspectives 137

7.1 Summary 137
7.2 Perspectives of the research 139

8 Appendix 141

8.1 Finite difference coefficient 141
8.2 Interpolation function of FOSD finite element method 143

8.3 Static modeling robustness check of EFM approach 145
8.4 Experimental equipment 147
8.5 Second-order forward-backward finite difference approximation 149

Bibliography **155**

Curriculum Vitae **173**

List of publications **175**

List of Figures

1.1 Composition of a MFC transducer 2

1.2 Work modes of MFC transducers 2

2.1 Polarization of piezoceramics 10

2.2 Different piezoelectric effects on a piezoelectric element 11

2.3 Work principle of a thin piezoelectric transducer 13

2.4 Multilayer piezoelectric actuators (The red and blue dash-lines represent the deformations of the actuators) 13

2.5 Schematic representation of MFC-d31 15

2.6 Schematic representation of MFC-d33 15

2.7 Electric field distribution on a rectangular piezoelectric fiber of an MFC-d33 transducer 16

2.8 Schematic representation of MFC-d15 16

2.9 Schematic representation of active vibration control 18

2.10 Schematic representation of piezoelectric shunted damping (The electrical shunt circuits are connected to the electrodes of each transducer) 19

2.11 Schematic representation of piezoelectric energy harvesters (a) Bimorph structure (b) Unimorph structure 21

2.12 Two modes of piezoelectric conversion of mechanical strain into Electric field E 21

2.13 Maximum extractable electrical power comparison between a linear and a nonlinear energy harvester 22

2.14 Displacement-voltage hysteresis in a typical piezoceramic actuator 24

2.15 Creep over time in a typical piezoceramic actuator 24

2.16 Displacement field of a plate 27

2.17 Plane deformations on a MFC transducer 29

2.18 Equivalent loads of an anisotropic rectangular piezoelectric actuator 31

2.19 Piezoelectric structures 32

2.20 Material-structural coordinates transformation 33

2.21 Strain transfer mechanism through adhesive bond layer 34

3.1 Lay-up of a laminated composite plate with an integrated MFC transducer 38

3.2 In-plane behaviors of a plate due to membrane forces 40

3.3 Out-plane behaviors of a plate due to bending moments 41

3.4 Work principle of MFC-d31 transducers 41

3.5 Work principle of MFC-d33 transducers 41

3.6 A rectangular orthotropic plate with integrated MFC transducers 46

3.7 The distribution of f_{zz} in x/y direction via forward finite difference approximation (Δs indicates either Δx or Δy.) . . . 56

3.8 The distribution of f_{zz} in x/y direction via a forward-backward finite difference approximation (Δs indicates either Δx or Δy.) 57

3.9 One-dimensional equivalent loads bending diagram of a rectangular MFC transducer 58

3.10 Bending diagram of piezoelectric transducer in x/y direction due to the equivalent forces 58

3.11 A composite plate with an integrated MFC transducer and an external electrical circuit 61

4.1 The displacement of the mid-surface (left) and a normal on a plate (middle-right) in FOSD theory 66

4.2 Distribution of f_{xx} on a rectangular transducer 68

4.3 Distribution of f_{yy} on a rectangular transducer 68

4.4 Distribution of f_{zz} on a rectangular transducer. The black, blue and green arrows indicate the bending forces along x, y and xy directions, respectively. 69

4.5 Equivalent substructure concept 70

4.6 A cantilever plate with integrated MFC transducers (The red spot indicates the force input and velocity output location in direct and inverse piezoelectric response analysis, respectively.) 73

4.7 Direct piezoelectric frequency responses of MFC-d31 for different sizes 75

4.8 Inverse piezoelectric frequency responses of MFC-d31 for different sizes 75

4.9 Piezoelectric fibrous orientations 76

4.10 Direct piezoelectric frequency responses of MFC-d33 for different piezoelectric fibrous orientations 77

4.11 Inverse piezoelectric frequency responses of MFC-d33 for different piezoelectric fibrous orientations 77

4.12 A cantilever plate with integrated MFC transducers (The red spots represent the master nodes of equivalent structural model.) 78

4.13 MFC-d31 direct piezoelectric frequency response of the cantilever plate ($\theta = 0^o$) 79

4.14 MFC-d31 inverse piezoelectric frequency response of the cantilever plate ($\theta = 0^o$) 79

4.15 MFC-d33 direct piezoelectric frequency response of the cantilever plate ($\theta = 60^o$) 80

4.16 MFC-d33 inverse piezoelectric frequency response of the cantilever plate ($\theta = 60^o$) 80

5.1 The composite plate with integrated MFC-d33 transducers used for dynamic response validation 84

5.2 Microscopic images of a region on MFC transducer 86

5.3 The effective length of the used transducer for direct piezoelectric effect 87

5.4 The effective width of the used transducer for direct piezoelectric effect 87

5.5 Experimental setup 88

5.6 Reciprocity check between 01 and 02 on the plate 89

5.7 Reciprocity check between the two MFC transducers 90

5.8 Comparison of FRFs between 26 and 22: blue curve: voltage to velocity FRF $[(m/s)/V]$ and red curve: force to voltage FRF $[V/N]$ 91

5.9 The master nodes of the low-order models on the studied plate (Left side is the reduced-order EFM model and right side is the ESM model.) 92

5.10 MAC correlation between experimental data and EFM model . 94

5.11 First 5 normalized mode shapes of the studied plate $((a)$ experimental data, (b) EFM model and (c) ESM model) 95

5.12 Inverse piezoelectric frequency response validation between 00 and 74 96

5.13 Inverse piezoelectric frequency response validation between 00 and 00 96

5.14 Inverse piezoelectric frequency response validation between 26 and 22 97

5.15 Inverse piezoelectric frequency response validation between 26 and 26 98

5.16 Direct piezoelectric frequency response validation between 00 and 74 98

5.17 Direct piezoelectric frequency response validation between 00 and 00 99

5.18 Direct piezoelectric frequency response validation between 26 and 22 100

5.19 Direct piezoelectric frequency response validation between 26 and 26 100

5.20 Mechanical influence of the MFC transducer to the inverse piezoelectric frequency response between 00 and 74 in ESM model 101

5.21 Mechanical influence of the MFC transducer to the direct piezoelectric frequency response between 00 and 00 in ESM model 101

5.22 Reciprocity validation between two MFC transducer (High operational voltage) 102

5.23 Reciprocity validation between two MFC transducer (Low operational voltage) 103

5.24 Estimated inverse piezoelectric frequency response between 26 and 22 by experimental data 105

5.25 Estimated inverse piezoelectric frequency response between 26 and 22 by ESM model 105

5.26 Force-to-voltage FRFs of the center MFC transducer for a set of piezoelectric fibrous orientations (The gray curve is experimental data.) 107

5.27 Force-to-voltage FRFs of the corner MFC transducer for a set of piezoelectric fibrous orientations (The gray curve is experimental data.) 107

5.28 Piezoelectric shunt damping system 108

5.29 Piezoelectric shunt damping on the composite plate: velocity over force FRF between 74 and 00 109

5.30 Real-time simulation of the $R - L$ shunted damping 110

5.31 Dynamic behaviors of the plate in non-shunted and shunted cases 111

5.32 The placement candidates of the transducer at the center of the plate 112

5.33 Performance of the negative capacitance shunt for different transducers' placements 113

6.1 The dimensions of KU Leuven soundbox (in *mm*) 116

6.2 Lay-up of a laminated composite plate with integrated MFC transducer 120

6.3 Comsol cavity-shell model 122

6.4 Distribution of the master nodes selected for ESM approach. Red spots and blue spots indicate the master nodes of the plate and the cavity, respectively. 124

6.5 Experimental setup of the vibro-acoustic system 125

6.6 MAC correlation between ESM plate model and experimental data 126

6.7 First eight vibro-acoustic modes of the cavity (normalized sound pressure in the cavity) 127

6.8 Frequency response validation of acceleration over force input between locations 43 and 34 on the plate 128

6.9 Frequency response validation of voltage output over force input between locations 00 and 34 on the plate 128

6.10 Frequency response validation of acceleration over acoustic volume velocity 129

6.11 Frequency response validation of voltage output over acoustic volume velocity 130

6.12 The poles (×) and zeros (∘) of the ESM model 130

6.13 Reciprocal relation validation positions 131

6.14 Structural reciprocal relation validation between the plate and the integrated transducer 132

6.15 Reciprocal relation validation between the plate and the integrated transducer in vibro-acoustic field 132

6.16 Reciprocal relation validation between the cavity and the integrated transducer 133

6.17 Piezoelectric reciprocal relation validation in time domain . . . 134

6.18 Validation of the identified acoustic source by using the piezoelectric vibro-acoustic reciprocal relation 135

8.1 Three node element 143

8.2 Static modeling robustness check for the MFC-d31 transducers of different size (Left) and for the MFC-d33 transducers of different piezoelectric fibrous orientations (Right) 145

8.3 The power bandwidth versus voltage and load capacitance of the voltage amplifier 148

8.4 Second-order EFM model inverse piezoelectric frequency response validation between $p00$ and $p74$ 150

8.5 Second-order EFM model inverse piezoelectric frequency response validation between $p00$ and $p00$ 150

8.6 Second-order EFM model inverse piezoelectric frequency response validation between $p26$ and $p22$ 151

8.7 Second-order EFM model inverse piezoelectric frequency response validation between $p26$ and $p26$ 151

8.8 Second-order EFM model direct piezoelectric frequency response validation between $p00$ and $p74$ 152

8.9 Second-order EFM model direct piezoelectric frequency response validation between $p00$ and $p00$ 152

8.10 Second-order EFM model direct piezoelectric frequency response validation between $p26$ and $p22$ 153

8.11 Second-order EFM model direct piezoelectric frequency response validation between $p26$ and $p26$ 153

List of Tables

4.1 Material properties of the used MFC transducers and composite plate 74
4.2 Coefficients of proportional damping 74

5.1 Material properties of a single laminate 84
5.2 Parameters of MFC M2814P1 85
5.3 Material properties of MFC M2814P1 85
5.4 Natural frequencies convergence via number of elements 91
5.5 Coefficients of proportional damping 93
5.6 Natural frequencies validations of the EFM and ESM models . 94
5.7 Amplitude reduction of some modes for each placement (in $[dB]$) 112

6.1 Structure and material properties of the laminated composite plate with integrated MFC-d33 transducers 122
6.2 Proportional damping coefficients 123
6.3 Validation of the first 8 natural frequencies of the equivalent plate 126
6.4 Validation of the first eight natural frequencies of the piezoelectric vibro-acoustic system 127

8.1 Central finite difference coefficients 141
8.2 Forward finite difference coefficients 141

8.3 Backward finite difference coefficients 142

Chapter 1

Introduction

1.1 Research context and motivation

Lightweight design benefits industrial products in many aspects such as energy and emissions reductions, and decreases of manufacturing and maintenance costs.[1] It has been increasingly applied to various industrial areas. Composite is one of the most important material options for designing the structural components due to its high stiffness-to-mass ratio. However, it could be susceptible to disturbances because of the mass reduction and low-damping in many cases. As a result, the noise and vibrations performance of these structural components deteriorates [1–3].

The vibrations that occur on the lightweight structures can be very discomforting and harmful in our daily lives. For example, the vibration of road vehicles and passenger jets affect passengers' comfort. Vibrations can also lead to other issues such as fatigue failure and delamination of laminated composite structures. The resonance phenomena in vibrations can even damage some structural components. Besides, noise results from those vibrations, due to the structural-acoustic interaction. It is typically an NVH problem that often needs to be addressed by vibro-acoustic analysis in vehicle design.

Traditional measures by using visco-elastic or porous materials for reducing noise and vibrations have reached certain limitations in lightweight design concept [4]. For this reason, smart structures have arisen in many research tracks, aiming at improving the structural performance without adding to much mass. Multifunctional materials, such as piezoelectric materials and shape memory alloys can be integrated into structural components as actuators/sensors for the usage of some control units or signal processing systems [5]. Piezoelectric transducers can be effectively used as actuators/sensors for noise and vibrations control, energy harvesting, and structural health monitoring [6–12]. MFC transducer is one of the most promising options. It consists of rectangular piezoelectric fibers, which are embedded into an epoxy matrix, as shown in Figure 1.1. Specially designed electrodes are integrated into the transducer in order to properly drive the piezoelectric fibers.

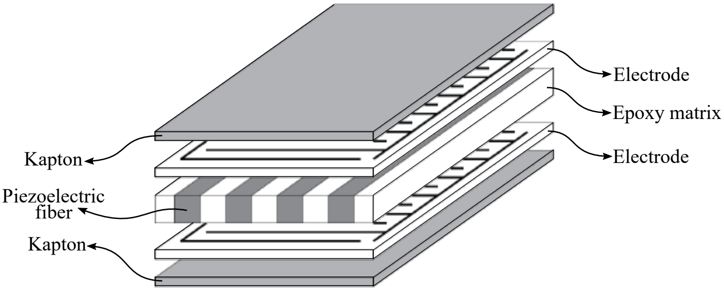
Electrode
Epoxy matrix
Electrode
Kapton
Piezoelectric fiber
Kapton

Figure 1.1: Composition of a MFC transducer [13]

The MFC transducer has many odds comparing to monolithic and multilayer piezoelectric patches: on the one hand, the MFC transducer provides high-flexibility, high-performance, and high reliable properties [14]; on the other hand, it enhances the design of piezoelectric systems because the performance of the transducer significantly relies on the piezoelectric fibrous orientation, which can lead to different actuation/sensing effects. For example, MFC transducer has different work modes as shown in Figure 1.2, when they are used as actuators. Hence, comprehensive design of MFC transducers spatially distributed on composite structures is necessary for ensuring the performance of the dynamic control systems.

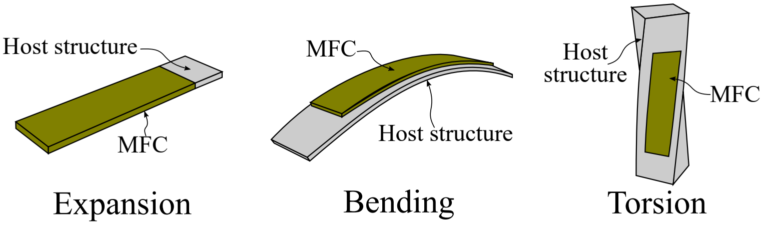
Host structure
MFC
Expansion
MFC
Host structure
Bending
Host structure
MFC
Torsion

Figure 1.2: Work modes of MFC transducers [15]

1.2 Research objectives

Considerable research has been carried out for studying the dynamic behaviors of different types of piezoelectric structures. Nevertheless, accurate and efficient predicting the response of piezoelectric structures is still a challenging task, even in the case of transducer-implemented beams and plates [4]. Currently, the structural dynamics are derived from either the Hamilton's principle or the elastic equilibrium principle in analytical characterization. A closed-form solution can be obtained to describe the performance of piezoelectric transducers on a host structure. The closed-form solutions, named equivalent loads, are commonly used to characterize the inverse piezoelectric effect. The direct piezoelectric effect is widely characterized for sensing and energy harvesting. However, the coupling between the two effects is often omitted in analyses. Besides, the transducers introduce additional stiffness and mass effects to the host structure, and they are difficult to be taken into account in analytical solutions. The existing work studied piezoelectric layered structure with partially covered electrodes, whose dynamics could be entirely different from the plate with distributed transducers. Hence, the plates with distributed piezoelectric transducers (monolithic or orthotropic) are not fully characterized yet by analytical methods.

Numerical methods can be used for enduring the limitations of analytical solutions, For instance, FEM method is widely used for piezoelectric modeling [16–23]. The mechanical properties of the piezoelectric transducers on a host structure can be properly handled, also, the piezoelectric coupling is simulated through strain field. Thus, the piezoelectric couplings strongly rely to the structural modeling. Thereby, the MFC transducers should be considered in modeling from the beginning. Meanwhile, the large-scale FEM models need to be reduced for dynamic applications. The usual model order reduction techniques such as Krylov subspace projection [24] and balanced truncation [25] project the system model into an equivalent vector space so that most of the physical parameters are not preserved in the reduced-order model, which leads to some challenges in designing advanced piezoelectric systems with MFC transducers:

Firstly, it is difficult to evaluate the performance of MFC transducers in dynamic application. There are methods in literature for determining the optimal placement of piezoelectric actuators/sensors [26, 27]. However, the mechanical influences of the transducers that could lead to significant changes in system dynamics are not included in these methods. For MFC transducers, the changes in piezoelectric fiber orientation will result in simultaneous changes in both the material and piezoelectric properties. There is no effective approach yet for determining the optimal properties of an MFC transducer on a non-homogeneous host structure in the literature.

Secondly, engineering applications often require intuitive validations such as experiments. The eigensolutions of the system are not fully preserved in the reduced order model. As a result, the Frequency Response Function (FRF) is widely used for model validation, but modal validations are difficult to be conveniently performed. And, the dynamic behaviors of the structural cannot be intuitive evaluated.

Thirdly, MFC transducers can be integrated into multiphysics systems, such as vibro-acoustic system. It would be challenging to reduce this kind of piezoelectric vibro-acoustic systems when the stability is required for active noise and vibrations control or real-time simulations. Moreover, the application of piezoelectric transducers such as MFC, are still limited to sensors/actuators. Potentials of piezoelectric transducers in vibro-acoustics need to be further explored. Therefore, it is significant to develop an effective modeling approach that enables the following capabilities for designing and modeling of advanced piezoelectric systems:

1. generate low-order system models that could be directly used in dynamic application;
2. conserve the structure of the system for design updating;
3. retain the modal parameters for experimental validations;
4. preserve the stability of the system for real-time simulations;
5. expand the application of MFC transducers towards vibro-acoustic fields.

1.3 Research approach

This dissertation focuses on the dynamic modeling of composite structures with distributed MFC transducers, involving non-homogeneous composite host materials, MFC transducers, and experimental testing. In the view of the research objectives, the following research approach is defined:

1. An analytical characterization of anisotropic piezoelectric transducers, which are integrated into laminated composite plates will be carried out by using the generalized Hamilton's principle. The assessment of the existing solutions is considered. Then, a new characterization of the inverse piezoelectric effect for anisotropic piezoelectric transducers can be

proposed. Accordingly, the corresponding direct piezoelectric effect will be determined by the electrical boundary conditions.

2. Based on the derived analytical solutions, a FEM-based semi-analytical modeling approach can be developed in order to relax the dependency between structural and piezoelectric modelings. More importantly, an effective modeling approach should be developed in order to generate low-order system models for the research objectives. The accuracy and sensitivity analysis of the developed approach is required for evaluating its performance and limitations.

3. The proposed modeling approach needs to be validated by experimental data. Firstly, laminated composite plates with integrated rectangular MFC transducers will be manufactured. Then, both the modal parameters and the dynamic responses of the system will be experimentally determined for the validations.

4. A vibro-acoustic study of a composite plate with integrated MFC transducers is planed. The developed approach should be able to deal with vibro-acoustic systems. Along with it, experimental validations need to be performed. The features of MFC transducers in vibro-acoustics will be investigated to explore the possibility for the usage of MFC transducers in vibro-acoustics.

1.4 Contributions and achievements

The research approach has allowed us to achieve the following contributions:

Characterization of non-homogeneous laminated composite plates with integrated MFC transducers

On the one hand, the generalized Hamilton's principle is reviewed for non-homogeneous anisotropic plates with spatially distributed anisotropic rectangular piezoelectric transducers. The placement of the transducers is expressed by spatial distributions on the plate so that the mechanical influences of the transducer can be included in the analysis. The equivalent loads that describe the inverse piezoelectric effect of the integrated transducer on the plate are derived. Equivalent forces are proposed as a novel inverse piezoelectric coupling. On the other hand, the direct piezoelectric effect of the transducer is derived from the electric boundary conditions of piezoelectric systems, which has the same coupling patterns as the equivalent force, hence, the reversibility of piezoelectric effect is ensured.

Development of an equivalent dynamic modeling approach

An equivalent dynamic modeling approach of laminated composite structures with integrated MFC transducers is developed. The main objective of the approach is to generate structure-preserving low-order system models for dynamic applications. The piezoelectric-induced mechanical properties can be included in system models. The composite plate, the MFC transducers and other physical subcomponents in the system can be individually treated in the modeling.

Experimental validation

Laminated composite plates with integrated MFC transducers are manufactured. A modal testing of the studied plates is elaborately carried out. The frequency responses of both the direct and inverse piezoelectric effects of the integrated transducers are measured. By doing so, the proposed modeling approaches are rigorously validated by the experimental data.

Vibro-acoustic study of MFC transducers integrated into composite plates

The vibro-acoustic study of a laminated composite plate with spatially distributed MFC transducers is carried out with the KU Leuven soundbox: (1) the vibro-acoustic reciprocity is mathematically proved and extended to the integrated MFC transducer; (2) the ESM approach is applied to vibro-acoustic problems for generating stable structure-preserving low-order models; (3) the piezoelectric vibro-acoustic reciprocal relations are verified by the low-order model in both the frequency and time domains. The study provided a basic understanding of the piezoelectric transducers' application in vibro-acoustics.

1.5 Outline of the dissertation

Chapter 1 The present chapter describes the research context, motivation, objectives, and research approach of the dissertation. The main contributions and achievements of the dissertation are highlighted.

Chapter 2 The chapter briefly introduces piezoelectricity, and selectively presents some well-known applications. The existing studies of MFC transducers are elaborated. Regarding piezoelectric modeling, the modeling hypothesis are first reviewed. Then, the material characterization of MFC transducers is presented. Finally, a detailed review of the modeling of MFC transducers is expounded.

Chapter 3 The constitutive relations of both laminated composite plates and MFC transducers are described. The generalized Hamilton's principle of an anisotropic plate with integrated anisotropic piezoelectric transducers is derived, and then, the equivalent loads of the integrated transducer are obtained. The assessments of different equivalent loads are expressed. A new characterization of the inverse piezoelectric coupling is proposed in terms of forces and the corresponding direct piezoelectric coupling is also derived. Finally, the accuracy of the proposed equivalent forces is analyzed.

Chapter 4 An Equivalent Force Modeling (EFM) approach is presented. A FEM method is adopted to model the structural dynamics of composite plates with integrated MFC transducers. Then, the implementation of the proposed piezoelectric couplings is described. After that, the ESM approach is presented to generate structure-preserving low-order system models. Finally, the sensitivity analysis of the proposed solution is carried out. Both the size and piezoelectric fibrous orientation of MFC transducers are considered as sensitive parameters.

Chapter 5 The structural dynamic validation of the proposed modeling methods is presented in this chapter. The tested subjects are presented in the beginning. The modal testing methods are expressed in detail and some interesting observations are illustrated. Then, both the EFM and ESM models of the tested plate are presented. The two models are validated in detail by the experimental data. Finally, two numerical study cases are given in order to demonstrate the odds of the ESM approach.

Chapter 6 This chapter describes a vibro-acoustic study of a laminated composite plate with integrated MFC transducers, which is conducted on the KU Leuven soundbox. The vibro-acoustic reciprocity is reviewed, and then, the piezoelectric vibro-acoustic reciprocal relation is derived. The modeling of the vibro-acoustic system is presented in detail. The ESM approach is used to generate a stable structure-preserving low-order model. Finally, the piezoelectric reciprocal relation is verified in both frequency and time domains. Simple acoustic source qualification study case is given to demonstrate the application of the derived piezoelectric reciprocal relations.

Chapter 7 The overall conclusions of the dissertation are sketched and some suggestions for future research and applications are given.

Chapter 2

State-of-the-art on dynamic modeling of MFC transducers

This chapter presents the existing work in the literature which is related to this dissertation's research. A brief introduction of piezoelectricity is given, and different modeling methods regarding to MFC transducers and their application are emphatically reviewed in order to provide sufficient fundamentals for the study.

2.1 Piezoelectricity

Piezoelectricity, a coupling between electric and mechanical fields, was discovered by the Curie brothers in 1880 [28]. It is a reversible process including both the direct and inverse piezoelectric effects. The direct piezoelectric effect is subject to the internal electric charge which is generated by a mechanical input on a piezoelectric material, and the inverse piezoelectric effect is that an operational electric field which is applied to the material generates mechanical deformations [29].

Many piezoelectric materials have been developed, and piezoceramics are the most used in engineering application [30–33]. As shown in Figure 2.1, the piezoceramics are naturally characterized by random piezoelectric oriented grains so that the piezoelectric effect exhibits only after a polarization [34, 35]. During a poling process, the electric dipole in each grain can be reoriented to a direction close to the direction of the applied electric field when the temperature is above the Curie point. But they are remained in the oriented direction by reducing the temperature under the Curie point. This process leads to a non-null external electric dipole moment which called remnant polarization. Hence, the piezoelectric materials possess some remnant of deformation after the polarization.

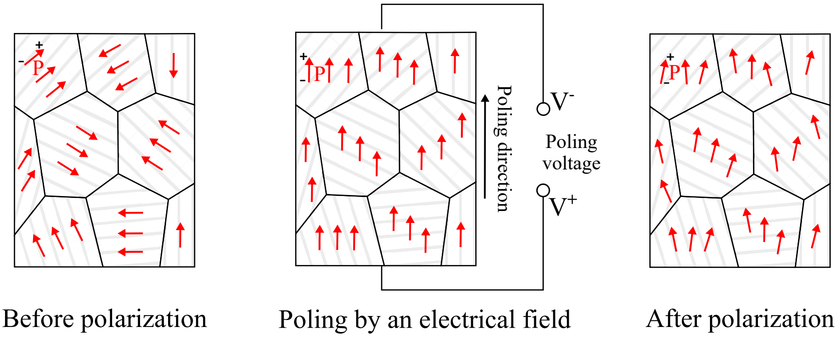

Figure 2.1: Polarization of piezoceramics

Linear piezoelectric effect includes the linear electrical behavior of the material and linear elastic deformation. The linear electrical behavior of the material is expressed as follows [36]:

$$\boldsymbol{D} = \boldsymbol{\epsilon}\boldsymbol{E} \tag{2.1}$$

where, $\boldsymbol{D}$ and $\boldsymbol{E}$ are the electric displacement and electric field vectors, respectively. The dielectric matrix is noted as $\boldsymbol{\epsilon}$. The linear elastic deformation is described by the Hooke's law [37]:

$$\boldsymbol{S} = \boldsymbol{s}^E\boldsymbol{T} \tag{2.2}$$

in which, $\boldsymbol{T}$ and $\boldsymbol{S}$ are the stress and strain vectors, respectively. The compliance matrix of the material is $\boldsymbol{S}^E$ under a constant electric field. The coupled equations of the two effect in strain-charge form can be written as:

$$\boldsymbol{S} = \boldsymbol{s}^E\boldsymbol{T} + \boldsymbol{d}^T\boldsymbol{E} \tag{2.3a}$$

$$\boldsymbol{D} = \boldsymbol{d}\boldsymbol{T} + \boldsymbol{\epsilon}^{\boldsymbol{T}}\boldsymbol{E} \tag{2.3b}$$

where, the piezoelectric effects are described by the piezoelectric strain constants d $[m/V]$, and $\square^T$ denotes the transposition of a matrix. The full piezoelectric constitutive equations are described as follows [38]:

$$\begin{Bmatrix} S_1 \\ S_2 \\ S_3 \\ S_4 \\ S_5 \\ S_6 \\ D_1 \\ D_2 \\ D_3 \end{Bmatrix} = \begin{bmatrix} s_{11}^E & s_{12}^E & s_{13}^E & 0 & 0 & 0 & 0 & 0 & d_{31} \\ s_{21}^E & s_{22}^E & s_{23}^E & 0 & 0 & 0 & 0 & 0 & d_{32} \\ s_{31}^E & s_{32}^E & s_{33}^E & 0 & 0 & 0 & 0 & 0 & d_{33} \\ 0 & 0 & 0 & s_{44}^E & 0 & 0 & 0 & d_{25} & 0 \\ 0 & 0 & 0 & 0 & s_{55}^E & 0 & d_{15} & 0 & 0 \\ 0 & 0 & 0 & 0 & 0 & s_{66}^E & 0 & 0 & 0 \\ 0 & 0 & 0 & 0 & d_{15} & 0 & \epsilon_{11}^{\boldsymbol{T}} & 0 & 0 \\ 0 & 0 & 0 & d_{25} & 0 & 0 & 0 & \epsilon_{22}^{\boldsymbol{T}} & 0 \\ d_{31} & d_{32} & d_{33} & 0 & 0 & 0 & 0 & 0 & \epsilon_{33}^{\boldsymbol{T}} \end{bmatrix} \begin{Bmatrix} T_1 \\ T_2 \\ T_3 \\ T_4 \\ T_5 \\ T_6 \\ E_1 \\ E_2 \\ E_3 \end{Bmatrix} \tag{2.4}$$

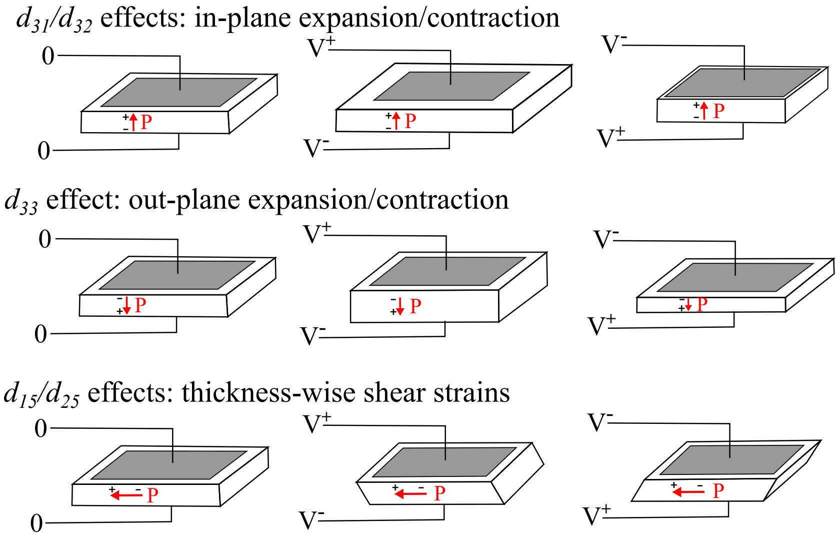
d31/d32 effects: in-plane expansion/contraction
0
0
V+
V-
V-
V+
+
-
P
d33 effect: out-plane expansion/contraction
0
0
V+
V-
V-
V+
-
+
P
d15/d25 effects: thickness-wise shear strains
0
0
V+
V-
V-
V+
+
-
P

Figure 2.2: Different piezoelectric effects on a piezoelectric element

It is worthwhile to mention that the Vigot notation [39] is commonly used in piezoelectric constitutive equations. The index $[1, 2, 3, 4, 5, 6]$ are corresponding to $[xx, yy, zz, yz, xz, xy]$ in a Cartesian coordinate system, respectively. Figure 2.2 shows all the piezoelectric effects in Equation (2.4). We can observe that d_{31} is the piezoelectric coupling between the strain S_1 and the electric field E_3, where the deformation direction and the poling direction of the material are perpendicular with each other. A similar case can be found for the piezoelectric coupling d_{32} too. However, d_{33} is the piezoelectric coupling between the stain S_3 and E_3, in this case, the poling direction and the deformation direction are in line with each other. The piezoelectric effects d_{15} and d_{25}, which are not related to the study in the dissertation, are the couplings between the electric fields and transverse shear deformations. All the piezoelectric effects are shown in Figure 2.2.

Equation (2.3a) and (2.3b) can be converted into different forms by using the linear electric behavior in Equation (2.1) or the linear elastic deformation in Equation (2.2) [29]. For example, By using Equation (2.2), the stress-charge form can be obtained as follows:

$$\boldsymbol{T} = \boldsymbol{Q}^E \boldsymbol{S} - \boldsymbol{e}^T \boldsymbol{E} \tag{2.5a}$$

$$\boldsymbol{D} = \boldsymbol{e}\boldsymbol{S} + \boldsymbol{\epsilon}^{\boldsymbol{S}^T} \boldsymbol{E} \tag{2.5b}$$

where, $\boldsymbol{Q}^E$ is the elasticity matrix of the material in a constant electric field with $\boldsymbol{Q}^E = [\boldsymbol{s}^E]^{-1}$. The relation between $\boldsymbol{d}$ and $\boldsymbol{e}$ is actually:

$$\boldsymbol{e}^T = \boldsymbol{Q}^E \boldsymbol{d}^T. \tag{2.6}$$

The full piezoelectric constitutive equations can be given as follows:

$$\begin{Bmatrix} T_1 \\ T_2 \\ T_3 \\ T_4 \\ T_5 \\ T_6 \\ D_1 \\ D_2 \\ D_3 \end{Bmatrix} = \begin{bmatrix} Q^E_{11} & Q^E_{12} & Q^E_{13} & 0 & 0 & 0 & 0 & 0 & -e_{31} \\ Q^E_{21} & Q^E_{22} & Q^E_{23} & 0 & 0 & 0 & 0 & 0 & -e_{32} \\ Q^E_{31} & Q^E_{32} & Q^E_{33} & 0 & 0 & 0 & 0 & 0 & -e_{33} \\ 0 & 0 & 0 & Q^E_{44} & 0 & 0 & 0 & -e_{25} & 0 \\ 0 & 0 & 0 & 0 & Q^E_{55} & 0 & -e_{15} & 0 & 0 \\ 0 & 0 & 0 & 0 & 0 & Q^E_{66} & 0 & 0 & 0 \\ 0 & 0 & 0 & 0 & e_{15} & 0 & \epsilon^{\boldsymbol{S}}_{11} & 0 & 0 \\ 0 & 0 & 0 & e_{25} & 0 & 0 & 0 & \epsilon^{\boldsymbol{S}}_{22} & 0 \\ e_{31} & e_{32} & e_{33} & 0 & 0 & 0 & 0 & 0 & \epsilon^{\boldsymbol{S}}_{33} \end{bmatrix} \begin{Bmatrix} S_1 \\ S_2 \\ S_3 \\ S_4 \\ S_5 \\ S_6 \\ E_1 \\ E_2 \\ E_3 \end{Bmatrix} \tag{2.7}$$

The piezoelectric constants $\boldsymbol{e}$ are the coupling coefficients between stresses and electrical field in the corresponding direction.

2.2 Advances of piezoelectric transducers

A simple piezoelectric transducer consists of a thin polarized piezo-patch with a pair of electrodes on the top and bottom surface of the patch. The thin piezo-patch can only have one work mode in the Figure 2.2 according to its poling direction. Let's take the d_{31}/d_{32} work mode as an example. It can only perform in-plane expansion/contraction when an operational voltage is applied to it. However, the piezo-patch can be easily integrated into a host structure, as shown in Figure 2.3. When it functions as an actuator, the asymmetric deformation in the thickness-wise of the structure results in both the local contraction/extension and bending at the same time. Conversely, the deformation of the piezo-patch will lead to a direct piezoelectric effect on the transducer too.

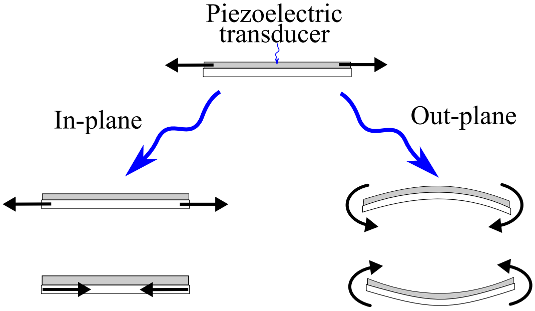

Figure 2.3: Work principle of a thin piezoelectric transducer

Based on the work mode of the thin piezo-patch, different piezoelectric actuators have been designed to generate different performances, such as piezo-stack actuators and piezo-benders, as shown in Figure 2.4. They consist of multilayer piezoelectric patches with electrodes in each other. The small distance between two neighboring electrodes can generate a large electric field with for a given operational voltage. On the piezo-stack actuators, all the patches deform in the same way under an operational voltage. Hence, they can generate large actuation force/deformation. The piezo-bender in Figure 2.4is composed by two piezoelectric layers. The difference in deformation between the two layers leads to bending deformations.

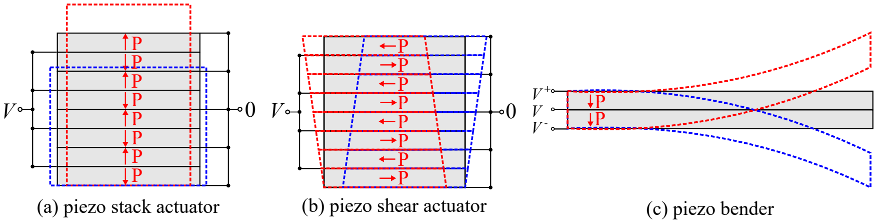

(a) piezo stack actuator (b) piezo shear actuator (c) piezo bender

Figure 2.4: Multilayer piezoelectric actuators (The red and blue dash-lines represent the deformations of the actuators)

All the mentioned piezoelectric transducers/actuators are made of monolithic piezoelectric layers and their high stiffness affords a large actuation force and a voltage-dependent actuation authority [40]. However, the limitations of monolithic piezoelectric transducers are pronounced too [14, 41]. The brittle nature makes them damage easily. Moreover, the high mass density and high stiffness may severely modify the dynamics of lightweight, flexible host structures. last but not the least, the limited mechanical flexibility makes them difficult to adapt non-flat host structures too.

Composite piezoelectric transducers have greatly overcome these limitations. The main idea of the composite transducers is to embed the piezoelectric fibers into an epoxy matrix so that the hybrid transducers have high performance, good flexibility, and high durability. Various advanced piezoelectric transducers have already been commercialized, such as MFC and Active Fiber Composite (AFC)[14, 41]. The MFC and AFC transducers share the same mechanism. But the rectangular piezoelectric fibers of MFC transducers lead to a higher fiber volume fraction than AFC, which uses the round piezoelectric fibers. As a result, the performance of MFC transducers is almost 1.5 times larger than AFC transducers. The experimental results also proved that the actuation performance of MFC is better than many other piezoelectric actuators after more than 90 million electrical cycles [14, 42]. Besides, the rectangular piezoelectric fibers make MFC transducers easier and less expensive to manufacture than AFC transducers. Hence, the MFC transducer is one of the most promising choices for engineering application. There are different kinds of MFC transducers: MFC-d31, MFC-d33 and MFC-d15, as shown in Figure 3.4-2.8. The MFC transducers commonly have a rectangular geometry. And they usually consist of five layers: two Kapton layers, two electrode layers, and one active layer. In the following schematic representation figures from [43], the acrylic layers are considered as an individual layer. Besides, it is worthwhile to notice that the MFC transducers produced by the different manufacturer could have different kinds of electrodes according to their production techniques.

The MFC-d31 transducer has a poling direction in the thickness-wise of the transducer. A pair of continuous electrodes is used in the transducer in the figure so that the electric field is uniform in the thickness-wise of the transducer. Thereby, both the d_{31} and d_{32} effects in the $X - Y$ plan can be used for the sensing/actuation. When it is used as an actuator on a host structure, it can generate both expansion/contraction and bending motions in both X and Y directions.

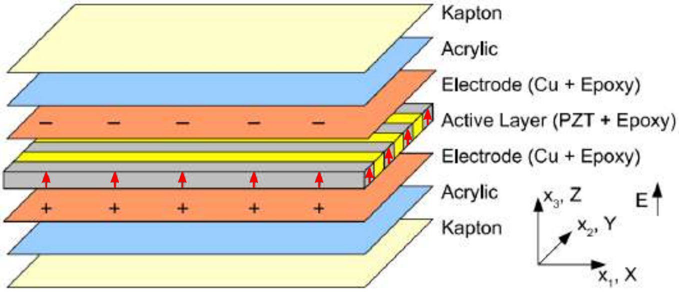
Kapton
Acrylic
Electrode (Cu + Epoxy)
Active Layer (PZT + Epoxy)
Electrode (Cu + Epoxy)
Acrylic
Kapton
x3, Z
x2, Y
x1, X
E

Figure 2.5: Schematic representation of MFC-d31 [43] ((X, Y, Z) represents the material coordinates system and (x_1, x_2, x_3) denote the structural coordinates system)

The MFC-d33 transducer has a complex poling direction along with the piezoelectric fiber according to the neighboring positive and negative electrodes fingers. The d_{33} effect, which is usually much larger than d_{31} and d_{32} has a unidirectional sensing/actuation. It can generate a unidirectional expansion/contraction and bending behaviors on a host structure when it works as an actuator. The performance of the transducer increases with the distance increasing between the adjacent electrode fingers, and a high operational voltage is required to generate the necessary electric field. That is due to the fact that the electrodes generate a non-uniform electric field, as shown in Figure 2.7. A larger distance between the adjacent electrode fingers can reduce the dead zone and generate a more uniform electric field in the piezoelectric fibers.

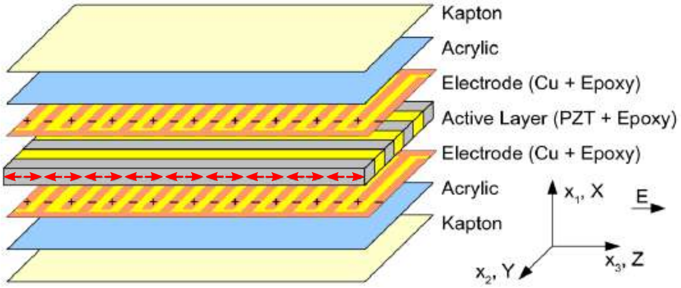
Kapton
Acrylic
Electrode (Cu + Epoxy)
Active Layer (PZT + Epoxy)
Electrode (Cu + Epoxy)
Acrylic
Kapton
x1, X
E
x3, Z
x2, Y

Figure 2.6: Schematic representation of MFC-d33 [43] ((X, Y, Z) represents the material coordinates system and (x_1, x_2, x_3) denote the structural coordinates system)

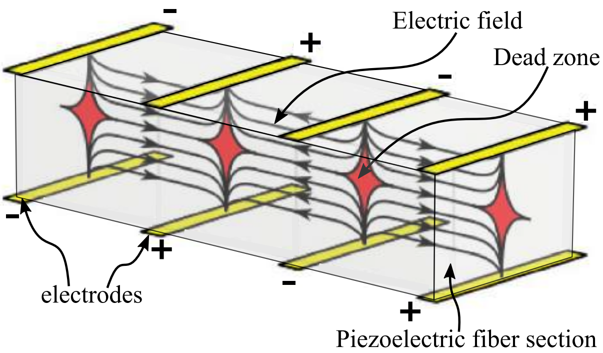
Electric field
Dead zone
electrodes
Piezoelectric fiber section
-
+
-
+
-
+
-
+

Figure 2.7: Electric field distribution on a rectangular piezoelectric fiber of an MFC-d33 transducer [44]

The motivation for the development of MFC-d15 is to use the large d_{15} effect, which directly couples to transverse shear strains [45]. As shown in the Figure 2.8, the poling direction is along with the piezoelectric fibrous direction. A uniform electric field is generated in the thickness-wise of the transducer by a pair of continuous electrodes. The packaging of different components significantly reduces the effective electromechanical coupling of this kind of transducer. A possible reason is owing to the small thickness of the transducer. Nevertheless, it can also be used in where the shear deformations could be problematic. Besides, MFC-d15 transducer could also generate bending deformation through its transverse shear deformations. Consequently, it can be placed close to the boundary or embedded in the thickness-wise of a host structure to ensure its performance.

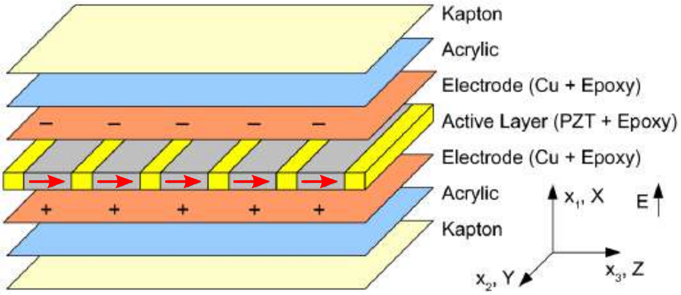
Kapton
Acrylic
Electrode (Cu + Epoxy)
Active Layer (PZT + Epoxy)
Electrode (Cu + Epoxy)
Acrylic
Kapton
x_1, X
E
x_2, Y
x_3, Z

Figure 2.8: Schematic representation of MFC-d15 [43] ((X, Y, Z) represents the material coordinates system and (x_1, x_2, x_3) denote the structural coordinates system)

Various piezoelectric transducers have been developed for industrial application. We just reviewed some of them, which are widely used in engineering. Since the multilayer piezoceramic transducers (piezo-stack-actuator, piezo-shear-actuator, and piezo-bender) can generate complex deformations, advanced piezoelectric devices are able to be developed such as the piezoelectric motor [46]. Regarding to the MFC transducers, the effective properties of the MFC transducers should be characterized for modeling and designing of systems with integrated MFC transducers because they are laminated composites. The piezoelectric fibrous orientation which is not presented in monolithic is a crucial parameter for designing advanced piezoelectric systems. The changes in fibrous orientation lead to the changes in material properties and piezoelectric effect. The MFC-d31 and MFC-d33 transducers are more suitable for reducing noise and vibrations on flexible structures because they can directly generate large bending and membrane efforts on a host structure. The MFC-d15 transducer has a much more limited application, due to the low effective electromechanical coupling.

2.3 Application of piezoelectric transducers for noise and vibration control

Piezoelectric transducers not only can generate large actuation forces but also can interact with dynamic systems in a wide frequency range up to megahertz [47]. A great achievement has been made in their application, for example, smart aircraft [48, 49], modal testing of lightweight flexible structures [14] and structural health monitoring [50, 51]. The most well-known application is structural vibration control. Both active and passive control of structural vibrations can be implemented by piezoelectric transducers. The active vibration control actively applies mechanical inputs to counteract the vibrations on a structure. The main components of an active control system are the plant, actuator, sensors and controllers, as shown in Figure 2.9. The piezoelectric transducers are used as actuators in the figure, They are possible to be used as sensors too [52, 53]. Different types of control algorithms are designed for reducing vibrations. LQG controller design is reported in [54, 55]. H_∞ controllers are developed in [27, 56]. These are centralized controllers which may create delay issues of control input computing. Hence, decentralized/distributed controller are investigated in [56–58]. The nonlinear active vibration control is studied in [59, 60]. The major advantage of active vibration control is high damping performance without adding to much mass or reducing too much stiffness, compared to the conventional vibration suppression measures. However, active vibration control has power consumption, and a power amplifier is commonly required to increase the control effort. Besides, the active vibration control is model-based, a stable, accurate low-order model is critical for the high-performance controller design. The placement of the actuators/sensors influences their controllability/observability so that the optimal placement of the actuators/sensors should be identified [26, 27].

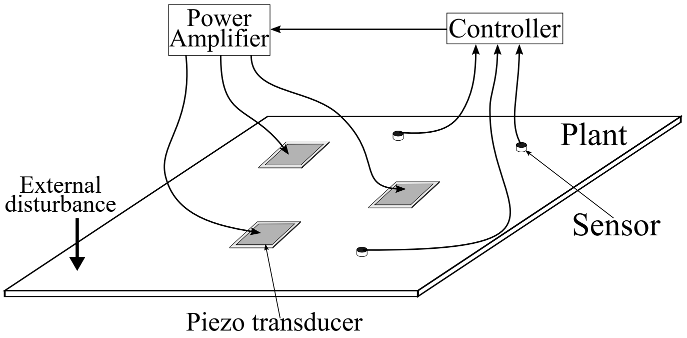

Figure 2.9: Schematic representation of active vibration control

The passive vibration control by using piezoelectric transducers is well-known for piezoelectric shunted damping. Different from the active vibration control, the piezoelectric transducers are used to convert mechanical energy to electric energy in the piezoelectric shunted damping. The direct piezoelectric effect caused by the motion of the host structure generates electrical energy. Then, the inverse piezoelectric effect of the shunted transducer generates a force, which counteracts the motion of the hot structure. Hence, an electrical network can be designed to dissipate energy from the host structures, as shown in Figure 2.10. Sensors, active control law design and power consumption are not required by piezoelectric shunted damping but are necessary for active vibration control. Nevertheless, it is essential to place the piezoelectric transducers at the optimal locations on a host structure for ensuring a high electromechanical efficiency. The piezoelectric shunt is not necessary model-based. However, it is vital to understand the dynamics of the system for designing the electrical shunt circuit. Wherefore, an accurate model of the system is preferred comparing to carrying on experiments. Besides, if the model is stable and preferable low-order, real-time simulations can be performed.

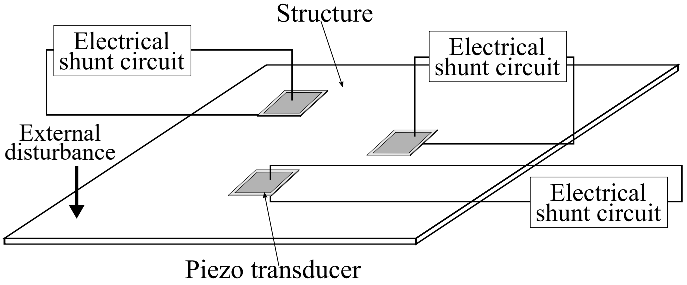

Figure 2.10: Schematic representation of piezoelectric shunted damping (The electrical shunt circuits are connected to the electrodes of each transducer)

In general, there are two types of piezoelectric shunted damping: inductance-resistance ($L - R$) shunted damping and negative capacitance shunted damping. The $L - R$ shunted damping are investigated in [61–65]. The $L - R$ circuit together with the capacitance of the transducer C_p results in a second-order electric dynamics. Its natural frequency matches the natural frequency of a mode on the host structure. A damping effect can be led into the mode through the resistance R. It is important to mention that an unrealistic large inductance L can be required by a simple $L - R$ circuit that connected to a piezoelectric transducer in parallel. Therefore, complex electrical circuit typologies that can perform optimal shunted damping with lower inductance are reported in [66–69]. Furthermore, the $L - R$ shunted damping solution is limited in a narrow frequency bandwidth (on the natural frequency of a mode). An alternative is to use multiple $L - R$ shunt units to expand the frequency bandwidth, as shown in Figure 2.10. However, the negative capacitance shunted damping can reduce the structural vibration in a broadband frequency range. The effect caused by the capacitance of the piezoelectric transducer can be eliminated by the negative capacitance generated from an equivalent electrical circuit so that the resistance in the circuit can effectively dissipate energy on the host structure in a wide frequency bandwidth [65, 70–73].

Both the active and passive vibration controls can be used in structural-acoustic interaction systems so that noise due to sound radiation and sound transmission can also be attenuated. The active and passive vibration controls are effective in the low-frequency range, while dissipative material such as visco-elastic or porous materials, or are efficient for the high-frequency range. Noise and vibrations suppression are elaborated in [6, 74]. Analytical modeling is carried out, and both the sound radiation control and sound transmission control of the piezoelectric layered plates are investigated. Large piezo-patches are distributed overall the host structure in [6], and the actuators can be considered as an additional layer overall the host structure. But piezoelectric materials generally have large mass density so that it is not recommended to use too many large piezo-patches for noise and vibrations control of lightweight structures. It is more attractive to place piezoelectric transducers on the optimal locations to prevent the noise and vibrations. In [75, 76], active structural acoustic control of rotating machinery is investigated. Special designed piezoelectric actuators are integrated into the rotating machinery to stop the noise transmission path, and the dynamics of the system is characterized for designing controllers. The $L-R$ shunted damping with small piezoelectric transducers is used in [77] for reducing the sound pressure in an acoustic cavity. FEM model is generated and reduced through a subspace projection technique so that the performance of the damping solution can be efficiently evaluated.

Effective modeling of piezoelectric systems is essential for proper design and deployment of dynamic control units in noise and vibrations control. A stable low-order model is crucial for designing controller in active measures. An efficient means to determine the dynamics of the system is also important to design the electrical shunt circuits for passive control. Optimal actuators/sensors placement should be determined in both cases. However, the influences and changes in the properties of the actuators/sensors are not considered in the optimal placement methods. The optimal piezoelectric fibrous orientation that results in the optimal material and piezoelectric properties at a fixed position on the structure allows for gaining a better actuation/sensing performance in noise and vibrations control.

2.4 Application of piezoelectric transducers for energy harvesting

Mechanical energy can be converted into electrical energy by piezoelectric, electromagnetic, energy sinks and electrostatic transducers. Piezoelectric materials are widely investigated for energy harvesting due to their high energy density [78]. Primary study of piezoelectric energy harvesting is based on linear beam and plate theories. The schematic representation of piezoelectric harvesters is given in Figure 2.11. Piezoelectric bimorph and unimorph configurations are adopted in most of studies. The electrical energy is extracted from the system through the electrodes by using a power management circuit. The proof-mass on the tip of the cantilever structure for either increasing the kinetic energy of the system and/or adjusting the natural frequency of the system. d_{31} and d_{33} effects of the piezoelectric element are generally used for energy conversions, and the corresponding work modes are given in Figure 2.12.

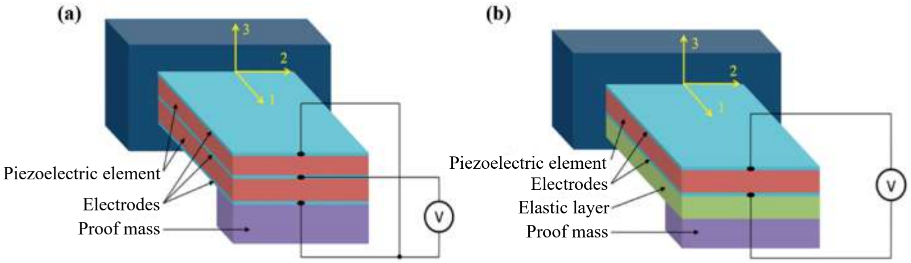
(a)
3
2
1
Piezoelectric element
Electrodes
Proof mass
V
(b)
3
2
1
Piezoelectric element
Electrodes
Elastic layer
Proof mass
V

Figure 2.11: Schematic representation of piezoelectric energy harvesters (a) Bimorph structure (b) Unimorph structure [79]

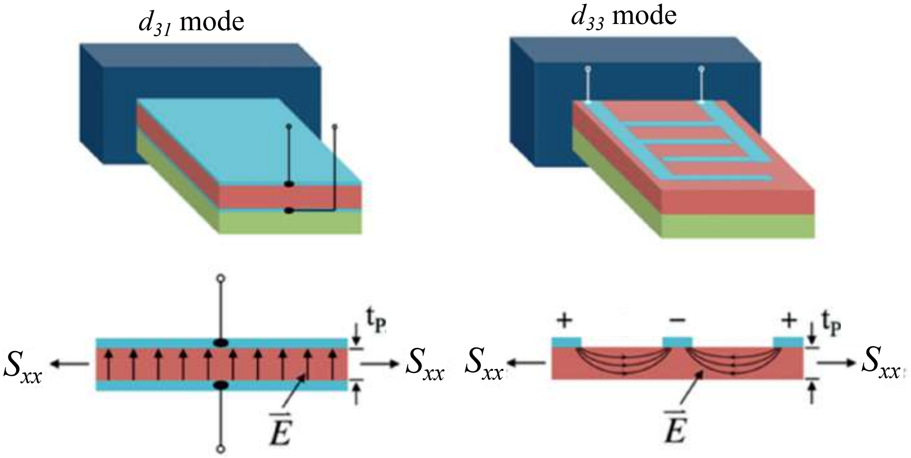
d_{31} mode
d_{33} mode
S_{xx}
S_{xx}
t_P
$\vec{E}$
+
−
+
t_P
S_{xx}
S_{xx}
$\vec{E}$

Figure 2.12: Two modes of piezoelectric conversion of mechanical strain into Electric field E [79]

Analytical modeling and experimental validation of a piezo-patch on a clamped plate are reported in [80]. The predicted results are quite obviously different from the experimental data. The imperfect clamped boundary condition in the experiment influences the validation. Neglecting the mechanical influences of the piezo-patch to the host plate in the analytical solution also affects the predicted results. MFC transducers are also used for vibration-based energy harvesting on a cantilever beam in [81]. A prototype is developed, and a FEM model is carried out. The experimental validation is limited up to $80Hz$, and an obvious mismatch can be observed on the natural frequency of the second structural mode even though the prototype used simple Aluminum beams integrated with small MFC transducers. Moreover, vibration-based piezoelectric energy harvesting using a circular piezoelectric wafer is presented in [82]. The perfect structural boundary conditions in modeling is corrected in order to have an excellent experimental validation. Hence, even in the case of a simple structure such as piezoelectric transducer-integrated plates, it is still a challenging task to accurate and efficient predict the responses of a real piezoelectric system.

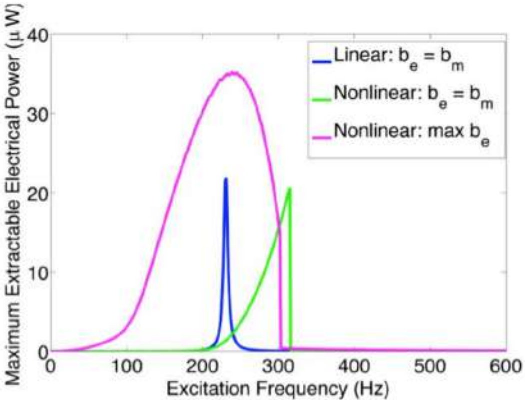

Figure 2.13: Maximum extracted electrical power comparison between a linear and a nonlinear energy harvester in [83]

Based on the simple piezoelectric energy harvesting mechanisms, essential technology can be investigated for developing low-power, maintenance-free electrical devices. Advanced piezoelectric energy harvesting systems have been already developed in the past decade. Piezoelectric micro-electromechanical system (MEMS) is one of the most attractive strategies for developing self-power micro-systems [79]. Different kinds of MEMS have been already developed, and the size of these devices varies from sub-micron to millimeter [84–86]. However, several key factors should be emphasized here for designing piezoelectric harvesters such as MEMS. Firstly, only a small portion of mechanical energy can be harvested from a vibration source. The extracted power is inversely proportional to the resonance frequency of the piezoelectric system [87]. As a result, the low-frequency design is favorable to increase the extracted power. Secondly, the impedance of the power management circuit should be the complex conjugate of the vibration source impedance in order to maximize the power extraction [88]. Thirdly, the output power of piezoelectric energy harvesting systems is frequency dependent. The harvester will convert mechanical to electrical energy more efficient when the frequency of the vibration source is close to the fixed natural frequency of the device. Thereby, a nonlinear energy harvester allows for maximizing the output power when external vibration source has variable frequency [83, 89]. The nonlinearity may come from magnetic force or constrained mechanical structures such as the cases in [90–92]. The power bandwidth of a nonlinear harvester is much larger than a linear harvester, as the example shown in Figure 2.13.

MFC transducer is not a mainstream option for energy harvesting. We can observe that the piezoelectric energy harvesters of small sizes are more attractive for the power supply of micro-systems. It also can be very challenging and costly to miniaturize the size of MFC transducers. Besides, there are proper methods for integrating the piezoelectric material into MEMS [79]. Moreover, the power density of MFC transducers should be small than monolithic piezoelectric materials, due to the epoxy in the active layer of MFC transducers. Nevertheless, MFC transducers can be used for large-scale piezoelectric harvesting systems such as human motion energy harvesting [94] and energy harvesting from vibrating structures [81, 95]. In these cases, it is critical to optimize the placement and piezoelectric fibrous orientation of the MFC transducers for increasing the extracted energy. The MFC-d31 and MFC-d33 transducers are most widely used in these researches, and the MFC-d15 transducer is not attractive which is due to the fact that current research on energy harvesting is based on bending and membrane behaviors of thin piezoelectric structures.

2.5 Nonlinearity of piezoelectric materials

When polarized piezoelectric materials are driven by electrical inputs, their nonlinearity is usually expressed by hysteresis and creep. Hysteresis is that the output displacement of the material depends on both the currently applied electric input and some values of the electrical input in the past, as shown in Figure 2.14. It is more prominent in long operating ranges, and it can be reduced by keeping the small amplitude of operating voltage. Creep is caused by the remnant of polarization in piezoelectric materials. As shown in Figure 2.15 When a constant voltage is applied to the transducer, its deformation continuously changes over time, due to the response of remnant polarization. Creep is more significant in slow and static application. For some input voltage profiles, one can also observe the simultaneous influence of hysteresis and creep on displacement responses [96].

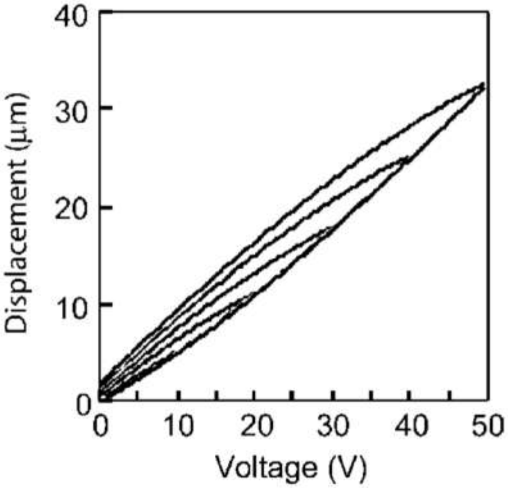

Figure 2.14: Displacement-voltage hysteresis in a typical piezoceramic actuator [97]

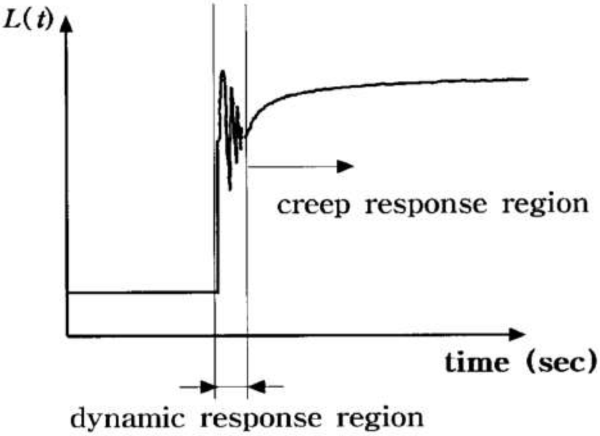

Figure 2.15: Creep over time of a typical piezoceramic actuator [98]

The existence of hysteresis and creep limits the performance of piezoelectric transducers so that it is highly desirable to compensate for them [99]. When a linear system assumption/model is used in real application, a local feedback loop can be designed for reducing their influences [12, 96, 100–102]. In this case, the piezoelectric devices can have a virtual linear performance or a linear mapping between the input and output [103]. The hysteresis effect can be described by various models such as the Jiles-Atherton model [104] and the Maxwell model [105] based on physical principles; the Prandtl-Ishlinskii model [12, 106], Dahl model [107] and Duhem model [108] based on mathematical descriptions. The Duhem model has a smaller modeling error comparing to the other hysteresis models because it includes both the electrical and mechanical domains. Parameter identification using experimental data or optimization techniques is required for making the model reflect the real system performance better [99, 106], where linear time-invariant model [109, 110] and logarithmic model [96, 111] can be introduced into the hysteresis model.

Nonlinear piezoelectric system modeling can also be performed. It has been observed that the piezoelectric and dielectric coefficients depend on the applied electric field [112, 113]. Then, it appears that the nonlinearity can be seen as an electric field- or induced strain-dependence of the piezoelectric coupling coefficients [114]. Nonlinear FEM methods are developed based on this observation. The first FEM method to model nonlinear bending/twisting responses under increasing applied electric field is based on strain concept [115]. A nonlinear FEM approach is reported in [116]. Piezoelectric constitutive relations are extended to include quadratic and cubic nonlinear terms. Modeling of finite deformation piezoelectric material behavior coupling transient electrical and mechanical fields is reported in [117]. A wavelet transformation induced multi-time scaling algorithm is developed for enhancing the computational efficiency of dynamic piezoelectric simulations. These work provide new possibilities to predict the behaviors of piezoelectric structures better.

Hence, the nonlinearity imposes difficulty for the use of piezoelectric transducers in applications. Two main approaches can be used to deal with them. The first one is to create a local closed-loop on a linear system model to compensate for them in practice. The second one is to generate nonlinear models directly. The nonlinearity of piezoelectric transducers can benefits engineering applications too. For example, a nonlinear skin is developed in [118] for vibration attenuation. A piezoelectric transducer is used for introducing the nonlinearity to the system. It is also used for nonlinear piezoelectric energy harvesting too in [119]. In this dissertation, the nonlinearity of piezoelectric transducers is not investigated. Effectively modeling of linear piezoelectric structures, which can be efficiently used for designing advanced control algorithms for noise and vibrations control, are carried out. However, it is important to mention that the nonlinearity of piezoelectric transducers should be compensated for ensuring their performance in practical application.

2.6 Modeling of MFC transducers integrated into a thin host structure

The above mentioned application require accurate system models for predicting the dynamics of the system and designing control solutions. Hence, comprehensive modeling of structures with integrated MFC transducers is an important task. MFC-d31 and MFC-d33 transducers should be investigated because they are much more suitable for noise and vibrations control. The performance of these MFC transducers depends on both the piezoelectric fibrous orientation and placement on host structures. A thin but stiff host structure helps to improve the performance of the integrated MFC transducers [120, 121] so that beams, plates, and shells are commonly investigated in the mentioned application because the large deformation of host structures ensures the performance of the integrated transducers. The following study analyzes plate-type host structures with integrated MFC transducers because they are one of the most used classes in engineering.

2.6.1 Modeling hypothesis

An inspection of the two-dimensional modeling hypothesis is essential for the study of this dissertation. Plates are an important class of two-dimensional structures. They are flat structures, and the thickness of plates t_s is much smaller than the other two dimensions (length a and width b). They can be subdivided into three classes according to the ratio b/t_s [122]:

1. Thick plates have a ratio $b/t_s \leqslant 10$. Therefore, a three-dimensional mechanical assumption is necessary. All the components of stress, strain, and displacement fields are involved in the analysis of this type of structures.

2. Membranes have a ratio $b/t_s \geqslant 100$. A membrane mainly sustains the in-plane loads called membrane forces on its mid-surface so that they are devoid of bending behaviors.

3. Thin plates have a b/t_s ratio between 10 and 100. They form the most extensive class. Depending on the ratio of maximum deflection of the plate to its thickness w/t_s, the contributions of flexural and membrane forces may be different. Thereby, this category can be subdivided into two groups:

> Stiff plates have a ratio $w/t_s \leqslant 0.2$. They sustain external loads mostly by internal bending, twisting moments and shear forces. The deformation of mid-surface and the membrane forces can be neglected.
>
> Flexible plates have a ratio $w/t_s \geqslant 0.3$. The plates' deflection is followed by a stretching of the mid-surface. Hence, a flexible plate behaves like a combination of stiff plates and membranes. They carry external loads by the combined action of bending moments, shear forces and membrane forces.

It is mentioned in [122] that the above classification is conditional because the reference of a plate to one or another group depends on the accuracy of analysis and boundary conditions, etc. Restricted by the small strain variation of MFC transducers, only thin plates are studied in this dissertation. Thereby, either the Kirchhoff plate theory or the Mindlin-Reissner plate hypothesis and their variations are applicable in the study. The displacement field of a plate is given in Figure 2.16, in which, u, v and w are the translational components in x, y and z directions, respectively. β_x and β_y are the rotational components in y and x directions, respectively.

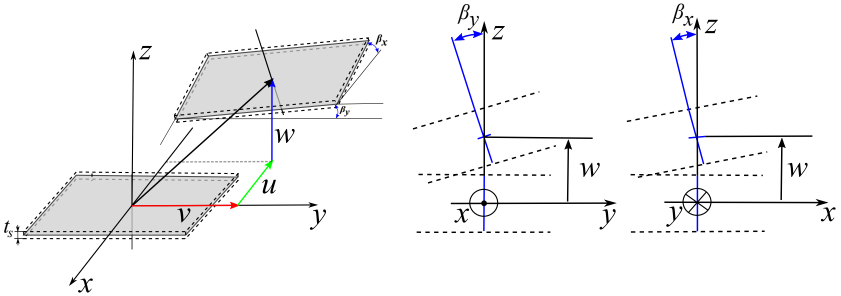

Figure 2.16: Displacement field of a plate

The Kirchhoff plate theory assumes that the thickness of the plate is remained during a deformation; the normal to the mid-surface remains straight and perpendicular to the mid-surface after the deformation too [123]. Then, β_x and β_y can be approximately expressed by the derivatives of the transverse displacement w. As a result, the Kirchhoff plate hypothesis significantly simplifies the strain-displacement relations. In the Mindlin-Reissner theory, the normal to the mid-surface remains straight but it is not always necessary to be perpendicular to the mid-surface of the plate [123]. The Mindlin-Reissner hypothesis [123] considers the rotational components β_x and β_y as independent variables in its strain-displacement relations. We can recognize that both of them decouple in-plane and bending motions of the plates in a similar way but with different physical variables for the bending behavior of the plate. Significant potential by using the Kirchhoff theory in this study is to create a straightforward coupling between the piezoelectric effect and the transverse displacement of a host plate, which has not been characterized in the literature.

Furthermore, there is also a class of modified plate theory, called Refined Plate Theories (RPT). It is like a combination of the Kirchhoff plate theory and Mindlin-Reissner theory. Huffington (1963) [124] firstly proposed that the deflection of a plate w can be split into two components: bending component w_b and shear component w_s. Subsequently, the RPT is adopted in many studies of composite structures and orthotropic plates [125–129]. Free vibrations of an orthotropic plate have been studied by using the RPT in [128]. A detailed check of the RPT is performed here to evaluate its potential for the modeling of plates with integrated MFC transducers. The displacement field of a plate that takes the high-order shear deformation into account in RPT is expressed as follows:

$$\begin{cases} u(x,y,t) = -z\frac{\partial w_b}{\partial x} + t_s\big[\frac{1}{4}\frac{z}{t_s} - \frac{5}{3}\big(\frac{z}{t_s}\big)^3\big]\frac{\partial w_s}{\partial x} \\ v(x,y,t) = -z\frac{\partial w_b}{\partial y} + t_s\big[\frac{1}{4}\frac{z}{t_s} - \frac{5}{3}\big(\frac{z}{t_s}\big)^3\big]\frac{\partial w_s}{\partial y} \\ w(x,y,t) = w_b(x,y,t) + w_s(x,y,t) \end{cases} \tag{2.8}$$

where, u and v are the in-plane displacement components in x and y directions, respectively. w_b and w_s are the bending and shear components of the transverse displacement w. The strain field can be written as follows according to the strain-displacement relations in [128]:

$$\begin{cases} S_{xx} = -z\frac{\partial^2 w_b}{\partial x^2} + t_s\big[\frac{1}{4}\frac{z}{t_s} - \frac{5}{3}\big(\frac{z}{t_s}\big)^3\big]\frac{\partial^2 w_s}{\partial x^2} \\ S_{yy} = -z\frac{\partial^2 w_b}{\partial y^2} + t_s\big[\frac{1}{4}\frac{z}{t_s} - \frac{5}{3}\big(\frac{z}{t_s}\big)^3\big]\frac{\partial^2 w_s}{\partial y^2} \\ S_{xy} = -2z\frac{\partial^2 w_b}{\partial x \partial y} + 2t_s\big[\frac{1}{4}\frac{z}{t_s} - \frac{5}{3}\big(\frac{z}{t_s}\big)^3\big]\frac{\partial^2 w_s}{\partial x \partial y} \\ S_{yz} = t_s\big[\frac{1}{4}\frac{z}{t_s} - \frac{5}{3}\big(\frac{z}{t_s}\big)^3\big]\frac{\partial w_s}{\partial y} \\ S_{zx} = t_s\big[\frac{1}{4}\frac{z}{t_s} - \frac{5}{3}\big(\frac{z}{t_s}\big)^3\big]\frac{\partial w_s}{\partial x}. \end{cases} \tag{2.9}$$

The stresses can be obtained through the Hooke's law [130]. Then, the bending moments M and shear force tau can be described as follows by integrating the stress components in the thickness-wise of the plate:

$$\begin{cases} M_{xx} = -D_{11}\frac{\partial^2 w_b}{\partial x^2} + D_{12}\frac{\partial^2 w_b}{\partial y^2} \\ M_{yy} = -D_{22}\frac{\partial^2 w_b}{\partial y^2} + D_{12}\frac{\partial^2 w_b}{\partial x^2} \\ M_{xy} = -2D_{66}\frac{\partial^2 w_b}{\partial x \partial y} \\ \tau_{yz} = D_{55}\frac{\partial w_s}{\partial y} \\ \tau_{zx} = D_{44}\frac{\partial w_s}{\partial x}. \end{cases} \tag{2.10}$$

Hence, we can observe from Equation (2.10) that the bending effect of the plate only depends on w_b. Also, the transverse shear forces depend on w_s. RPT uses a similar way according to the Kirchhoff plate theory to describe the bending effect on a plate. It uses a single variable w_s to express the transverse shear effect, which does not exist in the Kirchhoff plate theory. The transverse shear effect is included in the rotational variables β_x and β_y in the Mindlin-Reissner plate theory. Since the MFC-d31 and MFC-d33 transducers do not generate transverse shear deformations on a plate, and the Kirchhoff plate theory is sufficient to analytically investigate the piezoelectric coupling of the two types of MFC transducers on a host plate. This is also consistent with it the observation in [22]. However, the Mindlin-Reissner plate theory or RPT should be used to model MFC-d15 transducer, which generates transverse shear deformations on a host structure. It is also important to understand that a refined plate theory certainly improves the accuracy on mechanical modeling of a plate with integrated piezoelectric transducers.

2.6.2 Material characterization of MFC transducers

The modeling of structure integrated with MFC transducers could be problematic if the necessary material information is not complete. MFC transducers can be assumed to have transverse orthotropic mechanical properties, due to their laminated constitution. Since the thickness of MFC patches is small, the normal transverse strain is negligible. Hence, the mechanical property of MFC transducers normally are characterized by 4 elastic constants: The tensile Young's modulus Y_1 and Y_2 in 1 and 2 directions on the transducer, the shear modulus G_{12} Between 1 and 2 directions, and the Poisson's ratio ν_{12} (a ratio of transverse contraction strain in 2 to extension strain along 1 subject to a load in 1). The corresponding deformations of these four elastic constants are shown by (a), (b) and (c) in Figure 2.17.

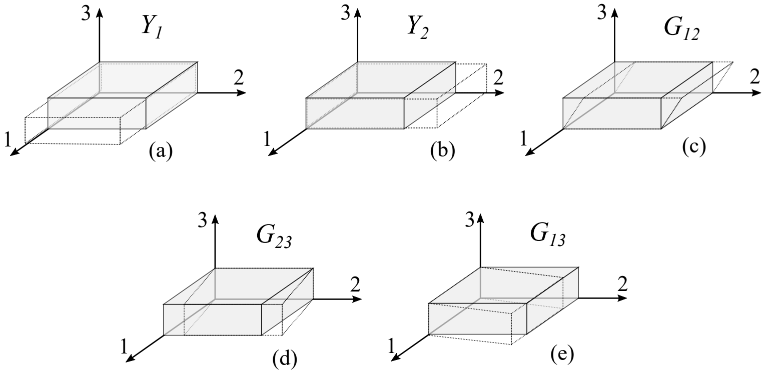

Figure 2.17: Plane deformations on a MFC transducer

These four elastic constants govern the in-plane deformations and they are suitable for the studies with Kirchhoff plate theory. However, this material information, which is commonly provided by the transducer suppliers, are not complete for the modeling by Mindline-Reissier plate theory. The shear modulus in the thickness-wise of a transducer ((d) and (e) in Figure 2.17) are not provided by the suppliers. Besides, the piezoelectric constants of the used piezoelectric material cannot express the effective piezoelectric performance of MFC transducers because of the epoxy in the active layer. Therefore, much work is done to characterize the effective properties of MFC transducers in the literature.

The material properties of MFC transducers were experimentally obtained by Williams *et al.*(2004) in both linear elastic and nonlinear constitutive behaviors [113]. The characterization of the linear elastic constants of MFC transducers is reported by [131] in a linear elastic region. The work in [132] investigated the nonlinear behaviors of MFC with monotonically increased electric fields under various mechanical load/stress levels. Subsequently, both the analytical mixing rule [133–135] and FEM techniques [136–138] based on linear assumptions have been investigated to estimate the effective properties of MFC (and AFC) transducers. Hagood *et al.*(1993) used mixing rule to estimate the effective properties of AFC transducers [139]. Park *et al.*(2005) [140] investigated the equivalent material properties of MFC by single crystal concept. The mechanical properties are studied by using classical lamination theory, and the piezoelectric strain constants are estimated through a uniform field model. The micro-mechanical homogenization models based on the asymptotic homogenization method is also reported in [20, 141]. A. Deraemaker *et al.*(2010) [142, 143] estimated the effective material properties through uniform field method with plane stress hypothesis based on the work in [134]. The asymptotic expansion homogenization has also been employed in [20] to predict the effective properties of MFC-d31 transducers. Recently, Li *et al.*(2016) [13] investigated the equivalent elastic and piezoelectric constants of MFC transducers through mixing rule and Mindlin-Reissner plate theory. Both the shear modulus and the piezoelectric constants of MFC transducers, which are not available in the datasheet, can be estimated. Therefore, the modeling of MFC transducers can be improved by using these more comprehensive material properties. [144].

2.6.3 Analytical modeling approaches

The analytical study of piezoelectric transducers, more precisely, the study of piezoelectric actuators are practical for modeling [9, 11, 74, 146]. It provides closed-form solutions for characterizing piezoelectric actuators [74, 145, 147–149]. MFC transducers can be considered as orthotropic actuators. The piezoelectric constitutive equations can be introduced into the elastic equilibrium principle or the Hamilton's principle [145, 147, 148]. Besides, the Green functions have also been used for deriving the equivalent loads of orthotropic transducers in [145]. The bending motions caused by piezoelectric actuators on a plate are mainly characterized. They provide physical insights for the application of the piezoelectric thin actuators on plate-type structures. Due to the closed-form solutions, we can quantify the actuation performance of different shapes/materials of piezoelectric actuators. However, the structures are greatly simplified to piezoelectric unimorph plates. The influences of electrical dynamics are also not included. The equivalent loads in the literature are commonly formulated by a combination of bending moment and point forces for a transverse orthotropic transducer, as shown in Figure 2.18. The bending motions caused by a piezoelectric actuator on a plate is, thus, characterized but the membrane effect and the coupling between bending and membrane effects on a laminated structure are omitted. Therefore, the mentioned research only focuses on the equivalent load to express the inverse piezoelectric effect, rather than fully characterizing a piezoelectric laminated structure.

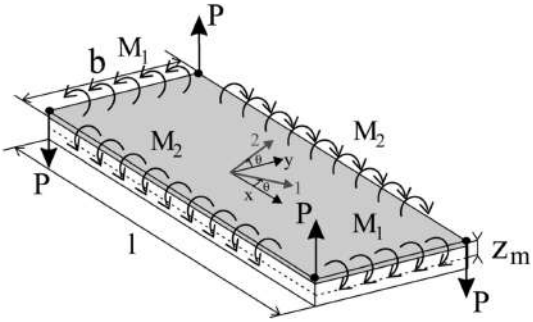

Figure 2.18: Equivalent loads of an anisotropic rectangular piezoelectric actuator [145] (The point forces **P** generate twisting effect on the actuator)

The early system-level studies of piezoelectric laminated beams are carried out in [150, 151]. Later on, Lee(1990) incorporated the piezoelectric effect into the classic laminate plate theory with the partial electrode covered piezoelectric layer and the reciprocity between distributed piezoelectric actuator and sensor are implicitly clarified [152]: the distributed moment (caused by the inverse piezoelectric effect) and its bending angle (generates direct piezoelectric effect) are reciprocal. However, the electrical boundary conditions are not included so that an explicit formulation is not defined in [152]. After that, similar work has been done in [153–156] to further explain the linear electro-elastic coupling of piezoelectric structures. However, it is important to notice that in the mentioned research, piezoelectric unimorph plates with distributed electrodes as shown in Figure. 2.19 (a) are commonly studied. Since the mechanical influences of the electrodes are negligible, piezoelectric unimorph plates are assumed as continuous structures. Even plates with uniformly distributed large piezo-patches are considered as continuous structures too in [6]. That is because the mechanical influences of the transducer in case (b) in the figure are difficult to be taken into account in analytical modeling. Even though the electro-elastic coupling caused by the locally distributed electrode is obtained, the dynamics of plates with piezoelectric layers is different from the case with distributed transducers. The equivalent loads of a rectangular piezoelectric actuator that obtained in [145, 147, 148, 152] are actually the same. They do not comply with the elastic equilibrium principle, and the distribution of the piezoelectric transducer on a host plate is not correctly taken into consideration in these analyses.

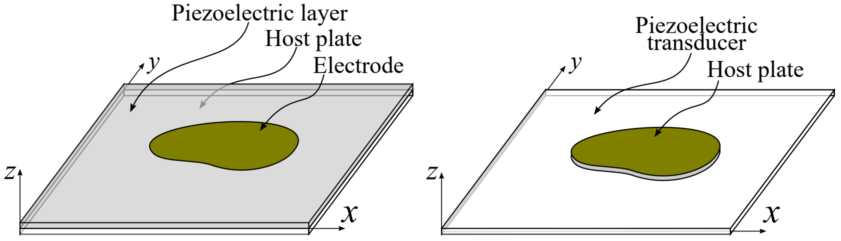

(a) piezoelectric unimorph plate (b) plate with integrated transducer

Figure 2.19: Piezoelectric structures

To fully characterize a laminated plate with distributed MFC transducers in this dissertation, we introduce the spatial distributions of the transducers into the Hamilton's principle. Given that laminated plates will be studied, both the bending and membrane effects should be taken into account in the analysis. As a result, the mechanical influences of the transducer on the plate can be correctly described in the system's dynamics. The equivalent loads of the transducer will be determined through the spatial distribution terms. The corresponding direct piezoelectric coupling together with the electrical dynamics should also be investigated. Then further dynamic features of the piezoelectric transducers integrated into a host plate can be studied.

2.6.4 Numerical modeling approaches

In the past decades, numerical modeling approaches have been extensively investigated to simulate piezoelectric structures. The numerical modeling path provided numerous possibilities: Early FEM formulation derived from the classical laminated plate theory is reported in [16] for active vibration control of composite plates with distributed piezoelectric sensors and actuators. The mesh-free model of piezoelectric composite structures has been reported in [19]. The method demonstrated a higher convergence rate than standard First-Order-Shear-Deformation (FOSD) FEM method. A shallow shell is presented in [17], which deals with the piezoelectric induced bending and twisting deformation of laminated composite structures. A rigorous multi-scale approach, based on the asymptotic expansion homogenization method, has been developed in [141] to analyze the behavior of laminated structures with integrated MFC sensors and actuators.

FEM methods are certainly the most widely used approach in different research tracks and application of piezoelectric transducers [11, 18, 21, 23, 157–160]. The piezoelectric effect is simulated through strain field so that the mechanical and electric domains are strongly coupled together in FEM formulations. It has been reported in [22] that the two-dimensional FEM models of MFC transducers, based on the Kirchhoff or the Mindlin-Reissner assumptions, agree well with both experimental results and 3D FEM models. Regarding to the anisotropic transducers such as MFC transducers, a material-structural coordinates transformation regarding MFC transducers is required in the mentioned FEM methods, as shown in Figure 2.20. That is because the properties of the transducers are defined in the material coordinates (1, 2), which is different from the structural coordinates (x, y). Recently, this transformation is taken into consideration in a FOSD-based FEM in [23].

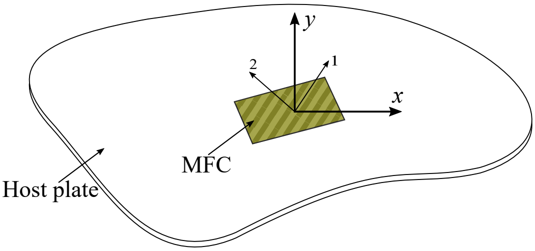

Figure 2.20: Material-structural coordinates transformation

In FEM methods, the discretizations of the electric field and the displacement field are independent with each other [161, 162]. An accurate electric assumption for the piezoelectric elements is essential for ensuring that both the mechanical displacement and the electric potential field converge to the exact solutions. Hybrid finite element methods have been developed to improve the discretization of the electrical field [20, 162–165], but the modeling complexity is increased.

The conventional assumption of the electric field distribution on the transducer might be too strong to simulate the MFC transducers. For example, the effective distribution of the electric field on an MFC-d33 transducer is shown in Figure 2.7. A uniform electric field leads to an over-estimation of the performance of the MFC-d33 transducer. A detailed description of the transducer in modeling would be too complicated because of the multilayer constitution. An alternative is to correct the uniform electric field assumption in modeling based on the effective electric field distribution shape of MFC transducers [44, 166, 167].

The performance of a piezoelectric transducer on a host structure also highly depends upon the quality of the adhesive bond layer, which transfers the stress/strain between the transducer and the host plate, as shown in Figure 2.21. Assuming that the stain in the thickness-wise of the transducer is linear, the adhesive layer undergoes shear deformation when the transducer functions as an actuator. At last, the deformation of the host plate is smaller than the transducer. A similar situation can also be found when the transducer is used as a sensor. This effect is called shear-lag effect and cannot be negligible in experimental studies [150, 168–171]. However, the adhesive layer between the host structure and transducer is commonly assumed to be perfect in numerical simulations because of the lack of material information. The corrections of both effects must be considered in the modeling in order to achieve an experimental validation.

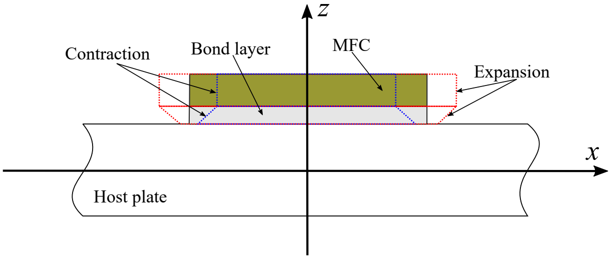

Figure 2.21: Strain transfer mechanism through adhesive bond layer

Furthermore, an obvious drawback of FEM methods concerning dynamic applications is that they generate large-scale models because a sufficiently fine mesh is required to discrete both the host structure and the integrated transducers. For plate-type structures, it is possible that the host structure and the integrated transducers share the same mesh to avoid the mesh coupling between them. As a result, the material properties of the transducers should be homogenized together with the host structure at the location of the transducers, and the adhesive layer is neglected in most of cases. Thus, the size of the model is mainly determined by the mesh of the host structure. A model order reduction needs to be performed on the FEM models for reducing computational time in dynamic application.

To sum up, MFC transducers must be simultaneously modeled together with host structures in FEM methods so that the bending coupling between them can be formed. The piezoelectric coupling matrix depends on both the placement and the properties of these transducers, and the structural model is also influenced by them too. For example, the piezoelectric fibrous orientation leads to changes in both of them. Thus, it is challenging to efficiently evaluate the influences of these parameters directly in dynamic application, where a reduced-order model is always required. The conventional model order reduction techniques, often used for designing control solutions such as Krylov subspace projection [24] and balanced truncation [25], transform the original model into an equivalent vector space, so that these useful physical parameters are not accessible anymore after the reduction.

A semi-analytical modeling approach based on the substructuring concept would efficiently evaluate the performance of MFC transducers in dynamic application. We can divide the system into subcomponents including the MFC transducers, and the size of each subcomponent can be efficiently reduced. The dynamics of the overall system is obtained by assembling the reduced-order models of all the subcomponents. The closed-form analytical solutions can be used to express the direct and inverse piezoelectric couplings. This concept retains the structure of full order system models so that each subcomponent can be easily updated including the placement and the properties of MFC transducers. Moreover, it is also essential to ensure the stability of the reduced-order model, for designing active control algorithms and performing real-time simulations.

2.7 Concluding remarks

In this chapter, firstly we introduced the piezoelectricity and reviewed different plate hypotheses for modeling two-dimensional piezoelectric structures. And we found that the Kirchhoff plate theory is sufficient to analyze and characterize the integrated piezoelectric transducers on a host plate. Then, both the noise and vibrations control, and energy harvesting application using piezoelectric materials are reviewed. An effective modeling approach of piezoelectric systems is very important for both of them. Stable low-order system models are essential for designing a controller and performing real-time simulations. When MFC transducers are used in above mentioned application, not only their placement but also their piezoelectric fibrous orientation on a host structure are crucial to optimize. However, there is no efficient way to evaluate the performance of

MFC transducers with different piezoelectric fibrous orientation and placements in the literature.

A semi-analytical modeling approach based-on substructuring concept would be able to generate stable structure-preserving low-order models. Analytical piezoelectric couplings should combine with an equivalent substructuring process. Therefore, the analytical modeling of piezoelectric structures is reviewed in detail. The piezoelectric layered plates with a partially covered electrode are widely studied in the literature. The dynamics of such kind of structure can be entirely different from plates with distributed piezoelectric transducers because the mechanical influences of the transducers, which may significantly change the structural dynamics, cannot be properly taken into account. Meanwhile, the analytical solutions are not fully implying with the elastic equilibrium principle. Furthermore, The piezoelectric reciprocal relation is reported in the literature, but an explicit formulation is not defined yet.

The numerical modeling approaches, such as the FEM method, are suitable to solve the multiphysics problems, including the mechanical influences of piezoelectric transducers. However, piezoelectric transducers should be modeled together with the host structure in order to formulate the bending coupling. The apparent drawback of the FEM method is that it generates large-scale models so that model order reduction is always required by dynamic application. Most of the important physical parameters, such as the placement and piezoelectric properties of MFC transducers, are not preserved in the reduced-order model due to the model order reduction. It is required to revise the full order model to optimize the placement and properties of MFC transducers for the desired performance in dynamic application. Therefore, the primary objective of this dissertation is to develop a novel framework for the modeling of MFC transducers in order to improve the mentioned deficiencies in the literature.

Chapter 3

Basic concept of equivalent dynamic modeling of MFC transducers

This chapter presents the analytical characterization of the MFC transducers integrated into a laminated composite plate. Both the inverse and direct piezoelectric effects of the MFC transducers are studied. We used a generalized two-dimensional piezoelectric constitutive formulation for characterizing both the MFC-d33 and MFC-d31 transducers in the same analysis. The dynamics of an anisotropic plate with an integrated MFC transducer is analyzed by using the generalized Hamilton's principle. The equivalent loads that express the inverse piezoelectric effect of the integrated transducer are obtained. The equivalent force of the MFC transducer is derived, and its accuracy is analyzed through a total bending effort balance. The corresponding direct piezoelectric effect is characterized by the electric boundary conditions of the piezoelectric system.

3.1 Constitutive relations

3.1.1 Constitutive relations of laminated plate

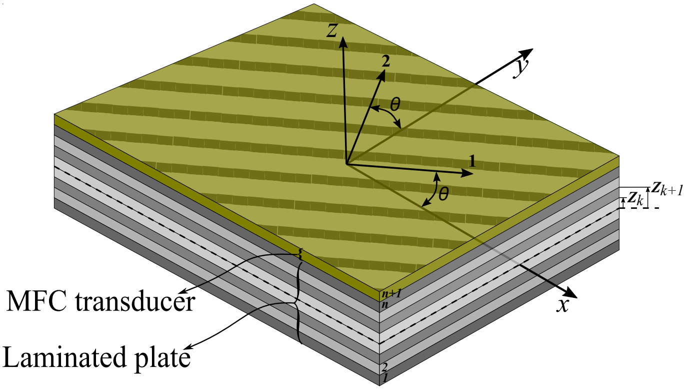

Figure 3.1: Lay-up of a laminated composite plate with an integrated MFC transducer

The lay-up of a laminated composite plate with an MFC transducer is shown in Figure 3.1. All the layers are orthotropic. The plane-stress is assumed because the thickness of the plate is small compared to the in-plane dimensions of the plate. Hooke's law is used to express the constitutive equations of the k^{th} layer in the laminated composite plate in material coordinates (1, 2) [130]:

$$\begin{Bmatrix} T_1 \\ T_2 \\ T_6 \\ T_5 \\ T_4 \end{Bmatrix}^{(k)} = \begin{bmatrix} Q_{11} & Q_{12} & 0 & 0 & 0 \\ Q_{21} & Q_{22} & 0 & 0 & 0 \\ 0 & 0 & Q_{66} & 0 & 0 \\ 0 & 0 & 0 & Q_{55} & 0 \\ 0 & 0 & 0 & 0 & Q_{44} \end{bmatrix}^{(k)} \begin{Bmatrix} S_1 \\ S_2 \\ S_6 \\ S_5 \\ S_4 \end{Bmatrix}^{(k)} \tag{3.1}$$

where

$$\begin{gathered} Q_{11} = \frac{Y_1}{1-\nu_{12}\nu_{21}},\ Q_{12} = \frac{\nu_{12}Y_1}{1-\nu_{12}\nu_{21}},\ Q_{22} = \frac{Y_2}{1-\nu_{12}\nu_{21}}, \\ Q_{21} = Q_{12},\ Q_{66} = G_{12},\ Q_{55} = G_{13},\ Q_{44} = G_{23} \end{gathered} \tag{3.2}$$

in which Y_1 and Y_2 are Young's modulus in the material coordinates, respectively. G_{ij} are the shear modulus. ν_{12} and ν_{21} are the Poisson's ratios. The stress components of each layer of the laminated plate need to be transformed into the global coordinates $(x,\ y)$ according to the following relations [130]:

$$\begin{Bmatrix} T_{xx} \\ T_{yy} \\ T_{xy} \\ T_{xz} \\ T_{yz} \end{Bmatrix}^{(k)} = \underbrace{\begin{bmatrix} c^2 & s^2 & cs & 0 & 0 \\ s^2 & c^2 & -cs & 0 & 0 \\ -2cs & 2cs & c^2-s^2 & 0 & 0 \\ 0 & 0 & 0 & c & -s \\ 0 & 0 & 0 & s & c \end{bmatrix}^{(k)}}_{R} \begin{Bmatrix} T_1 \\ T_2 \\ T_6 \\ T_5 \\ T_4 \end{Bmatrix}^{(k)} \tag{3.3}$$

where s and c indicate $\sin\theta$ and $\cos\theta$, respectively. θ is the angle between the material and structural coordinates, as shown in Figure 3.1. Hence, R is the material-structural coordinates transformation matrix. Therefore, the constitutive equations of k^{th} layer can be rewritten as follows in the structural coordinates:

$$\begin{Bmatrix} T_{xx} \\ T_{yy} \\ T_{xy} \\ T_{xz} \\ T_{yz} \end{Bmatrix}^{(k)} = \begin{bmatrix} \bar{Q}_{11} & \bar{Q}_{12} & \bar{Q}_{16} & 0 & 0 \\ \bar{Q}_{21} & \bar{Q}_{22} & \bar{Q}_{26} & 0 & 0 \\ \bar{Q}_{61} & \bar{Q}_{62} & \bar{Q}_{66} & 0 & 0 \\ 0 & 0 & 0 & \bar{Q}_{55} & \bar{Q}_{54} \\ 0 & 0 & 0 & \bar{Q}_{45} & \bar{Q}_{44} \end{bmatrix}^{(k)} \begin{Bmatrix} S_{xx} \\ S_{yy} \\ S_{xy} \\ S_{xz} \\ S_{yz} \end{Bmatrix}^{(k)} \tag{3.4}$$

where $\bar{Q}_{ij}$ are the transformed elastic constants of the k^{th} layer. According to the Kirchoff plate theory, the strain-displacement relation can be expressed as follows [172]:

$$\begin{cases} S_{xx}^{(k)} &= \varepsilon_{xx} + z\kappa_{xx} \\ S_{yy}^{(k)} &= \varepsilon_{yy} + z\kappa_{yy} \\ S_{xy}^{(k)} &= \varepsilon_{xy} + z\kappa_{xy} \end{cases} \tag{3.5}$$

where

$$\varepsilon_{xx} = \frac{\partial u^0}{\partial x},\ \varepsilon_{yy} = \frac{\partial v^0}{\partial y},\ \varepsilon_{xy} = (\frac{\partial u^0}{\partial y} + \frac{\partial v^0}{\partial x})$$
$$\kappa_{xx} = -\frac{\partial^2 w^0}{\partial x^2},\ \kappa_{yy} = -\frac{\partial^2 w^0}{\partial y^2},\ \kappa_{xy} = -2\frac{\partial^2 w^0}{\partial x \partial y}$$

in which, u^0, v^0 and w^0 are the displacement components on the mid-surface of the plate. The stress components of the composite plate can be expressed as follows by substituting Equation (3.5) into Equation (3.4):

$$\begin{cases} T_{xx}^{(k)} &= \bar{Q}_{11}^{(k)}(\varepsilon_{xx} + z\kappa_{xx}) + \bar{Q}_{12}^{(k)}(\varepsilon_{yy} + z\kappa_{yy}) + 2\bar{Q}_{16}^{(k)}(\varepsilon_{xy} + 2z\kappa_{xy}) \\ T_{yy}^{(k)} &= \bar{Q}_{21}^{(k)}(\varepsilon_{xx} + z\kappa_{xx}) + \bar{Q}_{22}^{(k)}(\varepsilon_{yy} + z\kappa_{yy}) + 2\bar{Q}_{26}^{(k)}(\varepsilon_{xy} + 2z\kappa_{xy}) \\ T_{xy}^{(k)} &= \bar{Q}_{16}^{(k)}(\varepsilon_{xx} + z\kappa_{xx}) + \bar{Q}_{26}^{(k)}(\varepsilon_{yy} + z\kappa_{yy}) + 2\bar{Q}_{66}^{(k)}(\varepsilon_{xy} + 2z\kappa_{xy}) \end{cases} \tag{3.7}$$

Then, the internal membrane forces, bending moments on each layer that resulted from the stress can be deduced as follows [172]:

$$\left\{\begin{array}{c} N_{xx} \\ N_{yy} \\ N_{xy} \\ M_{xx} \\ M_{yy} \\ M_{xy} \end{array}\right\}^{(k)} = \begin{bmatrix} A_{11} & A_{12} & A_{16} & B_{11} & B_{12} & B_{16} \\ A_{21} & A_{22} & A_{26} & B_{21} & B_{22} & B_{26} \\ A_{61} & A_{62} & A_{66} & B_{61} & B_{62} & B_{66} \\ B_{11} & B_{12} & B_{16} & D_{11} & D_{12} & D_{16} \\ B_{21} & B_{22} & B_{26} & D_{21} & D_{22} & D_{26} \\ B_{61} & B_{62} & B_{66} & D_{61} & D_{62} & D_{66} \end{bmatrix}^{(k)} \left\{\begin{array}{c} \varepsilon_{xx} \\ \varepsilon_{yy} \\ \varepsilon_{xy} \\ \kappa_{xx} \\ \kappa_{yy} \\ \kappa_{xy} \end{array}\right\}^{(k)} \tag{3.8}$$

where $A_{ij}^{(k)}, B_{ij}^{(k)}, D_{ij}^{(k)}$ are the extensional stiffness, membrane-bending coupling stiffness and bending stiffness of k^{th} layer, respectively.

$$(A_{ij}^{(k)}, B_{ij}^{(k)}, D_{ij}^{(k)}) = \int_{z_{k-1}}^{z_k} (1, z, z^2)\bar{Q}_{ij}^{(k)} dz \tag{3.9}$$

Hence, the mechanical properties of the homogenized laminated composite plate can be characterized as follows[21]:

$$(A_{ij}^s, B_{ij}^s, D_{ij}^s) = \sum_{k=1}^{n} (A_{ij}^{(k)}, B_{ij}^{(k)}, D_{ij}^{(k)}). \tag{3.10}$$

B_{ij}^s is null for a symmetrical lay-up. Hence, the stress and bending moment resultants of the homogenized plate are characterized as follows

$$\left\{\begin{array}{c} N_{xx}^s \\ N_{yy}^s \\ N_{xy}^s \\ M_{xx}^s \\ M_{yy}^s \\ M_{xy}^s \end{array}\right\} = \begin{bmatrix} A_{11}^s & A_{12}^s & A_{16}^s & B_{11}^s & B_{12}^s & B_{16}^s \\ A_{21}^s & A_{22}^s & A_{26}^s & B_{21}^s & B_{22}^s & B_{26}^s \\ A_{61}^s & A_{62}^s & A_{66}^s & B_{61}^s & B_{62}^s & B_{66}^s \\ B_{11}^s & B_{12}^s & B_{16}^s & D_{11}^s & D_{12}^s & D_{16}^s \\ B_{21}^s & B_{22}^s & B_{26}^s & D_{21}^s & D_{22}^s & D_{26}^s \\ B_{61}^s & B_{62}^s & B_{66}^s & D_{61}^s & D_{62}^s & D_{66}^s \end{bmatrix} \left\{\begin{array}{c} \varepsilon_{xx} \\ \varepsilon_{yy} \\ \varepsilon_{xy} \\ \kappa_{xx} \\ \kappa_{yy} \\ \kappa_{xy} \end{array}\right\}. \tag{3.11}$$

The corresponding in-plane and out-plane behaviors of the plate are shown in Figures 3.2 and 3.3.

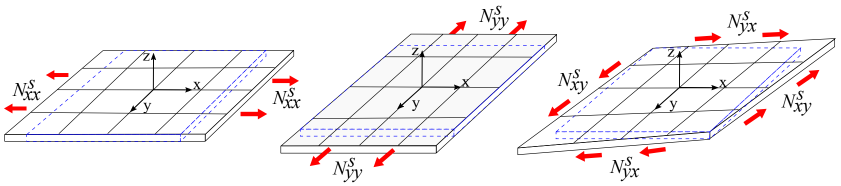

Figure 3.2: In-plane behaviors of a plate due to membrane forces

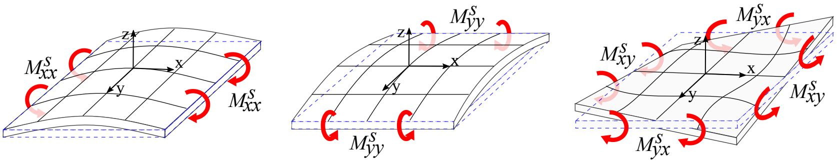
M_{xx}^S
z
x
y
M_{xx}^S
M_{yy}^S
z
x
y
M_{yy}^S
M_{yx}^S
M_{xy}^S
z
x
y
M_{xy}^S
M_{yx}^S

Figure 3.3: Out-plane behaviors of a plate due to bending moments

3.1.2 Piezoelectric constitutive relations of MFC transducers

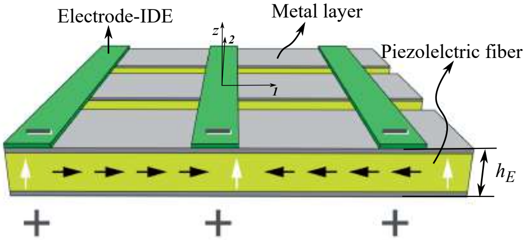
Electrode-IDE
Metal layer
Piezolelctric fiber
z
2
1
h_E
+
+
+

Figure 3.4: Work principle of MFC-d31 transducers [15] (The white arrows represent the operational electric field and the black arrows indicate the deformation of the transducer.)

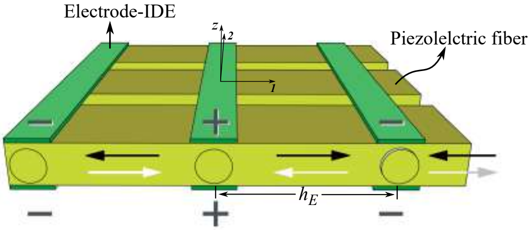
Electrode-IDE
Piezolelctric fiber
z
2
1
h_E
−
+
−

Figure 3.5: Work principle of MFC-d33 transducers [15] (The white arrows represent the operational electric field and the black arrows indicate the deformation of the transducer.)

The compositions of MFC-d31 and MFC-d33 transducers are shown in Figures 3.4 and 3.5. The MFC-d31 transducer uses the e_{31} and e_{32} effects that perform comparable performances in both x and y directions. The operational electric field is applied to the thickness-wise direction of the transducer so that the electrode distance h_E of the MFC-d31 equals the thickness of the transducer

t_p. The metal layer allows the electric field to distribute on the piezoelectric fibers uniformly. In contrast, the electric field distributes in the longitudinal direction of the piezoelectric fibers on an MFC-d33 transducer. This is due to the electrodes of MFC-d33, which allows it to take advantage of the large e_{33} effect. And the electrode distance is the distance between two electrodes' fingers as shown in Figure 3.5.

The two-dimensional piezoelectric constitutive equations of the MFC-d31 and MFC-d33 transducers are given as Equation (3.12) and Equation (3.13) according to Equation (2.7) under the in-plane stress hypothesis [143]:

$$\begin{Bmatrix} T_1 \\ T_2 \\ T_6 \\ T_5 \\ T_4 \\ D_3 \end{Bmatrix} = \begin{bmatrix} Q_{11}^E & Q_{12}^E & 0 & 0 & 0 & -e_{31} \\ Q_{21}^E & Q_{22}^E & 0 & 0 & 0 & -e_{32} \\ 0 & 0 & Q_{66}^E & 0 & 0 & -e_{36} \\ 0 & 0 & 0 & Q_{55}^E & 0 & 0 \\ 0 & 0 & 0 & 0 & Q_{44}^E & 0 \\ e_{31} & e_{32} & e_{36} & 0 & 0 & \epsilon_{33}^s \end{bmatrix} \begin{Bmatrix} S_1 \\ S_2 \\ S_6 \\ S_5 \\ S_4 \\ E_3 \end{Bmatrix} \tag{3.12}$$

where

$$Q_{11}^E = \frac{Y_1^E}{1-\nu_{12}\nu_{21}},\ Q_{12}^E = \frac{\nu_{12}Y_1^E}{1-\nu_{12}\nu_{21}},\ Q_{22}^E = \frac{Y_2^E}{1-\nu_{12}\nu_{21}},$$

$$Q_{21}^E = Q_{12}^E,\ Q_{66}^E = G_{12}^E,\ Q_{55}^E = G_{13}^E,\ Q_{44}^E = G_{23}^E.$$

Y_1^E and Y_2^E are the Young's modulus in the 1 and 2 directions of the MFC-d31 transducer, respectively. G_{12}^E is the shear modulus in the $(1, 2)$ coordinates. ν_{12} and ν_{21} indicate the Poisson's ratios.

$$\begin{Bmatrix} T_1 \\ T_2 \\ T_6 \\ T_5 \\ T_4 \\ D_1 \end{Bmatrix} = \begin{bmatrix} Q_{11}^E & Q_{12}^E & 0 & 0 & 0 & -e_{33} \\ Q_{21}^E & Q_{22}^E & 0 & 0 & 0 & -e_{32} \\ 0 & 0 & Q_{66}^E & 0 & 0 & -e_{16} \\ 0 & 0 & 0 & Q_{55}^E & 0 & 0 \\ 0 & 0 & 0 & 0 & Q_{44}^E & 0 \\ e_{33} & e_{32} & e_{16} & 0 & 0 & \epsilon_{11}^s \end{bmatrix} \begin{Bmatrix} S_1 \\ S_2 \\ S_6 \\ S_5 \\ S_4 \\ E_1 \end{Bmatrix} \tag{3.13}$$

with

$$Q_{11}^E = \frac{Y_3^E}{1-\nu_{32}\nu_{23}},\ Q_{12}^E = \frac{\nu_{32}Y_3^E}{1-\nu_{32}\nu_{23}},\ Q_{22}^E = \frac{Y_2^E}{1-\nu_{12}\nu_{21}},$$

$$Q_{21}^E = Q_{12}^E,\ Q_{66}^E = G_{32}^E,\ Q_{55}^E = G_{31}^E,\ Q_{44}^E = G_{21}^E$$

Y_3^E and Y_2^E are the Young's modulus in the 1 and 2 directions, respectively. G_{32}^E is the shear modulus in $(1, 2)$ plan and ν_{32} and ν_{23} indicate the Poisson's ratios.

The operational electric field applies to z direction on an MFC-d31 transducer but it applies to x direction on an MFC-d33 transducer. The distributions of the electric field are also different. As mentioned in chapter 2, a uniform field model is adopted here to simulate the electric field. The effective electric field applied to the piezoelectric fibers can be corrected according to its distribution [44, 167] for an MFC-d33 transducer. Wherefore, the different function mechanisms of the two types of transducer yield different piezoelectric constitutive equations in modeling. It is favorable to use a generalized formulation valid for both types of transducers for the convenience of the following analysis. The electrode of MFC-d33 transducer is converted into an MFC-d31 form in this analysis. The only prerequisite is that the transformation must guarantee that both the piezoelectric and electrical properties of the MFC-d33 remain unchanged [81]. Finally, The conversation is given as follows:

$$\begin{cases} d_{31}^{*}\frac{V}{t_p} = d_{33}\frac{V}{h_E} \\ d_{32}^{*}\frac{V}{t_p} = d_{32}\frac{V}{h_E} \\ d_{36}^{*}\frac{V}{t_p} = d_{36}\frac{V}{h_E} \end{cases} \Leftrightarrow \begin{cases} e_{31}^{*}\frac{V}{t_p} = e_{33}\frac{V}{h_E} \\ e_{32}^{*}\frac{V}{t_p} = e_{32}\frac{V}{h_E} \\ e_{36}^{*}\frac{V}{t_p} = e_{36}\frac{V}{h_E} \end{cases} \tag{3.14}$$

where h_E is the electrodes distance of the MFC-d33 transducer. The thickness of the active layer t_p equals the electrodes distance of the equivalent MFC-d31 model. The dielectric constant also needs to be converted to retain the capacitance of the MFC-d33 transducers. Then, Equation (3.12) is also available to describe the converted MFC-d33 model. Therefore, the MFC-d33 transducer can be considered as a special case of MFC-d31 transducer. Finally, a generalized formulation for both the MFC-d31 and MFC-d33 transducers is written as follows:

$$\begin{Bmatrix} T_1 \\ T_2 \\ T_6 \\ T_5 \\ T_4 \\ D \end{Bmatrix} = \begin{bmatrix} Q_{11}^E & Q_{12}^E & 0 & 0 & 0 & -e_{31}^{*} \\ Q_{21}^E & Q_{22}^E & 0 & 0 & 0 & -e_{32}^{*} \\ 0 & 0 & Q_{66}^E & 0 & 0 & -e_{36}^{*} \\ 0 & 0 & 0 & Q_{55}^E & 0 & 0 \\ 0 & 0 & 0 & 0 & Q_{44}^E & 0 \\ e_{31}^{*} & e_{32}^{*} & e_{36}^{*} & 0 & 0 & \epsilon^s \end{bmatrix} \begin{Bmatrix} S_1 \\ S_2 \\ S_6 \\ S_5 \\ S_4 \\ E \end{Bmatrix} \tag{3.15}$$

where e_{31}^{*} denotes e_{31} or e_{31}^{*} for MFC-d31 or MFC-d33 transducers, respectively; e_{32}^{*} indicates e_{32} or e_{32}^{*} for MFC-d31 or MFC-d33 transducers, respectively; and e_{36}^{*} expresses e_{36}^{*} or e_{36}^{*} for MFC-d31 or MFC-d33 transducers, respectively.

When MFC transducers are integrated into a host structure as shown in Figure 3.1, both the material and piezoelectric properties should be transformed into the global coordinates too. The corresponding piezoelectric constitutive equations are given in Equations (3.16a) and (3.16b) [23]:

$$\{T\} = [R]^T[Q^E][R]\{S\} - [R]^T[e^*]\{E\} \tag{3.16a}$$

$$\{D\} = [e^*]^T [R] \{S\} - [\epsilon^s] \{E\} \tag{3.16b}$$

where $[R]$ can be obtained from Equation (3.3). The stress in Equation (3.15) can be rewritten as follows in the structural coordinates:

$$\underbrace{\begin{Bmatrix} T_{xx} \\ T_{yy} \\ T_{xy} \\ T_{xz} \\ T_{yz} \\ D \end{Bmatrix}}_{\widetilde{T}_p} = \underbrace{\begin{bmatrix} \bar{Q}^E_{11} & \bar{Q}^E_{12} & \bar{Q}^E_{16} & 0 & 0 & -\bar{e}^*_{31} \\ \bar{Q}^E_{21} & \bar{Q}^E_{22} & \bar{Q}^E_{26} & 0 & 0 & -\bar{e}^*_{32} \\ \bar{Q}^E_{61} & \bar{Q}^E_{62} & \bar{Q}^E_{66} & 0 & 0 & -\bar{e}^*_{36} \\ 0 & 0 & 0 & \bar{Q}^E_{55} & \bar{Q}^E_{54} & 0 \\ 0 & 0 & 0 & \bar{Q}^E_{45} & \bar{Q}^E_{44} & 0 \\ \bar{e}^*_{31} & \bar{e}^*_{32} & \bar{e}^*_{36} & 0 & 0 & \epsilon^s \end{bmatrix}}_{\widetilde{Q}_p} \underbrace{\begin{Bmatrix} S_{xx} \\ S_{yy} \\ S_{xy} \\ S_{xz} \\ S_{yz} \\ E \end{Bmatrix}}_{\widetilde{S}_p} \tag{3.17}$$

where $\widetilde{T}_p$, $\widetilde{S}_p$ and $\widetilde{Q}_p$ are the augmented stress vector, augmented strain vector and augmented elastic matrix of MFC transducers, respectively. Using the same strain-displacement relations in Equation (3.5), the stress components of the MFC layer are given as follows:

$$\begin{cases} T^p_{xx} = \bar{Q}^E_{11}(\varepsilon_{xx} + \kappa_{xx}) + \bar{Q}^E_{12}(\varepsilon_{yy} + \kappa_{yy}) + 2\bar{Q}^E_{16}(\varepsilon_{xy} + \kappa_{xy}) - \bar{e}^*_{31}E \\ T^p_{yy} = \bar{Q}^E_{21}(\varepsilon_{xx} + \kappa_{xx}) + \bar{Q}^E_{22}(\varepsilon_{yy} + \kappa_{yy}) + 2\bar{Q}^E_{26}(\varepsilon_{xy} + \kappa_{xy}) - \bar{e}^*_{32}E \\ T^p_{xy} = \bar{Q}^E_{16}(\varepsilon_{xx} + \kappa_{xx}) + \bar{Q}^E_{26}(\varepsilon_{yy} + \kappa_{yy}) + 2\bar{Q}^E_{66}(\varepsilon_{xy} + \kappa_{xy}) - \bar{e}^*_{36}E \end{cases} \tag{3.18}$$

in which, the inverse piezoelectric effect is considered. Then, the piezoelectric constitutive relations of the transducer are described as:

$$\begin{Bmatrix} N^p_{xx} \\ N^p_{yy} \\ N^p_{xy} \\ M^p_{xx} \\ M^p_{yy} \\ M^p_{xy} \\ D \end{Bmatrix} = \begin{bmatrix} A^E_{11} & A^E_{12} & A^E_{16} & B^E_{11} & B^E_{12} & B^E_{16} & -t_p\bar{e}^*_{31} \\ A^E_{21} & A^E_{22} & A^E_{26} & B^E_{21} & B^E_{22} & B^E_{26} & -t_p\bar{e}^*_{32} \\ A^E_{61} & A^E_{62} & A^E_{66} & B^E_{61} & B^E_{62} & B^E_{66} & -t_p\bar{e}^*_{36} \\ B^E_{11} & B^E_{12} & B^E_{16} & D^E_{11} & D^E_{12} & D^E_{16} & -z_p\bar{e}^*_{31} \\ B^E_{21} & B^E_{22} & B^E_{26} & D^E_{21} & D^E_{22} & D^E_{26} & -z_p\bar{e}^*_{32} \\ B^E_{61} & B^E_{62} & B^E_{66} & D^E_{61} & D^E_{62} & D^E_{66} & -z_p\bar{e}^*_{36} \\ t_p\bar{e}^*_{31} & t_p\bar{e}^*_{32} & t_p\bar{e}^*_{36} & z_p\bar{e}^*_{31} & z_p\bar{e}^*_{32} & z_p\bar{e}^*_{36} & t_p\epsilon^s \end{bmatrix} \begin{Bmatrix} \varepsilon_{xx} \\ \varepsilon_{yy} \\ \varepsilon_{xy} \\ \kappa_{xx} \\ \kappa_{yy} \\ \kappa_{xy} \\ E \end{Bmatrix} \tag{3.19}$$

where, A^E_{ij}, B^E_{ij} and D^E_{ij} are the components of the extensional stiffness, membrane-bending coupling stiffness and bending stiffness of the transducer, respectively. z_p is the thickness-wise integration of the transducer from the surface of the composite plate z_s to $z_s + t_p$.

$$\int_{z_s}^{z_s+t_p} z\,dz = \frac{t_p(z_s + t_p)}{2}. \tag{3.20}$$

We can deduce the equivalent loads caused by the MFC transducer from Equation (3.19) in line with the elastic equilibrium principle. They include both membrane forces and bending moments when the transducer functions as an actuator. Regarding the bending effect, the equivalent loads from Equation (3.19) only consist of bending moments, which is different from the one in Figure 2.18 (a combination of point forces and bending moments). Hence, the equivalent loads of a piezoelectric actuator can be expressed in different forms. It is not possible to find the relations between them by only using the elastic equilibrium principle.

3.1.3 Transverse shear forces

The transverse shear forces are analyzed after the homogenization of the plate. Assuming that the transverse stresses T_{xz} and T_{yz} vanish on the surfaces $z = \pm t_s/2$, the transverse forces τ_{xz} and τ_{yz} are determined by the equilibrium equations of the homogenized plate [172]:

$$\begin{cases} \tau_{xz}^{(k)} &= \sum_{k=1}^{n+1} \left(\frac{\partial M_{xx}^{(k)}}{\partial x} + \frac{\partial M_{xy}^{(k)}}{\partial y}\right) \\ \tau_{yz}^{(k)} &= \sum_{k=1}^{n+1} \left(\frac{\partial M_{xy}^{(k)}}{\partial x} + \frac{\partial M_{yy}^{(k)}}{\partial y}\right) \end{cases} \tag{3.21}$$

According to the strain-stress relations, Equation (3.21) can be rewritten as:

$$\begin{cases} \tau_{xz} =&(B_{11}\frac{\partial}{\partial x} + B_{16}\frac{\partial}{\partial y})\varepsilon_{xx} + (B_{12}\frac{\partial}{\partial x} + B_{26}\frac{\partial}{\partial y})\varepsilon_{yy} + (B_{16}\frac{\partial}{\partial x} + B_{66}\frac{\partial}{\partial y})\varepsilon_{xy} \\ &+(D_{11}\frac{\partial}{\partial x} + D_{16}\frac{\partial}{\partial y})\kappa_{xx} + (D_{12}\frac{\partial}{\partial x} + D_{26}\frac{\partial}{\partial y})\kappa_{yy} + (D_{16}\frac{\partial}{\partial x} + D_{66}\frac{\partial}{\partial y})\kappa_{xy} \\ \tau_{yz} =&(B_{21}\frac{\partial}{\partial y} + B_{16}\frac{\partial}{\partial x})\varepsilon_{xx} + (B_{22}\frac{\partial}{\partial y} + B_{26}\frac{\partial}{\partial x})\varepsilon_{yy} + (B_{26}\frac{\partial}{\partial y} + B_{66}\frac{\partial}{\partial x})\varepsilon_{xy} \\ &+(D_{21}\frac{\partial}{\partial y} + D_{16}\frac{\partial}{\partial x})\kappa_{xx} + (D_{22}\frac{\partial}{\partial y} + D_{26}\frac{\partial}{\partial x})\kappa_{yy} + (D_{26}\frac{\partial}{\partial y} + D_{66}\frac{\partial}{\partial x})\kappa_{xy} \end{cases} \tag{3.22}$$

where

$$B_{ij} = B_{ij}^s + B_{ij}^E, \; D_{ij} = D_{ij}^s + D_{ij}^E.$$

In this case, the piezoelectric terms are vanished in Equation (3.22). That should not be the case because both the piezoelectric constants and electric field are independent of spatial variables.

In order to fully understand the equivalent load and overall structural dynamics of the MFC transducers on the laminated plate, the spatial distribution of the MFC transducer is introduced into the Hamilton principle in the following analysis.

3.2 Generalized Hamilton's principle of an anisotropic plate with integrated anisotropic transducers

A rectangular anisotropic plate with spatial distributed rectangular MFC transducers is considered in the study, as shown in Figure 3.6. Only one transducer is considered on the plate for convenience of analysis, but it is possible to introduce more transducers of different sizes.

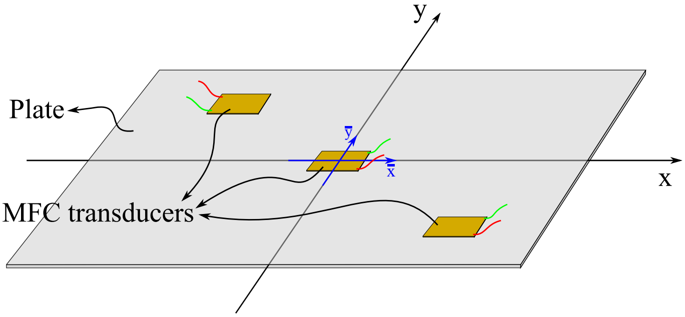

Figure 3.6: A rectangular orthotropic plate with integrated MFC transducers

The spatial distribution of the rectangular MFC transducer size $a \times b$ can be expressed by the Heaviside function H in its local coordinates $(\bar{x}, \bar{y})$ [152]:

$$\Lambda_x^p \Lambda_y^p = [H(\bar{x} + \frac{a}{2}) - H(\bar{x} - \frac{a}{2})] \times [H(\bar{y} + \frac{b}{2}) - H(\bar{y} - \frac{b}{2})]. \tag{3.23}$$

The Heaviside function can be used to describe the spatial distribution of transducers with different shapes so that the local-global coordinates transformation between the transducer and the plate is usually not trivial. In this analysis, as we assumed that the local coordinates $(\bar{x}, \bar{y})$ on the MFC transducer coincide with the global coordinates (x, y). The spatial distribution of the MFC transducer can be rewritten as:

$$\Lambda_x^p \Lambda_y^p = [H(x + \frac{a}{2}) - H(x - \frac{a}{2})] \times [H(y + \frac{b}{2}) - H(y - \frac{b}{2})]. \tag{3.24}$$

According to the property of the Heaviside function [173], the following generalized form retains:

$$\int_{\Gamma_p} G_p d\Gamma_p = \int_{\Gamma_p} G_p \Lambda_x^p \Lambda_y^p d\Gamma_p = \int_{\Gamma_s} G_p \Lambda_x^p \Lambda_y^p d\Gamma_s \tag{3.25}$$

where G_p is a generalized term that contains the spatial variables x and y. Γ_p and Γ_s are the surface dimensions of the host structure and MFC transducer, respectively. The spatial distribution combines the dimensional integration of the host structure and the transducer. Then, the kinetic and stored energies on the plate can be described in a similar way to Equation (3.25).

3.2.1 Potential energy and its variation

The potential energy of the system consists of both the strain energy and the electric energy. It can be expressed as follows:

$$U^* = -\frac{1}{2}\int_{\Gamma_s}\left\{\sum_{k=1}^{n}\int_{z_{k-1}}^{z_k} S^T[\bar{Q}_s^{(k)}]^T S dz + \int_{z_s}^{z_s+t_p}(\tilde{S}_p^T[\tilde{Q}_p]^T\tilde{S}_p)\Lambda_x^p\Lambda_y^p dz\right\}d\Gamma_s \quad (3.26)$$

where $[\bar{Q}_s^{(k)}]$ and $[\bar{Q}_p^*]$ are the stiffness of the k^{th} layer in the plate and the augmented stiffness of the MFC transducer, respectively. We can divide the potential energy into two parts: U_s^* and U_p^*, representing the potential energies in the host plate and the transducer respectively. The potential energy variation of the host plate subject to virtual displacements can be written as:

$$\Delta U_s^* = -\frac{1}{2}\int_{\Gamma_s}\sum_{k=1}^{n}\int_{z_{k-1}}^{z_k} S^T[\bar{Q}_s^{(k)}]^T\Delta S \; dz d\Gamma_s. \quad (3.27)$$

The constitutive relations in Equation (3.8) are adopted here to simplify the notations in the following equation. Thereby, ΔU_s^* can be rewritten as follows:

$$\begin{aligned}\Delta U_s^* = -\int_{\Gamma_s}\Bigg\{ & N_{xx}^s\frac{\partial\Delta u^0}{\partial x} + N_{yy}^s\frac{\partial\Delta v^0}{\partial y} + N_{xy}^s\left(\frac{\partial\Delta u^0}{\partial y} + \frac{\partial\Delta v^0}{\partial x}\right) \\ & - M_{xx}^s\frac{\partial^2\Delta w^0}{\partial x^2} - M_{yy}^s\frac{\partial^2\Delta w^0}{\partial y^2} - 2M_{xy}^s\frac{\partial^2\Delta w^0}{\partial x\partial y}\Bigg\}d\Gamma_s.\end{aligned} \quad (3.28)$$

The integration by parts is performed to obtain the virtual energy variations regarding Δu, Δv and Δw. Let the boundary conditions of host plate be either free, simply supported or clamped; the boundary constraints terms from the integration by parts are null. Then, Equation (3.28) can be rewritten as follows:

$$\begin{aligned}\Delta U_s^* = -\int_{\Gamma_s}\Big[& N_{xx,x}^s\Delta u^0 + N_{yy,y}^s\Delta v^0 + N_{xy,y}^s\Delta u^0 + N_{xy,x}^s\Delta v^0 \\ & - M_{xx,xx}^s\Delta w^0 - M_{yy,yy}^s\Delta w^0 - 2M_{xy,xy}^s\Delta w^0\Big]d\Gamma_s.\end{aligned} \quad (3.29)$$

The potential energy of the transducer is given in the form of

$$U_p^* = -\frac{1}{2}\int_{\Gamma_s}\int_{z_s}^{z_s+t_p} (\tilde{S}_p^T[\tilde{Q}_p]^T\tilde{S}_p)\Lambda_x^p\Lambda_y^p \; dz d\Gamma_s. \tag{3.30}$$

Its variation is simply given as

$$U_p^* = -\frac{1}{2}\int_{\Gamma_s}\int_{z_s}^{z_s+t_p} (\tilde{S}_p^T[\tilde{Q}_p]^T\Delta\tilde{S}_p)\Lambda_x^p\Lambda_y^p \; dz d\Gamma_s. \tag{3.31}$$

Hence, the variation of the stored energy on the transducer is expressed as:

$$\begin{aligned}\Delta U_p^* = \int_{\Gamma_s}\Bigg\{ & N_{xx}^p\frac{\partial\Delta u^0}{\partial x} + N_{yy}^p\frac{\partial\Delta v^0}{\partial y} + N_{xy}^p\left(\frac{\partial\Delta u^0}{\partial y} + \frac{\partial\Delta v^0}{\partial x}\right) \\ & - M_{xx}^p\frac{\partial^2\Delta w^0}{\partial x^2} - M_{yy}^p\frac{\partial^2\Delta w^0}{\partial y^2} - 2M_{xy}^p\frac{\partial^2\Delta w^0}{\partial x\partial y}\Bigg\}\Lambda_x^p\Lambda_y^p d\Gamma_s.\end{aligned} \tag{3.32}$$

The membrane forces and bending moments in Equation (3.32) are different from Equation (3.28) because the piezoelectric terms are included. The integration by parts is carried out here to obtain the variation of U_p^*:

$$\begin{aligned}\Delta U_p^* = & \int_{\Gamma_s}\Bigg[N_{xx,x}^p\Delta u^0 + N_{yy,y}^p\Delta v^0 + N_{xy,y}^p\Delta u^0 + N_{xy,x}^p\Delta v^0 - M_{xx,xx}^p\Delta w^0 \\ & - M_{yy,yy}^p\Delta w^0 - 2M_{xy,xy}^p\Delta w^0\Bigg]\Lambda_x^p\Lambda_y^p d\Gamma_s \\ & - \int_{-\frac{b}{2}}^{\frac{b}{2}}\Big[N_{xx}^p\Delta u^0\Big]_{x=-\frac{a}{2}}^{x=\frac{a}{2}} dy - \int_{-\frac{a}{2}}^{\frac{a}{2}}\Big[N_{yy}^p\Delta v^0\Big]_{y=-\frac{b}{2}}^{y=\frac{b}{2}} dx \\ & - \int_{-\frac{a}{2}}^{\frac{a}{2}}\Big[N_{xy}^p\Delta u^0\Big]_{y=-\frac{b}{2}}^{y=\frac{b}{2}} dx - \int_{-\frac{b}{2}}^{\frac{b}{2}}\Big[N_{xy}^p\Delta v^0\Big]_{x=-\frac{a}{2}}^{x=\frac{a}{2}} dy \\ & + \int_{-\frac{b}{2}}^{\frac{b}{2}}\left[M_{xx}^p\frac{\partial\Delta w^0}{\partial x}\right]_{x=-\frac{a}{2}}^{x=\frac{a}{2}} dy - \int_{-\frac{b}{2}}^{\frac{b}{2}}\Big[M_{xx,x}^p\Delta w^0\Big]_{y=-\frac{a}{2}}^{y=\frac{a}{2}} dy \\ & + \int_{-\frac{a}{2}}^{\frac{a}{2}}\left[M_{yy}^p\frac{\partial\Delta w^0}{\partial y}\right]_{y=-\frac{b}{2}}^{y=\frac{b}{2}} dx - \int_{-\frac{a}{2}}^{\frac{a}{2}}\Big[M_{yy,y}^p\Delta w^0\Big]_{y=-\frac{b}{2}}^{y=\frac{b}{2}} dx \\ & + \int_{-\frac{b}{2}}^{\frac{b}{2}}\left[M_{xy}^p\frac{\partial\Delta w^0}{\partial y}\right]_{x=-\frac{a}{2}}^{x=\frac{a}{2}} dy - \left[\Big[M_{xy,xy}^p\Delta w^0\Big]_{y=-\frac{b}{2}}^{y=\frac{b}{2}}\right]_{-\frac{b}{2}}^{\frac{b}{2}} dx \\ & + \int_{-\frac{a}{2}}^{\frac{a}{2}}\left[M_{xy}^p\frac{\partial\Delta w^0}{\partial x}\right]_{y=-\frac{b}{2}}^{y=\frac{b}{2}} dx - \left[\Big[M_{xy,xy}^p\Delta w^0\Big]_{y=-\frac{b}{2}}^{y=\frac{b}{2}}\right]_{-\frac{b}{2}}^{\frac{b}{2}} dx\end{aligned} \tag{3.33}$$

The boundary constraints terms of the transducer are not null because there are no clear boundary conditions for the transducer on the host plate.

3.2.2 Kinetic energy and its variation

The kinetic energy T^* of the system can be written as:

$$\begin{aligned} T^* = \frac{1}{2}\int_{\Gamma_s} \Bigg[\int_{Z_s} & \rho_s(\dot{u}^T\dot{u} + \dot{v}^T\dot{v} + \dot{w}^T\dot{w})\ dz \\ & + \int_{Z_p} \rho_p(\dot{u}^T\dot{u} + \dot{v}^T\dot{v} + \dot{w}^T\dot{w})\Lambda_x^p\Lambda_y^p\ dz \Bigg] d\Gamma_s \end{aligned} \tag{3.34}$$

where ρ_s, ρ_p are the mass densities of the host structure and the transducer, respectively. The displacement field is expressed as

$$\begin{cases} u = u^0 - z\frac{\partial w}{\partial x} \\ v = v^0 - z\frac{\partial w}{\partial y} \\ w = w^0. \end{cases} \tag{3.35}$$

Substituting Equation (3.35) into Equation (3.34) yields

$$\begin{aligned} T^* = \frac{1}{2}\int_{\Gamma_s} \Big[& t_s\rho_s(\dot{u}^0\dot{u}^0 + \dot{v}^0\dot{v}^0 + \dot{w}^0\dot{w}^0) \\ & + t_p\rho_p(\dot{u}^0\dot{u}^0 + \dot{v}^0\dot{v}^0 + \dot{w}^0\dot{w}^0)\Lambda_x^p\Lambda_y^p \Big] d\Gamma_s. \end{aligned} \tag{3.36}$$

The terms containing $\frac{\partial w}{\partial x}$ and $\frac{\partial w}{\partial y}$ are vanished because the rotations do not contribute to the kinetic energy. Then, the variation of kinetic energy can be easily obtained as follows:

$$\begin{aligned} \Delta T^* = & \int_{\Gamma_s} [t_s\rho_s(\dot{u}^0\Delta\dot{u}^0 + \dot{v}^0\Delta\dot{v}^0 + \dot{w}^0\Delta\dot{w}^0) \\ & + t_p\rho_p(\dot{u}^0\Delta\dot{u}^0 + \dot{v}^0\Delta\dot{v}^0 + \dot{w}^0\Delta\dot{w}^0)\Lambda_x^p\Lambda_y^p] d\Gamma_s \\ = & \int_{\Gamma_s} [t_s\rho_s(\ddot{u}^0\Delta u^0 + \ddot{v}^0\Delta v^0 + \ddot{w}^T\Delta w) \\ & + t_p\rho_p(\ddot{u}^0\Delta u^0 + \ddot{v}^0\Delta v^0 + \ddot{w}^0\Delta w^0)\Lambda_x^p\Lambda_y^p) d\Gamma_s. \end{aligned} \tag{3.37}$$

3.2.3 Work due to external loads and its variation

Let's have a look now the external work due to transverse loads and in-plane loads. As a transverse pointed force $f(t)$ excited at position (x_0, y_0) on the structure can be a representative of external loads, the induced external work can be written as:

$$W^* = \int_{\Gamma_s} f(t)w^0\delta(x - x_0)\delta(y - y_0)d\Gamma_s \tag{3.38}$$

where δ is the Dirac delta-function. In a large deflection analysis, the work of in-plane loads due to a deflection w is given as:

$$V^* = \int_{\Gamma_s} \Big(N_{xx}\varepsilon_{xx} + N_{yy}\varepsilon_{yy} + N_{xy}\varepsilon_{xy} \Big) d\Gamma_s \tag{3.39}$$

where N_{xx}, N_{yy} and N_{xy} are the pre-buckling loads applied to the mid-surface of the host plate and ε_{xx}, ε_{yy} and ε_{xy} are the strains on the mid-surface due to deflection w. Since small strain variation is considered in the present study, V^* can be neglected in the present analysis. Thus, the variation of the work due to external transverse loads is simply as follows:

$$\Delta W^* = \int_{\Gamma_s} f(t)\delta(x - x_0)\delta(y - y_0) \times \Delta w^0 d\Gamma_s \tag{3.40}$$

3.2.4 Governing equations and boundary constraints of the transducer

The generalized Hamilton's principle for an electro-elastic body can be described as [74]:

$$\int_{t_1}^{t_2} [\Delta T^* + \Delta U^* + \Delta W^*] dt = 0. \tag{3.41}$$

The variations of kinetic energy ΔT^*, potential energy ΔU^* and external work ΔW^* can be substituted in Equation (3.41). Then, all the terms can be regrouped according to the variations Δu, Δv and Δw. As these three variations can be arbitrary values, their factors should be null. Therefore, the equations of motion of the overall structure can be obtained as follows:

$$\frac{\partial N^s_{xx}}{\partial x} + \frac{\partial N^s_{xy}}{\partial y} + \left(\frac{\partial N^p_{xx}}{\partial x} + \frac{\partial N^p_{xy}}{\partial y} \right) \Lambda^p_x \Lambda^p_y = t_s \rho_s \frac{\partial^2 u^0}{\partial t^2} + t_p \rho_p \frac{\partial^2 u^0}{\partial t^2} \Lambda^p_x \Lambda^p_y; \tag{3.42a}$$

$$\frac{\partial N^s_{xy}}{\partial x} + \frac{\partial N^s_{yy}}{\partial y} + \left(\frac{\partial N^p_{xy}}{\partial x} + \frac{\partial N^p_{yy}}{\partial y} \right) \Lambda^p_x \Lambda^p_y = t_s \rho_s \frac{\partial^2 v^0}{\partial t^2} + t_p \rho_p \frac{\partial^2 v^0}{\partial t^2} \Lambda^p_x \Lambda^p_y; \tag{3.42b}$$

$$\begin{split} &\frac{\partial^2 M^s_{xx}}{\partial x^2} + 2\frac{\partial^2 M^s_{xy}}{\partial x \partial y} + \frac{\partial^2 M^s_{yy}}{\partial y^2} + \left(\frac{\partial^2 M^p_{xx}}{\partial x^2} + 2\frac{\partial^2 M^p_{xy}}{\partial x \partial y} + \frac{\partial^2 M^p_{yy}}{\partial y^2} \right) \Lambda^p_x \Lambda^p_y \\ &= t_s \rho_s \frac{\partial^2 w^0}{\partial t^2} + t_p \rho_p \frac{\partial^2 w^0}{\partial t^2} \Lambda^p_x \Lambda^p_y - f. \end{split} \tag{3.42c}$$

The generalized Hamilton's principle has transformed the system into a weak formulation. We can observe that the mechanical influences of the MFC transducers are described by the spatial distributions in the above equations. The inverse piezoelectric effect is included in the membrane forces N^p_{ij} and bending moments M_{ij}^{p} (see Equation (3.19)). The inverse piezoelectric effect can be deduced from Equations (3.42a) to (3.42c) so that the equivalent force per unit area of the MFC transducer is given as follows:

$$N_{xx} = t_p \bar{e}_{31}^{*} E \frac{\partial \Lambda_x^p \Lambda_y^p}{\partial x} + t_p \bar{e}_{36}^{*} E \frac{\partial \Lambda_x^p \Lambda_y^p}{\partial y} \tag{3.43a}$$

$$N_{yy} = t_p \bar{e}_{32}^{*} E \frac{\partial \Lambda_x^p \Lambda_y^p}{\partial y} + t_p \bar{e}_{36}^{*} E \frac{\partial \Lambda_x^p \Lambda_y^p}{\partial x} \tag{3.43b}$$

$$N_{zz} = -z_p \bar{e}_{31}^{*} E \frac{\partial^2 \Lambda_x^p \Lambda_y^p}{\partial x^2} - z_p \bar{e}_{32}^{*} E \frac{\partial^2 \Lambda_x^p \Lambda_y^p}{\partial y^2} - 2 z_p \bar{e}_{36}^{*} E \frac{\partial^2 \Lambda_x^p \Lambda_y^p}{\partial x \partial y}. \tag{3.43c}$$

We can observe again that the transducer generates both membrane and bending behaviors by its inverse piezoelectric effect. The spatial distributions terms determine the distribution of these equivalent loads. The boundary constraints of the transducer from Equation (3.41) result in the equivalent moment and equivalent transverse shear forces, respectively:

$$\begin{cases} M_{xx} = D_{11} \frac{\partial^2 w}{\partial x^2} + D_{12} \frac{\partial^2 w}{\partial y^2} = -z_p \bar{e}_{31}^{*} E \Lambda_x^p \Lambda_y^p \\ M_{yy} = D_{22} \frac{\partial^2 w}{\partial y^2} + D_{12} \frac{\partial^2 w}{\partial x^2} = -z_p \bar{e}_{32}^{*} E \Lambda_x^p \Lambda_y^p \\ M_{xy} = M_{yx} = 2 D_{66} \frac{\partial^2 w}{\partial x \partial y} = -z_p \bar{e}_{36}^{*} E \Lambda_x^p \Lambda_y^p \end{cases} \tag{3.44}$$

$$\begin{cases} \tau_{xz} = D_{11} \dfrac{\partial^3 w}{\partial x^3} + (D_{12} + 2 D_{66}) \dfrac{\partial^3 w}{\partial x \partial y^2} \\ \quad = -z_p \bar{e}_{31}^{*} E \dfrac{\partial}{\partial x} (\Lambda_x^p \Lambda_y^p) - z_p \bar{e}_{36}^{*} E \dfrac{\partial}{\partial y} (\Lambda_x^p \Lambda_y^p) \\ \tau_{yz} = D_{22} \dfrac{\partial^3 w}{\partial y^3} + (D_{12} + 2 D_{66}) \dfrac{\partial^3 w}{\partial y \partial x^2} \\ \quad = -z_p \bar{e}_{32}^{*} E \dfrac{\partial}{\partial y} (\Lambda_x^p \Lambda_y^p) - z_p \bar{e}_{36}^{*} E \dfrac{\partial}{\partial x} (\Lambda_x^p \Lambda_y^p). \end{cases} \tag{3.45}$$

By introducing the spatial distribution of the MFC transducer, the equivalent force per unit area, equivalent moments and transverse shear forces are determined, respectively. These three kinds of loads agree with the elastic equilibrium theory: The transverse shear loads are the first-order derivative of the bending moments and the force N_{zz} is the second-order derivative of the bending moments. The equivalent loads exist simultaneously and describe the actuation of a piezoelectric actuator through different parameters.

3.3 Inverse piezoelectric effect characterization using equivalent forces

The analysis in the previous section demonstrated that the transducer generates both membrane and bending motions on a host plate. In this section, the corresponding equivalent forces are going to be elaborated.

3.3.1 Equivalent membrane forces

We can observe from Equation (3.43) that both N_{xx} and N_{yy} are actually the membrane forces, which are expressed in the same way but in different directions. Let's take N_{xx} as an example. Substituting $\Lambda_x^p \Lambda_y^p$ into N_{xx} yields:

$$\begin{aligned} N_{xx} =& t_p \bar{e}_{31}^* E \frac{\partial}{\partial x}\Big([H(x+\frac{a}{2}) - H(x-\frac{a}{2})] \times [H(y+\frac{b}{2}) - H(y-\frac{b}{2})] \Big) \\ &+ t_p \bar{e}_{36}^* E \frac{\partial}{\partial y}\Big([H(x+\frac{a}{2}) - H(x-\frac{a}{2})] \times [H(y+\frac{b}{2}) - H(y-\frac{b}{2})] \Big). \end{aligned} \tag{3.46}$$

Since the Heaviside function is the integral of the Dirac delta-function, Equation (3.46) can be rewritten as:

$$\begin{aligned} N_{xx} =& t_p \bar{e}_{31}^* E \Big([\delta(x+\frac{a}{2}) - \delta(x-\frac{a}{2})] \times [H(y+\frac{b}{2}) - H(y-\frac{b}{2})] \Big) \\ &+ t_p \bar{e}_{36}^* E \Big([H(x+\frac{a}{2}) - H(x-\frac{a}{2})] \times [\delta(y+\frac{b}{2}) - \delta(y-\frac{b}{2})] \Big) \end{aligned} \tag{3.47}$$

in which, δ is the Dirac delta function. Because $E = -V/t_p$, the membrane force in x direction on the host structure can be expressed as:

$$\begin{aligned} f_{xx} =& - V \bar{e}_{31}^* \int_{\Gamma_s} \Big([\delta(x+\frac{a}{2}) - \delta(x-\frac{a}{2})] \times [H(y+\frac{b}{2}) - H(y-\frac{b}{2})] \Big) d\Gamma_s \\ &- V \bar{e}_{36}^* \int_{\Gamma_s} \Big([H(x+\frac{a}{2}) - H(x-\frac{a}{2})] \times [\delta(y+\frac{b}{2}) - \delta(y-\frac{b}{2})] \Big) d\Gamma_s. \end{aligned} \tag{3.48}$$

Similarly, the membrane force in y direction is given as follows:

$$\begin{aligned} f_{yy} =& - V \bar{e}_{32}^* \int_{\Gamma_s} \Big([H(x+\frac{a}{2}) - H(x-\frac{a}{2})] \times [\delta(y+\frac{b}{2}) - \delta(y-\frac{b}{2})] \Big) d\Gamma_s \\ &- V \bar{e}_{36}^* \int_{\Gamma_s} \Big([\delta(x+\frac{a}{2}) - \delta(x-\frac{a}{2})] \times [H(y+\frac{b}{2}) - H(y-\frac{b}{2})] \Big) d\Gamma_s. \end{aligned} \tag{3.49}$$

3.3.2 Equivalent bending forces

The analysis here focuses on the transverse equivalent force N_{zz}. Substituting the spatial distribution of Equation (3.24) into Equation (3.43), the equivalent force N_{zz} for a rectangular MFC transducer is rewritten as follows:

$$\begin{aligned} f_{zz} = \int_{\Gamma_s} \Bigg\{ & - z_p \bar{e}_{31}^* E \frac{\partial^2}{\partial x^2} \Big([H(x+\frac{a}{2}) - H(x-\frac{a}{2})] \times [H(y+\frac{b}{2}) - H(y-\frac{b}{2})] \Big) \\ & - z_p \bar{e}_{32}^* E \frac{\partial^2}{\partial y^2} \Big([H(x+\frac{a}{2}) - H(x-\frac{a}{2})] \times [H(y+\frac{b}{2}) - H(y-\frac{b}{2})] \Big) \\ & - 2 z_p \bar{e}_{36}^* E \frac{\partial^2}{\partial x \partial y} \Big([H(x+\frac{a}{2}) - H(x-\frac{a}{2})] \times [H(y+\frac{b}{2}) - H(y-\frac{b}{2})] \Big) \Bigg\} d\Gamma_s . \end{aligned} \tag{3.50}$$

The three terms in the above equation represent the transverse equivalent forces, which distribute along x, y and xy directions, respectively. The distributional derivation should be performed on the partial derivatives of the Heaviside functions in (3.50):

1. Given a test function $\varphi(x, y)$, which is smooth and derivable, then:

$$\begin{aligned} & \int_{\Gamma_s} \varphi(x,y) \frac{\partial^2}{\partial x^2} \Big([H(x+\frac{a}{2}) - H(x-\frac{a}{2})] \times [H(y+\frac{b}{2}) - H(y-\frac{b}{2})] \Big) d\Gamma_s \\ & = \int_{-\frac{b}{2}}^{\frac{b}{2}} \int_{-\frac{a}{2}}^{\frac{a}{2}} \varphi(x,y) [\delta'(x+\frac{a}{2}) - \delta'(x-\frac{a}{2})] \times [H(y+\frac{b}{2}) - H(y-\frac{b}{2})] dx dy \\ & = \int_{-\frac{b}{2}}^{\frac{b}{2}} \Big(\frac{\partial \varphi(x,y)}{\partial x}\Big|_{x=\frac{a}{2}} - \frac{\partial \varphi(x,y)}{\partial x}\Big|_{x=-\frac{a}{2}} \Big) [H(y+\frac{b}{2}) - H(y-\frac{b}{2})] dy. \end{aligned} \tag{3.51}$$

   As $\varphi(x, y)$ can be considered as the deflection of the host plate, the transverse equivalent force distributed along x direction is, thus, equivalent to the bending moment M_{xx} in Equation (3.44). The partial derivative of $\varphi(x, y)$ can be approximated by the finite difference method, while, the uniform spacing Δx of finite difference interval in x direction is adopted in the analysis. Applying the first-order forward finite difference approximation to Equation (3.51) yields:

$$\begin{aligned} & \int_{\Gamma_s} \varphi(x,y) \frac{\partial^2}{\partial x^2} \Big([H(x+\frac{a}{2}) - H(x-\frac{a}{2})] \times [H(y+\frac{b}{2}) - H(y-\frac{b}{2})] \Big) d\Gamma_s \\ & = \int_{-\frac{b}{2}}^{\frac{b}{2}} \Big(\frac{1}{\Delta x} (\varphi(\frac{a}{2} + \Delta x, y) - \varphi(\frac{a}{2}, y)) - \frac{1}{\Delta x} (\varphi(-\frac{a}{2} + \Delta x, y) - \varphi(-\frac{a}{2}, y)) \Big) \\ & \qquad \times [H(y+\frac{b}{2}) - H(y-\frac{b}{2})] dy \end{aligned} \tag{3.52}$$

The sampling property of the Dirac delta-function given in Equation (3.53) can be introduced to Equation (3.52).

$$\int_{c-\varepsilon}^{c+\varepsilon} \varphi(x,y)\delta(x)dx = \varphi(c,y) \tag{3.53}$$

where c is a constant and $\varepsilon > 0$. Then Equation (3.52) can be rewritten as:

$$\begin{aligned}
&\int_{\Gamma_s} \varphi(x,y)\frac{\partial^2}{\partial x^2}\left([H(x+\frac{a}{2})-H(x-\frac{a}{2})]\times[H(y+\frac{b}{2})-H(y-\frac{b}{2})]\right)d\Gamma_s \\
&=\int_{-\frac{b}{2}}^{\frac{b}{2}}\int_{-\frac{a}{2}}^{\frac{a}{2}}\frac{1}{\Delta x}[\delta(x-\frac{a}{2}-\Delta x)-\delta(x-\frac{a}{2})-\delta(x+\frac{a}{2}-\Delta x)+\delta(x+\frac{a}{2})] \\
&\qquad\times[H(y+\frac{b}{2})-H(y-\frac{b}{2})]\varphi(x,y)dxdy.
\end{aligned} \tag{3.54}$$

Finally,

$$\begin{aligned}
&\int_{\Gamma_s} \frac{\partial^2}{\partial x^2}\left([H(x+\frac{a}{2})-H(x-\frac{a}{2})]\times[H(y+\frac{b}{2})-H(y-\frac{b}{2})]\right)d\Gamma_s \\
&=\int_{\Gamma_s}\frac{1}{\Delta x}[\delta(x-\frac{a}{2}-\Delta x)-\delta(x-\frac{a}{2})-\delta(x+\frac{a}{2}-\Delta x)+\delta(x+\frac{a}{2})] \\
&\qquad\times[H(y+\frac{b}{2})-H(y-\frac{b}{2})]d\Gamma_s.
\end{aligned} \tag{3.55}$$

2. The partial derivatives in y can be similarly treated:

$$\begin{aligned}
&\int_{\Gamma_s} \frac{\partial^2}{\partial y^2}\left([H(x+\frac{a}{2})-H(x-\frac{a}{2})]\times[H(y+\frac{b}{2})-H(y-\frac{b}{2})]\right)d\Gamma_s \\
&=\int_{\Gamma_s}\frac{1}{\Delta y}[\delta(y-\frac{b}{2}-\Delta y)-\delta(y-\frac{b}{2})-\delta(y+\frac{b}{2}-\Delta y)+\delta(y+\frac{b}{2})] \\
&\qquad\times[H(x+\frac{a}{2})-H(x-\frac{a}{2})]d\Gamma_s.
\end{aligned} \tag{3.56}$$

3. In addition, the partial derivatives in xy direction can be given as:

$$\begin{aligned}
&\int_{\Gamma_s} \frac{\partial^2}{\partial x\partial y}\left([H(x+\frac{a}{2})-H(x-\frac{a}{2})]\times[H(y+\frac{b}{2})-H(y-\frac{b}{2})]\right)d\Gamma_s \\
&=\int_{\Gamma_s}[\delta(x+\frac{a}{2})-\delta(x-\frac{a}{2})]\times[\delta(y+\frac{b}{2})-\delta(y-\frac{b}{2})]d\Gamma_s.
\end{aligned} \tag{3.57}$$

It is worthwhile to mention that the point forces in Equation (3.57) are actually consistent with the equivalent loads from [145, 148]. They generate the same twisting effect on the structure as the bending moments M_{xy} and M_{yx} in Equation (3.44). We can also conclude that the equivalent loads derived in [145, 148] are combinations of the equivalent forces and equivalent bending moments that are obtained from Equation (3.50).

Therefore, Equation (3.50) can be finally rewritten as follows:

$$\begin{aligned} f_{zz} = \int_{\Gamma_s} \Big\{ & - z_p \bar{e}^*_{31} E \frac{1}{\Delta x} [\delta(x - \frac{a}{2} - \Delta x) - \delta(x - \frac{a}{2}) - \delta(x + \frac{a}{2} - \Delta x) \\ & \quad + \delta(x + \frac{a}{2})] \times [H(y + \frac{b}{2}) - H(y - \frac{b}{2})] \\ & - z_p \bar{e}^*_{32} E \frac{1}{\Delta y} [\delta(y - \frac{b}{2} - \Delta y) - \delta(y - \frac{b}{2}) - \delta(y + \frac{b}{2} - \Delta y) \\ & \quad + \delta(y + \frac{b}{2})] \times [H(x + \frac{a}{2}) - H(x - \frac{a}{2})] \\ & - 2 z_p \bar{e}^*_{36} E [\delta(x + \frac{a}{2}) - \delta(x - \frac{a}{2})] \times [\delta(y + \frac{b}{2}) - \delta(y - \frac{b}{2})] \Big\} d\Gamma_s. \end{aligned} \tag{3.58}$$

Supposing a uniform distribution of the electric field between the electrodes $E = -V/t_p$, Equation (3.58) is given as:

$$\begin{aligned} f_{zz} = \int_{\Gamma_s} \Big\{ & z_p \bar{e}^*_{31} \frac{V}{t_p} \frac{1}{\Delta x} [\delta(x - \frac{a}{2} - \Delta x) - \delta(x - \frac{a}{2}) - \delta(x + \frac{a}{2} - \Delta x) \\ & \quad + \delta(x + \frac{a}{2})] \times [H(y + \frac{b}{2}) - H(y - \frac{b}{2})] \\ & + z_p \bar{e}^*_{32} \frac{V}{t_p} \frac{1}{\Delta y} [\delta(y - \frac{b}{2} - \Delta y) - \delta(y - \frac{b}{2}) - \delta(y + \frac{b}{2} - \Delta y) \\ & \quad + \delta(y + \frac{b}{2})] \times [H(x + \frac{a}{2}) - H(x - \frac{a}{2})] \\ & + 2 z_p \bar{e}^*_{36} \frac{V}{t_p} [\delta(x + \frac{a}{2}) - \delta(x - \frac{a}{2})] \times [\delta(y + \frac{b}{2}) - \delta(y - \frac{b}{2})] \Big\} d\Gamma_s. \end{aligned} \tag{3.59}$$

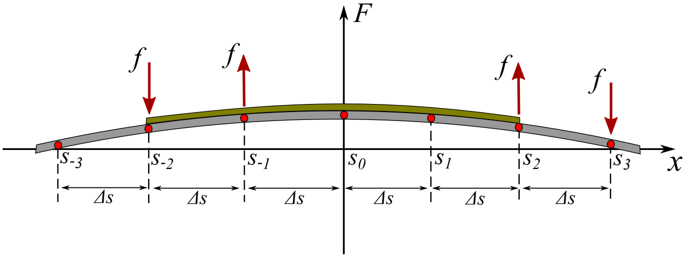

Figure 3.7: The distribution of f_{zz} in x/y direction via forward finite difference approximation (Δs indicates either Δx or Δy.)

The distribution of f_{zz} along x (or y) direction is shown in Figure 3.7. The resultant of f_{zz} is null, and this confirms that the piezoelectric actuators are self-equilibrium [74]. However, We can observe from the figure that f_{zz} is not symmetrically applied to the MFC transducer because a first-order forward finite difference is used here. As the right side derivative should be equal to the left side one if the derivative exists at a certain point on a smooth function, the backward finite difference approximation can be adopted at s_2. Hence f_{zz} can be symmetrically applied on the transducer, as shown in Figure 3.8, but this could lead to approximation error. This error is analyzed in the next section. Finally, the equivalent force f_{zz} is rewritten as follows:

$$
\begin{aligned}
f_{zz} = \int_{\Gamma_s} \Bigg\{ & z_p \bar{e}^*_{31} \frac{V}{t_p} \frac{1}{\Delta x} [\delta(x - \frac{a}{2} - \delta(x - \frac{a}{2} + \Delta x)) - \delta(x + \frac{a}{2}) \\
& + \delta(x + \frac{a}{2} + \Delta(x))] \times [H(y + \frac{b}{2}) - H(y - \frac{b}{2})] \\
& z_p \bar{e}^*_{32} \frac{V}{t_p} \frac{1}{\Delta y} [\delta(y - \frac{b}{2}) - \delta(y - \frac{b}{2} + \Delta y) - \delta(y + \frac{b}{2} - \Delta y) \\
& + \delta(y + \frac{b}{2})] \times [H(x + \frac{a}{2}) - H(x - \frac{a}{2})] \\
& 2 z_p \bar{e}^*_{36} \frac{V}{t_p} [\delta(x + \frac{a}{2}) - \delta(x - \frac{a}{2})] \times [\delta(y + \frac{b}{2}) - \delta(y - \frac{b}{2})] \Bigg\} d\Gamma_s.
\end{aligned}
\tag{3.60}
$$

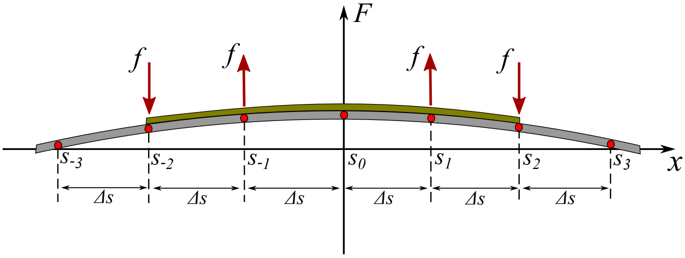

Figure 3.8: The distribution of f_{zz} in x/y direction via a forward-backward finite difference approximation (Δs indicates either Δx or Δy.)

A finite difference approximation can be central, forward or backward and the coefficients of each type are given in the tables in Appendix 8.1. A first-order forward finite difference approximation is used as a demonstration in the analysis, but higher order approximations can be derived by following the same approach. In fact, the finite difference approximation that used in the bending forces provides many possibilities to describe the inverse piezoelectric effect of the transducer. Let's take the equivalent force f_{zz} in Figure 3.8 as an example, a spacing of $2\Delta s$ will result in a "three-point" bending distribution. As we mentioned above, the used-finite difference approximation may lead to unwanted error so that the accuracy of the equivalent forces needs to verify for ensuring its reliability in modeling.

3.3.3 Accuracy analysis of the inverse piezoelectric coupling

The accuracy of the equivalent force f_{zz} is analyzed through a bending diagram. Let's take the inverse piezoelectric effect in x direction in Figure 3.9 as an example. The equivalent bending moments are a pair of opposite sign bending moments assigned on the edges of the transducer. They generate a uniform moment distribution in (**a.3**). The equivalent forces result in a similar shear force and moment distribution when Δx in (**b**) tends to zero. In contrast, the equivalent forces form a three-point force bending configuration when Δx equals to the half-length of the transducer, as shown in (**c**). The "three-point" bending configuration generates different shear force and moment distributions from the pair of opposite sign bending moments. Different finite difference approximations may severely influence the accuracy of the corresponding equivalent force. As the equivalent bending moment and equivalent force should generate the same bending motions on the plate, the total bending effort balance of the bending moments is a reasonable reference for analyzing the accuracy of the proposed equivalent forces.

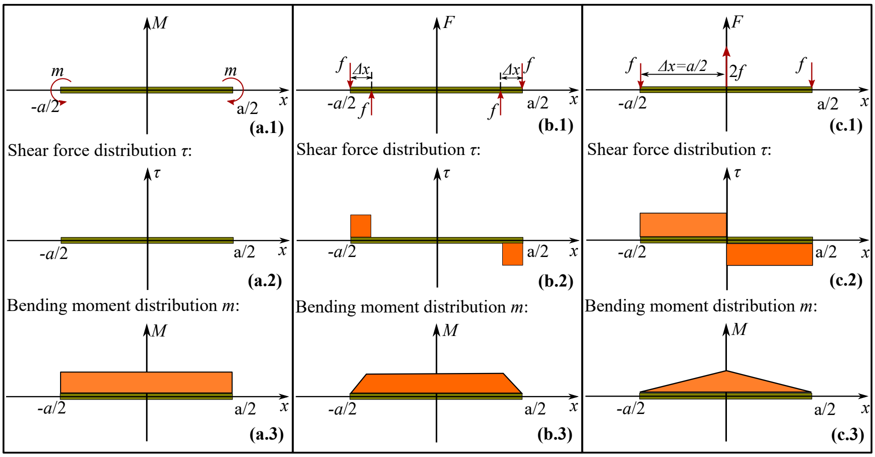
M
m
m
-a/2
a/2
x
(a.1)
Shear force distribution τ:
τ
-a/2
a/2
x
(a.2)
Bending moment distribution m:
M
-a/2
a/2
x
(a.3)
F
f
Δx
Δx
f
-a/2
f
f
a/2
x
(b.1)
Shear force distribution τ:
τ
-a/2
a/2
x
(b.2)
Bending moment distribution m:
M
-a/2
a/2
x
(b.3)
F
f
Δx=a/2
2f
f
-a/2
a/2
x
(c.1)
Shear force distribution τ:
τ
-a/2
a/2
x
(c.2)
Bending moment distribution m:
M
-a/2
a/2
x
(c.3)

Figure 3.9: One-dimensional equivalent loads bending diagram of a rectangular MFC transducer

The total bending effort balance implies that the integrals of moment distribution caused by the three types of equivalent loads in Figure 3.9 are equal. Taking the cases **(a)** and **(b)** in the Figure 3.9 as a demonstration, the integral of the bending moment distribution equals to $a \times m$, in **(a.3)**, where m is the magnitude of the bending moment and a is the size of the transducer. In the case of **(b)**, the detailed notation for the bending moment distribution is given in Figure 3.10. The maximum bending moment caused by f is equal to fd_s. Hence, the integral of the bending moment distribution equals to $fd_s(2a - 2d_s)/2$.

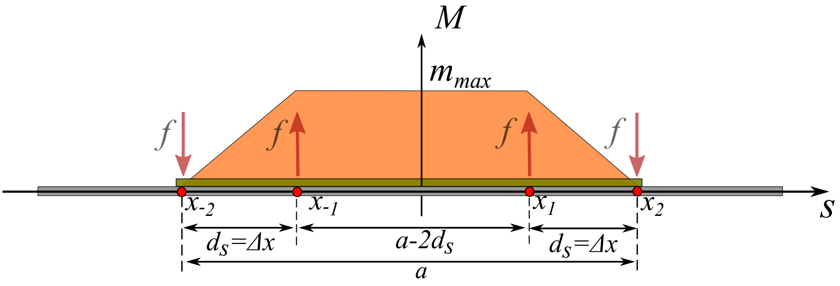
M
m_max
f
f
f
f
x-2
x-1
x1
x2
S
ds=Δx
a-2ds
ds=Δx
a

Figure 3.10: Bending diagram of piezoelectric transducer in x/y direction due to the equivalent forces

A coefficient α_x can be introduced here to indicate the ratio of total bending efforts between the equivalent bending moment and the equivalent forces along x direction. Then, the following relation retains:

$$\begin{aligned} ma &= \alpha_x f d_s (a + (a - 2d_s))/2 \\ \Rightarrow \alpha &= \frac{am}{(a - d_s) f d_s} \end{aligned} \tag{3.61}$$

As f is quantitatively equal to m according to Equations (3.44) and (3.60), α_x can be determined as follows:

$$\Rightarrow \alpha_x = \frac{a}{a - d_s}. \tag{3.62}$$

Hence, the accuracy of the two kinds of equivalent forces in Figure 3.9 can be quantified by α_x: $\alpha_x = 4/3$ for the configuration **(b)** and $\alpha_x = 2$ for the concentrated equivalent force **(c)**. $\alpha_x \neq 1$ implies that the adopted first-order finite difference approximation in f_{zz} is not accurate enough, but α_x can be used to correct the equivalent force. This analysis is also applicable to the transverse equivalent force along y direction (named as α_y). A higher order of approximation can effectively improve the accuracy of the equivalent force. A second-order finite difference approach is given in Appendix 8.5, can already achieve accurate approximations. It is important to mention that this analysis is based on the static bending effect. A significant modification on the distribution of the equivalent forces may lead to inaccurate results in dynamic applications.

3.4 Assessments of different equivalent loads

Firstly, we derived the equivalent forces due to the inverse piezoelectric effect of the integrated transducer. Both the equivalent membrane forces and equivalent bending forces are obtained. The equivalent bending forces are flexible to be assigned on the transducer because they are approximated solutions.

Secondly, we can observe form the above analysis that the spatial distribution terms determine the distribution of the equivalent bending moments that apply to the edges of the MFC transducer. M_{xy} and M_{yx} generate the same twisting effect on the transducer as the point forces in [145, 148]. The membrane forces should also be considered in modeling to fully characterize the inverse piezoelectric effect.

Thirdly, we also obtained the transverse shear loads caused by the inverse piezoelectric effect of the studied transducer. We can find that the bending moments, the transverse shear forces and the equivalent forces comply with the elastic equilibrium principle. Wherefore, the mechanical effect caused by the inverse piezoelectric effect of the transducer can be properly characterized.

Fourthly, the equivalent loads in Figure 2.18 from [145, 148] can be considered as a combination of the equivalent force and bending moments. We can obtain the same equivalent loads for a rectangular MFC transducer before we apply the finite difference approximations in the determination of f_{zz}.

Finally, it is worthwhile to notice that all the equivalent loads can be used to model MFC transducers. The most convenient option should be selected according to the practical requirements in applications. The following study focuses on the equivalent forces that have not been investigated in the literature.

3.5 Direct piezoelectric effect characterization using electric boundary conditions

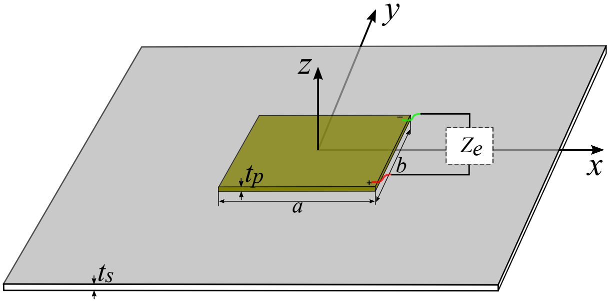

Figure 3.11: A composite plate with an integrated MFC transducer and an external electrical circuit

Let's consider the same rectangular MFC transducer, which is analyzed in the previous section, as shown in Figure 3.11. An electric circuit connected to the MFC transducer and the impedance of the electric circuit is Z_e. The direct piezoelectric effect of the transducer is expressed as follows according to Equation (3.16b):

$$D = \bar{e}^*_{31} S^p_{xx} + 2\bar{e}^*_{36} S^p_{xy} + \bar{e}^*_{32} S^p_{yy} + \epsilon^S E. \tag{3.63}$$

Then, the current flux in the electric circuit can be described as

$$\frac{d}{dt} \int_\Gamma D \times \vec{n} d\Gamma = \frac{V}{Z_e} \tag{3.64}$$

where $\vec{n}$ is the outer normal vector on the electrodes of the transducer, D is the electric displacement, V is voltage and A is the electrode surface. Substituting Equation (3.63) into Equation (3.64) yields:

$$\frac{d}{dt} \int_{\Gamma_s} [(\bar{e}^*_{31} S^p_{xx} + \bar{e}^*_{36} S^p_{xy} + \bar{e}^*_{32} S^p_{yy}) - \epsilon^S \frac{V(t)}{t_p}] \Lambda^p_x \Lambda^p_y d\Gamma_s = \frac{V(t)}{Z_e} \tag{3.65}$$

where t_p is the electrodes distance in the generalized piezoelectric formulation. $\Lambda^p_x \Lambda^p_y$ indicates that only the strains at the placement of the transducer contributes to the piezoelectric effect on the plate. Assuming that small strains occur on the MFC transducers, the strain-displacement relations in

Equation (3.5) can be adopted, and Equation (3.65) is rewritten as:

$$\begin{aligned}\frac{d}{dt}\int_{\Gamma_s}\Bigg[&\bar{e}_{31}^{*}\left(\frac{\partial u^0}{\partial x}-z\frac{\partial^2 w^0}{\partial x^2}\right)+\bar{e}_{36}^{*}\left(\frac{\partial u^0}{\partial y}+\frac{\partial v^0}{\partial x}-2z\frac{\partial^2 w^0}{\partial x\partial y}\right)\\ &+\bar{e}_{32}^{*}\left(\frac{\partial v^0}{\partial y}-z\frac{\partial^2 w^0}{\partial x^2}\right)-\epsilon^{S}\frac{V(t)}{t_p}\Bigg]\Lambda_x^p\Lambda_y^p d\Gamma_s=\frac{V(t)}{Z_e}.\end{aligned}\tag{3.66}$$

Integrating Equation (3.66) in the thickness-wise of the transducer yields:

$$\begin{aligned}\frac{d}{dt}\int_{\Gamma_s}\Bigg[&\left(\bar{e}_{31}^{*}\frac{\partial u^0}{\partial x}+\bar{e}_{36}^{*}\Big(\frac{\partial u^0}{\partial y}+\frac{\partial v^0}{\partial x}\Big)+\bar{e}_{32}^{*}\frac{\partial v^0}{\partial y}\right)-\frac{z_p}{t_p}\left(\bar{e}_{31}^{*}\frac{\partial^2 w^0}{\partial x^2}\right.\\ &\left.+2\bar{e}_{36}^{*}\frac{\partial^2 w^0}{\partial x\partial y}+\bar{e}_{32}^{*}\frac{\partial^2 w^0}{\partial x^2}\right)-\epsilon^{S}\frac{V(t)}{t_p}\Bigg]\Lambda_x^p\Lambda_y^p d\Gamma_s=\frac{V(t)}{Z_e}.\end{aligned}\tag{3.67}$$

If the transducer is surface-bonded on a host structure, then $z_s = t_s/2$. It appears in Equation (3.67) that only the strains on the middle surface of the transducer contribute to the piezoelectric effect. The dielectric constant term results in a capacitance effect as follows:

$$\int_{\Gamma_s}\epsilon_{33}^{S}\frac{V}{t_p}\Lambda_x^p\Lambda_y^p d\Gamma_s=C_pV.\tag{3.68}$$

Substituting Equation (3.68) into Equation (3.67) yields:

$$\begin{aligned}C_p\dot{V}+\frac{V}{Z_e}=\int_{\Gamma_s}\Bigg[&\Bigg(\underbrace{\Big(\bar{e}_{31}^{*}\frac{\partial\dot{u}^0}{\partial x}+\bar{e}_{36}^{*}\frac{\partial\dot{u}^0}{\partial y}\Big)}_{\Psi_u}+\underbrace{\Big(\tilde{e}_{36}^{*}\frac{\partial\dot{v}^0}{\partial x}+\bar{e}_{32}^{*}\frac{\partial\dot{v}^0}{\partial y}\Big)}_{\Psi_v}\Bigg)\\ &\underbrace{-\Big(z_s+\frac{t_p}{2}\Big)\left(\bar{e}_{31}^{*}\frac{\partial^2\dot{w}^0}{\partial x^2}+2\bar{e}_{36}^{*}\frac{\partial^2\dot{w}^0}{\partial x\partial y}+\bar{e}_{32}^{*}\frac{\partial^2\dot{w}^0}{\partial x^2}\right)}_{\Psi_w}\Bigg]\Lambda_x^p\Lambda_y^p d\Gamma_s.\end{aligned}\tag{3.69}$$

The terms on the right side of Equation (3.69) are regrouped into Ψ_u, Ψ_v and Ψ_w with respect to u^0, v^0 and w^0, respectively. Let's first take Ψ_u as an example. The integration by parts yields:

$$\begin{aligned}\Psi_u=\int_{\Gamma_s}\Big(&\bar{e}_{31}^{*}[\delta(x+\frac{a}{2})-\delta(x-\frac{a}{2})]\times[H(y+\frac{b}{2})-H(y-\frac{b}{2})]\\ &+\bar{e}_{36}^{*}[H(x+\frac{a}{2})-H(x-\frac{a}{2})]\times[\delta(y+\frac{b}{2})-\delta(y-\frac{b}{2})]\Big)\dot{u}^0 d\Gamma_s\end{aligned}\tag{3.70}$$

where the spatial distribution of the transducer in Equation (3.24) is already substituted. Similarly, Ψ_v can be deduced as:

$$\begin{aligned}\Psi_v=\int_{\Gamma_s}\Big(&\bar{e}_{36}^{*}[\delta(x+\frac{a}{2})-\delta(x-\frac{a}{2})]\times[H(y+\frac{b}{2})-H(y-\frac{b}{2})]\\ &+\bar{e}_{32}^{*}[H(x+\frac{a}{2})-H(x-\frac{a}{2})]\times[\delta(y+\frac{b}{2})-\delta(y-\frac{b}{2})]\Big)\dot{v}^0 d\Gamma_s.\end{aligned}\tag{3.71}$$

Ψ_u and Ψ_v represent the direct piezoelectric effects caused by the in-plane behaviors of the plate. Finally, Ψ_w is given as follows by introducing the spatial distribution of the transducer in Equation (3.24):

$$\begin{aligned}\Psi_w = &-\frac{z_p}{t_p}\bar{e}^*_{31}\int_{\Gamma_s}\frac{\partial^2\dot{w}^0}{\partial x^2}[H(x+\frac{a}{2})-H(x-\frac{a}{2})]\\ &\times[H(y+\frac{b}{2})-H(y-\frac{b}{2})]d\Gamma_s\\ &-\frac{z_p}{t_p}\bar{e}^*_{32}\int_{\Gamma_s}\frac{\partial^2\dot{w}^0}{\partial y^2}[H(x+\frac{a}{2})-H(x-\frac{a}{2})]\\ &\times[H(y+\frac{b}{2})-H(y-\frac{b}{2})]d\Gamma_s\\ &-\frac{z_p}{t_p}2\bar{e}^*_{36}\int_{\Gamma_s}\frac{\partial^2\dot{w}^0}{\partial x\partial y}[H(x+\frac{a}{2})-H(x-\frac{a}{2})]\\ &\times[H(y+\frac{b}{2})-H(y-\frac{b}{2})]d\Gamma_s.\end{aligned} \tag{3.72}$$

The partial derivative terms in Equation (3.72) are treated individually by the integration by parts. Finally, Ψ_w is expressed as follows:

$$\begin{aligned}\Psi_w = -\frac{z_p}{t_p}\int_{\Gamma_s}\Bigg\{&\frac{\bar{e}^*_{31}}{\Delta x}[\delta(x-\frac{a}{2})-\delta(x-\frac{a}{2}+\Delta x)\\ &-\delta(x+\frac{a}{2}-\Delta x)+\delta(x+\frac{a}{2})]\times[H(y+\frac{b}{2})-H(y-\frac{b}{2})]\dot{w}\\ &+\frac{\bar{e}^*_{32}}{\Delta y}[\delta(y-\frac{b}{2})-\delta(y-\frac{b}{2}+\Delta y)-\delta(y+\frac{b}{2}-\Delta y)\\ &+\delta(y+\frac{b}{2})]\times[H(x+\frac{a}{2})-H(x-\frac{a}{2})]\dot{w}\\ &+2\bar{e}^*_{36}\big[\delta(x-\frac{a}{2})\delta(y-\frac{b}{2})-\delta(x+\frac{a}{2})\delta(y-\frac{b}{2})\\ &-\delta(x-\frac{a}{2})\delta(y+\frac{b}{2})+\delta(x+\frac{a}{2})\delta(y+\frac{b}{2})\big]\Bigg\}\dot{w}^0 d\Gamma_s.\end{aligned} \tag{3.73}$$

The direct piezoelectric coupling can be characterized by substituting Ψ_u, Ψ_v and Ψ_w into Equation (3.69). We can find that the same coupling patterns as the equivalent force are obtained but with a minus sign so that the reversibility of the piezoelectric effect is ensured. As analyzed in the previous section, the low-order finite difference approximation causes the error which is quantified by coefficient α, should also be applicable to Equation (3.73) because of the linear relation between bending moment and strain.

3.6 Concluding remarks

This chapter describes the basic concept of equivalent dynamic modeling of MFC transducers. We investigated laminated composite plates with integrated rectangular MFC transducers. The piezoelectric constitutive equations of MFC-d33 transducer are converted into the form of MFC-d31 transducer so that a single analysis can analyze the two types of transducers at the same time. A laminated plate with distributed rectangular MFC transducers is studied. On the one hand, the generalized Hamilton's principle is used to fully characterize the inverse piezoelectric effect of the integrated MFC transducers. Different forms of equivalent loads are obtained. Equivalent forces are novel closed-form solutions for characterizing the inverse piezoelectric effect of rectangular MFC transducers. And then, we assessed the equivalent loads. On the other hand, the corresponding direct piezoelectric effect is characterized under the electrical boundary conditions. As a result, the integrated MFC transducer can be fully characterized on a non-homogeneous laminated composite plate. The obtained results provide a basic understanding of the equivalent modeling approach of MFC transducers in the next chapter.

Chapter 4

Equivalent dynamic modeling of MFC transducers integrated into composite plates

First of all, This chapter describes the Equivalent Force Modeling (EFM) of MFC transducers integrated into plate-type composite structures. A FOSD-based FEM method is adopted to simulate the structural dynamics of the system. The piezoelectric couplings from the previous chapter, which includes both the direct and inverse piezoelectric effects, are used to model the integrated MFC transducers. After that, the Equivalent Substructure Modeling (ESM) approach based on a dynamic condensation technique is described to generate structure-preserving low-order models of piezoelectric systems. Finally, a modeling sensitivity analysis is carried out to verify the robustness of the proposed methods. Both the size of the used piezoelectric transducers and their piezoelectric fibrous orientation are considered as sensitive parameters.

4.1 Equivalent Force Modeling approach

According to the equation of motion in Equations (3.42a), (3.42b), and (3.42c) in the previous chapter, the dynamics of a laminated composite plate with integrated MFC transducers can be briefly given as follows in a weak formulation:

$$\begin{aligned}
&\int_{\Gamma_s} (\boldsymbol{\varepsilon^m} A^s \Delta\boldsymbol{\varepsilon^m} + \boldsymbol{\kappa^b} B^s \Delta\boldsymbol{\varepsilon^m} + \boldsymbol{\varepsilon^m} B^s \Delta\boldsymbol{\kappa^b} + \Delta\boldsymbol{\kappa^b} D^s \boldsymbol{\kappa^b}) d\Gamma_s \\
&+ \int_{\Gamma_s} (\boldsymbol{\varepsilon^m} A^E \Delta\boldsymbol{\varepsilon^m} + \boldsymbol{\kappa^b} B^E \Delta\boldsymbol{\varepsilon^m} + \boldsymbol{\varepsilon^m} B^E \Delta\boldsymbol{\kappa^b} + \Delta\boldsymbol{\kappa^b} D^E \boldsymbol{\kappa^b}) \Lambda_x^p \Lambda_y^p d\Gamma_s \\
&+ \int_{\Gamma_s} (\ddot{u}^0 \rho_s t_s \Delta u^0 + \ddot{u}^0 \rho_p t_p \Delta u^0 \Lambda_x^p \Lambda_y^p) d\Gamma_s + \int_{\Gamma_s} (\ddot{v}^0 \rho_s t_s \Delta v^0 + \ddot{v}^0 \rho_p t_p \Delta v^0 \Lambda_x^p \Lambda_y^p) d\Gamma_s \\
&+ \int_{\Gamma_s} (\ddot{w}^0 \rho_s t_s \Delta w^0 + \ddot{w}^0 \rho_p t_p \Delta w^0 \Lambda_x^p \Lambda_y^p) d\Gamma_s = \int_{\Gamma_s} f \delta(x - x_0) \delta(y - y_0) \Delta w^0 d\Gamma_s,
\end{aligned} \tag{4.1}$$

where $\boldsymbol{\varepsilon^m}$ and $\boldsymbol{\kappa^b}$ are the slopes and curvatures on the plate, respectively.

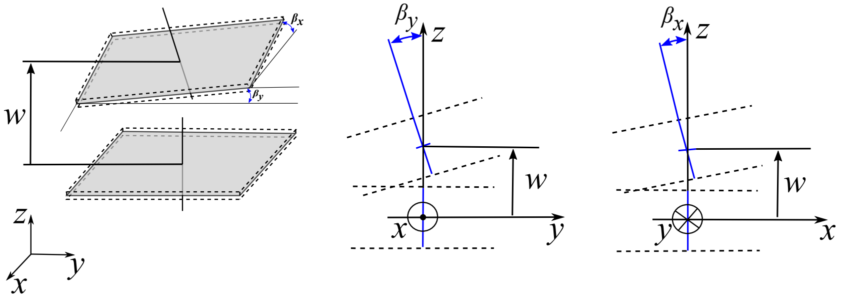

Figure 4.1: The displacement of the mid-surface (left) and a normal on a plate (middle-right) in FOSD theory

As shown in Figure 4.1, the displacements of an arbitrary point on the plate can be expressed as follows according to the FOSD theory [174]:

$$\begin{cases} u(x,y,z) = u^0 + z\beta_x \\ v(x,y,z) = v^0 + z\beta_y \\ w(x,y,z) = w^0 \end{cases} \tag{4.2}$$

Then, the strain-displacement relations of the membrane and bending effects are expressed as:

$$\boldsymbol{\varepsilon^m} = \begin{cases} \varepsilon_{xx}^m = \frac{\partial u^0}{\partial x} \\ \varepsilon_{yy}^m = \frac{\partial v^0}{\partial y} \\ \gamma_{xy}^m = \frac{\partial u^0}{\partial y} + \frac{\partial v^0}{\partial x} \\ \gamma_{xz} = \beta_x + \frac{\partial w^0}{\partial x} \\ \gamma_{yz} = \beta_x + \frac{\partial w^0}{\partial x} \end{cases} \quad \boldsymbol{\kappa^b} = \begin{cases} \varepsilon_{xx}^b = \frac{\partial \beta_x}{\partial x} \\ \varepsilon_{yy}^b = \frac{\partial \beta_y}{\partial y} \\ \gamma_{xy}^b = \frac{\partial \beta_x}{\partial y} + \frac{\partial \beta_y}{\partial x} \end{cases} \tag{4.3}$$

The transverse shear deformations γ_{xz} and γ_{yz} are included into $\boldsymbol{\varepsilon^m}$ for the convenience of formulation. A generalized displacement vector, which includes both the displacements and the rotations of the normals on the mid-surface, can be defined as $\boldsymbol{u} = [u_0, v_0, w_0, \beta_x, \beta_y]^T$. $\boldsymbol{u}$ can be approximated by the nodal displacements u_i via interpolation functions N_i:

$$\boldsymbol{u} = \sum_{i=1}^{n} N_i u_i \tag{4.4}$$

Then the nodal membrane, bending and shear strains of laminated plates are given as:

$$\boldsymbol{\varepsilon^m} = \sum_i B_i^m u_i, \ \boldsymbol{\kappa^b} = \sum_i B_i^b u_i, \tag{4.5}$$

with

$$B_i^m = \begin{bmatrix} N_{i,x} & 0 & 0 & 0 & 0 \\ 0 & N_{i,y} & 0 & 0 & 0 \\ N_{i,y} & N_{i,x} & 0 & 0 & 0 \\ 0 & 0 & N_{i,x} & N_i & 0 \\ 0 & 0 & N_{i,y} & 0 & N_i \end{bmatrix}, B_i^b = \begin{bmatrix} 0 & 0 & 0 & N_{i,x} & 0 \\ 0 & 0 & 0 & 0 & N_{i,y} \\ 0 & 0 & 0 & N_{i,y} & N_{i,x} \\ 0 & 0 & 0 & 0 & 0 \\ 0 & 0 & 0 & 0 & 0 \end{bmatrix} \tag{4.6}$$

Considering that B_m, B_b and N are the elemental interpolation functions of membrane strain field, bending strain field and displacement field on a discretized plate, which are given in Appendix 8.2, the global stiffness, and mass matrix are obtained by assembling the elemental matrix in the following way:

$$\begin{aligned} \boldsymbol{K} = & \int_{\Gamma_s} \left(B_m^T A^s B_m + B_m^T B^s B_b + B_b^T B^s B_m + B_b^T D^s B_b \right) d\Gamma_s \\ & + \int_{\Gamma_s} \left(B_m^T A^E B_m + B_m^T B^E B_b + B_b^T B^E B_m + B_b^T D^E B_b \right) \Lambda_x^p \Lambda_y^p d\Gamma_s; \end{aligned} \tag{4.7}$$

$$\boldsymbol{M} = \int_{\Gamma_s} \rho_s N^T \boldsymbol{Z}_s N dA_s + \int_{A_s} \rho_p N^T \boldsymbol{Z}_p N \Lambda_x^p \Lambda_y^p d\Gamma_s \tag{4.8}$$

in which,

$$\boldsymbol{Z}_s = \begin{bmatrix} t_s & 0 & 0 & 0 & 0 \\ 0 & t_s & 0 & 0 & 0 \\ 0 & 0 & t_s & 0 & 0 \\ 0 & 0 & 0 & \frac{t_s^3}{12} & 0 \\ 0 & 0 & 0 & 0 & \frac{t_s^3}{12} \end{bmatrix}, \ \boldsymbol{Z}_p = \begin{bmatrix} t_p & 0 & 0 & 0 & 0 \\ 0 & t_p & 0 & 0 & 0 \\ 0 & 0 & t_p & 0 & 0 \\ 0 & 0 & 0 & \frac{t_p^3}{12} & 0 \\ 0 & 0 & 0 & 0 & \frac{t_p^3}{12} \end{bmatrix}.$$

$\boldsymbol{Z}_s$ and $\boldsymbol{Z}_p$ are the thickness-wise integrations for the inertia of the plate and the transducer, respectively.

When an MFC transducer is integrated into the plate, the spatial distribution $\Lambda_x^p \Lambda_y^p$ of the integrated MFC transducer becomes an element selector. The spatial distribution terms in the equivalent forces should be discretized by following the mesh and nodes on the transducer. Thus, the analytical equivalent forces that are given in the following discretized-form can be easily assigned to the structural model as follows:

$$f = \widetilde{\boldsymbol{\Theta}} V_{in} \tag{4.9}$$

where V_{in} is the operational voltage of the transducer. $\widetilde{\boldsymbol{\Theta}} = \left[\Theta_{u\psi}\ \Theta_{v\psi}\ \Theta_{w\psi}\right]^T$ is defined by f_{xx}, f_{yy} and f_{zz} in the previous chapter. The distributions of f_{xx}, f_{yy} and f_{zz} on a rectangular transducer are representatively shown in Figures 4.2 to 4.4.

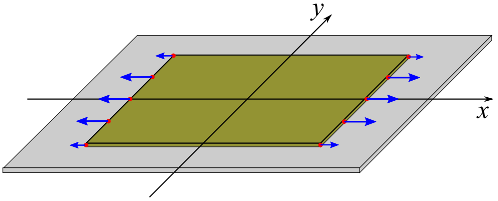

Figure 4.2: Distribution of f_{xx} on a rectangular transducer

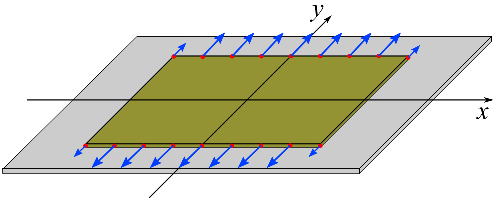

Figure 4.3: Distribution of f_{yy} on a rectangular transducer

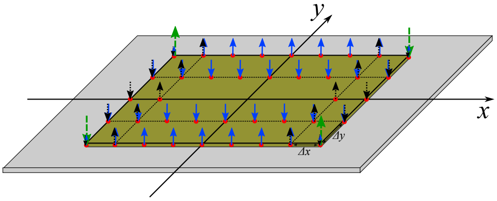

Figure 4.4: Distribution of f_{zz} on a rectangular transducer. The black, blue and green arrows indicate the bending forces along x, y and xy directions, respectively.

f_{xx} and f_{yy} are assigned to the u and v Dofs on the edges of the transducer because they generate the membrane motions. f_{zz} comprises three terms that apply to w Dofs on the transducer. They are corresponding to the bending motions along x, y and xy directions. It seems that the distribution of f_{zz} is quite complex but the three terms in f_{zz} can be easily treated as line-forces and point forces as long as the mesh is regular on the transducer. Hence, the dynamics of the plate with an integrated transducer is given as follows:

$$\boldsymbol{K}\boldsymbol{u} + \boldsymbol{C}\dot{\boldsymbol{u}} + \boldsymbol{M}\ddot{\boldsymbol{u}} = \widetilde{\boldsymbol{\Theta}}V \tag{4.10}$$

In addition, the electrical dynamics of the piezoelectric system is expressed as follows according to section 3.5 in the previous chapter:

$$C_p\dot{V} + \frac{V}{Z_e} = -\widetilde{\boldsymbol{\Theta}}^T\dot{\boldsymbol{u}} \tag{4.11}$$

where $-\widetilde{\boldsymbol{\Theta}}^T$, which is actually defined by Ψ_u, Ψ_v and Ψ_w, is the transposition of $\widetilde{\boldsymbol{\Theta}}$ with a negative sign. The dynamics of the overall piezoelectric system then can be expressed as:

$$\begin{bmatrix} \boldsymbol{M} & 0 \\ 0 & 0 \end{bmatrix} \begin{bmatrix} \ddot{\boldsymbol{u}} \\ \ddot{\boldsymbol{\psi}} \end{bmatrix} + \begin{bmatrix} \boldsymbol{C} & 0 \\ 0 & 0 \end{bmatrix} \begin{bmatrix} \dot{\boldsymbol{u}} \\ \dot{\boldsymbol{\psi}} \end{bmatrix} + \begin{bmatrix} \boldsymbol{K} & \widetilde{\boldsymbol{\Theta}} \\ \widetilde{\boldsymbol{\Theta}}^T & C_p \end{bmatrix} \begin{bmatrix} \boldsymbol{u} \\ \boldsymbol{\psi} \end{bmatrix} = \begin{bmatrix} \boldsymbol{F_s} \\ Q_q \end{bmatrix} \tag{4.12}$$

where $\boldsymbol{\psi}$ is the electric Dofs of the transducer and Q_q is electrical charge input depends on Z_e. F_s is the mechanical input exited on the plate. The following transform can be used for eliminating the electric Dofs $\boldsymbol{\psi}$:

$$\psi = -C_p^{-1}\widetilde{\boldsymbol{\Theta}}^T\boldsymbol{u} + C_p^{-1}Q_q \tag{4.13}$$

Substituting (4.13) into (4.12) yields:

$$\boldsymbol{M}\ddot{\boldsymbol{u}} + \boldsymbol{C}\dot{\boldsymbol{u}} + \underbrace{(\boldsymbol{K} + \widetilde{\boldsymbol{\Theta}}C_p^{-1}\widetilde{\boldsymbol{\Theta}}^T)}_{\boldsymbol{K}_{Ag}}\boldsymbol{u} = \boldsymbol{F_s} + \boldsymbol{\Theta}V_{in} \tag{4.14}$$

where $\widetilde{\boldsymbol{\Theta}}C_p^{-1}\widetilde{\boldsymbol{\Theta}}^T$ is called the piezoelectric induced stiffness matrix. $\boldsymbol{K}^{Ag}$ is the augmented stiffness matrix.

4.2 Equivalent Substructure Modeling approach

The EFM approach uses the FEM method for structural modeling and FEM models are usually large-scale that is challenging the dynamic application. The substructuring method is preferable to deal with large-scale structure because the individual substructures can be analyzed independently, and the dynamics of the overall system is obtained by assembling the substructures [175]. Hence, it is more convenient to analyze and update the global system through the substructuring concept [176, 177]. When some substructures are modified, the rest substructures remain unchanged. Also, the substructuring concept can combine with the model order reduction techniques in calculating the modal parameters of the overall system [178, 179]. Therefore, the ESM approach, proposed in this section, is based on the substructuring concept. The proposed approach aims to generate structure-preserving low-order models of piezoelectric systems. Both the structural complexity and the physical parameters such as transducer placement and modal parameters of the system can be preserved in the low-order system model.

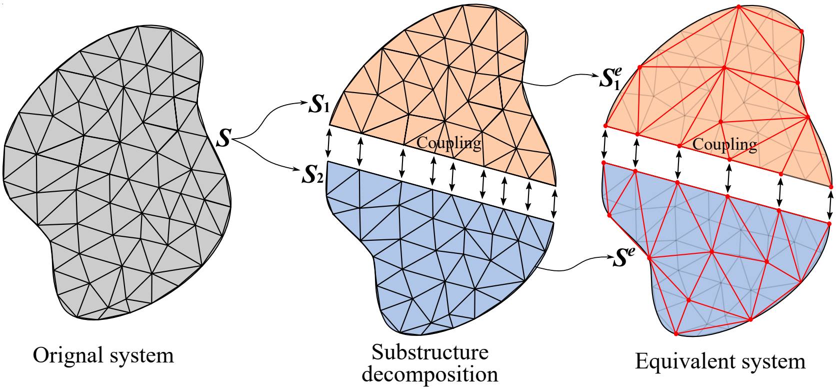

Figure 4.5: Equivalent substructure concept

The idea of the equivalent substructures is to reduce the order of the model of each substructure, while the complexity of the overall structure is always retained after the assembling. A mechanical structure $\boldsymbol{S}$ can be divided into substructures, as shown in Figure 4.5. The mechanical dynamics of each substructure in free vibration is described as follows:

$$\widetilde{\boldsymbol{M}}\ddot{\boldsymbol{u}} + \widetilde{\boldsymbol{K}}\boldsymbol{u} = \boldsymbol{0} \tag{4.15}$$

where $\widetilde{\boldsymbol{M}}$ and $\widetilde{\boldsymbol{K}}$ are the mass and stiffness matrix of a substructure generated by FEM methods. Equation (4.15) can be partitioned according to the retained

Dofs on the master nodes subscribed r and deleted Dofs on servant nodes subscribed as d:

$$\begin{bmatrix} \widetilde{\boldsymbol{M}}_{rr} & \widetilde{\boldsymbol{M}}_{rd} \\ \widetilde{\boldsymbol{M}}_{dr} & \widetilde{\boldsymbol{M}}_{dd} \end{bmatrix} \begin{Bmatrix} \ddot{\boldsymbol{u}}_r \\ \ddot{\boldsymbol{u}}_d \end{Bmatrix} + \begin{bmatrix} \widetilde{\boldsymbol{K}}_{rr} & \widetilde{\boldsymbol{K}}_{rd} \\ \widetilde{\boldsymbol{K}}_{dr} & \widetilde{\boldsymbol{K}}_{dd} \end{bmatrix} \begin{Bmatrix} \boldsymbol{u}_r \\ \boldsymbol{u}_d \end{Bmatrix} = \begin{Bmatrix} \boldsymbol{0} \\ \boldsymbol{0} \end{Bmatrix}. \tag{4.16}$$

The second row in Equation (4.16) leads to the following relation according to the static condensation:

$$\boldsymbol{u}_d = \boldsymbol{R}^{(0)} \boldsymbol{u}_r \tag{4.17}$$

where $\boldsymbol{R}^{(0)} = -\widetilde{\boldsymbol{K}}_{dd}^{-1} \widetilde{\boldsymbol{K}}_{dr}$. The reduced-order model of the substructure is obtained by introducing Equation (4.17) into the first row in Equation (4.16). A dynamic condensation is adopted here for partially including the mass effect in the model order reduction transformation matrix. The new $R^{(i)}$ to replace $R^{(0)}$ in Equation (4.17) is given as follows according to [180]:

$$\boldsymbol{R}^{(i)} = \widetilde{\boldsymbol{K}}_{dd}^{-1} [(\widetilde{\boldsymbol{M}}_{dr} + \widetilde{\boldsymbol{M}}_{dd} \boldsymbol{R}^{(i-1)})(\widetilde{\boldsymbol{M}}_s^{(i-1)})^{-1} \widetilde{\boldsymbol{K}}_s^{(i-1)} - \widetilde{\boldsymbol{K}}_{dr}] \tag{4.18}$$

where $\widetilde{\boldsymbol{M}}_s^{(i-1)}$ and $\widetilde{\boldsymbol{K}}_s^{(i-1)}$ are the reduced-order mass and stiffness matrix of each substructure from $i-1$ step $(i = 1, 2, 3...)$. Therefore, a model order reduction transformation matrix of the dynamic condensation is given as follows:

$$\boldsymbol{T} = \begin{bmatrix} \boldsymbol{I} \\ \mathbf{R}^{(i)} \end{bmatrix} \tag{4.19}$$

in which, $\boldsymbol{I}$ is an identity matrix. The reduced-order model of the substructure is thus expressed as

$$\overline{\boldsymbol{M}} \ddot{\boldsymbol{u}} + \overline{\boldsymbol{K}} \boldsymbol{u} = 0. \tag{4.20}$$

where $\overline{\boldsymbol{M}} = \boldsymbol{T}^T \widetilde{\boldsymbol{M}} \boldsymbol{T}$ and $\overline{\boldsymbol{K}} = \boldsymbol{T}^T \widetilde{\boldsymbol{K}} \boldsymbol{T}$ are the mass and stiffness matrix of the equivalent substructure model. When an MFC transducer is integrated into a substructure of the host plate, its equivalent substructure model can be easily assembled with the equivalent substructure model of the plate. Meanwhile, the piezoelectric couplings also need to be transformed to the equivalent substructure model too. We can observe from the constitutive relations that the couplings are applied to the plate that dominates the mechanical dynamics of the system. Hence, the following transformation can be achieved:

$$\widehat{\boldsymbol{\Theta}} = \boldsymbol{T}^T \widetilde{\boldsymbol{\Theta}} \tag{4.21}$$

where $\boldsymbol{T}$ is the order reduction transformation matrix of the plate substructure model. $\widehat{\boldsymbol{\Theta}}$ is the coupling applied on all the master nodes of the plate equivalent substructure model. Now, a static condensation can be applied to $\widehat{\boldsymbol{\Theta}}$ in order to convert the coupling on certain desired Dofs of the equivalent substructure model [181]:

$$\overline{\boldsymbol{\Theta}} = \boldsymbol{T}_{\boldsymbol{s}}^{T} \widehat{\boldsymbol{\Theta}}, \; \boldsymbol{T}_{\boldsymbol{s}} = \begin{bmatrix} I \\ -\overline{\boldsymbol{K}}_{rd} \overline{\boldsymbol{K}}_{dd}^{-1} \end{bmatrix} \tag{4.22}$$

where $\overline{\boldsymbol{K}}$ is partitioned by the desired degrees of freedoms subscripted r and the rest of degrees of freedom subscripted d. Finally, the piezoelectric coupling can be transformed to the equivalent substructure models as follows:

$$\overline{\boldsymbol{\Theta}} = \boldsymbol{T}_{\boldsymbol{s}}^{T} \boldsymbol{T}^{T} \widetilde{\boldsymbol{\Theta}} \tag{4.23}$$

It is worthwhile to mention that the mass and stiffness influence of the integrated transducer can be included into $\overline{\boldsymbol{M}}$ and $\overline{\boldsymbol{K}}$ before generate $\overline{\boldsymbol{\Theta}}$. Then, the mechanical influences of the transducer can be partially taken into account. When the transducer significantly influences the mechanical dynamics of the system, it can be coupled to the corresponding host substructure in FEM before generating the low-order substructure models. As a result, the transducer is embedded into the plate substructure. Conclusively, the equivalent substructure models can be easily assembled, and the dynamics of the overall system can be expressed as:

$$\boldsymbol{M}\ddot{\boldsymbol{u}} + \boldsymbol{C}\dot{\boldsymbol{u}} + \boldsymbol{K}\boldsymbol{u} = \boldsymbol{F}_{\boldsymbol{s}} + \boldsymbol{\Theta} V \tag{4.24a}$$

$$C_p \dot{V} + \frac{V}{Ze} + \boldsymbol{\Theta}^{T} \dot{\boldsymbol{u}} = 0 \tag{4.24b}$$

where $\boldsymbol{M}$, $\boldsymbol{C}$ and $\boldsymbol{K}$ are the mass matrix, damping matrix and stiffness matrix of the low-order structural model of the system. $\boldsymbol{\Theta}$ is the assembled piezoelectric coupling due to the integrated transducer. Equation (4.14) can be also deduced from Equations (4.24a) and (4.24b). Furthermore, it is possible to use other types of equivalent loads in the ESM approach as long as the corresponding direct piezoelectric coupling is known.

4.3 Modeling sensitivity analysis

The reliability of the presented modeling approaches is critical to verify because the used piezoelectric couplings are approximated solutions. They may be very sensitive to the size of MFC transducers or the piezoelectric fibrous orientation. Thereby, the modeling sensitivity analysis is carried out in this section. The piezoelectric FEM approach in [23] is used as a validation reference. The following analysis focuses on the dynamic validations. A static modeling reliability check is given in Appendix 8.3. Furthermore, the mechanical influence of the integrated MFC transducers is also evaluated in this analysis.

4.3.1 Cantilever laminated plate with integrated MFC transducers

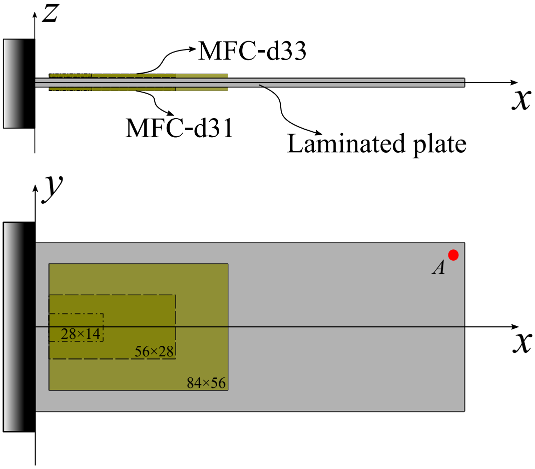

Figure 4.6: A cantilever plate with integrated MFC transducers (The red spot indicates the force input and velocity output location in direct and inverse piezoelectric response analysis, respectively.)

The laminated cantilever plates with integrated MFC transducers in Figure 4.6 are simulated. One of each MFC-d33 and MFC-d31 transducers are glued on the top and bottom surfaces of the plate with a distance of $7mm$ from the clamped side. Three different sizes of transducers are used in the analysis: $84mm \times 56mmm$, $56mm \times 28mmm$ and $28mm \times 14mmm$. The thickness of the transducers is $0.3mm$. The size of the plate is $210mm \times 70mmm$. The lay-up of the plate is $[-60^o\ 60^o\ 0^o]_s$, and the thickness of each layer is assumed to be $0.15625mm$, resulting in a total plate thickness of $0.9375mm$. The material properties of the composite laminates and the used MFC transducers are given in Table 4.1. We can recognize that the thickness of the plate is in the same order as the thickness of the integrated transducers. Hence, the integrated transducers should be able to influence the dynamics of the overall system significantly.

MFC-d33	**MFC-d31**	**composite laminate**
$\rho_p = 5440 Kg/m^3$	$\rho_p = 5440 Kg/m^3$	$\rho_s = 1510 Kg/m^3$
$Y_3 = 29.4 GPa$	$Y_1 = 30.2 GPa$	$Y_1 = 110.15 GPa$
$Y_2 = 15.2 GPa$	$Y_2 = 14.8 GPa$	$Y_2 = 7.867 GPa$
$G_{23} = 5.79 GPa$	$G_{12} = 4.13 GPa$	$G_{12} = 4.05 GPa$
$d31 = -210 \times 10^{-12} m/V$	$d31 = -170 \times 10^{-12} m/V$	$\nu_{12} = 0.32$
$d33 = 460 \times 10^{-12} m/V$	$d32 = -100 \times 10^{-12} m/V$	
$h_{_E} = 0.5 \times 10^{-3} m$	$h_{_E} = 0.18 \times 10^{-3} m$	

Table 4.1: Material properties of the used MFC transducers and composite plate

The overall structure is simulated by the FEM method. A uniform triangular mesh of size $0.35mm \times 0.35mm$ is used to mesh the plate, and the MFC transducers use the same mesh. All the Dofs on the clamped boundary are eliminated from the model. The size of the full FEM model is 6300×6300. The FEM method in [23] is used for validation. In contrast, the piezoelectric couplings are assigned to the corresponding translational Dofs in EFM approach as shown in Figures 4.2 to 4.4. In the frequency response analysis, proportional damping is adopted in the frequency response calculations, and the damping coefficients are given in Table 4.2. Since the size of the FEM system is large, the Second-Order-Rational-Arnoldi (SORA) technique from [24] is used for model order reduction. All the reduced-order systems have a size of 30×30 in all cases. In the direct piezoelectric frequency response predictions, a force input is applied to location A on the plate, and a resistive load of $R = 1,000\Omega$ is used to generate voltage output from the transducer. In the inverse piezoelectric frequency response predictions, a voltage input is applied to the transducer, and the velocity at location A is measured.

	$\lambda[1/s]$	$\eta[s]$
value	3.8	1.8×10^{-6}

Table 4.2: Coefficients of proportional damping

4.3.2 Sensitivity analysis on the size of MFC transducers

The integrated MFC-d31 transducer is used in frequency response verification in this case because it has similar piezoelectric effects in both x and y directions. It should be more sensitive to the distribution of piezoelectric couplings. The piezoelectric fibrous orientation is set as 0^o. The electric dynamic effect, due to the transducer, is considered in the frequency responses. As shown in

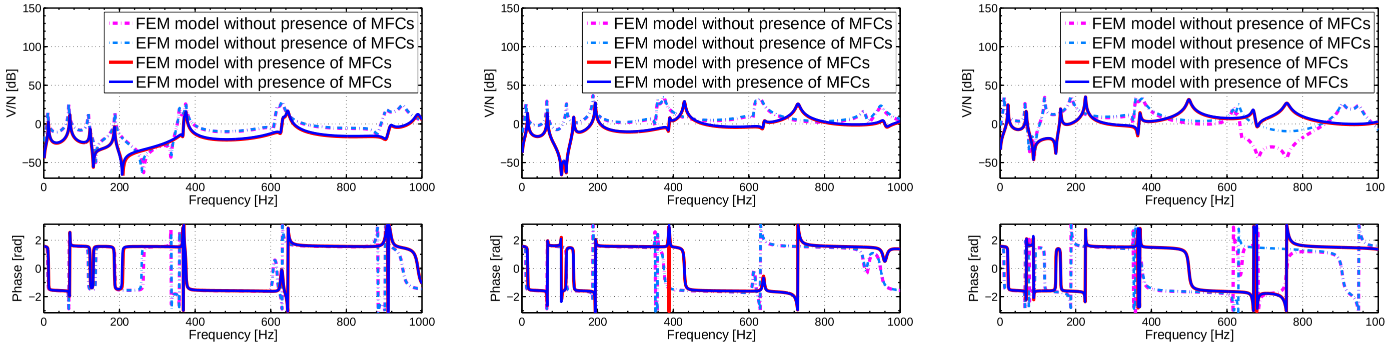

$28mm \times 14mm$ $56mm \times 28mm$ $84mm \times 56mm$

Figure 4.7: Direct piezoelectric frequency responses of MFC-d31 for different sizes

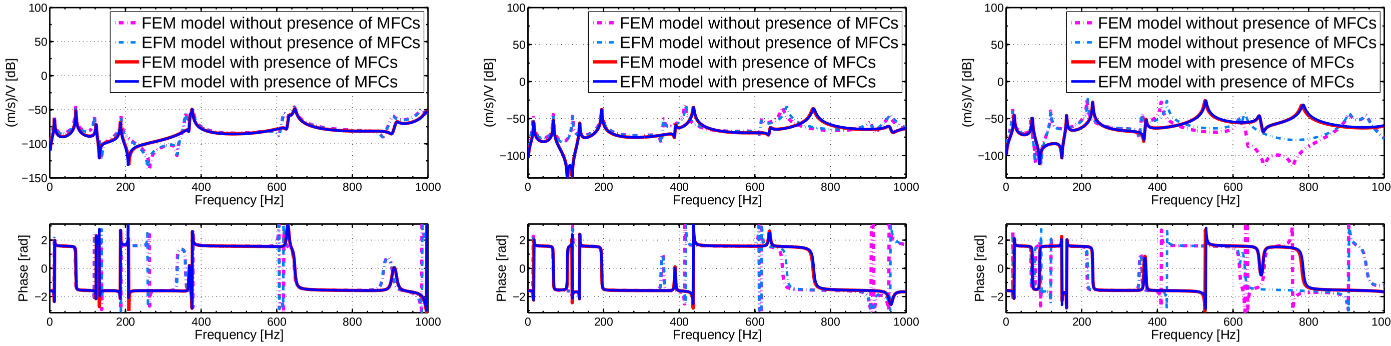

$28mm \times 14mm$ $56mm \times 28mm$ $84mm \times 56mm$

Figure 4.8: Inverse piezoelectric frequency responses of MFC-d31 for different sizes

Figures 4.7 and 4.8, the mechanical influences of the integrated transducers can be significant to the dynamics of the overall system. Both the amplitude and the natural frequencies of the modes shifted when the mechanical influences of the transducers are not included in the modeling. Hence, it is crucial to include the transducers in the structural modeling properly. The EFM modes agree well with the FEM models in the considered frequency range $0Hz - 1,000Hz$. The equivalent force is able to simulate the MFC transducers of different sizes accurately. We can observe the piezoelectric reciprocal relation in the two figures. However, the piezoelectric reciprocal relation does not entirely hold without considering the electrical boundary conditions. The experimental data in the next chapter will demonstrate that.

4.3.3 Sensitivity analysis on the piezoelectric fibrous orientation of MFC transducers

The clamped composite plate with MFC transducers of size $84mm \times 56mm$ is used to check the piezoelectric fiber orientation sensitivity. As shown in Figure 4.9, three different piezoelectric fibrous orientations are checked: (i) -45^o, (ii) 0^o and (iii) 60^o. The integrated MFC-d33 transducer is used in the frequency response calculations because its piezoelectric effects in x and y directions are considerable dissimilar. This can result in a large sensitivity to the piezoelectric fibrous orientation.

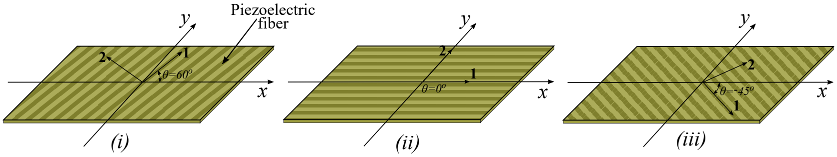

Figure 4.9: Piezoelectric fibrous orientations

We can observe from Figures 4.10 and 4.11 that the mechanical influence of the transducers become more significant for MFC-d33 transducers. That due to the effect that the piezoelectric fibrous orientation can significantly change the structural dynamics of the overall system. In the case of the fibrous orientation $\theta = 60^o$, where the mechanical influences of the transducers are considered, the anti-resonance at $630Hz$ slightly shifted. That might be due to the equivalent forces that assigned to the translational degrees of freedoms. Apart from this, we can conclude that the equivalent forces are reliable to simulate MFC transducer with different piezoelectric fibrous orientations.

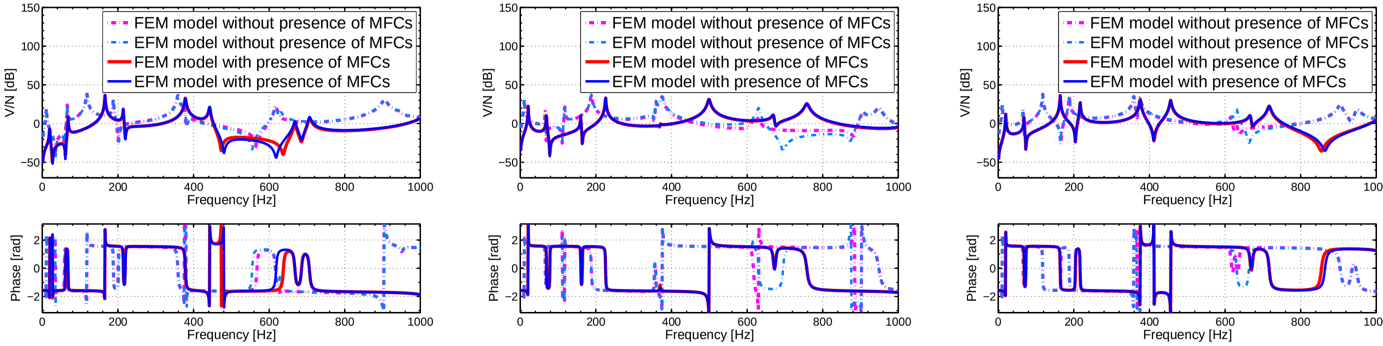

60^o 0^o -45^o

Figure 4.10: Direct piezoelectric frequency responses of MFC-d33 for different piezoelectric fibrous orientations

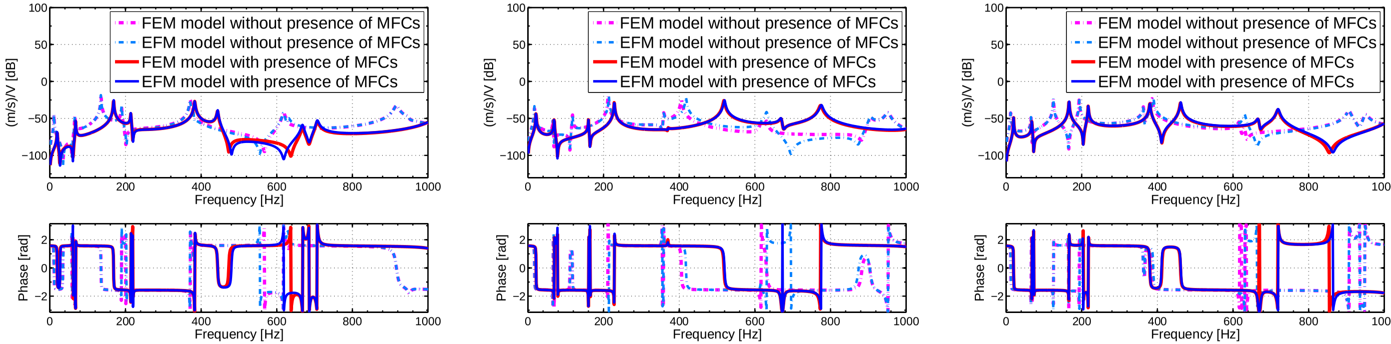

60^o 0^o -45^o

Figure 4.11: Inverse piezoelectric frequency responses of MFC-d33 for different piezoelectric fibrous orientations

4.3.4 Verification of ESM approach

We used thin and long MFC transducers in this verification in order to generate a significant geometrical difference between x and y directions. The size of the transducers is $168mm \times 14mm$, and the piezoelectric fiber orientation is 0^o in respect of x axis.

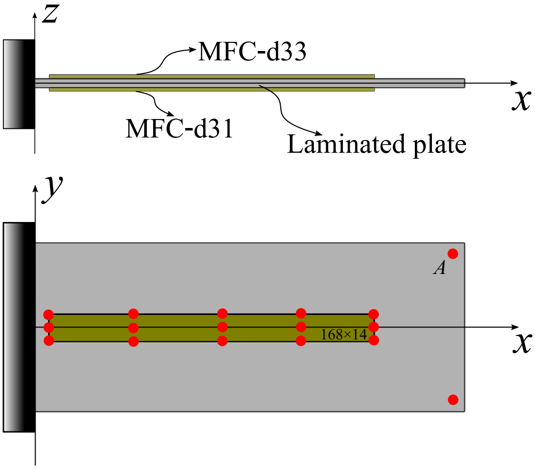

Figure 4.12: A cantilever plate with integrated MFC transducers (The red spots represent the master nodes of equivalent structural model.)

The ESM model is generated to verify its reliability. The plate and MFC transducers are separately modeled by the FEM method. Then, the equivalent model of each substructure is generated by the dynamic condensation technique. The master nodes of the substructures are indicated as red spots in Figure 4.12. The equivalent models can be easily assembled to formulate the equivalent structural model. The piezoelectric couplings are assigned to the plate model, after that, transformed into the equivalent structural model. It is shown in Figures 4.13 and 4.14 that the EFM model always agrees well with the FEM model. The ESM model has a good agreement with the FEM model up to $600Hz$. The natural frequencies of the modes at a higher frequency range shifted. Moreover, it is important to notice the used dynamic condensation technique is more accurate for the low-mid frequency range [180] so that the ESM approach only well maintains the dynamics of the system in the low-mid frequency range. Better selection of the master nodes of both the transducer and the plate could also help to improve the ESM model. Another validation

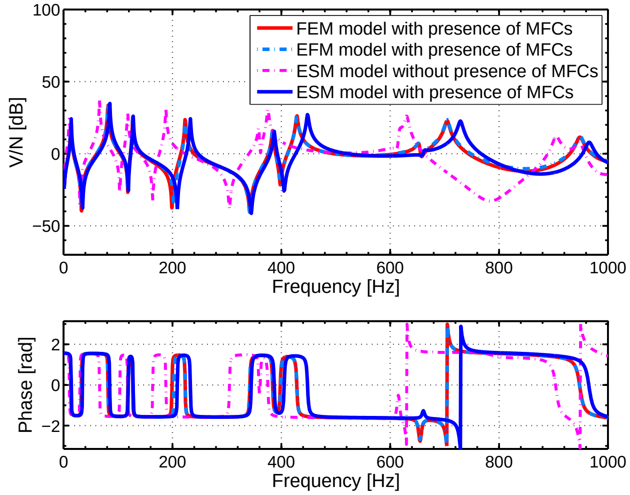

Figure 4.13: MFC-d31 direct piezoelectric frequency response of the cantilever plate ($\theta = 0^o$)

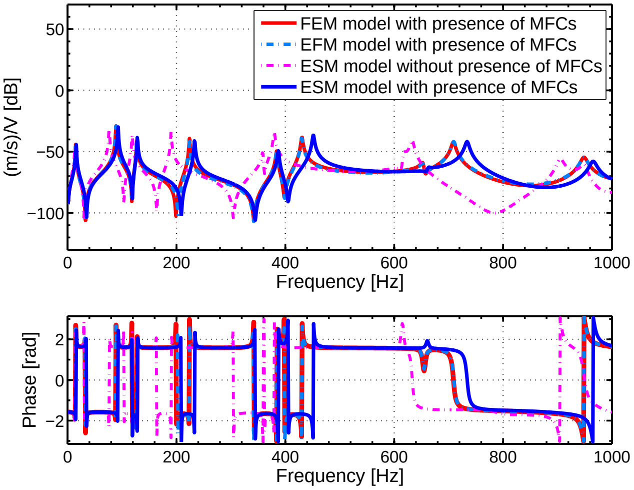

Figure 4.14: MFC-d31 inverse piezoelectric frequency response of the cantilever plate ($\theta = 0^o$)

for MFC-d33 transducer with a piezoelectric fibrous orientation of 60^o is given in Figures 4.15 and 4.16. Similar conclusions can be drawn.

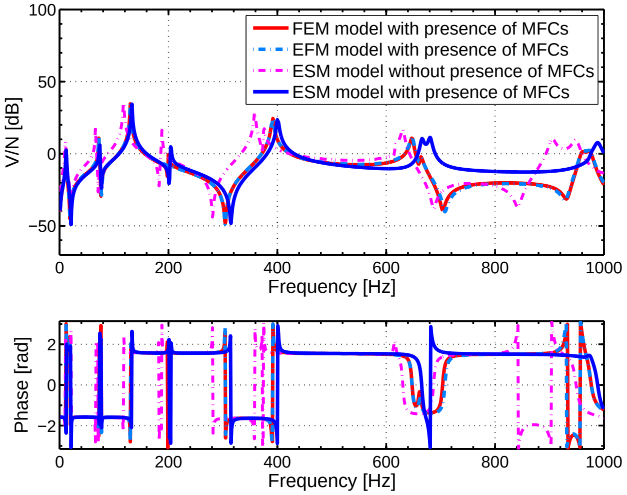

Figure 4.15: MFC-d33 direct piezoelectric frequency response of the cantilever plate ($\theta = 60^o$)

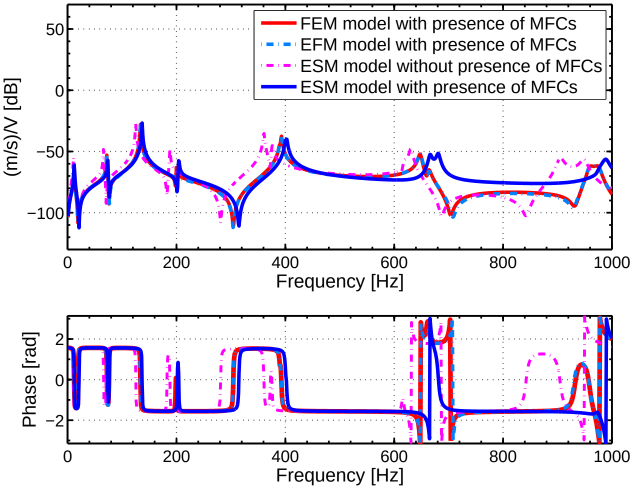

Figure 4.16: MFC-d33 inverse piezoelectric frequency response of the cantilever plate ($\theta = 60^o$)

4.4 Limitations of the proposed methods

A novel framework on the equivalent dynamic modeling of MFC transducers integrated into composite plates is proposed. The proposed equivalent forces, which is only valid for rectangular MFC transducers, is adopted in the proposed methods. Both the EFM and ESM approach are only applicable to plate-type structures. In the EFM approach, the equivalent forces can be assigned as line forces on a transducer, and a mapped mesh is required. The EFM approach can elaborately simulate piezoelectric systems, but it generates large-scale system models. The ESM approach is developed to generate low-order system models by using a substructuring concept, while the structure of the original model is preserved. The ESM approach is mostly valid for low-mid frequency range application due to the used dynamic condensation technique. Besides, both methods do not take the damping matrix into account. The proportional damping is the most convenient option to be adopted in simulations.

4.5 Concluding remarks

This chapter presents the equivalent dynamic modeling of MFC transducers. Both the direct and inverse piezoelectric solutions obtained from the previous chapter are used to simulate the inverse and direct piezoelectric effects of MFC transducers which are integrated into a plate-type structure. The EFM approach demonstrates the general modeling process by the derived equivalent forces, while the ESM approach generates structure-preserving low-order models that facilitate the design and modeling of advanced piezoelectric systems. Both the two approaches are numerically validated by a piezoelectric FEM method. Moreover, the mechanical influences of the transducers are essential to piezoelectric system modeling. Besides, we checked the modeling reliability of the EFM and ESM approaches for dynamic cases. Both the size and the piezoelectric fibrous orientation of the MFC transducers are considered as sensitive parameters. And both the EFM and ESM approaches are demonstrated that they agree well with the piezoelectric FEM method in the literature. Therefore, further researches of piezoelectric application can be performed with the proposed modeling approaches.

Chapter 5

Structural dynamic validation of equivalent modeling approaches

This chapter presents the structural dynamic validation of the equivalent modeling approaches. The experimental modal analysis of a laminated composite plate with integrated MFC transducers is described. Then, both the EFM and ESM models of the tested subject are presented. After that, both modal parameter validations and frequency response validations of the numerical models are carried out. We used the experimental measurements to validate the predicted dynamic responses of the plate. Finally, two kinds of dynamic application of the studied subject are numerically performed to demonstrate the potential of the ESM approach.

5.1 Experimental testing of a laminated plate with integrated MFC transducers

A laminated composite plate with integrated MFC-d33 transducers is manufactured for the dynamic validation of the presented modeling approach. As shown in Figure 5.1, two MFC transducers type M2814P1 (MFC-d33 transducers) from Smart Material Co. are surface-bonded on the plate with a piezoelectric fibrous orientation of 0^o. The first one is placed in the center of the plate and the second one is located close to the border of the plate. A thin adhesive layer between the MFC transducers and the host structure is essential for guaranteeing the high performance of the transducer. Hence, the bonding process in [182] is used by the 3M DP460 epoxy-based adhesive [183].

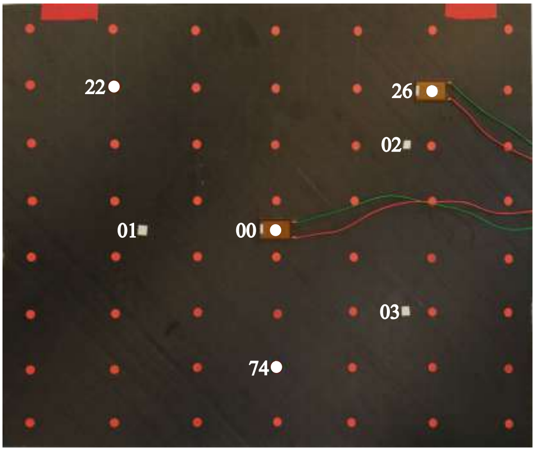

Figure 5.1: The composite plate with integrated MFC-d33 transducers used for dynamic response validation

5.1.1 Laminated composite plate

The studied plate is shown in Figure 5.1. The size of the plate is $503mm \times 400mm$. It consists of unidirectional fibrous composite material layers which are joined by an epoxy matrix. Each layer has the same orthotropic material, as given in Table 5.1. The plate has a symmetric lay-up $[-45°, 45°, 0°, 90°]_s$, so that it has quasi-isotropic properties: isotropic in-plane response and anisotropic out-plane response. The thickness of each layer is $0.3125mm$, resulting in a plate thickness of $2.5mm$.

	density$[Kg/m^3]$	$Y_1[GPa]$	$Y_2[GPa]$	$G_{12}[GPa]$	ν_{12}
laminate	1500	110.15	7.868	4.05	0.26

Table 5.1: Material properties of a single laminate

5.1.2 MFC-d33 transducers

The parameters of the used transducer are given in Table 5.2 and the material properties of the MFC-d33 transducers are given in Table 6.1. The piezoelectric constants d_{33} and d_{32} are adopted from [113] for $250V$ peak to peak operating voltage with $0V$ offset voltage, which is in accordance with the experiment.

MFC2814P1	value
active layer length $[mm]$	28
active layer width $[mm]$	14
active layer thickness $[mm]$	0.3
Capacitance $[nF]$	1.15
free strain in ppm	1550
maximum operational positive voltage $[V]$	1500
maximum operational negative voltage $[V]$	-500
operational bandwidth as actuator (low electric field) $[kHz]$	up to 700
operational bandwidth as sensor $[MHz]$	up to 1

Table 5.2: Parameters of MFC M2814P1 [15]

MFC2814P1	**value**
density $[Kg/m^3]$	5440
Y_1 $[GPa]$	27.142
Y_2 $[GPa]$	14.8
ν_{12}	0.2922
G_{12} $[GPa]$	4.1312
G_{13} $[GPa]$	5.385
G_{23} $[GPa]$	10.5
d_{33} $[m/V]$	272
d_{32} $[m/V]$	-133

Table 5.3: Material properties of MFC M2814P1

The integrated transducers can be used as either actuators or sensors in dynamic application. When the experimental results are used to validate the numerical models, a mismatch between them may happen because of the perfect assumptions in numerical models. Therefore, the corresponding corrections should be taken into account in modeling to make the performance of numerical models close to the experiment. In this study, both the assumptions of the electric field and the effect of the adhesive layer between the transducer and the host plate need to be corrected.

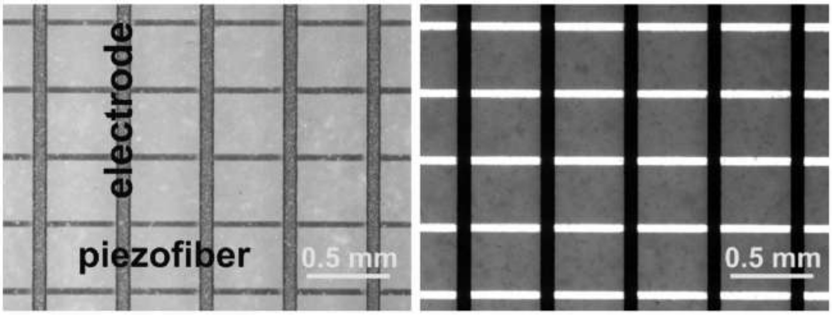

Figure 5.2: Microscopic images of a region on MFC transducer [184] (Left: reflected light image Right: transmitted light image)

A microscopic view of a region on M2814P1 transducer is shown in Figure 5.2. The electrodes are perpendicularly located on the piezoelectric fibers. The distance between electrodes is $h_E \approx 0.5mm$ and the width of each finger on the electrodes is $2w_f \approx 0.08mm$. The distribution of the operational electric field has been shown in Figure 2.7. The effective operational electric field is less intense than a uniform distributed electric field, which we assumed in our analysis. The scaling factor α_E that corrects this over-estimation is given as follows by [167]:

$$\alpha_E = \left[1 - \frac{t_p}{h_E}\left(\frac{1}{2} + \frac{2}{\pi}\right)\right]\left[\frac{h_E - w_f}{h_E - t_p}\right] = 0.8948 \tag{5.1}$$

where t_p is the thickness of the active-layer of the used MFC-d33 transducers.

The shear deformation in the thickness-wise of the adhesive layer causes a shear-lag effect. The correction factor α_P is determined by the product of the effective length and width fractions from [150, 168, 169]. The effective length and width fractions of the used transducers are shown in Figures 5.3 and 5.4 according to different thicknesses of the adhesive layer t_a. The effective length and width fractions are obtained by integrating the areas under the curves in Figures 5.3 and 5.4.

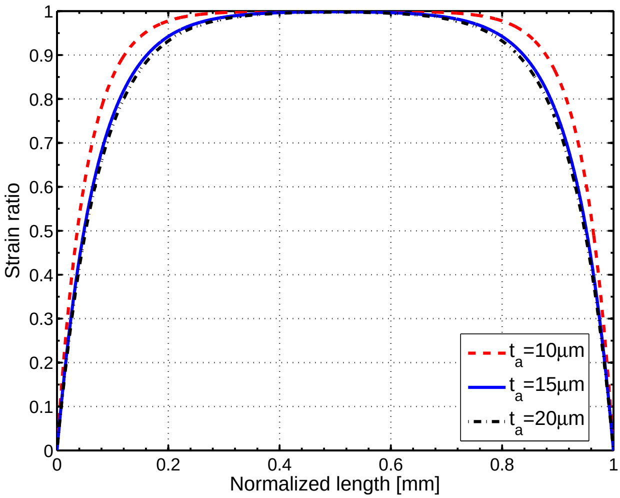

Figure 5.3: The effective length of the used transducer for direct piezoelectric effect

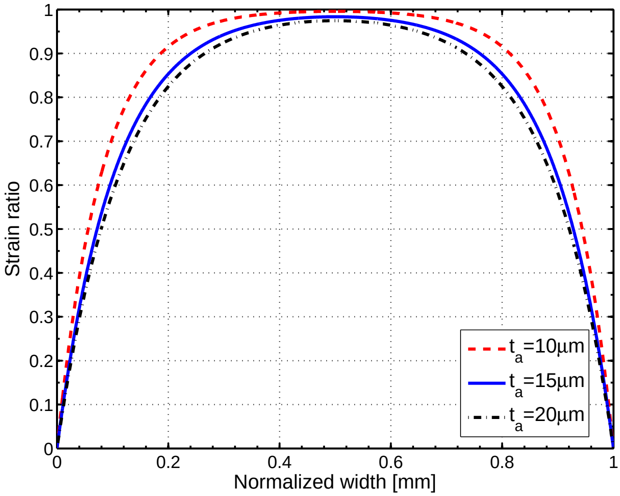

Figure 5.4: The effective width of the used transducer for direct piezoelectric effect

Assuming that the adhesive layer between the composite plate and the MFC transducer is $t_a = 15\mu m$, the shear-lag effect correction factor is $\alpha_P = 0.6808$. Finally, a correction factor $\alpha = \alpha_E \times \alpha_P$ is obtained for both the operational electrical field and the shear-lag effect.

5.1.3 Experimental analysis

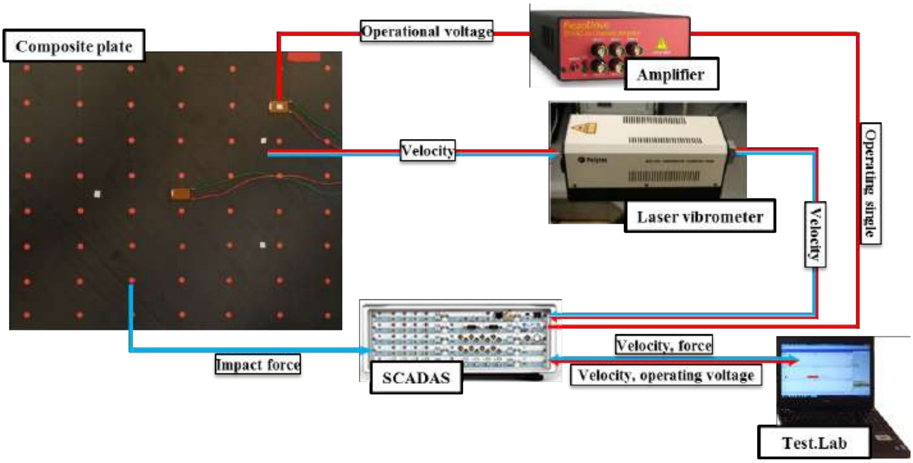
Composite plate
Operational voltage
Amplifier
Velocity
Laser vibrometer
Operating single
Velocity
Impact force
SCADAS
Velocity, force
Velocity, operating voltage
Test.Lab

Figure 5.5: Experimental setup

Both impact testing and transducer actuation testing are carried out. The overall experimental system is illustrated in Figure 5.5 and the specification of the equipment is presented in Appendix 8.4. The plate is suspended by elastic chords to mimic free-free boundary conditions.

The blue arrows illustrate the impact testing in the figure. A PCB-086E80 impact hammer is used to perform the impact on the plate. A Polytec OFV 055 Laser vibrometer is used to measure the transverse velocity response of the plate. The transducers are also connected to SCADAS to measure the voltage output caused by the impact. Since the transducers are fixed on the plate, the laser beam needs to focus on a fixed location on the plate too. Then, a roving hammer technique [185] is applied to measure the responses on the plate, in which situation the reciprocity properties should be retained on the test subject. SCADAS is used to acquire the force signal, velocity signal and the voltage signals from the transducers and saved by TestLab. 14A. The measured frequency bandwidth is $0 - 2,560Hz$ with a resolution of $0.3125Hz$.

The acquisition time is $3.2s$ to ensure that the motions on the plate can decay very well after each impact execution. Then, a uniform window is applied to the input channels. The trigger setting is performed for the force signal measured from the impact hammer, and the H1 estimator is applied to provide a better estimation of the anti-resonance [186]. We did five times linear averaging on each impacted location because more than five times averaging did not significantly improve the quality of the measured FRFs. Each impact is selected by the coherence between the executions and the energy distribution in the measured frequency bandwidth. The overloaded and double-impact executions are rejected. Spectral testing is used for the transducer actuation testing, which is indicated by red arrows in Figure 5.5. A zero-mean random signal is generated from Test.Lab source control module and sent to the PiezoDirve TD250 amplifier by SCADAS. PiezoDirve TD250 amplifies the input signal up to $250V$, which exceeds the input range of the SCADAS. As the linearity of the voltage amplifier is assumed, the random signals directly connect to the used SCADAS and the gain of the voltage amplifier is set as the sensitivity of the corresponding input channel in the Test.Lab. The velocity FRFs are measured at the predefined location by the Laser vibrometer. A hanning window is applied to all input channels in the spectral testing to avoid the aliasing issue [187]. The measured bandwidth is $0 - 4,096Hz$ with a resolution of $0.5Hz$. Twenty times linear averaging is used for each measured location. The H1 FRF estimator is applied to the measurements. The overloaded executions are rejected.

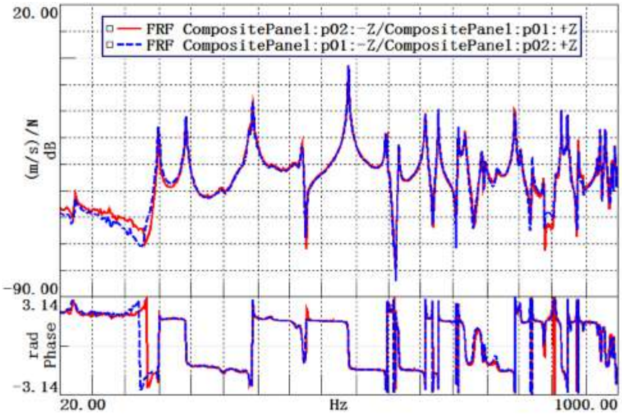

Figure 5.6: Reciprocity check between 01 and 02 on the plate

Before performing the tests, the reciprocity between different locations on the plate has been checked to guarantee the assumption of a linear system. In the impact testing, the velocity over force FRFs is measured. The reciprocity check has been executed between location 01, 02 and 03, as shown in Figure 5.1. Figure 5.6 demonstrated that the reciprocity between 01, 02 retains on the plate.

In the spectral testing, the operational voltage level has to be fixed to reduce the influences of the hysteresis effect of the MFC transducers. Figure 5.7 illustrated that the reciprocity between two MFC transducers retains quite well for a given operational voltage level. The mismatches at $370Hz$ and $630Hz$ might be caused by the small signal-to-noise ratio because the excitation of the transducer to the plate is quite limited.

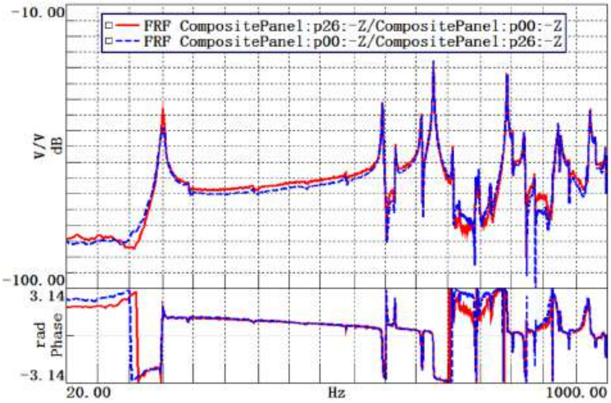

Figure 5.7: Reciprocity check between the two MFC transducers

Standard modal analysis techniques apply to the piezoelectric composite plate because the typical principles of a linear system are observed. The experimental modal analysis is carried out through the PolyMAX technique in Test.Lab [188]. The impact testing can determine the modal parameters of the piezoelectric composite plate and measured FRFs will be used to validate the direct piezoelectric effect of numerical models. The force to voltage FRFs will be used as validations of the inverse piezoelectric effect of the numerical models.

The reciprocity has been briefly reported in [152]. An interesting observation from the experimental data is shown in Figure 5.8. The FRFs of voltage output over force input and velocity output over voltage input is very close to each other. There is a frequency dependent amplitude scaling between these two FRFs, as shown in the figure. This relation might be useful in dynamic application.

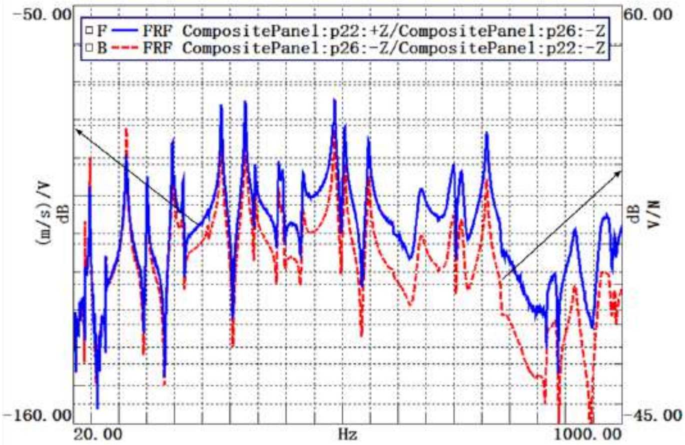

Figure 5.8: Comparison of FRFs between 26 and 22: blue curve: voltage to velocity FRF $[(m/s)/V]$ and red curve: force to voltage FRF $[V/N]$

5.2 Equivalent modeling of composite plate with integrated MFC transducers

A FEM convergence analysis is carried out in order to figure out the optimal element size. The plate is divided into $n \times m$ segments, and each one is discretized by using two triangular elements. The following table shows the predicted natural frequencies via different numbers of elements:

Mode	**Impact testing**	FEM 36×28		FEM 72×56		FEM 144×116	
	freq.$[Hz]$	freq.$[Hz]$	error	freq.$[Hz]$	error	freq.$[Hz]$	error
1^{st}	**39.8**	40.6	-2.0%	40.5	-1.8%	40.5	-1.8%
2^{nd}	**48.3**	49.7	-2.8%	49.6	-2.7%	49.5	-2.5%
3^{rd}	**77**	78.4	-1.8%	77.9	-1.2%	77.7	-0.9%
4^{th}	**109.2**	110.8	-1.5%	110.1	-0.8%	109.8	-0.5%
5^{th}	**113.4**	116.2	-2.5%	115.2	-1.4%	114.3	-0.8%
6^{th}	**150.9**	152.9	-1.3%	151.0	-0.1%	150.0	0.6%
7^{th}	**196.3**	200.7	-2.2%	198.2	-1.0%	197.2	-0.5%
8^{th}	**200.9**	205.0	-2.0%	200.3	0.3%	201.0	-0.5%
9^{th}	**215.2**	221.1	-2.7%	218.3	-1.4%	217.4	-1.0%
10^{th}	**259.2**	268.9	-3.7%	262.7	-1.4%	261.1	-0.7%

Table 5.4: Natural frequencies convergence via number of elements

The predicted natural frequencies converge to the experimental results along with refining the elements. An element size $7mm \times 7mm$ provided an accurate prediction of the dynamics of the plate. There are $4,307$ nodes in total in this case. Each node has 5 Dofs, including three translational and two rotational Dofs. Finally, the size of the structural FEM model is 21535×21535.

In the EFM approach, the structural model of the plate, including the presence of the transducers, is modeled by the FEM method. The electromechanical couplings, including both the direct and inverse piezoelectric effects, are assigned to the corresponding nodes on the transducers. A model order reduction is performed to EFM model in order to reduce the computing time of the frequency responses on the plate. A minimum number of out-plane translational Dofs for the proposed equivalent forces and some additional rotational Dofs on the transducers are retained in the reduced-order model. The additional Dofs, which are used to ensure the accuracy of the reduced-order model, are shown in Figure 5.9 (a). The size of the reduced-order model is 329×329.

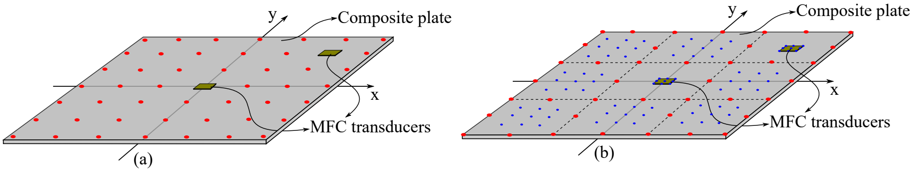

Figure 5.9: The master nodes of the low-order models on the studied plate (Left side is the reduced-order EFM model and right side is the ESM model.)

In the ESM approach, the plate with integrated transducers is subdivided into substructures, as shown in Figure 5.9 (b). The transducers are also considered as substructures. Each substructure is modeled by the FEM method. The equivalent structural model of the transducer can be easily obtained by the dynamic condensation technique. As the substructures of the plate are identical, a single FEM model is sufficient for modeling all the nine components. A specific set of master nodes on each plate substructure is selected. Two types of master nodes can be recognized: The outer nodes (red spots) serve to couple the adjacent substructures and the inner nodes (blue spots) can be used for coupling the integrated transducers. Then, the placement of the transducer is also preserved. The piezoelectric couplings are assigned to the corresponding plate substructures. All the reduced-order models of the substructures can easily be assembled. Finally, the size of the ESM model is 363×363. It is worthwhile to mention that the size of the model depends on the substructure decomposition, as well as the selected master nodes.

In the dynamic response calculations of the plate, a proportional damping is adopted for both models:

$$C = \lambda M + \eta K. \tag{5.2}$$

As the proportional damping maintains the orthogonality properties of the modes, the above equation can be rewritten in the modal coordinates:

$$\xi_i = \frac{1}{2\omega_i}\lambda + \frac{\omega_i}{2}\eta \tag{5.3}$$

where ξ_i and ω_i are the critical damping ratio and the natural frequency of i^{th} mode. The experimental critical damping ratio of the modes at $39.8 Hz$ and $284.0 Hz$ are 0.27% and 0.15%, respectively. Then, the corresponding λ and η can easily be obtained according to Equation (5.3).

	λ	η
value	1.27	1.28×10^{-6}

Table 5.5: Coefficients of proportional damping

5.3 Validations of EFM and ESM models

5.3.1 Modal validation

The experimental modal validation is carried out in order to check the fidelity of the EFM and ESM models. The natural frequencies for the first ten modes are given in Table 5.6, where both the models agree well with the experimental data. The ESM model is slightly less accurate than the EFM model for certain modes because of the substructure concept may slightly impair the accuracy of the final system models. The corresponding mode shapes of the EFM model are validated using Modal Assurance Criterion (MAC) [189], as shown in Figure 5.10. It is difficult to validate the mode shapes of the ESM model by MAC because the selected master nodes did not match the measured locations on the plate in the experiment. Nevertheless, Figure 5.11 shows that the ESM model well preserves the mode shapes of the studied plate.

Mode	**Impact test**	**EFM model**		**ESM model**	
	freq.$[Hz]$	freq.$[Hz]$	error	freq.$[Hz]$	error
1^{st}	**39.8**	40.6	-2.0%	41.6	4.5%
2^{nd}	**48.3**	49.6	-2.7%	49.6	2.7%
3^{rd}	**77**	77.7	-0.9%	76.6	-0.5%
4^{th}	**109.2**	109.8	-0.5%	110.3	1.0%
5^{th}	**113.4**	114.8	-1.3%	116.0	2.3%
6^{th}	**150.9**	150.3	0.4%	149.3	-1.1%
7^{th}	**196.3**	197.4	-0.5%	195.8	-0.3%
8^{th}	**200.9**	199.3	-0.6%	199.0	-1.0%
9^{th}	**215.2**	217.3	-1.0%	216.5	1.3%
10^{th}	**259.2**	260.8	-0.6%	257.4	-0.7%

Table 5.6: Natural frequencies validations of the EFM and ESM models

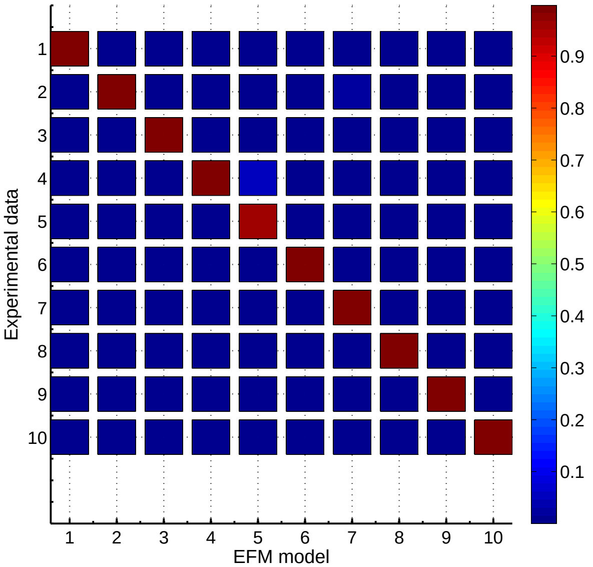

Figure 5.10: MAC correlation between experimental data and EFM model

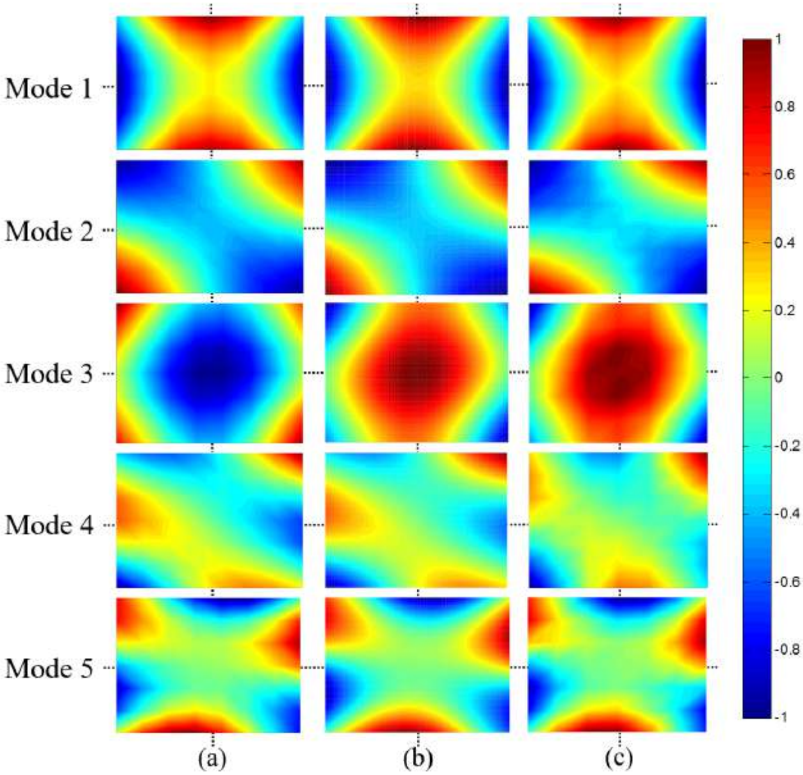

Figure 5.11: First 5 normalized mode shapes of the studied plate ((a) experimental data, (b) EFM model and (c) ESM model)

5.3.2 Dynamic response validation

Both the collocated (measurement at the driving point) and non-collocated (measurement not at the driving point) frequency response measurements are used in this validation. The collocated measurement is more sensitive to the static contributions of the unconsidered dynamics of the system. The frequency response validations are limited to a frequency range of $[20Hz - 1,000Hz]$. Two kinds of FRFs are considered: velocity output on the plate over voltage input to the transducers (inverse piezoelectric effect) and voltage output from the transducers over force input on the plate (direct piezoelectric effect). Hence, the numerical models can be fully validated for both actuation and sensing of the MFC transducers. The validated locations on the plate are given in Figure 5.1.

Inverse piezoelectric effect validation

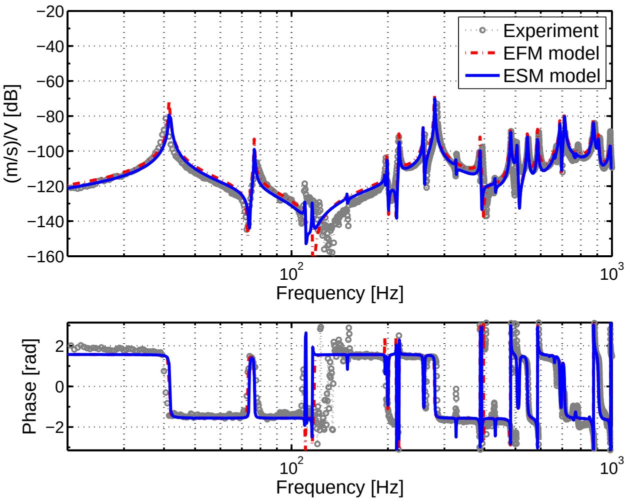

Figure 5.12: Inverse piezoelectric frequency response validation between 00 and 74

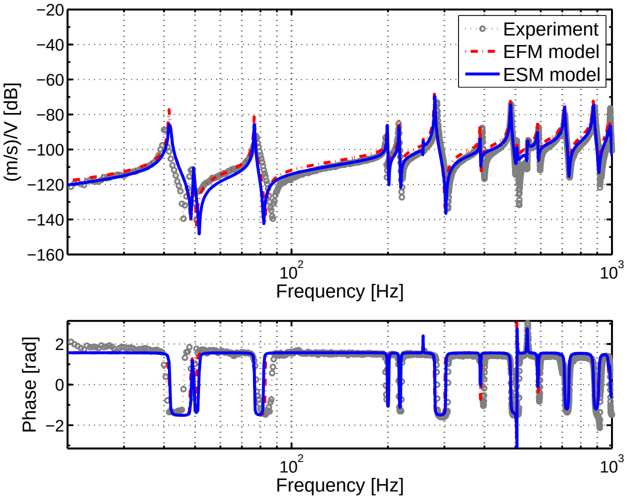

Figure 5.13: Inverse piezoelectric frequency response validation between 00 and 00

The inverse piezoelectric frequency response validations are shown in Figures 5.12 to 5.15. Both the EFM and ESM models can well predict the dynamic responses on the plate caused by the integrated transducers. Meanwhile, the structural complexity of the system is well retained in the low-order models. We can observe from the mode shapes in Figure 5.11 that the transducer placed at 00 has very low controllability for the 4^{th} and 5^{th} modes. Also, the observability of the two modes at 74 is also very low. Thus, the measurement has a quite large uncertainty around $110Hz$ in Figure 5.12. Meanwhile, the experimental measurements are sensitive to external disturbances because of the free-free boundary conditions. The laser vibrometers can easily catch the influences of wind and other disturbances on the plate. The fluctuation of the measured FRF in Figure 5.14 is a typical example.

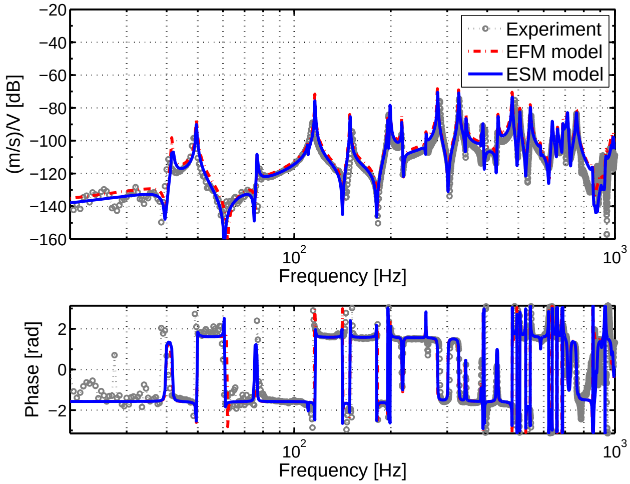

Figure 5.14: Inverse piezoelectric frequency response validation between 26 and 22

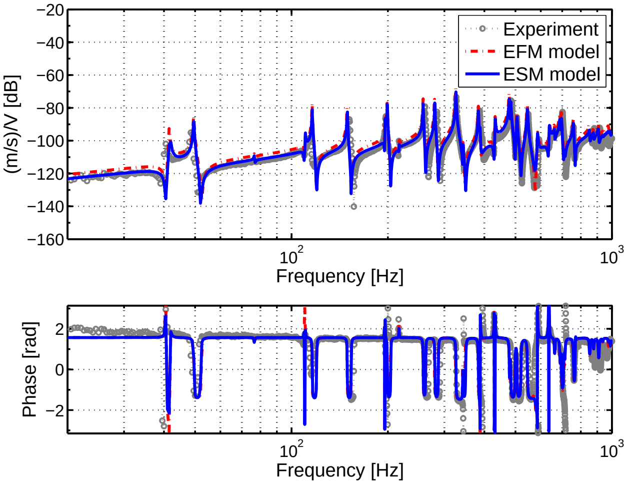

Figure 5.15: Inverse piezoelectric frequency response validation between 26 and 26

Direct piezoelectric effect validation

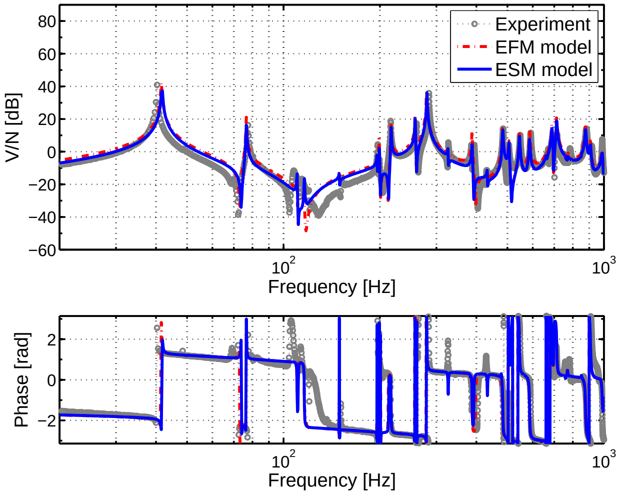

Figure 5.16: Direct piezoelectric frequency response validation between 00 and 74

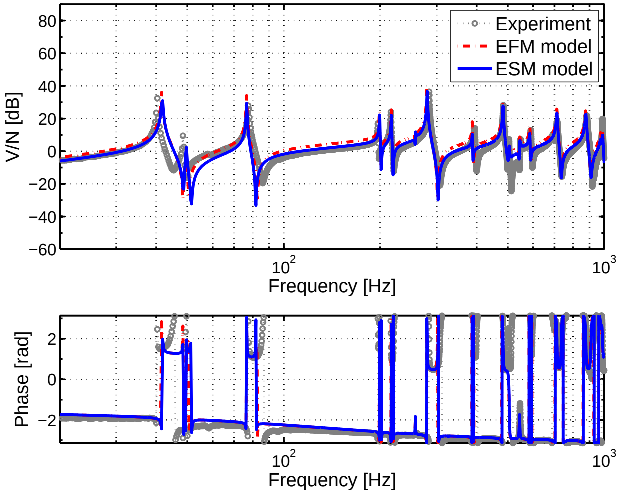

Figure 5.17: Direct piezoelectric frequency response validation between 00 and 00

The direct piezoelectric effect is validated by voltage over force FRFs. From Figures 5.16 to 5.19, we can observe that the predicted FRFs agree well with the experimental measurements too.

For the integrated MFC transducers, low controllability also actually means low observability because the inverse piezoelectric effect is the reversible process of the direct piezoelectric effect. Therefore, it is expected that there are amplitude deviation around the 2^{nd}, 4^{th} and 5^{th} modes in Figures 5.16 and 5.17. The integrated transducer at 26 has better observability than the one at 00 so that high-quality FRFs are measured. The numerical models predicted very good results as shown in Figures 5.18 and 5.19.

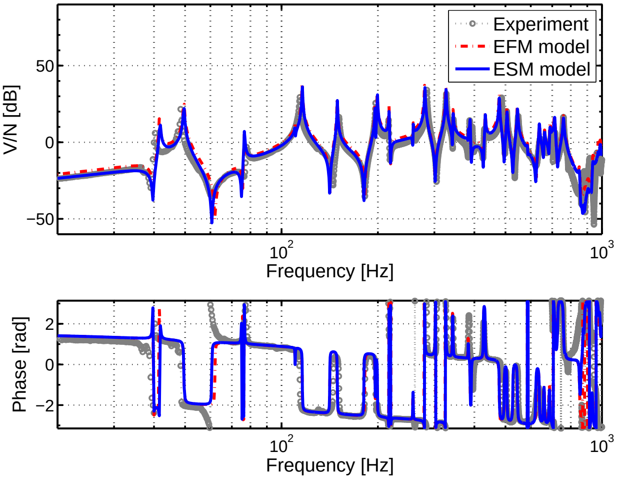

Figure 5.18: Direct piezoelectric frequency response validation between 26 and 22

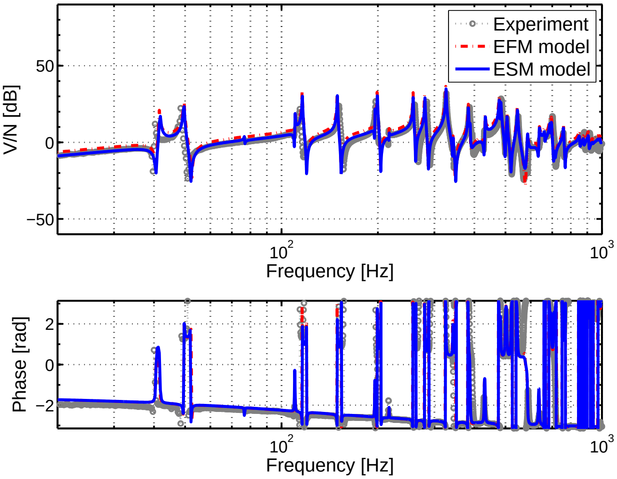

Figure 5.19: Direct piezoelectric frequency response validation between 26 and 26

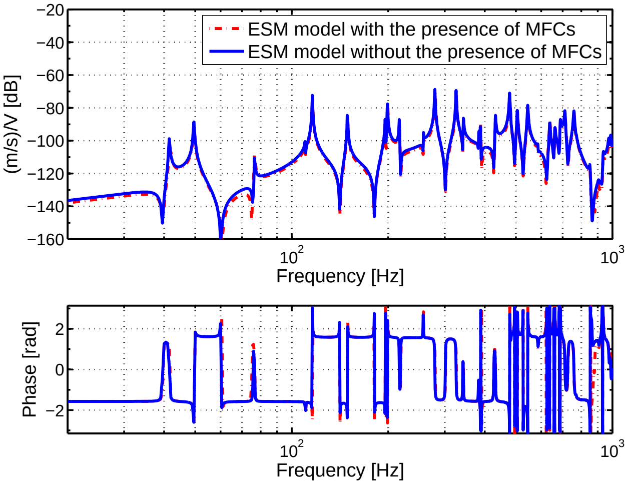

Figure 5.20: Mechanical influence of the MFC transducer to the inverse piezoelectric frequency response between 00 and 74 in ESM model

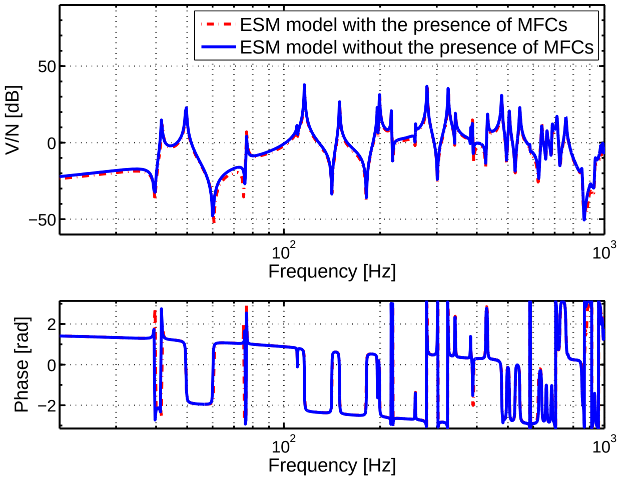

Figure 5.21: Mechanical influence of the MFC transducer to the direct piezoelectric frequency response between 00 and 00 in ESM model

A similar conclusion can be drawn for the ESM approach. However, the variations of the zeros on the FRFs are less significant than the EFM approach.

That is mostly due to the mechanical contribution of the transducer is weakened by the dynamic condensation techniques when we generate the low-order transducer model.

Reciprocity between two MFC transducers

The experimental data demonstrated that the reciprocity between two MFC transducers retains. As both the inverse and direct piezoelectric couplings of the integrated transducers are strain-based, the reciprocity between the two transducers can be theoretically proven. However, we used the numerical models to demonstrate the reciprocity in this section.

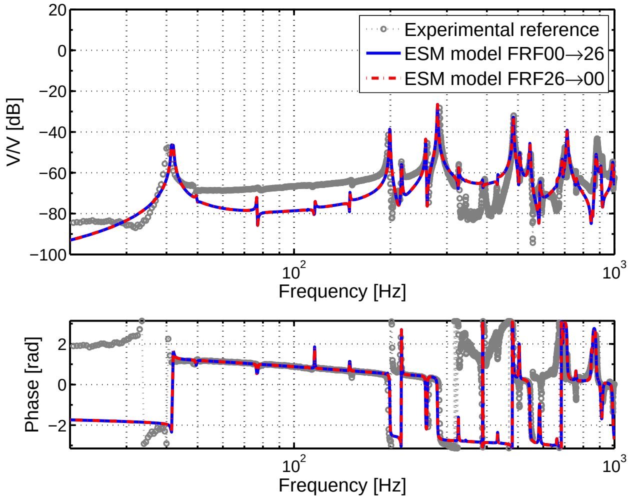

Figure 5.22: Reciprocity validation between two MFC transducer (High operational voltage)

Figure 5.22 shows the reciprocity between the two transducers. The experimental reference is a voltage over voltage FRF between them. We can observe that the modes of the host plate are well captured in the predicted FRFs by the ESM models. However, there is a large amplitude deviation between the numerical and experimental results. That is mainly due to the hysteresis effect of the MFC transducers in the experimental measurements. The larger the operational voltage on the MFC transducers, the stronger the hysteresis effect [101]. When a high operational voltage drives one of the MFC transducers, the output voltage from the other MFC transducer is also high. Then the hysteresis effect gives a more significant influences on the measured FRFs. The hysteresis effect can be mitigated by giving a lower excitation level according to the hysteresis characteristics of the MFC transducer. Therefore, the predicted FRFs are closer to the measurement obtained from a lower level operational voltage, as shown in Figure 5.23.

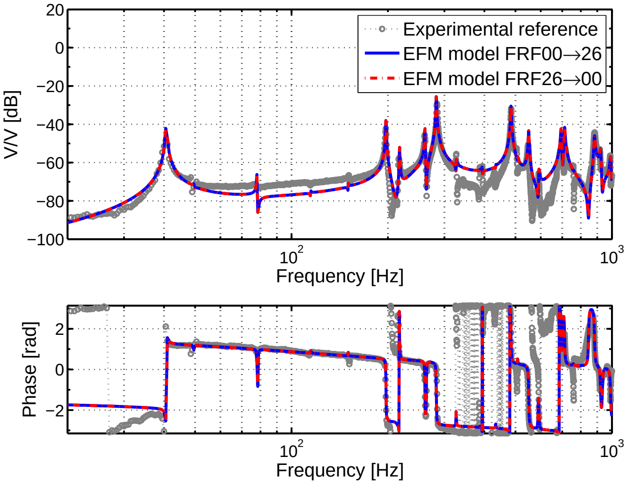

Figure 5.23: Reciprocity validation between two MFC transducer (Low operational voltage)

5.4 Piezoelectric reciprocal relation

We observed in Figure 5.8 that the voltage over force FRFs (piezoelectric sensing) is close to the velocity over voltage FRFs (piezoelectric actuating), but with amplitude and phase scalings. Hence, there should be a relation between these two kinds of FRFs. It is interesting to figure out this relation because it could be useful for dynamics application. The dynamics of the plate with an integrated MFC transducer can be described as follows in the frequency domain:

$$(\boldsymbol{K} + j\omega\boldsymbol{C} - \omega^2\boldsymbol{M})\boldsymbol{u} = \boldsymbol{L}_f F_s + \boldsymbol{\Theta} V \tag{5.4a}$$

$$j\omega C_p V + \frac{V}{Z_e} + j\omega\boldsymbol{\Theta}^T\boldsymbol{u} = 0 \tag{5.4b}$$

where $\boldsymbol{K}$, $\boldsymbol{C}$ and $\boldsymbol{M}$ are the stiffness, damping, and mass of the piezoelectric structure, respectively. $\boldsymbol{L}_f$ is the localization matrix of a force F_s on the plate.

$\boldsymbol{\Theta}$ is the electromechanical coupling of the integrated transducer. C_p is the capacitance of the transducer. When the transducer is used as an actuator, the voltage V becomes an input. Hence, Equation (5.4b) needs to be rewritten as follows according to the electric current balance:

$$j\omega C_p V - \frac{V}{Z_e} + j\omega \boldsymbol{\Theta}^T \boldsymbol{u} = 0 \tag{5.5}$$

where the dynamics of Z_e is included into V_{in}. Substituting Equation (5.5) into Equation (5.4a) yields:

$$(\boldsymbol{K} + C_p^{-1}\boldsymbol{\Theta}\boldsymbol{\Theta}^T + j\omega\boldsymbol{C} - \omega^2\boldsymbol{M})\boldsymbol{u} = \boldsymbol{L}_f F_s + \boldsymbol{\Theta} V_{in}. \tag{5.6}$$

Then, the velocity frequency response at a specific location $\boldsymbol{L}_{\dot{u}}$ caused by the integrated transducer is given as

$$\frac{\dot{u}}{V_{in}} = j\omega \boldsymbol{L}_{\dot{u}}^T \frac{1}{\boldsymbol{K} + C_p^{-1}\boldsymbol{\Theta}\boldsymbol{\Theta}^T + j\omega\boldsymbol{C} - \omega^2\boldsymbol{M}} \boldsymbol{\Theta}. \tag{5.7}$$

When the transducer is used as a sensor, the voltage output of the transducer is expressed by Equation (5.4b):

$$V_{out} = -\frac{j\omega}{j\omega Cp + \frac{1}{Z_e}} \boldsymbol{\Theta}^T \boldsymbol{u}. \tag{5.8}$$

Then, the frequency response of V_{out} subjected to a mechanical input F_s at a specific location $\boldsymbol{L}_f$ on the plate is given by substituting Equation (5.6) into Equation (5.8), as follows:

$$\frac{V_{out}}{F_s} = -\frac{j\omega}{j\omega Cp + \frac{1}{R}} \boldsymbol{\Theta}^T \frac{1}{\boldsymbol{K} + C_p^{-1}\boldsymbol{\Theta}\boldsymbol{\Theta}^T + j\omega\boldsymbol{C} - \omega^2\boldsymbol{M}} \boldsymbol{L}_f \tag{5.9}$$

When $\boldsymbol{L}_{\dot{u}} = \boldsymbol{L}_f$, the following relation can be obtained from Equation (5.9) and Equation (5.7)

$$\frac{V_{out}}{F} \equiv -\frac{1}{(j\omega C_p + \frac{1}{Z_e})} \frac{\dot{u}}{V_{in}} \tag{5.10}$$

Thereby, the force to voltage FRFs are similar to the voltage to velocity FRFs, and the above relation can quantify the amplitude and phase scalings. There is a frequency dependent scaling between V_{out}/F and $j\omega u/V_{in}$ in Equation (5.10) because the asymmetry of the electrical boundary conditions when the studied transducer is used as an actuator or a sensor. It is important to mention that it is assumed that the electrical dynamics do not significantly influence the dynamics of the system. Then, the dynamics of the overall system is consistent whenever the integrated transducer is used either as an actuator or as a sensor. However, the reciprocal relations may be impaired if the asymmetrical electrical boundary conditions introduce influences significantly to the dynamics of the system. Figure 5.24 and 5.25 demonstrated that Equation (5.10) retains.

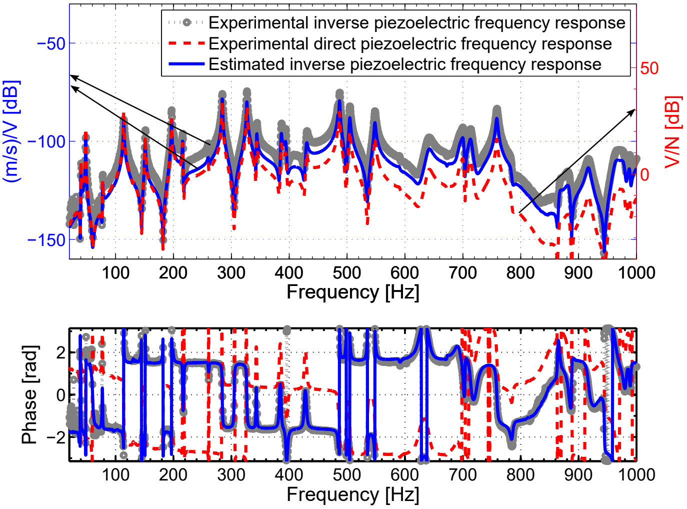

Figure 5.24: Estimated inverse piezoelectric frequency response between 26 and 22 by experimental data

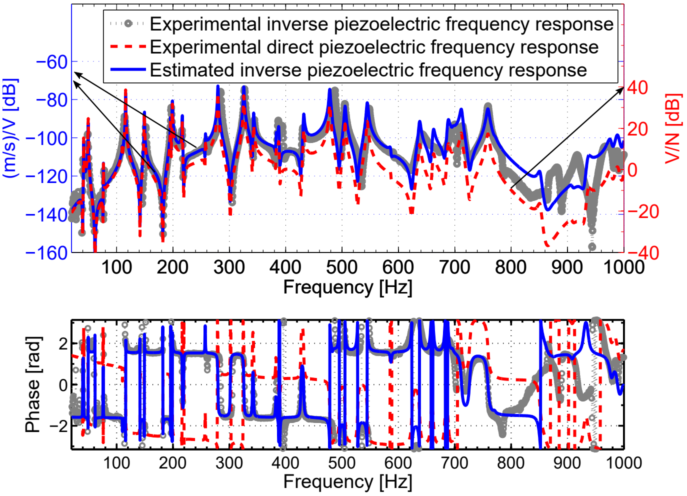

Figure 5.25: Estimated inverse piezoelectric frequency response between 26 and 22 by ESM model

The transducers can be used for load identification problems because it is easy to obtain $\dot{u}/V_{in}$ at a specific location on a structure with a piezoelectric transducer, and V_{out} generated by an unknown excitation load F can be directly measured.

5.5 Dynamic application of ESM approach

The ESM approach can efficiently assess the performance of the used MFC transducer in dynamic application. Two study cases are presented in this section to demonstrate the potential of the ESM approach in dynamic application.

5.5.1 Energy harvesting

The direct piezoelectric effect is widely applied to energy harvesting application. The performance of the MFC transducers is dominated by the piezoelectric fibrous orientation when its placement and external electrical circuit are fixed. It could be challenging to optimize the piezoelectric fibrous orientation because it modifies both the mechanical dynamics and piezoelectric coupling of the piezoelectric system. Especially, model order reduction is always required when the system model is large-scale. The ESM approach can efficiently evaluate the effect of the piezoelectric fibrous orientation on the electric output of the transducer, and it can be useful in the design of advanced piezoelectric systems. The voltage over force FRFs for a set of piezoelectric fibrous orientation on the studied composite plate are shown in Figures 5.26 and 5.27. The input of the FRFs is a concentrated force at location 74, and the output is the voltage extracted by a resistive load $R = 1M\Omega$ connected to the transducers.

The simulated FRFs of $\theta = 0^o$ agree well with the experimental data. We can observe from the two figures that the performance of each transducer depends on its piezoelectric fibrous orientation. The MFC transducer at the corner of the composite plate captured more modes than the one in the middle at low frequency. The peak voltages are usually the most important for energy harvesting. We can observe from the two figures that the optimal fibrous orientation of the middle transducer is in $\pm[0^o - 15^o]$ by comparing the peak values. The optimal fibrous orientation of the transducer at the corner of the plate is the range of $\pm[45^o - 75^o]$. It is worthwhile to mention that it is more difficult than the example to design the optimal piezoelectric fiber orientation because the electric output of the transducers depends on the placement of transducers, as well as the corresponding electrical system and external disturbances. Nevertheless, the presented approach offers high flexibility that can be applied to the design and modeling of advanced energy harvesting system.

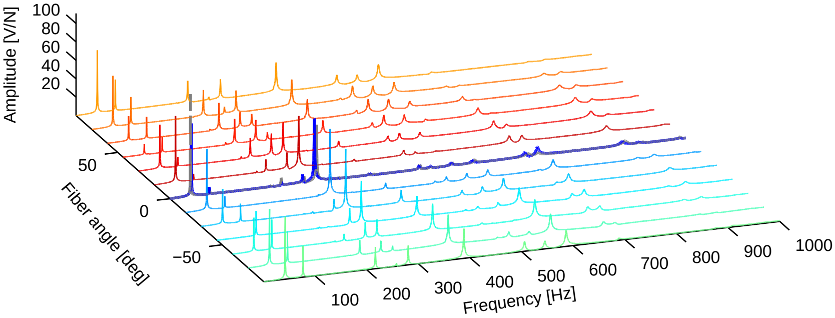

Figure 5.26: Force-to-voltage FRFs of the center MFC transducer for a set of piezoelectric fibrous orientations (The gray curve is experimental data.)

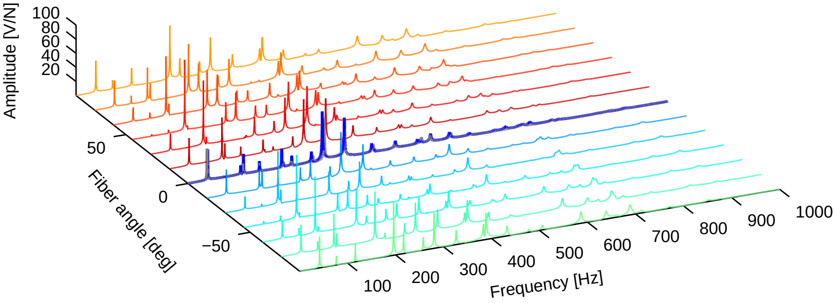

Figure 5.27: Force-to-voltage FRFs of the corner MFC transducer for a set of piezoelectric fibrous orientations (The gray curve is experimental data.)

5.5.2 Piezoelectric shunt damping

A piezoelectric shunt damping study is used to demonstrate the ESM approach can take the dynamics of electrical components into account. Figure 5.28 shows a $L - R$ piezoelectric shunt damping system.

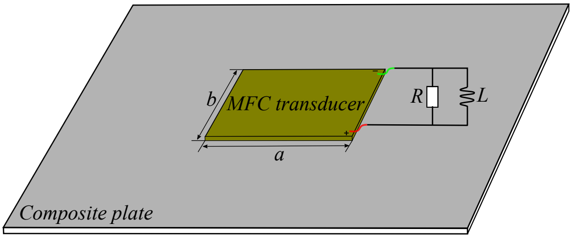

Figure 5.28: Piezoelectric shunt damping system

Since both the inductor L and resistor R are connected to the transducer in parallel, Equation (5.4b) yields the following relation in the frequency domain:

$$V(j\omega C_p + \frac{1}{R} + \frac{1}{j\omega L}) + j\omega \boldsymbol{\Theta}^T \boldsymbol{u} = 0 \tag{5.11}$$

The electric dynamics have a resonant frequency $\omega_e = \frac{1}{LC_p}$. As the piezoelectric shunt damping is achieved by coupling the direct piezoelectric effect to the inverse piezoelectric effect of the transducer, substituting (5.11) into (5.4a) yields:

$$(\boldsymbol{K} + j\omega \boldsymbol{C} - \omega^2 \boldsymbol{M} + \frac{j\omega \boldsymbol{\Theta}\boldsymbol{\Theta}^T}{j\omega C_p + \frac{1}{R} + \frac{1}{j\omega L}})\boldsymbol{u} = \boldsymbol{L}_f F_s \tag{5.12}$$

As $\dot{\boldsymbol{u}}$ is the transverse velocity output which is localized by $\boldsymbol{L}_{\dot{\boldsymbol{u}}}$ on the plate, the velocity over a force disturbance FRF can be given as:

$$\frac{\dot{\boldsymbol{u}}}{F_s} = \boldsymbol{L}_{\dot{\boldsymbol{u}}} \frac{j\omega}{\boldsymbol{K} + j\omega \boldsymbol{C} - \omega^2 \boldsymbol{M} + \frac{j\omega \boldsymbol{\Theta}\boldsymbol{\Theta}^T}{j\omega C_p + \frac{1}{R} + \frac{1}{j\omega L}}} \boldsymbol{L}_f \tag{5.13}$$

When ω_e is close to the natural frequency of a specific mode on the composite plate, the electric dynamics will resonant together with the mode, and shunt damping can be introduced to the mode of the composite plate by the electric circuit. L depends on the targeted mode because C_p is fixed, while R is the tuning parameter that dominates the damping performance. An individual electric circuit connects to each transducer on the plate in Figure 5.28 in order to finally damp two different modes of the plate. From Figures 5.26 and 5.27, we can observe that the transducer in the middle of the plate can well capture the modes at $41Hz$ and the one at the corner can well observe the modes at $283.5Hz$. Therefore, the two modes are targeted by the two transducers, respectively. The corresponding inductance L are $1221.1H$ and $269H$, respectively. The resistances R are tuned as $1.3 \times 10^8\Omega$ and $2.5 \times 10^7\Omega$ for the two modes according to engineering expertise.

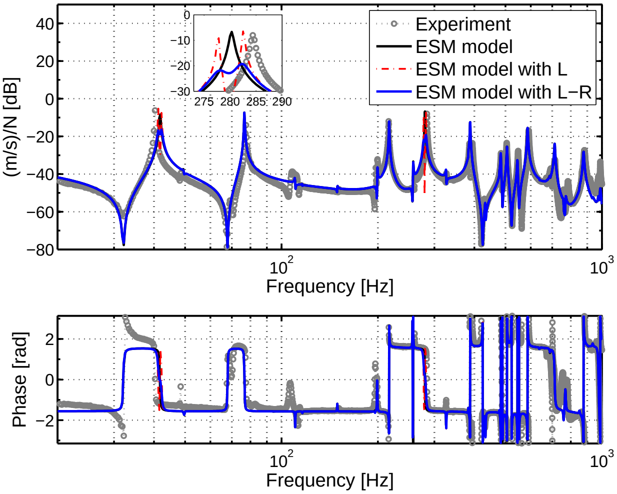

Figure 5.29: Piezoelectric shunt damping on the composite plate: velocity over force FRF between 74 and 00

The velocity over force FRFs are shown in Figures 5.29. Although the used L and R might be not the optimal setting, the piezoelectric shunt damping achieved $8.46dB$ and $12.56dB$ amplitude reductions on the modes at $41Hz$ and $283Hz$, respectively. The performance of the shunt damping is quite good considering the limited size of the MFC transducer compared to the composite plate. All the properties including the efficiency of the transducers and mechanical damping of the composite plate are included in the model. The ESM model can simulate the dynamic effects induced by both the inductance and resistance. Since the low-order system is stable, a real-time simulation is given in Figure 5.30. A swept sine force $(0 - 1000Hz)$ is used as a disturbance at position 74, and the amplitude of the force is $1N$. The performance of the piezoelectric shunted damping can be evaluated in the time domain, as shown in the figure. We can observe that the velocity amplitude of the plate is reduced, due to the shunted damping. However, it is difficult to understand the behaviors of the non-shunted and shunted plate from the figure. It is feasible to visualize the dynamic behaviors of the plate by using the reduced-order model because it remains in nodal coordinates. Figure 5.31 shows the behaviors of the plate at two instantaneous of the real-time simulation. The reduced-amplitude is the difference in displacements between the non-shunted and shunted plate. We can observe the reduced-amplitude contains the mode shapes of the two targeted modes.

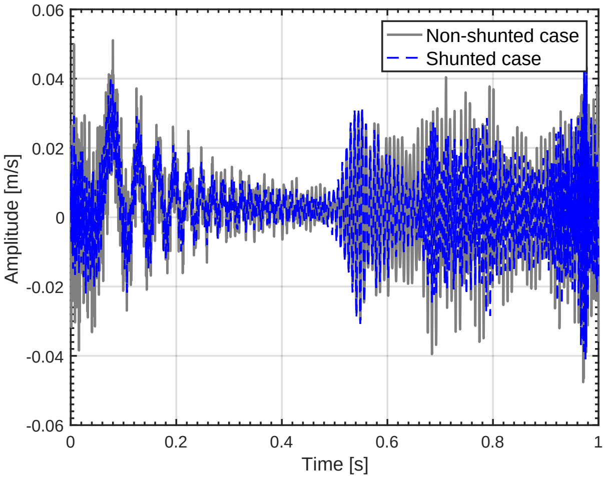

Figure 5.30: Real-time simulation of the $R - L$ shunted damping

In the next step, we use the ESM approach to evaluate the optimal placement of a transducer within its substructure. The ESM model is efficient because we only need to update the reduced-order substructure model, on which we want to place transducers. The transducer at the center of the plate is used as the study case. As shown in Figure 5.32, nine placements are evaluated at the center of the plate. A negative capacitance piezoelectric shunt controller is used in the analysis. Different from $L - R$ shunt damping, the negative capacitance shunt damping performs damping to a broadband frequency range. Each transducer is connected to an individual electrical circuit, by which, the capacitance effect on the transducers is counteracted, and damping phenomena are introduced to the plate due to resistive loads. The connected resistance to the transducers are $2.98\text{e}^8\Omega$ (Center MFC) and $5.73\text{e}^7\Omega$ (Corner MFC), respectively.

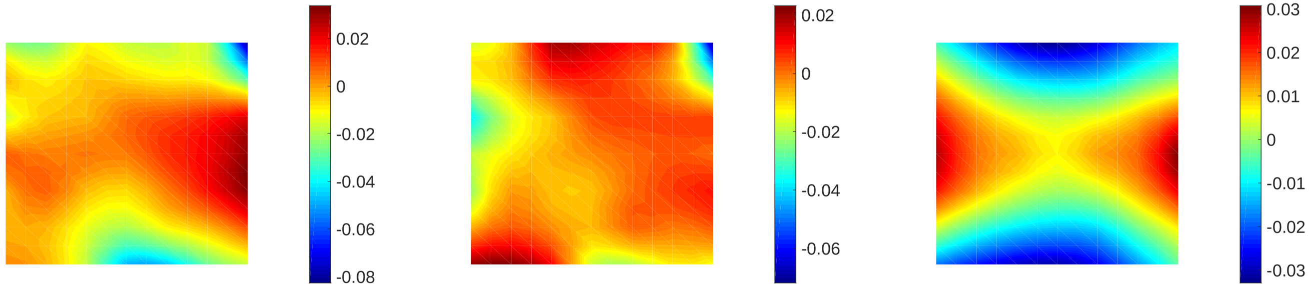

non-shunted plate at $0.322s$ shunted plate at $0.322s$ reduced ammplitude at $0.322s$

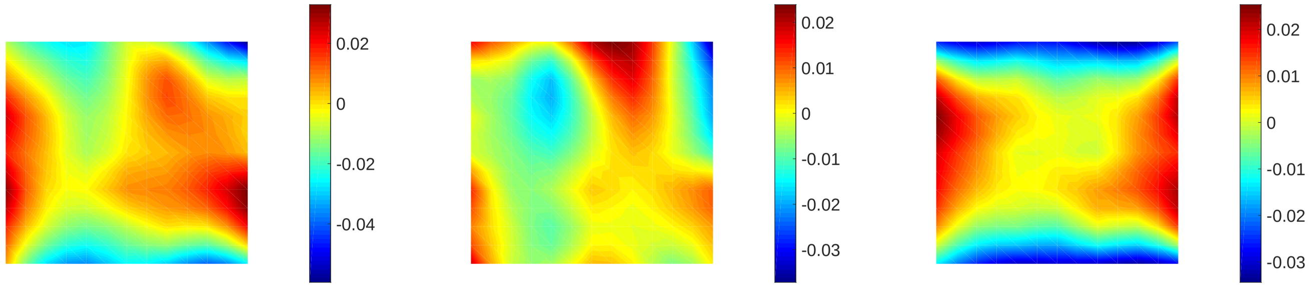

non-shunted plate at $0.331s$ shunted plate at $0.331s$ reduced ammplitude at $0.331s$

Figure 5.31: Dynamic behaviors of the plate in non-shunted and shunted cases

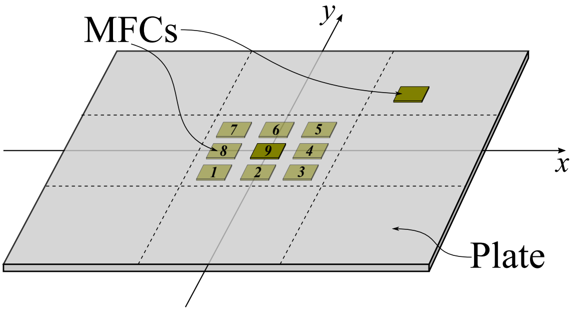

Figure 5.32: The placement candidates of the transducer at the center of the plate

Mode	MFC placements								
	1^{st}	2^{nd}	3^{rd}	4^{th}	5^{th}	6^{th}	7^{th}	8^{th}	9^{th}
1^{st}	10.28	11.04	9.93	11.04	11.14	**11.55**	8.86	8.12	10.88
2^{nd}	4.17	3.04	**9.00**	1.66	3.28	3.56	3.22	1.07	0.01
5^{th}	**10.93**	10.00	9.72	9.52	9.24	8.30	8.10	7.98	7.04
6^{th}	6.56	4.86	6.69	7.37	5.87	3.95	7.09	**8.45**	0.38
10^{th}	**10.87**	11.07	9.31	9.45	8.77	9.06	7.57	7.82	9.30
11^{th}	**11.75**	11.60	10.98	10.70	10.29	9.74	9.13	9.07	8.27

Table 5.7: Amplitude reduction of some modes for each placement (in $[dB]$)

Table 5.7 shows the performance of the negative capacitance shunt damping for different transducers' placements. A force input and velocity output FRF between 22 and 26 is used to check the damping performance. The performance of the negative capacitance shunted damping depends on the placement of the transducers. We can observe that it is not recommended to use the 9^{th} placement in this study case. The best placements of the transducer are most likely the 1^{st} and 2^{nd}. It is difficult to figure out the physical reason because the structural dynamics and damping are changed by the influences of the transducers in each case. Figure 5.33 shows the damping performance by using the 1^{st} placement. We only performed the simulation in the frequency domain, but it is possible to do analysis in the time domain.

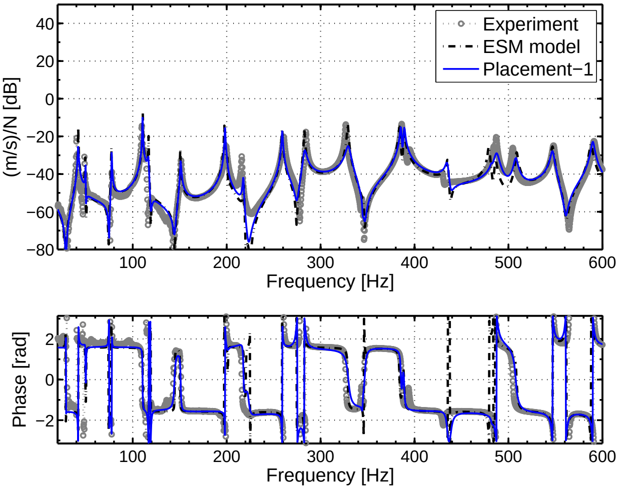

Figure 5.33: Performance of the negative capacitance shunt for different transducers' placements

5.6 Concluding remarks

In this chapter, the equivalent modeling approaches are validated by the experimental data. First of all, the dynamic testing of the composite plate with integrated MFC-d33 transducers is presented in detail. Then, both the EFM and ESM models of the tested plate are generated, and the two models well predict the dynamics of the tested plates. After that, the mechanical contribution of the MFC transducers in numerical models is evaluated, and the reciprocity between two MFC transducers is also validated. The piezoelectric reciprocal relation between direct and inverse piezoelectric FRFs is characterized. According to it, the inverse piezoelectric frequency response can be determined by the direct piezoelectric frequency response and vice versa.

Subsequently, two kinds of numerical study cases are given to present the potential of the ESM approach. The piezoelectric energy harvesting case shows that the piezoelectric fibrous orientation of the transducer can be efficiently evaluated in both the frequency and time domain to achieve an optimal design of the piezoelectric systems of MFC transducers. The piezoelectric shunted damping case demonstrates that the induced mechanical properties caused by electric components could be properly simulated. In consequence, the ESM approach permits a convenient evaluation of the optimal placement of the integrated MFC transducers. Further application on the proposed modeling approach can be investigated in future.

Chapter 6

Vibro-acoustic study on MFC transducers

Vibro-acoustics is the interaction between a vibrating structure and a fluid, that causes sound radiation. At the interface of the two components, the vibrating structure imposes a normal velocity to the fluid particles, and the fluid generates a sound pressure applied to the structure. The usage of piezoelectric transducers in vibro-acoustics could offer many benefits to the vibro-acoustic techniques: Piezoelectric transducers can be integrated into a structure as sublayers without any rotating or moving parts. Hence, they do not generate unwanted noise when they are used for structural excitation. They are also quite sensitive in a large operational frequency bandwidth up to a few hundreds of kilohertz so that they are suitable for acoustic measurements too. Hence, they instigated many research tracks in acoustic and vibro-acoustic domains [190–196]. However, the transducers are often used only as sensors or as actuators in most of the mentioned studies, so that the reversibility of piezoelectric effect, which could enable the switching between excitation and sensing, is not being explored yet. The work in this chapter investigated this possibility of piezoelectric transducers towards a vibro-acoustic field.

To demonstrate the dynamic properties of a piezoelectric transducer in vibro-acoustic fields, a laminated composite plate, which is conducted to a sound cavity is given as a study case. An MFC transducer [197] is integrated into the plate either for sensing or for actuating. The vibro-acoustic reciprocity is mathematically verified and extended to the integrated transducer. After that, a stable structure-preserving low-order model is generated and validated by experimental data. The vibro-acoustic reciprocal relations are verified by simulations in both the frequency and time domain.

6.1 Reciprocal relations of a piezoelectric vibro-acoustic system

The piezoelectric vibro-acoustic system, being used in the study, consists of a laminated composite plate with an integrated MFC transducer, which is conducted to a soundbox, as shown in Figure 6.1. The soundbox, developed by the noise and vibration research group at KU Leuven, is an acoustic cavity of $0.83m^3$ with a rectangular window, to which a shell-like structure can be clamped. The sketch and inner dimensions of the cavity are shown in Figure 6.1. None of the inner walls is parallel to each other in order to have a decent modal distribution in the low-frequency range and avoid coincident acoustic resonances [198].

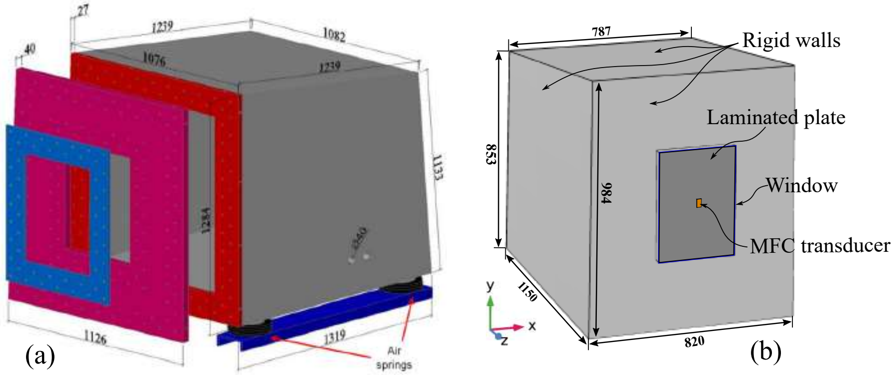

Figure 6.1: The dimensions of KU Leuven soundbox (in mm) [198]: (a) Sketch of KU Leuven soundbox (b) inner dimensions of the cavity with the studied plate

The size of the laminated composite plate is $297mm \times 420mm$. It consists of 8 unidirectional layers with a lay-up of $[-45^o\ 45^o\ 90^o\ 0^o]_s$. The thickness of the plate is $2.5mm$. An M2814-P1 ($28mm \times 14mm$) transducer fabricated by Smart Material Co. is surface-bonded to the plate. On the one hand, the integrated transducers can generate a distributed mechanical input on the plate when it is used as an actuator. On the other hand, the motion of the plate is also able to generate electric output from the transducers. The dynamics of the composite plate with integrated transducers is recalled as follows in the frequency domain:

$$(\boldsymbol{K}_s + j\omega\boldsymbol{C}_s - \omega^2\boldsymbol{M}_s)\boldsymbol{u} = \boldsymbol{F_s} + \boldsymbol{\Theta}V \tag{6.1a}$$

$$j\omega C_p V + \frac{V}{Z_e} + j\omega\boldsymbol{\Theta}^T\boldsymbol{u} = 0 \tag{6.1b}$$

where $\boldsymbol{K}_s$, $\boldsymbol{C}_s$ and $\boldsymbol{M}_s$ are the stiffness, damping and mass of the plate, respectively. When the electrical circuit provides an input V for operating the transducer, Equation (6.1b) is rewritten as follows, according to the charge flux:

$$j\omega C_p V - \frac{V}{Z_e} + \boldsymbol{\Theta}^T\dot{\boldsymbol{u}} = 0 \tag{6.2}$$

Substituting (6.2) into (6.1a) yields:

$$(\underbrace{\boldsymbol{K}_s + C_p^{-1}\boldsymbol{\Theta}^T\boldsymbol{\Theta}}_{\boldsymbol{K}_{Ag}} + j\omega\boldsymbol{C}_s - \omega^2\boldsymbol{M}_s)\boldsymbol{u} = \boldsymbol{\Theta}V + \boldsymbol{F_s}. \tag{6.3}$$

Hence, coupling the augmented structure to the acoustic domain in a classical $u - p$ formulation, the equations for the coupled vibro-acoustic system can be written as follows:

$$(\boldsymbol{K}_{Ag} + j\omega\boldsymbol{C}_s - \omega^2\boldsymbol{M}_s)\boldsymbol{u} + \boldsymbol{K}_c\boldsymbol{p} = \boldsymbol{F_s} \tag{6.4a}$$

$$(\boldsymbol{K}_a + j\omega\boldsymbol{C}_a - \omega^2\boldsymbol{M}_a)\boldsymbol{p} - \omega^2\boldsymbol{M_c}\boldsymbol{u} = \boldsymbol{F_a}. \tag{6.4b}$$

where $\boldsymbol{K}_a$, $\boldsymbol{C}_a$ and $\boldsymbol{M}_a$ are the stiffness, damping and mass of the cavity, respectively. $\boldsymbol{K}_c$ and $\boldsymbol{M}_c$ are the structural-acoustic couplings with $\boldsymbol{M}_c = -\rho_a\boldsymbol{K}_c^T$. $\boldsymbol{p}$ is acoustic pressure in the cavity. F_s and F_a are the mechanical and acoustic loads, respectively. A volume velocity monopole source in the cavity is given as $F_a = \rho_a j\omega Q$ and Q is the amplitude of the monopole source. Equation (6.4a) can be easily transformed as the following form:

$$(\boldsymbol{K}_{Ag} + j\omega\boldsymbol{C}_s - \omega^2\boldsymbol{M}_s)(j\omega)^{-1}\dot{\boldsymbol{u}} + \boldsymbol{K}_c\boldsymbol{p} = \boldsymbol{F_s}. \tag{6.5}$$

Meanwhile, Equation (6.4b) is rewritten as

$$(\boldsymbol{K}_a + j\omega\boldsymbol{C}_a - \omega^2\boldsymbol{M}_a)\boldsymbol{p} + j\omega\boldsymbol{M_c}\dot{\boldsymbol{u}} = \rho_a j\omega\boldsymbol{Q} \tag{6.6}$$

where a volume velocity source is substituted as an acoustic excitation. Equation (6.6) can be further simplified to the following expression:

$$-(\boldsymbol{K}_a + j\omega\boldsymbol{C}_a - \omega^2\boldsymbol{M}_a)(\rho_a j\omega)^{-1}\boldsymbol{p} + \boldsymbol{K_c}^T\dot{\boldsymbol{u}} = -\boldsymbol{Q}. \tag{6.7}$$

Hence, a modified second order system can be obtained as follows from Equation (6.5) and Equation (6.7):

$$\begin{bmatrix} \frac{\boldsymbol{H_s}}{j\omega} & \boldsymbol{K}_c \\ \boldsymbol{K}_c^T & -\frac{\boldsymbol{H_a}}{j\omega\rho_a} \end{bmatrix} \begin{Bmatrix} \dot{\boldsymbol{u}} \\ \boldsymbol{p} \end{Bmatrix} = \begin{Bmatrix} \boldsymbol{F_s} \\ -\boldsymbol{Q} \end{Bmatrix} \tag{6.8}$$

in which, $\boldsymbol{H}_s = \boldsymbol{K}_{Ag} + j\omega\boldsymbol{C}_s - \omega^2\boldsymbol{M}_s$ and $\boldsymbol{H}_a = \boldsymbol{K}_a + j\omega\boldsymbol{C}_a - \omega^2\boldsymbol{M}_a$ are the dynamics of the plate and the cavity, respectively. $\boldsymbol{H}_s$ and $\boldsymbol{H}_a$ are symmetrical for each frequency ω. Without any assumption on the coupling matrix, the system matrix is actually symmetrical. This mathematically confirms the existence of vibro-acoustic reciprocity. In addition, a transformation of Equation (6.8) can be performed as follows:

$$\begin{bmatrix} \frac{\boldsymbol{H}_s}{\omega^2} & -\boldsymbol{K}_c \\ -\boldsymbol{K}_c^T & \frac{\boldsymbol{H}_a}{\rho_a} \end{bmatrix} \begin{Bmatrix} \ddot{\boldsymbol{u}} \\ \boldsymbol{p} \end{Bmatrix} = \begin{Bmatrix} -\boldsymbol{F_s} \\ j\omega\boldsymbol{Q} \end{Bmatrix}. \tag{6.9}$$

Hence, the vibro-acoustic reciprocity can be expressed into different forms according to Equation (6.8) and Equation (6.9). The reciprocity, which has been mentioned in [199] can be deduced from Equation (6.9). An important notation is that there is a scaling of $j\omega$ between the structural response and the acoustic excitation. Equation (6.9) can be also reformulated into $(u-p)$ form, where a scaling factor of ω^2 on the acoustic excitation case will be required.

The vibro-acoustic reciprocity between a point A on the plate and a location B in the acoustic field can be expressed as follows according to Equation (6.8):

$$\frac{p_B}{F_A} = -\frac{\dot{u}_A}{Q_B}. \tag{6.10}$$

The frequency response of the sound pressure p_B over the structural excitation F_A can be expressed as follows by using Equation (6.8) with $Q = 0$:

$$\frac{p_B}{F_A} = \begin{Bmatrix} 0 \\ \boldsymbol{L}_B \end{Bmatrix}^T \begin{bmatrix} \frac{\boldsymbol{H}_s}{j\omega} & \boldsymbol{K}_c \\ \boldsymbol{K}_c^T & -\frac{\boldsymbol{H}_a}{j\omega\rho_a} \end{bmatrix}^{-1} \begin{Bmatrix} \boldsymbol{L}_A \\ 0 \end{Bmatrix} \tag{6.11}$$

where $\boldsymbol{L}_A$ and $\boldsymbol{L}_B$ are the input and output localization matrix of F_A and p_B, respectively. Similarly, the frequency response of the velocity $\dot{u}_B$ over the amplitude of the volume velocity source Q_B can be obtained from (6.8) with $F_s = 0$:

$$\frac{\dot{u}_A}{Q_B} = -\begin{Bmatrix} \boldsymbol{L}_A \\ 0 \end{Bmatrix}^T \begin{bmatrix} \frac{\boldsymbol{H}_s}{j\omega} & \boldsymbol{K}_c \\ \boldsymbol{K}_c^T & -\frac{\boldsymbol{H}_a}{j\omega\rho_a} \end{bmatrix}^{-1} \begin{Bmatrix} 0 \\ \boldsymbol{L}_B \end{Bmatrix}. \tag{6.12}$$

A matrix transformation, which aims to switch the input/output locations can be performed as follows to either Equation (6.11) or Equation (6.12):

$$\left(\begin{Bmatrix} 0 \\ \boldsymbol{L}_{B} \end{Bmatrix}^T \begin{bmatrix} \frac{\boldsymbol{H}_s}{j\omega} & \boldsymbol{K}_c \\ \boldsymbol{K}_c^T & -\frac{\boldsymbol{H}_a}{j\omega\rho_a} \end{bmatrix}^{-1} \begin{Bmatrix} \boldsymbol{L}_{A} \\ 0 \end{Bmatrix}\right)^T = \begin{Bmatrix} \boldsymbol{L}_{A} \\ 0 \end{Bmatrix}^T \begin{bmatrix} \frac{\boldsymbol{H}_s}{j\omega} & \boldsymbol{K}_c \\ \boldsymbol{K}_c^T & -\frac{\boldsymbol{H}_a}{j\omega\rho_a} \end{bmatrix}^{-1} \begin{Bmatrix} 0 \\ \boldsymbol{L}_{B} \end{Bmatrix}. \tag{6.13}$$

We can find that the vibro-acoustic reciprocity should be valid for any possible $\boldsymbol{L}_{A}$ and $\boldsymbol{L}_{B}$. The piezoelectric coupling $\boldsymbol{\Theta}$ of the integrated transducer, which has a distributed interaction with the plate is also applicable. The actuated plate subjected to an operational voltage V_{in} generates acoustic pressure p inside the cavity. The transfer function between the voltage input V_{in} and acoustic pressure p_{B} at location B in the cavity can deduced from Equation (6.11):

$$\frac{p_{B}}{V_{in}} = \begin{Bmatrix} 0 \\ \boldsymbol{L}_{B} \end{Bmatrix}^T \begin{bmatrix} \frac{\boldsymbol{H}_s}{j\omega} & \boldsymbol{K}_c \\ \boldsymbol{K}_c^T & -\frac{\boldsymbol{H}_a}{j\omega\rho_a} \end{bmatrix}^{-1} \begin{Bmatrix} \boldsymbol{\Theta} \\ 0 \end{Bmatrix}. \tag{6.14}$$

In contrast, a volume velocity monopole source of amplitude Q at location B in the cavity is able to generate a voltage output V_{out} on the transducer. Introducing Equation (6.1b) into Equation (6.12) yields:

$$\frac{V_{out}}{Q_{B}} = -\frac{1}{(j\omega C_p + \frac{1}{Z_e})} \begin{Bmatrix} \boldsymbol{\Theta} \\ 0 \end{Bmatrix}^T \begin{bmatrix} \frac{\boldsymbol{H}_s}{j\omega} & \boldsymbol{K}_c \\ \boldsymbol{K}_c^T & -\frac{\boldsymbol{H}_a}{j\omega\rho_a} \end{bmatrix}^{-1} \begin{Bmatrix} 0 \\ -\boldsymbol{L}_{B} \end{Bmatrix}. \tag{6.15}$$

Similar to the piezoelectric reciprocal relation, there is a scaling between Equation (6.14) and Equation (6.15) which is actually defined by the electrical boundary conditions. The piezoelectric vibro-acoustic reciprocal relation can be deduced from Equation (6.14) and Equation (6.15) as

$$\frac{V_{out}}{Q_{B}} \equiv \frac{1}{(j\omega C_p + \frac{1}{Z_e})} \frac{p_{B}}{V_{in}}. \tag{6.16}$$

Furthermore, when the acoustic excitation is not present, Equation (6.8) can be rewritten as:

$$\left(\frac{\boldsymbol{H_s}}{j\omega} + \boldsymbol{K}_c \left(\frac{\boldsymbol{H_a}}{j\omega\rho_a}\right)^{-1} \boldsymbol{K}_c^T\right)\dot{\boldsymbol{u}} = \boldsymbol{F_s} \tag{6.17}$$

A force input at a specific location C, which can be the same location as A on the plate generates an electric output from the transducer. The force over voltage FRF is given as:

$$\frac{V_{out}}{F_s} = -\boldsymbol{\Theta}^T \left(\frac{\boldsymbol{H_s}}{j\omega} + \boldsymbol{K}_c \left(\frac{\boldsymbol{H_a}}{j\omega\rho_a}\right)^{-1} \boldsymbol{K}_c^T\right)^{-1} \boldsymbol{L}_{C} \tag{6.18}$$

where $\boldsymbol{L}_C$ defines the location of F_s on the plate. Meanwhile, a voltage input on the transducer generates also velocity output on the plate, which can be described as follows:

$$\frac{\dot{u}_C}{V_{in}} = -\frac{1}{(j\omega C_p + \frac{1}{Z_e})}\boldsymbol{L}_C^T\left(\frac{\boldsymbol{H_s}}{j\omega} + \boldsymbol{K}_c\left(\frac{\boldsymbol{H_a}}{j\omega\rho_a}\right)^{-1}\boldsymbol{K}_c^T\right)^{-1}\boldsymbol{\Theta} \tag{6.19}$$

Thus, the following relation can be deduced by using Equation (6.18) and Equation (6.19):

$$\frac{V_{out}}{F_s} = -\frac{1}{(j\omega C_p + \frac{1}{Z_e})}\frac{\dot{u}_C}{V_{in}}. \tag{6.20}$$

The piezoelectric reciprocal relation in Equation (5.10) is deduced.

6.2 Equivalent substructure modeling of the piezoelectric vibro-acoustic system

The modeling of the piezoelectric vibro-acoustic system is divided into two phases: (i) the pure structural-acoustic interaction model of the studied system is generated by the acoustic module of Comsol 5.3 [200]; (ii) the piezoelectric effect of the integrated MFC transducer is coupled to the Comsol model by using equivalent forces.

6.2.1 FEM modeling in Comsol

Given that the used Comsol solver does not support the modeling of laminated structures in acoustic-shell interaction simulation, the equivalent properties of the laminated composite plate should be determined by a material homogenization approach with the FOSD theory.

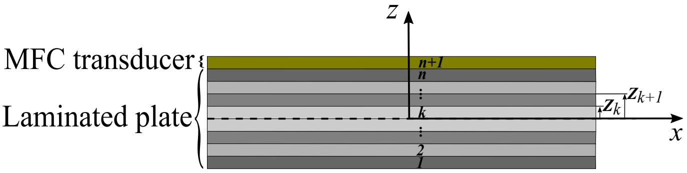

Figure 6.2: Lay-up of a laminated composite plate with integrated MFC transducer

The laminated composite plate consists of n orthotropic layers which are joint by an epoxy matrix, as shown in Figure 6.2. The membrane, bending motions and their coupling on the plate can be expressed as follows [172]:

$$\left\{\begin{array}{c} N_{xx} \\ N_{yy} \\ N_{xy} \\ M_{xx} \\ M_{yy} \\ M_{xy} \end{array}\right\} = \begin{bmatrix} A_{11} & A_{12} & A_{16} & B_{11} & B_{12} & B_{16} \\ A_{21} & A_{22} & A_{26} & B_{21} & B_{22} & B_{26} \\ A_{61} & A_{62} & A_{66} & B_{61} & B_{62} & B_{66} \\ B_{11} & B_{12} & B_{16} & D_{11} & D_{12} & D_{16} \\ B_{21} & B_{22} & B_{26} & D_{21} & D_{22} & D_{26} \\ B_{61} & B_{62} & B_{66} & D_{61} & D_{62} & D_{66} \end{bmatrix} \left\{\begin{array}{c} \varepsilon_{xx} \\ \varepsilon_{yy} \\ \varepsilon_{xy} \\ \kappa_{xx} \\ \kappa_{yy} \\ \kappa_{xy} \end{array}\right\} \tag{6.21}$$

in which,

$$(A_{ij},\ B_{ij},\ D_{ij}) = \sum_{k=1}^{n} \int_{z_{k-1}}^{z_k} (1, z, z^2) \bar{Q}_{ij}^{(k)} dz \ (i, j = 1, 2, 3). \tag{6.22}$$

Three symmetrical submatrix can be obtained from Equation (6.21): A, B, D, which are extensional stiffness, extensional-bending coupling stiffness and bending stiffness, respectively. $\bar{Q}$ is the elasticity of each layer in the structural coordinates system. Assuming that there is a neutral surface in the thickness-wise of the plate, on which the stress resultants N vanishes. The effective bending stiffness of the laminated plate can be obtained from Equation (3.8) as follows:

$$D^* = D - BA^{-1}B. \tag{6.23}$$

The effect of the extensional-bending coupling on the plate is included in Equation (6.23). For a symmetrical lay-up, the coupling matrix B is null. In FOSD plate theory, the transverse shear components are expressed as follows:

$$\left\{\begin{array}{c} \tau_{xz} \\ \tau_{yz} \end{array}\right\} = \begin{bmatrix} D_{55}^s & D_{54}^s \\ D_{45}^s & D_{44}^s \end{bmatrix} \left\{\begin{array}{c} \beta_x \\ \beta_y \end{array}\right\} \tag{6.24}$$

with

$$D_{ij}^s = \sum_{k=1}^{n} \int_{z_{k-1}}^{z_k} \bar{Q}_{ij}^{(k)} dz,\ (i, j = 4, 5). \tag{6.25}$$

Equation (6.23) includs the effect of the extensional-bending coupling on the plate. For a symmetrical lay-up, the coupling matrix B is null. In FOSD plate theory, the transverse shear components are expressed as follows:

$$\begin{aligned} \hat{Q}_{ij}^* &= \frac{12}{t_s^3} D_{ij}^*,\ (i, j = 1, 2, 3) \\ \hat{Q}_{ij}^s &= \frac{1}{t_s} D_{ij}^s,\ (i, j = 4, 5) \end{aligned} \tag{6.26}$$

where t_s is the thickness of the plate. The mechanical properties of the MFC transducers can also be included into the material homogenization as an additional sublayer. It is important to notice that this material homogenization only preserves the bending motion of the plate which predominates the structural-acoustic interaction in this study.

The FEM model generated by Comsol is shown in Figure 6.3. The material properties, which are used for material homogenization of the laminated composite plate are given in Table 6.1. The speed of sound and the air density are given as $c = 343.12 m/s$ $\rho_a = 1.204 kg/m^3$, respectively. Quadratic Lagrange tetrahedral elements are used to discretize the cavity, and quadratic shell elements are used to discretize the plate. The size of the FEM model is 45072×45072.

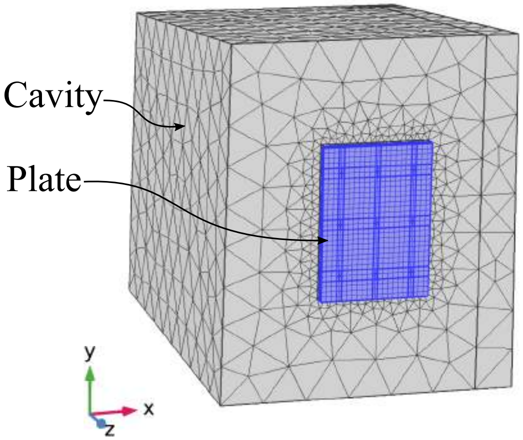

Figure 6.3: Comsol cavity-shell model

	density$[Kg/m^3]$	$c_{11}[GPa]$	$c_{22}[GPa]$	$G_{12}[GPa]$	ν_{12}	$G_{13}[GPa]$	$G_{23}[GPa]$	d_{33}	d_{32}
Composite layer	1500	110.15	7.868	4.05	0.26	–	–	–	–
MFC	5440	27.142	14.8	4.1312	0.2922	5.385	10.5	272	−133

Table 6.1: Structure and material properties of the laminated composite plate with integrated MFC-d33 transducers

Proportional damping is adopted here for dynamic response predictions. The corresponding damping coefficients λ and η are listed in the Table 6.2. Those two values are estimated from the critical damping ratios of two experimental modes at $290Hz$ and $385Hz$ in the impact testing.

	λ $[1/s]$	η $[s]$
value	6.4436	7.3093×10^{-7}

Table 6.2: Proportional damping coefficients

6.2.2 ESM approach

The ESM approach is adopted to create a suitable size model for simulations in both the frequency and time domain. Before perform the ESM approach, a transformation $\boldsymbol{p} = -\rho_a \dot{\boldsymbol{\phi}}$ between the sound pressure $\boldsymbol{p}$ and the velocity potential $\boldsymbol{\phi}$ is firstly applied to Equation (6.4a) and Equation (6.4b), in order to guarantee the stability of the final system model [201]. The transformed system is given as follows:

$$\left\{\begin{bmatrix} \boldsymbol{K}_{Ag} & 0 \\ 0 & \boldsymbol{K}_a \end{bmatrix} + j\omega \begin{bmatrix} \boldsymbol{C}_s & -\rho_a \boldsymbol{K}_c \\ \rho_a \boldsymbol{K}_c & \boldsymbol{C}_a \end{bmatrix} - \omega^2 \begin{bmatrix} \boldsymbol{M}_s & 0 \\ 0 & \boldsymbol{M}_a \end{bmatrix}\right\} \begin{Bmatrix} \boldsymbol{u} \\ \boldsymbol{\phi} \end{Bmatrix} = \begin{Bmatrix} \boldsymbol{F_s} \\ -\boldsymbol{F_\phi} \end{Bmatrix}. \tag{6.27}$$

The structural-acoustic coupling is in the damping matrix. The stability of the system is preserved because the coupled stiffness and damping matrix are positive semi-definite and the coupled mass matrix is positive-definite.

In the ESM approach, the plate and the cavity are considered as two subcomponents. The selected master nodes for dynamic condensation are shown in Figure 6.4. Only 34 structural nodes are selected for the plate, and only the transverse displacement Dofs are retained for the order reduction. Meanwhile, 156 acoustic nodes are kept for the cavity. Hence, the size of the final ESM model would be only 190, which is much smaller than the original FEM model. Numerous acoustic master nodes are kept in the reduced-order model because the modes of the cavity are desired to be presented in the modal validations.

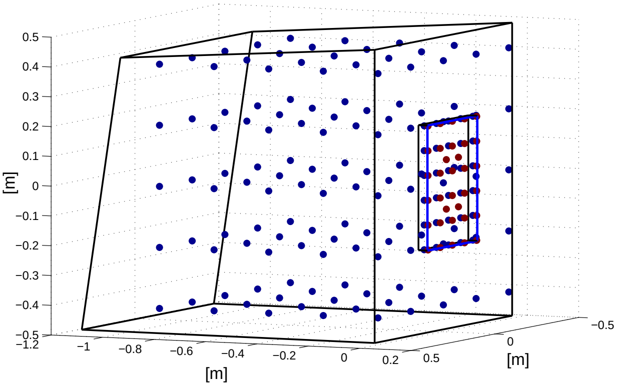

Figure 6.4: Distribution of the master nodes selected for ESM approach. Red spots and blue spots indicate the master nodes of the plate and the cavity, respectively.

An order reduction basis $\boldsymbol{R}$ can be easily generated for each subcomponent by dynamic condensation techniques. Then, the reduction transformations can be formulated as:

$$\boldsymbol{u} = \boldsymbol{T}_s \boldsymbol{u}^r, \ \boldsymbol{\phi} = \boldsymbol{T}_a \boldsymbol{\phi}^r \tag{6.28}$$

Hence, the reduced-order system is given as

$$\left\{ \begin{bmatrix} \boldsymbol{K}^r_{Ag} & 0 \\ 0 & \boldsymbol{K}^r_a \end{bmatrix} + j\omega \begin{bmatrix} \boldsymbol{C}^r_s & -\rho_a \boldsymbol{K}^r_c \\ \rho_a \boldsymbol{K}^r_c & \boldsymbol{C}^r_a \end{bmatrix} - \omega^2 \begin{bmatrix} \boldsymbol{M}^r_s & 0 \\ 0 & \boldsymbol{M}^r_a \end{bmatrix} \right\} \begin{Bmatrix} \boldsymbol{u}^r \\ \boldsymbol{\phi}^r \end{Bmatrix} = \begin{Bmatrix} \boldsymbol{F}^r_{\boldsymbol{s}} \\ -\boldsymbol{F}^r_{\boldsymbol{\phi}} \end{Bmatrix} \tag{6.29}$$

with

$$\begin{aligned}
&\boldsymbol{K}^r_{Ag} = \boldsymbol{T}^T_s \boldsymbol{K}_{Ag} \boldsymbol{T}_s, \ \boldsymbol{K}^r_a = \boldsymbol{T}^T_a \boldsymbol{K}_a \boldsymbol{T}_a \\
&\boldsymbol{M}^r_s = \boldsymbol{T}^T_s \boldsymbol{M}_s \boldsymbol{T}_s, \ \boldsymbol{M}^r_a = \boldsymbol{T}^T_a \boldsymbol{M}_a \boldsymbol{T}_a \\
&\boldsymbol{C}^r_s = \boldsymbol{T}^T_s \boldsymbol{C}_s \boldsymbol{T}_s, \ \boldsymbol{C}^r_a = \boldsymbol{T}^T_a \boldsymbol{C}_a \boldsymbol{T}_a \\
&\boldsymbol{K}^r_c = \boldsymbol{T}^T_s \boldsymbol{K}_c \boldsymbol{T}_a, \ \boldsymbol{u}^r = \boldsymbol{T}^T_s u, \ \boldsymbol{\phi}^r = \boldsymbol{T}^T_a \boldsymbol{\phi}. \\
&\boldsymbol{F}^r_{\boldsymbol{s}} = \boldsymbol{T}^T_s \boldsymbol{F}_{\boldsymbol{s}}, \ \boldsymbol{F}^r_{\boldsymbol{\phi}} = \boldsymbol{T}^T_a \boldsymbol{F}_{\boldsymbol{\phi}}.
\end{aligned}$$

Similar as F^r_s, the piezoelectric coupling $\boldsymbol{\Theta}$ of the integrated transducers is converted to the desired nodes on the reduced-order system model. The structure of Equation (6.27) is preserved in the reduced-order model. Therefore, the reduced-order model is still stable. Since the reduced-order remains in the nodal coordinates, it is possible to transform it back to the $u - p$ form. Hence, the

ESM model in $u-p$ form can be deduced as follows:

$$\left\{\begin{bmatrix}\boldsymbol{K}_{Ag}^{r} & \boldsymbol{K}_{c}^{r}\\ 0 & \boldsymbol{K}_{a}^{r}\end{bmatrix}+j\omega\begin{bmatrix}\boldsymbol{C}_{s}^{r} & 0\\ 0 & \boldsymbol{C}_{a}^{r}\end{bmatrix}-\omega^{2}\begin{bmatrix}\boldsymbol{M}_{s}^{r} & 0\\ -\boldsymbol{K}_{c}^{r} & \boldsymbol{M}_{a}^{r}\end{bmatrix}\right\}\begin{Bmatrix}\boldsymbol{u}^{r}\\ \boldsymbol{p}^{r}\end{Bmatrix}=\begin{Bmatrix}\boldsymbol{F}_{\boldsymbol{s}}^{r}\\ \boldsymbol{F}_{\boldsymbol{a}}^{r}\end{Bmatrix}. \tag{6.30}$$

6.3 Validation of ESM model

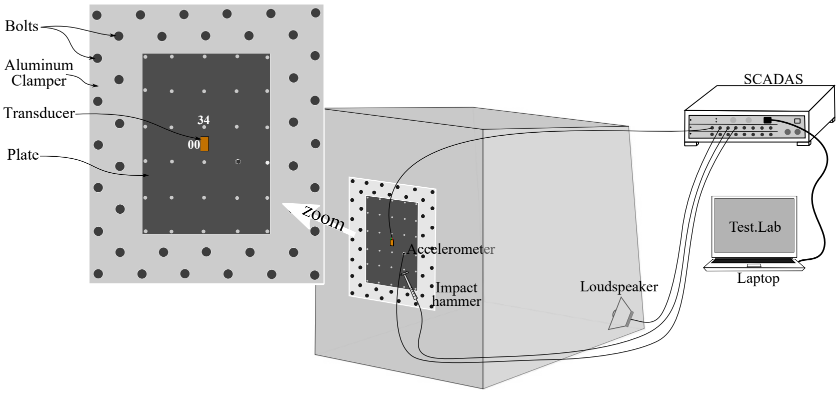

Figure 6.5: Experimental setup of the vibro-acoustic system

A dynamic analysis of the vibro-acoustic system is carried out to verify that the equivalent plate model is a good representation of the real structure, as shown in Figure 6.5. A PCB hammer is used to execute the impacts. Test.Lab 14A and SCADAS mobile are used as data acquisition software and hardware, respectively. The studied plate is clamped to the soundbox by an A3 size aluminum frame. Thus, the dimension of the tested area is $297mm \times 420mm$. A measurement grid of 5×6 is used in the testing. An accelerometer is mounted at location 43. The transducer is directly connected to the input channel of SCADAS mobile. Hence, a resistance of the input module on SCADAS ($R = 10^6\Omega$) is used to measure the voltage output of the integrated transducer. The structural reciprocity on the plate is checked, and the roving hammer technique is used in the experiment because the transducer is surface-bonded on the plate at location 00. PolyMAX is used to carry out the experimental modal analysis [188]. After that, a loudspeaker is used to perform the acoustic excitation in order to identify the natural frequencies of the studied vibro-acoustic system. The voltage output of the transducer is also measured in this case.

It is important to mention that the clamp frame of the soundbox is not rigid enough compared to the perfect clamped boundary conditions in the numerical model. Hence, a model updating of the plate is required for the compensation. In this validation, a dimensionless factor of 0.83 is applied to the stiffness of the plate as a rough model updating due to the limitation of the used FEM solver. The natural frequencies of the predicted modes are well-matched to the experimental data, as shown in table 6.3. The errors in the table are relative errors between the experimental data and the ESM model. The corresponding mode shapes are evaluated using MAC as shown in Figure 6.6. The modal parameters of the equivalent plate agree with the experimental data. The natural frequency of the first mode predicted by the ESM model has the largest error compared to other modes. That is mainly due to the used dynamic condensation technique in ESM approach. The numerical mode shapes do not perfectly match with the experimental data because the adopted model updating does not compensate for the local boundary condition uncertainties at the edges of the plate in the experiment.

mode	1^{st}	2^{nd}	3^{rd}	4^{th}	5^{th}	6^{th}	7^{th}	8^{th}
Experiment $[Hz]$	166	290.9	385.9	476.6	536.8	704.6	720.0	760.7
Comsol plate model $[Hz]$	171.8	295.3	394.9	476.0	538.5	704.6	722.5	755.5
ESM plate model $[Hz]$	173.6	295.8	395.2	476.2	538.4	704.9	722.7	755.6
Error	4.58%	1.68%	2.41%	−0.08%	0.30%	0.04%	0.36%	−0.67%

Table 6.3: Validation of the first 8 natural frequencies of the equivalent plate

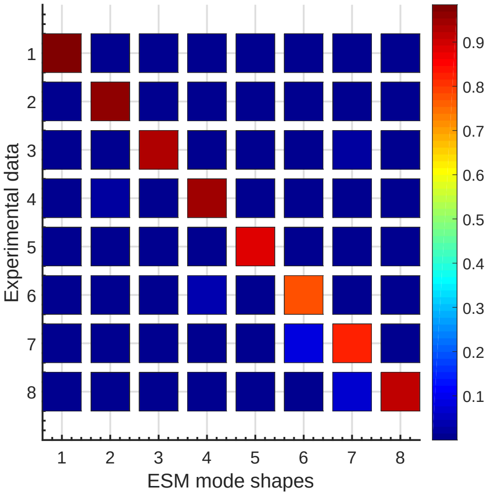

Figure 6.6: MAC correlation between ESM plate model and experimental data

We can observe from Table 6.4 that the ESM model well predicted the natural frequencies of the vibro-acoustic system. The errors shown in the table are the relative error between the ESM model and the experimental data. The corresponding mode shapes, obtained from the ESM model, are given in Figure 6.7. The second and eighth modes are dominated by the first and second modes of the plate.

mode	1^{st}	2^{nd}	3^{rd}	4^{th}	5^{th}	6^{th}	7^{th}	8^{th}
Experiment [Hz]	150.3	169.6	187.7	216.3	243.9	265.6	285.4	294.2
Comsol [Hz]	150.7	171.0	187.3	214.8	243.1	265.0	285.7	292.2
ESM model [Hz]	151.4	173.0	188.2	215.6	243.7	265.3	285.7	293.4
Error	0.73%	2.00%	0.27%	−0.32%	−0.08%	−0.11%	−0.11%	−0.20%

Table 6.4: Validation of the first eight natural frequencies of the piezoelectric vibro-acoustic system

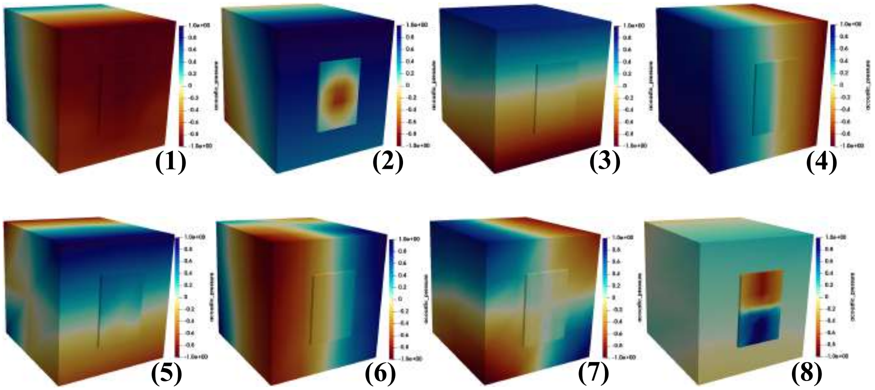

Figure 6.7: First eight vibro-acoustic modes of the cavity (normalized sound pressure in the cavity)

6.3.1 Frequency response validations

The frequency response validations on the plate are given in Figures 6.8 and 6.9, respectively. The ESM model agrees well with the experimental data. The amplitude deviations are mainly caused by the uncertainty of the boundary conditions in the experiment. The dynamic responses at locations 43 and 00 are affected differently by the imperfect boundary conditions in the experiment. Hence, the amplitude deviations occurred in different frequency bandwidths in Figures 6.8 and 6.9.

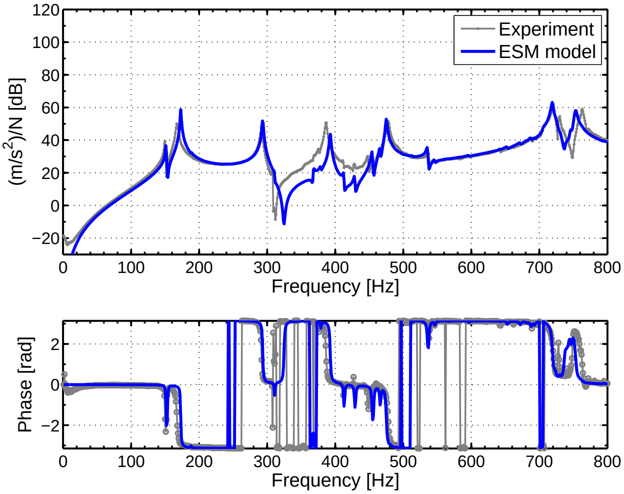

Figure 6.8: Frequency response validation of acceleration over force input between locations 43 and 34 on the plate

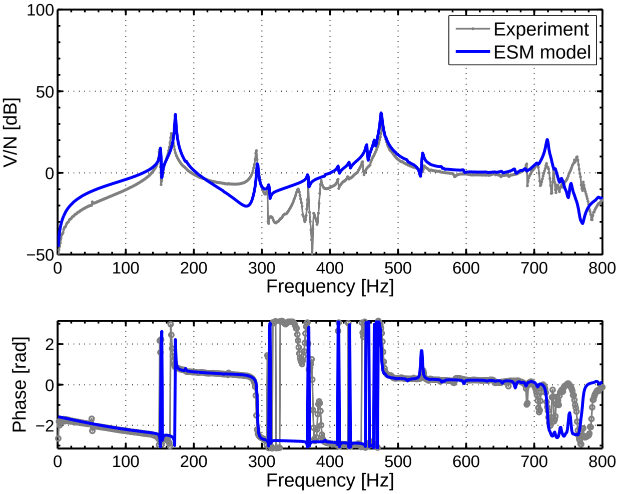

Figure 6.9: Frequency response validation of voltage output over force input between locations 00 and 34 on the plate

As the loudspeaker that used to perform the acoustic excitation is not calibrated, the ESM model is qualitatively verified in this case. Figure 6.10 shows the frequency response validation of the acceleration output at location 43 over a unit acoustic volume velocity input at the loudspeaker location. The amplitude of the experimental data is manually shifted in order to have a clear comparison. Figure 6.11 shows the FRF of an acoustic volume velocity over voltage output, which is validated by the experimental data and the experimental data is shifted by using the same scaling as in Figure 6.10. The numerical results agree well with the experimental data up to $450Hz$ in both validations. The profiles of the predicted FRFs deviate obviously from the experimental data at a higher frequency range, and that is expected, due to the performance of the soundbox [3]. The failure of the boundary conditions on the soundbox at higher frequency range could be the main reason. Also, the excitation difference between the loudspeaker in the experiment and the monopole source in the ESM model also contributes to the amplitude deviation. Finally, the proportional damping used in the ESM model cannot perfectly simulate the real damping in the experiment too.

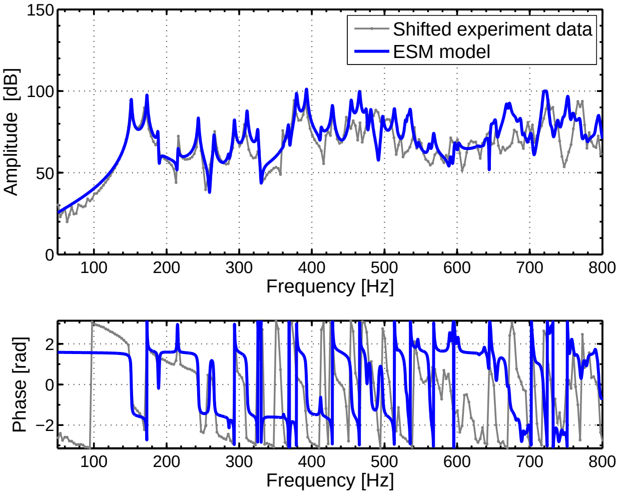

Figure 6.10: Frequency response validation of acceleration over acoustic volume velocity

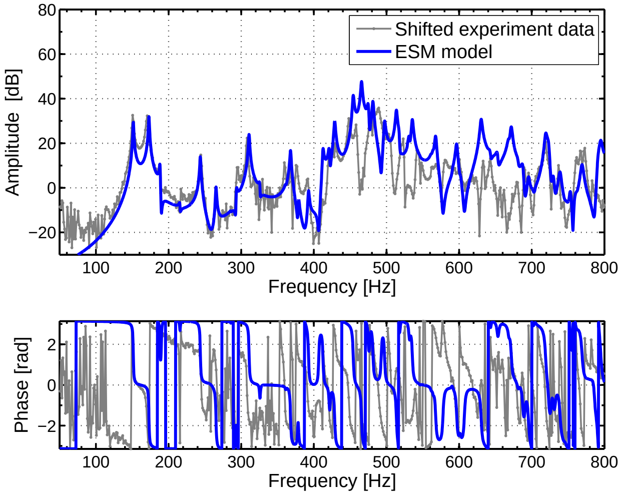

Figure 6.11: Frequency response validation of voltage output over acoustic volume velocity

6.3.2 Stability verification of ESM model

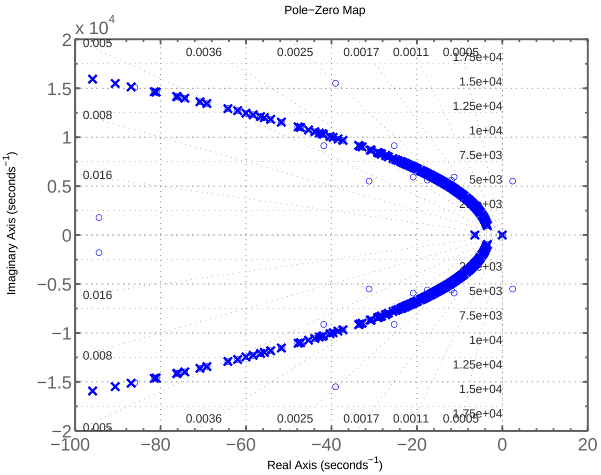

Figure 6.12: The poles (×) and zeros (○) of the ESM model

The ESM model is stable because all the poles of the coupled system are in the negative semi-plane of the complex space, as shown in Figure 6.12. The order reduction technique in the ESM approach only involves the mass and stiffness matrix of each subsystem, which is positive definite and positive semi-definite, respectively. The ESM model is stable if the original system is stable. A benefit from the stability-preserving low-order model is thus the simulations in the time domain.

6.4 Reciprocal relations verification

6.4.1 Verification in the frequency domain

The derived reciprocal relations are virtually verified by using the experimentally validated ESM model because of the practical difficulties in the experiment. On the one hand, it is hard to calibrate the sensitivity between the input voltage and the volume velocity output of the loudspeaker. On the other hand, the transducer, which integrated on the clamped composite plate is very sensitive to the external noises in the acoustic excitation case, as shown in the experimental data in 6.11. Hence, it is challenging to experimentally validate the derived reciprocal relations on both the amplitude and phase of FRFs.

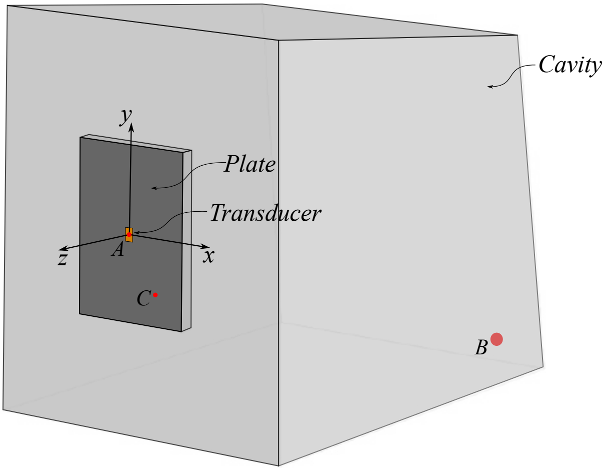

Figure 6.13: Reciprocal relation validation positions

The reciprocal relation between the plate and the transducer is validated between

A and C and the reciprocal relation between the cavity, and the transducer is validated between A and B, as shown in Figure 6.13.

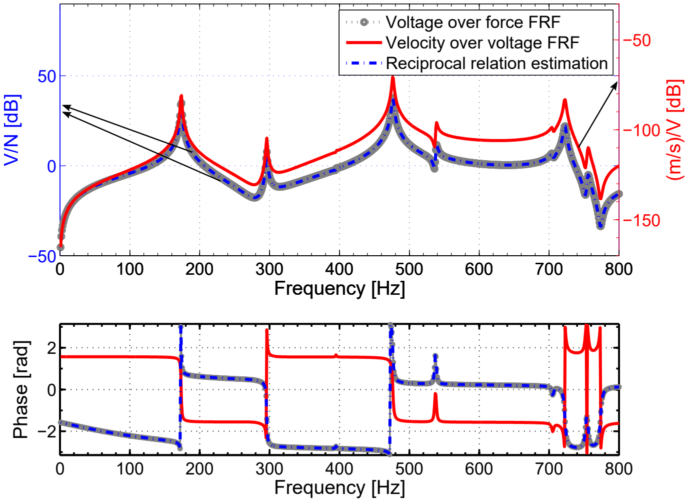

Figure 6.14: Structural reciprocal relation validation between the plate and the integrated transducer

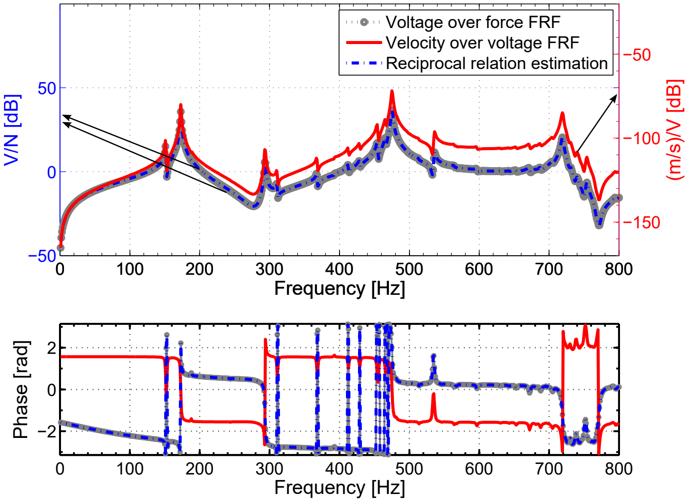

Figure 6.15: Reciprocal relation validation between the plate and the integrated transducer in vibro-acoustic field

The frequency response validations of Equation (6.20) are given in Figures 6.14 and 6.15. The gray curves in the figures are the FRFs of the voltage output of the transducer caused by a force input at location C on the plate. The red curves are the FRFs of the velocity output at location C on the plate subjected to a voltage input on the transducer. The blue dash-lines are the estimated voltage output over force input FRFs by using the Equation (6.20). Thus, the reciprocal relation in Equation (6.20) is well retained on the plate, whenever the acoustic part is included or not. The scaling in Equation (6.20) creates shifts both on the amplitude and phase.

A voltage input to the transducer can generate a sound pressure in the cavity, and a sound source in the cavity can also generate a voltage output from the transducer. Figure 6.16 shows that Equation (6.16) retains between the transducer and the cavity. The voltage output over the volume velocity FRF can be estimated from FRF of voltage input on the transducer over the sound pressure in the cavity by using the piezoelectric reciprocal relation, and vice versa. The importance of Equation (6.16) is to demonstrate the relation between piezoelectric sensing and actuation in a vibro-acoustic field.

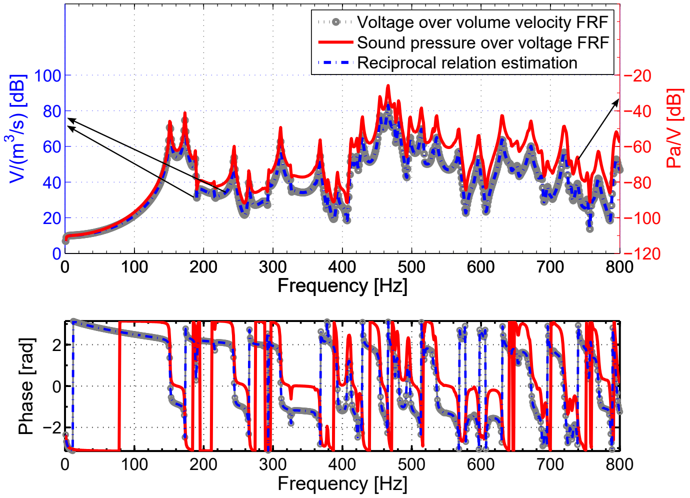

Figure 6.16: Reciprocal relation validation between the cavity and the integrated transducer

6.4.2 Verification in the time domain

Since the ESM model is stable, a real-time simulation is given to demonstrate the piezoelectric reciprocal relation in the time domain. In the piezoelectric excitation case, a damped sin wave signal is used as a voltage input to the transducer. The sound pressure at location B is measured and used to generate the acoustic signal in the time domain. When the transducer functions as a sensor, the damped sin wave signal is used as a volume velocity source at location B. The voltage output from the transducer is transformed in the time domain. The two outputs are shown in Figure 6.17.

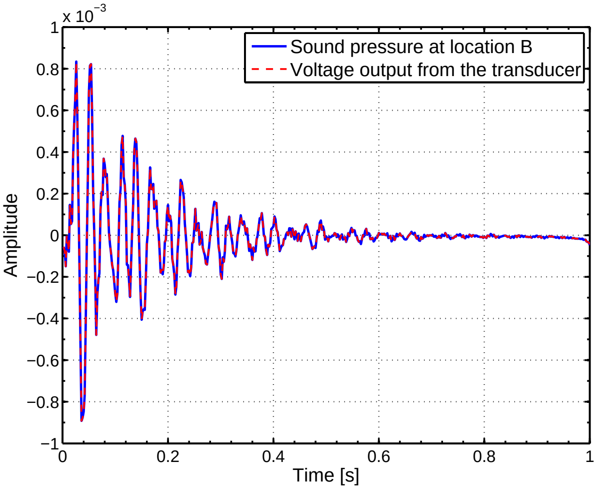

Figure 6.17: Piezoelectric reciprocal relation validation in time domain

We can observe that the two signals agree very well, due to the piezoelectric vibro-acoustic reciprocal relation. In fact, piezoelectric transducers can be used in the application of load identification. It is also possible to develop invisible loudspeakers and microphones by using the piezoelectric transducers. The piezoelectric vibro-acoustic reciprocal relation is important to these applications because it enables the switching between actuation and sensing. Figure 6.18 shows that the acoustic source at location B in the cavity can be identified according to Equation (6.16). The FRF of sound pressure over voltage input between location B and the transducer can be easily obtained, and the voltage output from the transducer due to the excitation of an acoustic source at location B can be easily measured too. Hence, this acoustic source can be quantified. Besides, it is important to mention that the location of the acoustic source is known in this study case.

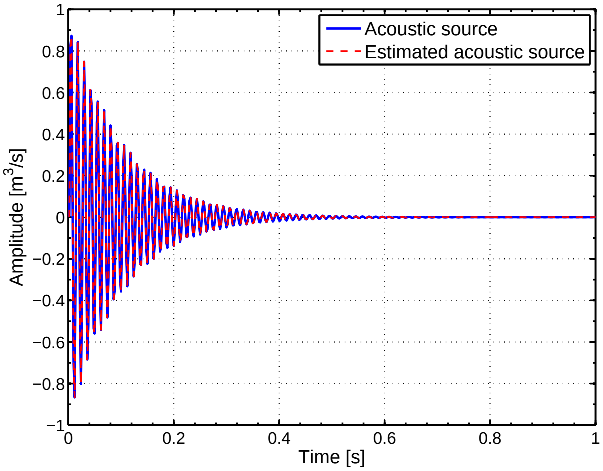

Figure 6.18: Validation of the identified acoustic source by using the piezoelectric vibro-acoustic reciprocal relation

6.5 Concluding remarks

This chapter investigates the dynamic features of piezoelectric transducers in vibro-acoustic field. The vibro-acoustic reciprocity is reviewed and extended to the piezoelectric transducer. A laminated composite plate with an integrated transducer is tested by the KU Leuven soundbox which was given as a demonstration. And the ESM approach is used to generate a stable structural-preserving low-order model of the studied piezoelectric vibro-acoustic system. After the validation of the ESM model by the experimental data, the derived piezoelectric reciprocal relations are numerically validated in the frequency domain. And a real-time simulation demonstrates the piezoelectric reciprocal relation. Meanwhile, an acoustic source identification study by the piezoelectric transducer is also given.

The work in this chapter provides a basic understanding regarding to piezoelectric devices for vibro-acoustic application such as acoustic source qualification. Further researches on the sensitivity characterization of piezoelectric transducers need to be carried out when the transducers are used as actuators/sensors in vibro-acoustics.

Chapter 7

Conclusions and Perspectives

Smart composite structure with integrated MFC transducers is one of the most promising solutions to reduce noise and vibrations of lightweight, flexible structures. The placement and piezoelectric fibrous orientations of MFC transducers on non-homogeneous composite structures are important for ensuring their performance. This dissertation investigated the effective modeling of MFC transducers integrated into composite plates, which allow us to efficient assess the optimal performance of the integrated MFC transducers. This chapter concludes the research of the dissertation and presents future research proposals.

7.1 Summary

In this dissertation, laminate composite plates with spatially distributed rectangular MFC transducers are studied. Spatial distributions, which describe the placement of the transducers are introduced into the generalized Hamilton's principle analysis for characterizing the equivalent loads of MFC transducers. Equivalent forces are proposed as the new method to express the inverse piezoelectric effect of the MFC transducers. Moreover, the corresponding piezoelectric effect is derived through the electrical boundary conditions of the system. The two couplings have the same coupling patterns so that the reversibility of piezoelectricity is ensured. Given that a generalized formula of piezoelectric constitutive equations is adopted in the analysis, both MFC-d31 and MFC-d33 transducers are characterized at the same time.

FEM-based semi-analytical modeling approaches (EFM approach and ESM approach) are proposed, and a rigorous modeling process is presented. The EFM approach allows us to individually model the mechanical and piezoelectric aspects of piezoelectric composite plates because closed-form piezoelectric couplings are used. Based on the EFM approach, the ESM approach, which can efficiently process the different subcomponents of a piezoelectric system is developed. Being that, the size of the original system can be effectively reduced on the substructure level. Besides, the reduced-order model remains the physical parameters and the structure of the system. As a result, the placement and piezoelectric fibrous orientation of an MFC transducer on a composite plate can be efficiently evaluated for maximizing its performance. Furthermore, the ESM approach also preserves the stability of the original system models. That allows for designing advanced controller in noise and vibrations control and realizing real-time simulations. The reliability of the proposed approaches is verified by using cantilever plates with MFC transducers of different sizes and piezoelectric fibrous orientations. Meanwhile, the mechanical influences of the MFC transducers are also evaluated that they are not negligible if the transducers are considerable stiff compared to the host structures.

Laminated composite plates are manufactured, and the MFC-d33 transducers are surface-bonded to the plate through a vacuum-bagging process. Both the impact testing and MFC actuation testing are elaborately carried out. The linearity of the piezoelectric composite plate is verified, and the dynamics of the composite plate is experimentally characterized. Both the EFM and ESM models agree well with the experimental data. The reciprocity between two MFC transducers is verified too. Finally, the piezoelectric reciprocal relation between MFC transducers and host structures that can be used in dynamic application, e.g., load identification is explicitly defined. Two types of study cases are given to demonstrate the potentials of the ESM approach. The piezoelectric energy harvesting one demonstrated that the piezoelectric fibrous orientation of the MFC transducer could be efficiently designed. The piezoelectric shunt damping cases performed a verification on the electrical dynamics modeling, and the placement of the transducers can be effectively optimized. Hence, the ESM approach not only can generate accurate low-order system models but also can be used in the optimal design of piezoelectric systems.

The dynamic property of MFC transducers in vibro-acoustics is also studied with the KU Leuven soundbox. Firstly, the vibro-acoustic reciprocity is reviewed, and the reciprocal relation between piezoelectric and acoustic fields is characterized. Then, the ESM approach is used to simulate the vibro-acoustic problem, and experimental data is used to validate the numerical model. After that, We proved that the ESM approach could also preserve the stability of vibro-acoustic systems. Hence, a stable structure-preserved low-order model can be generated at the end. The piezoelectric reciprocal relations are numerically verified both in the frequency and time domain. Further studies of MFC transducers in a vibro-acoustic field can be performed using the ESM approach.

7.2 Perspectives of the research

Many research directions can be extended to model and design advanced piezoelectric composite structures. The following aspects are considered as the most valuable parts for future work:

1. **Generalized equivalent forces of piezoelectric transducers**

   The characterization of thin piezoelectric transducers in terms of force is an important work for expanding piezoelectric transducers' application. A study on a non-flat shell host structure is attractive to extend the limitations of the derived equivalent forces because the performance of the transducers significantly depends on the host structures. Moreover, the study in this dissertation is only valid for rectangular transducers. Other interesting shapes, for example, circle and triangle are valuable to investigate because they can generate special forces on a host structure but they are not well characterized yet.

2. **Nonlinear properties of MFC transducers together with composite host structures:**

   The nonlinear properties of MFC transducers have not been included in the presented study. Although the studied MFC transducers on the composite plates gave high linear dynamic performance on the aspects of piezoelectric actuation and sensing, the hysteresis may strongly reduce the performance of the MFC transducers. Therefore, the nonlinear effects of the MFC transducers need to be compensated for practical application. In some cases, the host structure may also show nonlinear dynamics. Therefore, the nonlinear characterization of the overall system is necessary to guarantee the performance of the piezoelectric system.

3. **Application of the piezoelectric reciprocal relations:**

   The piezoelectric reciprocal relation between MFC transducers and host structures has been verified and extended into vibro-acoustic fields. In some cases, only the direct or inverse piezoelectric coupling of the transducer, which is integrated into mechanical structures, needs to be characterized in practice. The piezoelectric reciprocal relations can apply to many engineering application such as load identification for the MFC transducers offer large operation bandwidth, high reliability as well as high robustness. In the acoustic domain, piezoelectric transducers can be used in the application of load identification, model-based virtual sensing, etc. It is also possible to develop invisible loudspeakers and microphones with piezoelectric materials.

Chapter 8

Appendix

8.1 Finite difference coefficient

The following tables give the coefficient of finite difference to approximate a derivative to an arbitrary order of accuracy.

Accuracy order	**-4**	**-3**	**-2**	**-1**	**0**	**1**	**2**	**3**	**4**
2				$-1/2$	0	$1/2$			
4			$1/12$	$-2/3$	0	$2/3$	$-1/12$		
6		$-1/60$	$3/20$	$-3/4$	0	$3/4$	$-3/20$	$1/60$	
8	$1/280$	$-4/105$	$1/5$	$-4/5$	0	$4/5$	$-1/5$	$4/105$	$-1/280$

Table 8.1: Central finite difference coefficients

Accuracy order	**0**	**1**	**2**	**3**	**4**	**5**	**6**
1	-1	1					
2	$-3/2$	2	$-1/2$				
3	$-11/6$	3	$-3/2$	$1/3$			
4	$-25/12$	4	-3	$4/3$	$-1/4$		
5	$-137/60$	5	-5	$10/3$	$-5/4$	$1/5$	
6	$-49/20$	6	$-15/2$	$20/3$	$-15/4$	$6/5$	$-1/6$

Table 8.2: Forward finite difference coefficients

Accuracy order	**-6**	**-5**	**-4**	**-3**	**-2**	**-1**	**0**
1						-1	1
2					$1/2$	-2	$3/2$
3				$-1/3$	$3/2$	-3	$11/6$
4			$1/4$	$-4/3$	3	-4	$25/12$
5		$-1/5$	$5/4$	$-10/3$	5	-5	$137/60$
6	$1/6$	$-6/5$	$15/4$	$-20/3$	$15/2$	-6	$49/20$

Table 8.3: Backward finite difference coefficients

8.2 Interpolation function of FOSD finite element method

A shear locking-free FEM formulation from [202] is used to model laminated composite plate. The discretized displacement filed by triangular elements is shown in Fig.8.1, whose elemental interpolation functions of displacement field are given as:

$$N_1 = 1 - \xi - \eta,\ N_2 = \xi,\ N_3 = \eta \tag{8.1}$$

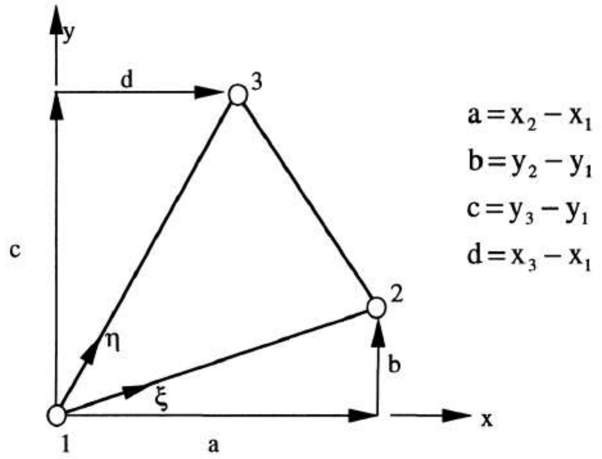

Figure 8.1: Three node element [202]

The interpolation function of membrane strain field can be expressed as:

$$B_m = \frac{1}{detJ}\begin{bmatrix} b-c & 0 & 0 & 0 & 0 & c & 0 & 0 & 0 & 0 & -b & 0 & 0 & 0 & 0 \\ 0 & d-a & 0 & 0 & 0 & 0 & -d & 0 & 0 & 0 & 0 & a & 0 & 0 & 0 \\ d-a & b-c & 0 & 0 & 0 & -d & c & 0 & 0 & 0 & a & -b & 0 & 0 & 0 \\ 0 & 0 & b-c & \frac{detJ}{2} & 0 & 0 & 0 & c & \frac{ac}{2} & \frac{bc}{2} & 0 & 0 & -b & -\frac{bd}{2} & -\frac{bc}{2} \\ 0 & 0 & d-a & 0 & \frac{detJ}{2} & 0 & 0 & -d & -\frac{ad}{2} & -\frac{bd}{2} & 0 & 0 & a & \frac{ad}{2} & \frac{ac}{2} \end{bmatrix} \tag{8.2}$$

The interpolation function of bending strain field are thus:

$$B_b = \frac{1}{detJ}\begin{bmatrix} 0 & 0 & 0 & b-c & 0 & 0 & 0 & 0 & c & 0 & 0 & 0 & 0 & -b & 0 \\ 0 & 0 & 0 & 0 & d-a & 0 & 0 & 0 & 0 & -d & 0 & 0 & 0 & 0 & a \\ 0 & 0 & 0 & d-a & b-c & 0 & 0 & 0 & -d & c & 0 & 0 & 0 & a & -b \\ 0 & 0 & 0 & 0 & 0 & 0 & 0 & 0 & 0 & 0 & 0 & 0 & 0 & 0 & 0 \\ 0 & 0 & 0 & 0 & 0 & 0 & 0 & 0 & 0 & 0 & 0 & 0 & 0 & 0 & 0 \end{bmatrix} \tag{8.3}$$

In addition, the Jacobian matrix and its inverse are determined as:

$$J = \begin{bmatrix} \frac{\partial x}{\partial \xi} & \frac{\partial y}{\partial \xi} \\ \frac{\partial x}{\partial \eta} & \frac{\partial y}{\partial \eta} \end{bmatrix} = \begin{bmatrix} a & b \\ d & c \end{bmatrix} \tag{8.4}$$

$$J^{-1} = \begin{bmatrix} \frac{\partial \xi}{\partial x} & \frac{\partial \xi}{\partial x} \\ \frac{\partial \eta}{\partial y} & \frac{\partial \eta}{\partial y} \end{bmatrix} = \frac{1}{detJ} \begin{bmatrix} c & -b \\ -d & a \end{bmatrix} \text{with } detJ = ac - bd \tag{8.5}$$

8.3 Static modeling robustness check of EFM approach

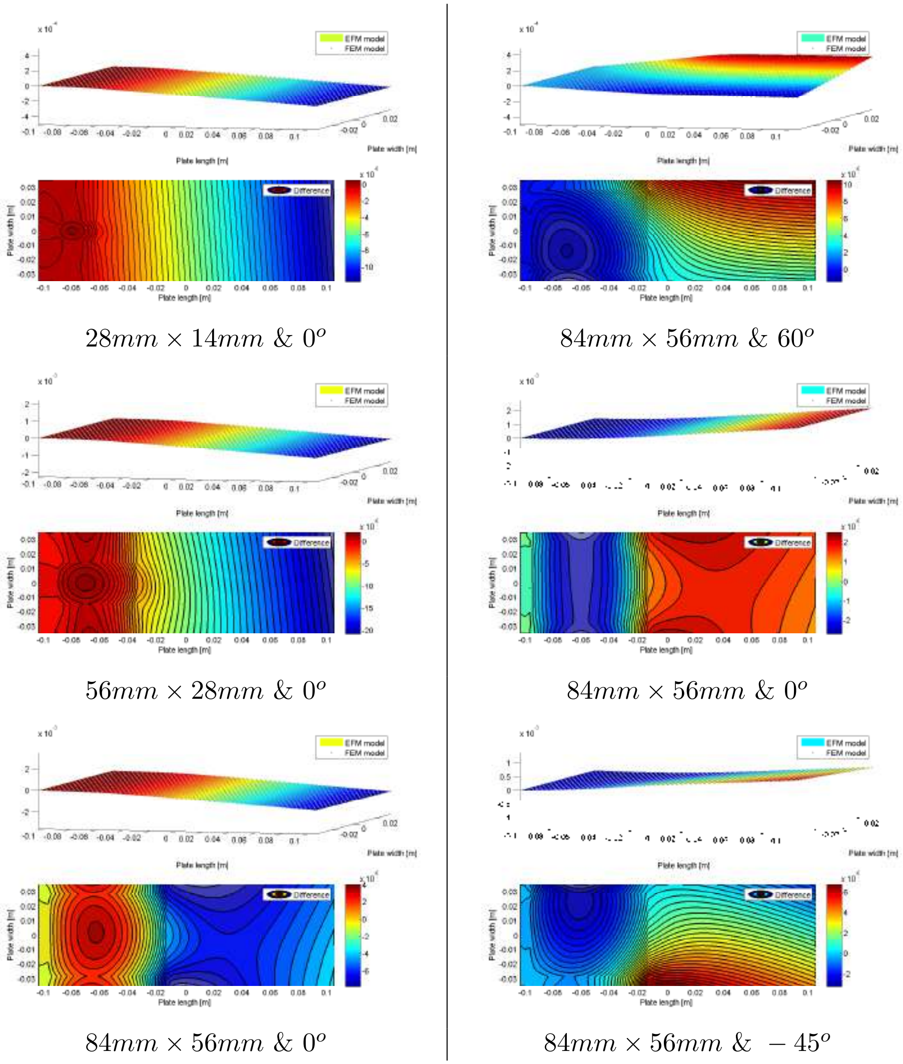

$28mm \times 14mm$ & 0^o

$84mm \times 56mm$ & 60^o

$56mm \times 28mm$ & 0^o

$84mm \times 56mm$ & 0^o

$84mm \times 56mm$ & 0^o

$84mm \times 56mm$ & -45^o

Figure 8.2: Static modeling robustness check for the MFC-d31 transducers of different size (Left) and for the MFC-d33 transducers of different piezoelectric fibrous orientations (Right)

The same cantilever plate in figure 4.6 is used in the static robustness verifications. On the one hand, a virtual operational voltage of $400V$ is applied to the MFC-d31 transducers, which are used to check the modeling sensitivity regarding the sizes of the integrated MFC transducers. One the other hand, the same operational voltage is applied to the MFC-d33 transducers which are used to check the modeling sensitivity regarding the piezoelectric fibrous orientation. We can observe that the equivalent forces can well predict the bending motion due to the inverse piezoelectric effect of the integrated MFC transducers on the plate.

8.4 Experimental equipment

The equipment used in the dynamic response measurement of the composite plate is listed below:

1. **Data acquisition software:** The Test.Lab (14A) from Siemens PLM Software is used to perform the data acquisition and experimental modal analysis. Both the impact testing and spectral testing can be performed. The geometry of the test subject should be generated in the geometry module according to the measured locations. Then, the channel ID, measured quantity, sensitivity of each input channel should be set in the channel setup module. It is worthwhile to mention that differential channels are used to measure the output from the MFC transducer for it is more immune to noise [203].

   In an impact testing, the scope setting permits to define the measured bandwidth and resolution. The trigger setting should be performed for the force signal from the impact hammer. A force-exponential and an exponential windows can be applied to the channels of impact force and measurements, respectively. However, in a spectral testing, hanning window should be applied to the all the channels. A signal can be generated from Test.lab in the scope module that can be used to drive the excitation device. The PolyMax modal analysis in Test.Lab can accurately estimate the modal parameter of the tested subject in post processing [188].

2. **Data acquisition hardware:** A SCADAS mobile III is used as the data acquisition hardware. It is equipped with VB8-II input modulus that permits either the differential or signal-ended channel setting and they also support voltage, ICP, DC and AC input signals. In addition, its 150dB dynamic range allows for avoiding rang setting in the measurements.

3. **Voltage amplifier for MFC transducers:** A PiezoDrive T250 voltage amplifier is used to drive the MFC transducers. It has 6 input-output channels. Each input channel has an admissible range of $\pm 10V$. The output gain of each output channel is 25. The maximum frequency periodic signal is plotted versus the peak-to-peak voltage in Fig.8.3, the linearity of the amplifier is ensured in a frequency bandwidth of $8.3KHz$ for a load capacitance less that $3nF$ [204].

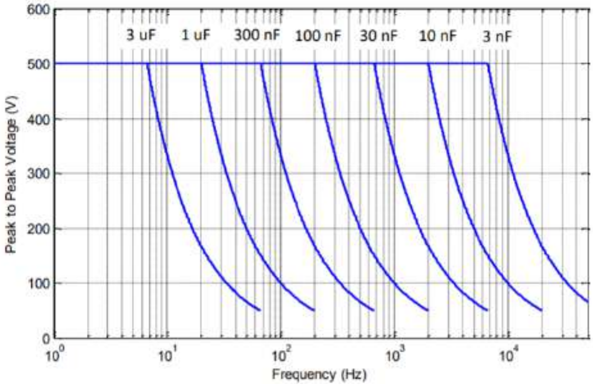

Figure 8.3: The power bandwidth versus voltage and load capacitance of the voltage amplifier [204]

4. **Impact hammer:** A PCB-086E80 hammer is used in the impact testing. As the composite plate is lightweight and free-free boundary condition is applied to the tested subject. The miniature hammer allows for avoiding large rigid body motions of the plate which can severely influence the measurements.

5. **Laser vibrometer:** A Polytec OFV 055 Laser vibrometer is used to realize the non-contact measurement. This is essential for the modal test of lightweight structures. Different velocity ranges setting provide a flexibility to optimize the normal velocity measurement on the tested subject.

8.5 Second-order forward-backward finite difference approximation

An equivalent forces is also derived by using the second-order forward and backward finite difference approximations. The in-plane inverse piezoelectric couplings with respect to f_{xx} and f_{yy} remain unchanged compared to the first-order approximations because they are independent from the finite different approximations. The coupling with respect to f_{zz} can be written as follows:

$$\begin{aligned} f_{zz} = &- \frac{\bar{e}_{31}^{*} z_p}{\Delta x}\frac{V}{t_p}\int_{\Gamma_s}[-\frac{3}{2}\delta(x+\frac{a}{2}) + 2\delta(x+\frac{a}{2}-\Delta x) - \frac{1}{2}\delta(x+\frac{a}{2}-2\Delta x) \\ &- \frac{1}{2}\delta(x-\frac{a}{2}+2\Delta x) + 2\delta(x-\frac{a}{2}+\Delta x) - \frac{3}{2}\delta(x-\frac{a}{2})] \times [H(y+\frac{b}{2}) - H(y-\frac{b}{2})]d\Gamma_s \\ &- \frac{\bar{e}_{32}^{*} z_p}{\Delta y}\frac{V}{t_p}\int_{\Gamma_s}[-\frac{3}{2}\delta(y-\frac{b}{2}) + 2\delta(y+\frac{b}{2}-\Delta y) - \frac{1}{2}\delta(y+\frac{b}{2}-2\Delta y) \\ &- \frac{1}{2}\delta(y+\frac{b}{2}+2\Delta y) + 2\delta(y+\frac{b}{2}+\Delta y)) - \frac{3}{2}\delta(y-\frac{b}{2})] \times [H(x+\frac{a}{2}) - H(x-\frac{a}{2})]d\Gamma_s \\ &- 2\bar{e}_{36}^{*} z_p \frac{V}{t_p}\int_{\Gamma_s}[\delta(x+\frac{a}{2}) - \delta(x-\frac{a}{2})] \times [\delta(y+\frac{b}{2}) - \delta(y-\frac{b}{2})]d\Gamma_s \end{aligned} \tag{8.6}$$

We can decompose (8.6) into three parts according to the coupling directions of x, y and xy. Then, the accuracy of the electromechanical coupling can be analyzed by the total bending effort balance in x and y directions. As we discretized the transducer like $a = 4\Delta x$ and $b = 2\Delta y$, a correction factor $\alpha = 0.98 \approx 1$ has been obtained in x direction and $\alpha = 1$ in y direction. Therefore, a second-order finite approximation can preserve the total bending effort balance. The direct piezoelectric coupling can be obtained from this inverse piezoelectric coupling.

The frequency response validations are given in the following figures. The predicted FRFs agree well with the experimental measurements for both the inverse and direct piezoelectric effects:

1. Inverse piezoelectric coupling validation:

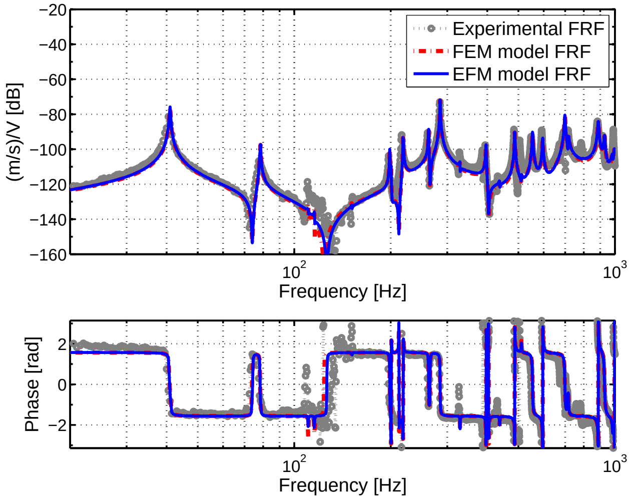

Figure 8.4: Second-order EFM model inverse piezoelectric frequency response validation between $p00$ and $p74$

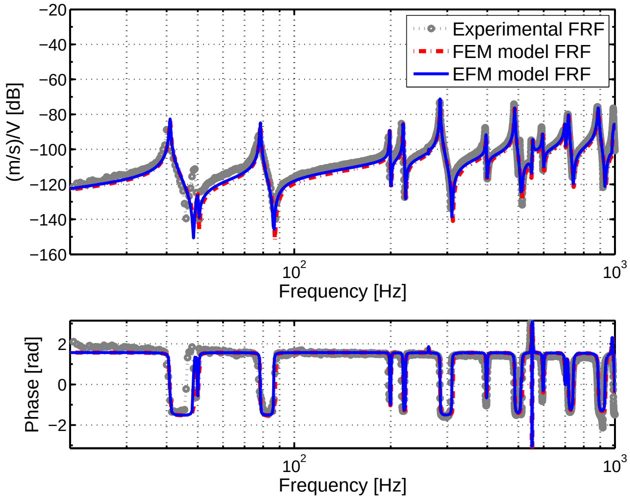

Figure 8.5: Second-order EFM model inverse piezoelectric frequency response validation between $p00$ and $p00$

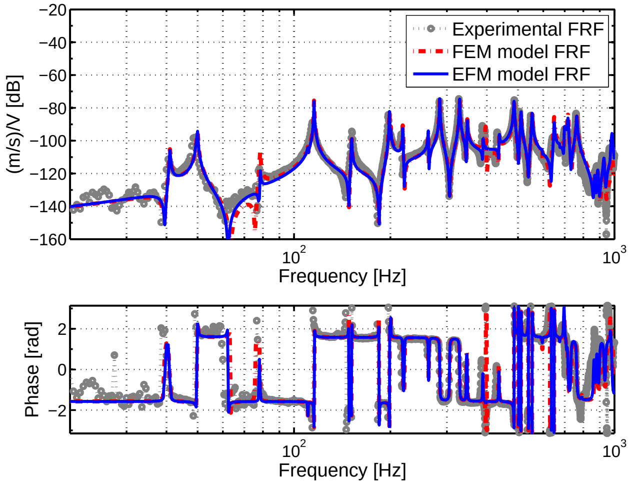

Figure 8.6: Second-order EFM model inverse piezoelectric frequency response validation between $p26$ and $p22$

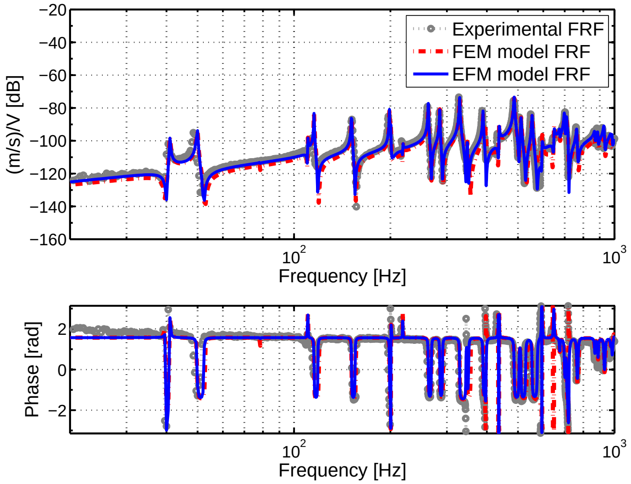

Figure 8.7: Second-order EFM model inverse piezoelectric frequency response validation between $p26$ and $p26$

2. Direct piezoelectric coupling validation:

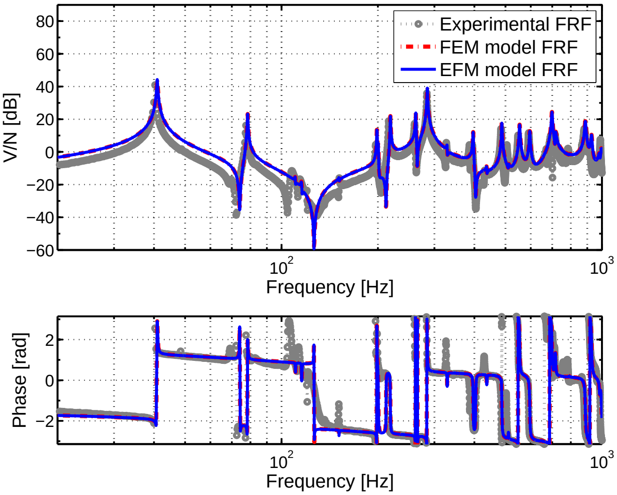

Figure 8.8: Second-order EFM model direct piezoelectric frequency response validation between $p00$ and $p74$

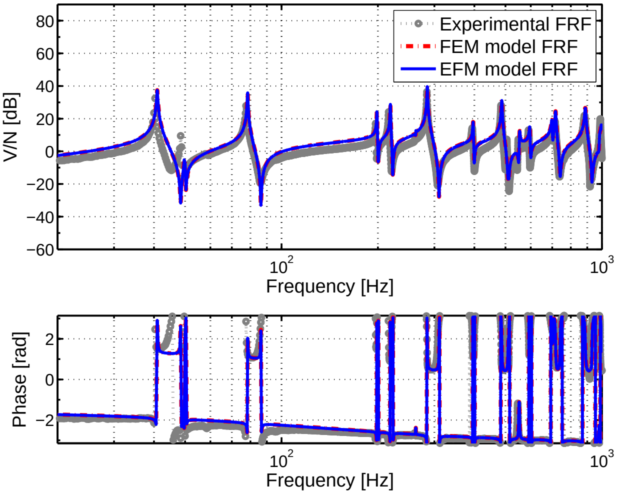

Figure 8.9: Second-order EFM model direct piezoelectric frequency response validation between $p00$ and $p00$

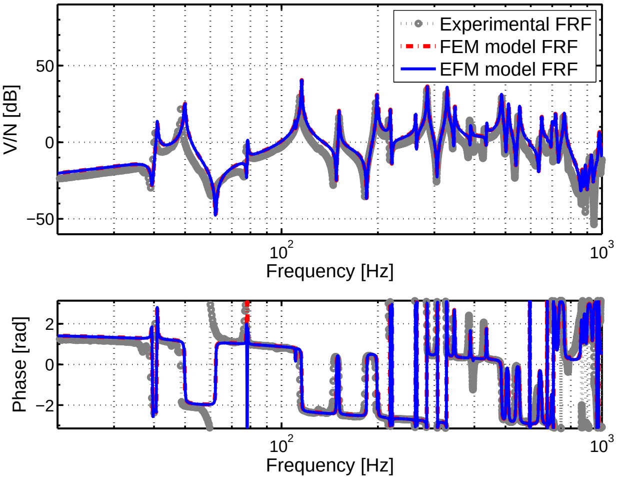

Figure 8.10: Second-order EFM model direct piezoelectric frequency response validation between $p26$ and $p22$

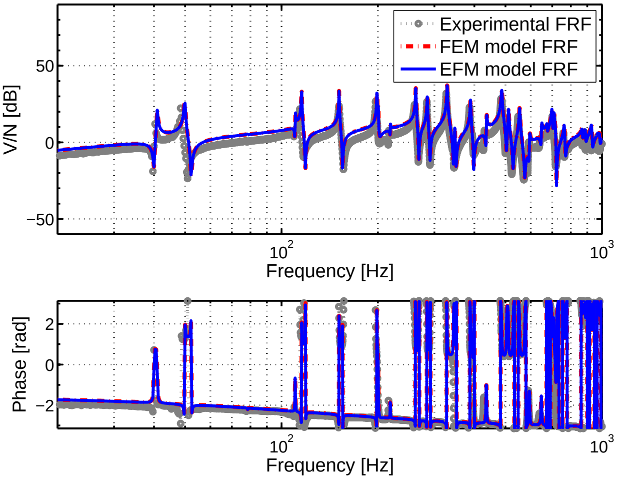

Figure 8.11: Second-order EFM model direct piezoelectric frequency response validation between $p26$ and $p26$

Bibliography

[1] Rajan G. and Gangadhara P. *Structural health monitoring of composite structures using fiber optic method.* CRC Press, 2016.

[2] Vivolo M., Pluymers B., Vandepitte D., and W. Desmet. Vibro-acoustic study of lightweight components based on a new experimental setup. *18th International Congress on Sound and Vibration*, 2011.

[3] Jonckheere S., Vivolo M., Pluymers B., Vandepitte D., and Desmet W. Vibro-acoustic characterisation of lightweight structures: a numerical-experimental approach. *SAE Technical Paper*, page pp15, 2012.

[4] Hurlebaus S. and Gaul L. Smart structure dynamics. *Mechanical Systems and Signal Processing*, 20:255–281, 2006.

[5] Ferreira A.D., P. Novoa, and Marques A.T. Multifunctional material systems: A state-of-the-art review. *Composite Structures*, 151:3–35, 2016.

[6] Henrioulle K. *Distributed actuators and sensors for active noise control.* KU Leuven PhD thesis, 2001.

[7] Bowen C.R., Giddings P.F., Salo A.I.T., and Kim H.A. *Modeling and Characterization of Piezoelectrically Actuated Bistable Composites*, volume 58. 2011.

[8] Ren L.B. A theoretical study on shape control of arbitrary lay-up laminates using piezoelectric actautors. *Journal of Composite Structures*, 83:110–118, 2007.

[9] Aoki Y., Gardonio P., and Elliott S.J. Modelling of a piezoceramic patch actuator for velocity feedback control. *Smart Materials and Structures*, 17:13pp, 2008.

[10] Novakova K., Mokry P., and Vaclavik J. Application of piezoelectric macro-fiber-composite actauators to the suppression of noise transmission

through curved glass plates. *IEEE Transactions on Ultrasonics, Ferroelectrics, and Fr 2004 equency Control*, 59:2004–2014, 2012.

[11] Gao L., Lu Q., Fei F., Liu L., Liu Y., and Leng J. Active vibration control based on piezoelectric smart composite. *Smart Materials And Structures*, 22:1–12, 2013.

[12] Wang X. *Shape control of a deformable spatial mirror with piezoelectric actuators PhD thesis.* Département Mathématique Informatique Automatique (DMIA-ISAE).

[13] Y.X. Li, S.Q. Zhang, R. Schmidt, and X.S. Qin. Homogenization for macro-fiber composites using reissner-mindlin plate theory. *Journal of Intelligent Material Systems and Structures*, 27:2477–2488, 2016.

[14] Lin X.J., Zhou K.C., Zhang X.Y., and Zhang D. Development, modeling and application of piezoelectric fiber composites. *Transactions of Nonferrous Metals Society of China*, 23:98–107, 2013.

[15] Smart Material Corp. Macro fiber composite-mfc. `www.smart-material.com`. Accessed on 2017-07-12.

[16] Lam K.Y., Peng X.Q., Liu G.R., and Reddy J.N. A finite element model for piezoelectric composite laminates. *Smart Materials and Structures*, 6:583–591, 1997.

[17] Kioua H. and Mirza S. Piezoelectric induced bending and twisting of laminated composite shallow shells. *Smart Materials and Structures*, 9:476–484, 2000.

[18] Qu Z.Q. An efficient modelling method for laminated composite plates with piezoelectric sensors and actuators. *Smart Materials and Structures*, 10:807–818, 2001.

[19] Liu G.R., Dai K.Y., and Lim K.M. Static and vibration control of composite laminates integrated with piezoelectric snesors and actuators using the radial point interpolation method. *Smart Materials and Structures*, 13:1438–1447, 2004.

[20] Biscani F. *Modeling-based design of anisotropic piezocomposite transducers and multi-domain analysis of smart structures.*

[21] Phung-Van P., De Lorenzis L., Thai C.H., Abdel-Wanhad M., and Nguyen-Xuan H. Analysis of laminated composite plates integrated with piezoelectric sensors and actuators using higher-order shear deformation theory and isogeometric finite elements. *Computational Materials Science*, 96(0927-0256), 2014.

[22] Pandey A. and Arockiarajan A. Actuation performance of macro fiber composite (mfc):modeling and experimental studies. *Sensors and actuators*, 248:114–129, 2016.

[23] Zhang S.Q., Li Y.X., and Schmidt R. Modeling and simulation of macro-fiber composite layered smart structures. *Journal of Composite Structures*, 126:89–100, 2015.

[24] Bai Z.J. and Su Y.F. Dimension reduction of large-scale second-order dynamical systems via a second-order arnoldi method. *Journal of Scientific Computing*, 26:1692–1709, 2005.

[25] Gugercin S. and Antoulas A.C. A survey of model reduction by balanced truncation and some new results. *International Journal of Control*, 77:748–766, 2004.

[26] Gawronski W.K. *Advanced structural dynamics and active control of structures.* Spring, 1998.

[27] Rao Kannan Natesan A.K., Seetharama Bhat M., and Ganguli R. Experimental demonstration of h_∞ control based on active vibration suppression in composite fin-tip of aircraft using optimal placed piezoelectric patch actuators. *Journal of intelligent material systems and structures*, 19:651–669, 2008.

[28] Zhang S.Q., Wang Z.X., Qin X.S., Zhao G.Z., and Schmidt R. Development by pressure of polar electricity in hemihedral crystals with inclined faces. *Bulletin De La Societe De France*, 9:90, 1880.

[29] IEEE Std. *IEEE Standard on Piezoelectricity.* IEEE/ANSI Std., 1988.

[30] Vives A. *Piezoelectric transducers and applications.* Spring, 2008.

[31] Jain A., Subba Rao S., and Kumar J. Pvdf-pzt composite films for strain sensing applications. *ISSS National Conference on MEMS, Smart Materials, Structures and Systems, India*, 2013.

[32] Gusarov B. *PVDF piezoelectric polymers : characterization and application to thermal energy harvesting.* 2015.

[33] Ramadan K.S., Sameoto D., and Evoy S. A review of piezoelectric polymers as functional materials for electromechanical transducers. *Smart Materials and Structures*, 23:1–24, 2006.

[34] Lines M. and Glass E.M. *Principles and applications of ferroelectrics and related materials.* Oxford Universtiy Press, 1977.

[35] Minase J., Lu T.F., Cazzolato B., and Grainger S. A review, supported by experimental results, of voltage, charge and capacitor insertion method for driving piezoelectric actuators. *Precision Engineering*, 34:692–700, 2010.

[36] Gevorgian S., Tagantsev A.K., and Vorobiev A. *Tuneable film bulk acoustic wave resonators.* Spring, 2013.

[37] Wikipedia. Hooke's law. `https://en.wikipedia.org/wiki/Hooke%27s_law`. Accessed on 2017-07-12.

[38] Ikeda T. *Fundamentals of piezoelectricity.* Soringer, 1990.

[39] Wikipedia. Vigot notation. `https://en.wikipedia.org/wiki/Voigt_notation`. Accessed on 2017-07-12.

[40] Elhajjar R., La Saponara V., and Muliana A. *Smart Composites: Mechanics and Design.* CRC Press, 2014.

[41] Williams R.B., Park G., Inman D.J., and Wikie W.K. An overview of composite actuators with piezoelectric fibers. *Proceeding of SPIE-The international society for optical engineering*, 2002.

[42] Wilkie W.K., Bryant R.G., High J.W., Fox R.L., and Hellbaum R.F. Low-cost piezocomposite actuators for structural control applications. *Proceedings of SPIE, Smart Structures and Materials 2000: Industrial and Commercial Applications of Smart Structures Technologies. Newport Beach*, pages 323–324, 2000.

[43] Trindade M.A. and Benjeddou A. Finite element homogenization technique for the characterization of d_{15} shear piezoelectric macro-fiber composites. *Smart Materials and Structures*, 20:17pp, 2011.

[44] Nielsen B.B., Nielsen M.S., and Santos I.F. A layered shell containing patches of piezoelectric fibers and interdigitated electrodes: Finite element modeling and experiemental validation. *Intelligent Material Systems and Structures*, 28:78–96, 2017.

[45] Raja S. and T. Ikeda. Concept and electro-elastic modeling of shear actuated fiber composite using micro-mechanics approach. *Journal of Intelligent Material Systems and Structures*, 19:1173–1183, 2008.

[46] Spanner K. and B. Koc. Piezoelectric motors, an overview. *Actuators*, 6:5010006, 2016.

[47] Sharapov V. *Piezoecramic Sensors.* Springer, 2011.

[48] Bilgen O., Kochersberger K.B., and Inman D.J. macro-fiber composite actuators for a swept wing unmanned aircraft. *The aeronautical journal*, 113:385–395, 2009.

[49] Pankonien A.M. *Smart material wing morphing for unmanned aerial vehicles.*

[50] Farrar C.R. and Claytor T.N. High-frequency response function for composite plate monitoring with ultrasonic validation. *AIAA Journal*, 43:2431–2437, 2005.

[51] Salamone S., Bartoli I., Di Leo P., Di Scalea F.L., Ajovalasit A., D'acquisto L., Rhymer J., and Kim H. High-velocity impact location on aircraft panels using macro-fiber composite piezoelectric rosettes. *Journal of Intelligent Materials Systems and Structures*, 21:887–896, 2010.

[52] Balachandran B., Sampath B., and Park J. Active control of interior noise in a three dimensional enclosure. *Smart Materials and Structures*, 5:89–97, 1996.

[53] Ahmadian M., Jeric M., and Inman D. An experimental evaluation of smart damping materials for reducing structural noise and vibrations. *Journal of Vibration and Acoustics*, 123:533–536, 2001.

[54] Chen Y. and Viresh W. Development and verification of real-time controllers for f/a-18 vertical fin buffet load alleviation. *Proceeding of SPIE, Smart Structures and Materials 2006, Smart Structures and Integrated Systems 2006*, 2006.

[55] Zhang J., He L., Wang E., and Gao R. Active vibration control of flexible structures using piezoelectric materials. *International Conference on Advanced Computer Control*, pages 540–545, 2008.

[56] Zhang X., Desmet W., Faria C., Dong Z.Z., and Sebek M. Decentralized/distributed output feedback h_∞ controller desgin for vibration reduction of smart structures. *ISMA conference on Noise and Vibration Engineering*, 2016.

[57] Zhang X., Dong Z.Z., Faria C., Movric K., and Desmet W. Observer-based distributed controller design for a cantilever beam. *Proceedings of the 34th IMAC, A Conference and Exposition on Structural Dynamics 2016*, 5:7–17, 2016.

[58] Faria C., Dong Z.Z., and Zhang X. On the decentralized observe/controller strategy for disturbance rejection. *SPIE Smart structure and Materials + Nodestructive Evaluation and Health Monitoring*, 2017.

[59] Rodriguez-Fortun J.M., Orus j., Alfonso J., and Castellanos J.A. Nonlinear active vibration control using piezoelectric actuators. *2010 American Control Conference*, pages 744–794, 2010.

[60] Zhang Y., Lou Y., and Zhang X. Nonlinear vibration control of a piezoelectric beam with a fuzzy logic controller. *Proceedings from the 17th International Symposium on Applied Electromagnetics and Mechanics (ISEM 2015)*, 52:251–260, 2015.

[61] Hagood N.W. and von Flotow A. Damping of structural vibrations with piezoelectric materials and passive electrical networks. *Journal of Sound and Vibration*, 146:243–268, 1991.

[62] Adachi K., Park G., and Inman D.J. Passive damping augmentation using macro-fiber composite actuators. *Proceedings of IMECE2002, ASME International Mechanical Engineering Congress and Exposition, New Orleans, LA*, pages 71–78, 2002.

[63] Belloli A., Niederberger D., Pietrzko S., Morari M., and Ermanni A. Structural vibration contril via $r - l$ shunted active fiber composite. *Journal of Intelligent Material Systems and Structures*, 18:275–287, 2007.

[64] Shevtsov S.N., Samochenko I.G., Axenov V.N., and Snegina N.G. Transient analysis of a piezoelectric shunt damping for composite beam vibration suppression. 3^{rd} *International Conference on Experiments/Process/System modeling/Simulation and Optimization*, 2009.

[65] Neubauer M. and Wallaschek J. Vibration damping with piezoceramics shunted to negative capacitance network. *2009 IEEE/ASME International Conference on Advanced Intelligent Mechatronics, Singapore*, 2009.

[66] Kozlowski M.V., Cole D.G., and Clark R.L. A comprehensive study of the rl series resonant shunted piezoelectric: A feedback controls perspective. *Journal of Vibration and Acoustics*, 133, 2011.

[67] Hogsberg J. and Krenk S. Piezoelectric rl shunt damping of flexible structures. 7^{th} *ECCOMAS Thematic Conference on Smart Structures and Materials*, 2015.

[68] Hogsberg J. and Krenk S. Calibration of piezoelectric rl shunts with explicit residual mode correction. *Journal of Sound and Vibration*, 386:65–81, 2016.

[69] Hogsberg J. and Krenk S. Balanced calibration of resonant shunt circuits for piezoelectric vibration control. *Journal of Intelligent Material Systems and Structures*, 23:1937–1948, 2012.

[70] Marneffe B. and Preumont A. Vibration damping with negative capacitance shunts: theory and experiment. *Smart Materials and Structures*, 17, 2008.

[71] Ji H., Qiu J., Cheng J., and D.J. Inman. Application of a negative capacitance circuit in synchronized switch damping techniques for vibration suppression. *Journal of Vibration and Acoustics*, 133, 2011.

[72] Ji H., Qiu J., Cheng J., and Inman D.J. Increasing the performance of negative capacitance shunts by enlarging the output voltage to the requirements of piezoelectric transducers. *Journal of Intelligent Material Systems and Structures*, 28:1379–1390, 2017.

[73] Novakova N. and Mokry P. Numerical simulation of mechanical behavior of a macro fiber composite piezoelectric actuator shunted by a negative capacitor. 10^{th} *International Workshop on Electronics, Control, Measurement and Signals*, 2011.

[74] Preumont A. Vibration control of active structures, an introduction 2nd edition. *Kluwer*, 2002.

[75] Zhao G., Alujevic N., Depraetere B., and Sas P. Dynamic analysis and h_2 optimisation of a piezo-based tuned vibration absorber. *Journal of Intelligent Material Systems and Structures*, 26:1995–2010, 2015.

[76] Zhao X., Zhang B., and Li Y. Vibration and acoustic radiation of an orthotropic composite cylindrical shell in a hygroscopic environment. *Journal of Vibraton and Control*, 23:673–692, 2015.

[77] Deu J.F., Larbi W., Ohayon R., and Sampaio R. Piezoelectric shunt vibration damping of structural-acoustic systems: Finite element formulation and reduced-order model. *Journal of Vibration and Acoustics*, 136:8pp, 2014.

[78] Roundy S. and Wright P.K. A piezoelectric vibration based generator for wireless electronics. *Smart Materials and Structures*, 13:11–31, 2004.

[79] Priya S., Song H.-C., Zhou Y., Varghese R., Chopra A., Kim S.-G., Kanno I., Wu L., Ha D.S., Ryu J., and Polcawich R.G. A review on piezoelectric energy harvesting: material, methods and circuits. *Energy harvesting and Systems*, 4:3–39, 2017.

[80] Aridogan U., Basdogan I., and Erturk A. Analytical modeling and experimental validation of a structurally integrated piezoelectric energy harverster on a thin plate. *Smart Materials and Structures*, 23:13pp, 2014.

[81] Yang Y.W., Tang L.H., and Li H.Y. Vibration energy harvesting using macro-fiber composites. *Smart Materials and Structures*, 18:8pp, 2009.

[82] Yang Y., Wang S., Stein P., Xu B., and Yang T. Vibration-based energy harvesting with a clamped piezoelectric circular diaphragm: analysis and identification of optimal structural parameters. *Smart Materials and Structures*, 26:17pp, 2017.

[83] Hajati A. and Kim S.G. Ultra-wide bandwidth piezoelectric energy harvesting. *Applied Physics Letter*, 99:083105, 2011.

[84] Renaud M., Karakaya K., Sterken T., Fiorini P., Van Hoof C., and Puers R. Fabrication, modeling and characterization of mems piezoelectric vibration harvesters. *Sensors and Actuators*, 145-146:380–386, 2008.

[85] Jo S.E., Kim M.S., and Kim Y.J. A resoance frequency switching scheme of a cantilever based on polyvinylidene fluoride for vibration energy harvesting. *Smart Materials and Structures*, 21:8pp, 2012.

[86] Sharpes N., Abdelkefi A., and Priya S. Two-dimensional concentrated-stress low-frequency piezoelectric vibration energy harvesters. *Applied Physics Letter*, 107:093901, 2015.

[87] Xu R. *The design of low-frequency, Low-G piezoelectirc micro energy harvesters.* PhD dissertation in Massachusetts Institute of Technology, 2012.

[88] Saggini S., Giro S., Ongaro F., and Mattavelli P. Implementation of reactive and resistive load matching for optimal energy harvesting from piezoelectric generators. *Paper presented at the IEEE Workshop on Control and Modeling for Power Electronics (COMPEL)*, pages 1–6, 2010.

[89] Fan K., Chang J., Pedryycz W., Liu Z., and Zhu Y. A nonlinear piezoelectric energy harvester for various mechanical motions. *Applied Physics Letter*, 106:223902, 2015.

[90] Ando B., Baglio S., Trigona C., Dumas N., Latorre L., and Nouet P. Nonlinear mechanism in mems devices for energy harvesting applications. *Journal of Micromechanics and Microengineering*, 20:125020, 2010.

[91] Barton D.A., Burrow S.G., and Clare L.R. Energy harvesting from vibrations with a nonlinear oscillator. *Journal of Vibration and Acoustics*, 132:021009, 2010.

[92] Erturk A. and Inman D. Broadband piezoelectric power generation on high-energy orbits of the bistable duffing oscillator with electromechanical coupling. *Journal of Sound and Vibration*, 330:2339–2353, 2010.

[93] Vakakis A.F. Including passive nonlinear energy sinks in vibrationg systems. *Journal of Vibration and Acoustics*, 123:324–332, 2001.

[94] Bassani G., Filippeschi A., and Ruffaldi E. Human motion energy harvesting using a piezoelectric mfc patch. *IEEE Conference: Engineering in Medicine and Biology Society*, page 4pp, 2015.

[95] Eziwarman G.L. and I.M. Howard. Experimental power harvesting from a pipe using a macro-fiber composite. *Proceeding of the 2011 2nd International Congress on Computer Applicaitons and Computational Science*, 144:443–449, 2011.

[96] Liu Y., Shan J., Gabbert U., and Qi N. Hysteresis and creep modeling and compensation for a piezoelectric actuator using a fractional-order maxwell resistive capacitor approach. *Smart Materials and Structures*, 22:12pp, 2013.

[97] Mayergoyz I., Bertotti G., and Vorobiev A. *The Science of Hysteresis.* Elsevier, 2005.

[98] Jung H. and Gweon D.-G. Creep characteristics of piezoelectric actuators. *American Institute of Physics*, 71:1896–1990, 2000.

[99] An D., Li H., Xu Y., and Zhang L. Compensation of hysteresis on piezoelectric actuators based on tripartite pi model. *Micromachines*, 9:pp22, 2018.

[100] Shindo Y., Narita F., Sato K., and Takeda T. Nonlinear electromechanical coupling fields and localized polarization switching of piezoelectric macrofiber composites. *Journal of Mechanics of Materials and Structures*, 6:1496–1483, 2011.

[101] Xue X., Chen L., Wu X., and Sun Q. Study on electric-emchanical hysteretic model of macro-fiber composite actuator. *Journal of Intelligent Material Systems and Structures*, 25:1496–1483, 2013.

[102] Xue Z., Li L., Ichchou M.N., and Li C. Hysteresis and the nonlinear equivalent piezoelectric coefficient of mfcs for actuation. *Chinese Journal of Aeronautics*, 30:88–98, 2017.

[103] Zhu W. and Rui X. Hysteresis modeling and displacement control of piezoelectric actuators with the frequency-dependent behavior using a generalized bouc–wen model. *Precis Engineering*, 43:299–307, 2016.

[104] Jiles D.C., Atherton D.L., Wu H., and Zhou H. Theory of ferromagnetic hysteresis. *Journal of Magnetism and Magnetic Materials*, 61:48–60, 1986.

[105] Liu Y., Lui H., Wu H., and Zhou H. Modelling and compensation of hysteresis in piezoelectric actuators based on maxwell approach. *Electrimics Letters*, 52:188–190, 2015.

[106] Xie Y., Fu J.L., and Chen B.Y. Parameter identification of hysteresis nonlinear dynamic model for piezoelectric positioning system based on the improved particle swarm optimization. *Mechanical Engineering*, 9:1–12, 2017.

[107] Xu Q.S., Li Y.M., and Xu Y. Dahl model-based hysteresis compensation and precise positioning control of an xy parallel micromanipulator with piezoelectric actuation. *Journal of Dynamic Systems ASME*, 132:pp12, 2010.

[108] Lin C.J. and Lin P.T. Tracking control of a biaxial piezoactuated positioning stage using generalized duhem model. *Computers & Mathematics with Applications*, 64:766–787, 2012.

[109] Janocha H. and Kuhnen K. Adaptive compensation of hysteresis and creep non-linearities in solid-state actuators. *Journal of Intelligent Material Systems and Structures*, 21:1437–1446, 2000.

[110] Kuhnen K. Modelling, identification, and compensation of complex hysteretic and log(t)-type creep nonlinearities. *Control and Intelligent Systems*, 33:134–147, 2005.

[111] Mokaberi B. and Requicha A.G. Compensation of scanner creep and hysteresis for afm nanomanipulation. *IEEE Transactions on Automation Science and Engineering*, 5:197–206, 2008.

[112] Kugel D. and Cross L.E. Behavior of soft piezoelectric ceramics under high sinusoidal electric fields. *Journal of Applied Physics*, 84:2815–2830, 1998.

[113] Williams R.B. *Nonlinear mechanical and actuation characterization of piezoceramic fiber composites.* 2004.

[114] Benjeddou A. Field-depedent nonlinear piezoelectricity: a focused review. *International Journal of Smart and Nano Materials*, 9:68–84, 2018.

[115] Crawley E.F. and Lazarus K.B. , induced strain actuator of isotropic and anisotropic plates. *AIAA Journal*, 29:944–951, 1991.

[116] Parashar S.K., von Wagner U., and P. Hagedorn. Finite element modeling of nonlinear vibration behavior of piezo-integrated structures. *Computers and Structures*, 119:37–47, 2013.

[117] Yaghmaie R. and Ghosh S. Computational modeling of finite deformation piezoelectric material behavior coupling transient electrical and mechanical fields. *Journal of Computational Physics*, 373:148–170, 2018.

[118] Silva T., Celemntino M., De Marqui Jr. C., and Erturk A. An experimentally validated piezoelectric nonlinear energy sink for wideband vibration attenuation. *Journal of Sound and Vibration*, page pp20, 2018.

[119] Silva T., Celemntino M., Erturk A., and De Marqui Jr. C. Equivalent electrical circuit framework for nonlinear and high quality factor piezoelectric structures. *Mechatronics*, 54:133–143, 2018.

[120] LaCroix B. and Ifju P. Quasi-static four point bend testing of macro fiber composite unimorphs. *Experimental Mechanics*, 54:1139–1149, 2014.

[121] Rajan G. and Gangadhara P. *Advanced Piezoelectric Materials: Science and Technology, Second Edition.* Woodhead Publishing, Elsevier Ltd., 2017.

[122] Ventisel E. and Krauthammer T. *Thin Plates and Shells: Theory, Analysis, and Applications.* Marcel Dekker, Inc., 2001.

[123] Wikipedia. Plate theory. `https://en.wikipedia.org/wiki/Plate_theory#Mindlin.E2.80.93Reissner_theory_for_thick_plates`. Accessed on 2017-07-12.

[124] Huffington N.J. Response of elastic columns to axial pluse loading. *AIAA*, 1:2099–2104, 1963.

[125] Krishna Murty A.V. Flexure of composite plates. *Composite Structures*, 7:161–177, 1987.

[126] Vo T.P. and Thai H.T. Vibration and buckling of composite beams using refined shear deformation theory. *International Journal of Mechanical Science*, 62:67–76, 2012.

[127] Vo T.P. and Thai H.T. Free vibration of axially loaded rectangular composite beams using refined shear deformation theory. *International Journal of Mechanical Science*, 94:3379–3387, 2012.

[128] Shimpi R.P. and Patel H.G. A two variable refined plate theory for orthotropic plate analysis. *Journal of Solids and Structures*, 43:6783–6799, 2006.

[129] Thai H.T. and Choi D.H. A simple first order shear deformation theory for laminated composite plates. *Composite Structure*, 106:754–763, 2013.

[130] Jones R.M. *Mechanics of Compsite Materials, second edition.* Taylor and Francis Inc., 1999.

[131] Williams R.B., Inman D.J., Schultz M.R., and Hyer M.W. Nonlinear tensile and shear behavior of macro fiber composite actuators. *Composite Materials*, 38:855–869, 2004.

[132] Williams R.B., Inman D.J., and Wilkie W.K. Nonlinear response of the macro fiber composite actuator to monotonically increasing excitation voltage. *Journal of Intelligent Material Systems and Structures*, 17:601–608, 2006.

[133] Bent A.A. and Hagood N.W. Piezoelectric fiber composites with interdigitated electrodes. *Smart Materials and Structures*, 8:903–919, 1997.

[134] Tan P. and Tong L. Micro-electromechanics models for piezoelectric-fiber-reinforced composite materials. *Composite Science Technology*, 61:759–769, 2001.

[135] Tan P. and Tong L. Investigation of loading assumptions on the effective electroelastic constants for pfrc materials. *Composite Structures*, 57:101–108, 2002.

[136] Berger H., Kari S., Gabbert U., Rodriguez-Ramos R., Bravo-Castillero J., and R. Guinovart-Diaz. A comprehensive numerical homogenisation technique for calculating effective coefficients of uniaxial piezoelectric fibre composites. *Material Science Engineering: A*, 412:53–60, 2005.

[137] Tang T. and Yu W. Variational asymptotic micromechanics modeling of heterogeneous piezoelectric materials. *Mechanics and Materials*, 40:812–824, 2008.

[138] Oliveira J.A., Pinho-da-Cruz J., and Teixeira-Dias F. Asymptotic homogenisation in linear elasticity. part ii: finite element procedures and multiscale applications. *Computational Materials Science*, 45:1081–1096, 2009.

[139] Hagood N.W. and Bent A.A. Development of piezoelectric fiber composites for structural actuation. *: Collection of technical papers – AIAA/ASME structures, structural dynamics and materials conference. Pt 6. Massachusetts Inst of Technology, Cambridge, United States*, pages 3625–3638, 1993.

[140] Park J.S. and Kim J.H. Analytical development of signle crystal macro fiber composite actautors for active twist rotor blades. *Smart Materials and Structures*, 14:745–753, 2005.

[141] Cook A.C. Multiscale analysis of laminated smart structures with integrated piezoelectric fiber composite sensors and actuators.

[142] Deraemaeker A., Nasser H., Benjeddou A., and Preumont A. Mixing rules for the piezoelectric properties of macro fiber composites. *Journal of Intelligent Materials system and Structures*, 12:1475–1482, 2009.

[143] Deraemaeker A. and Nasser H. Numerical evaluation of the equivalent properties of macro fiber composite (mfc) transfucers using periodic homogenization. *Journal of Intelligent Materials system and Structures*, 47:3272–3285, 2010.

[144] Dermaemaeker A., Benelechi S., Benjeddou A., and Preumont A. Analytical and numerical computation of homogenized properties of mfcs: Application to a composite boom with mfc actuators and sensors. *III ECCOMAS Thematic Conference on Smart Structures and Materials*, page 22p, 2007.

[145] Deraemaeker A. and Tondreau G. Equivalent loads for two-dimensional distributed anisotropic piezoelectric transducers with arbitrary shapes attached to thin plate structures. *Journal of Acoustical Society of America*, 129:681–690, 2011.

[146] Hansen C., Snyder S., Qui X., Brooks L., and Morceau D. *Active control of noise and vibration, second edition*, volume 1. CRC Press Taylor and Francis Group, 2013.

[147] Lam K.Y. and Ng T.Y. Active control of composite plates with integrated piezoelectric sensors and actuators under various dynamic loading conditions. *Smart Materials and Structures*, 8:223–237, 1999.

[148] Sullivan J.M., Hubbard J.E., and Burke S.E. Modeling approach for two-dimensional distributed transducers of arbitrary spatial distribution. *Journal of Acoustical Society of America*, 99:2965–2974, 1996.

[149] Huang Y.M. and Hung S.C. Analytical study of an active piezoelectric absorber on vibration attenuation of a plate. *Journal of Sound and Vibration*, 330:361–373, 2011.

[150] Crawley E.F. and de Luis J. Use of piezoelectric actuators as elements of intelligent structures. *AIAA Journal*, 25:1373–1385, 1987.

[151] Crawley E. and Anderson E. Detailed model of piezoelectric actuation of beams. *In proceedings of the 30th AIAA/ASME/SAE Structure, Structural Dynamics and Material Conference, Washington, DC.*, pages 2000–2010, 1989.

[152] Lee C.K. Theory of laminated piezoelectric plates for the design of distributed sensors/actuators. part i: Governing equations and reciprocal relationships. *Journal of the Acoustical Society of America*, 87:1144–1158, 1990.

[153] Zhang X.D. and Sun C.T. Formulation of an adaptive sandwich beam. *Smart Material and Structures*, 5:814–823, 1996.

[154] Zhang X.D. and Sun C.T. Analysis of a sandwich plate containing a piezoelectric core. *Smart Material and Structures*, 8:31–40, 1999.

[155] Reddy J.N. On laminated composite plates with integrated sensors and actuators. *Engineering Structures*, 21:568–593, 1999.

[156] Liu G.R., Peng X.Q., and Lam K.Y. Vibration control simulation of laminated composite plates with integrated piezoelectrics. *Journal of Sound and Vibration*, 220:716–735, 1999.

[157] Zhang S.Q., Wang Z.X., Qin X.S., Zhao G.Z., and Schmidt R. Geometrically nonlinear analysis of composite laminated structures with multiple macro-fiber composite (mfc) actuators. *Composite Structures*, 130:62–72, 2016.

[158] Pandey A. and Arockiarajan A. Performance studies on macro fiber composite (mfc) under thermal condition using kirchhoff and mindlin plate theories. *Journal of Mechanical Science*, 130:416–425, 2017.

[159] Steiger K. and Mokry P. Finite element analysis of the macro fiber composite actuator: macroscopic elastic and piezoelectric properties and active control thereof by means of negative capacitance shunt circuit. *Smart Materials and Structures*, 24:14pp, 2014.

[160] Boutros Y.A. Finte element modeling of macro fiber composite actuators with application to wing de-icing, 2014.

[161] Gopinathan S.V., Varadan V.V., and Varadan V.K. A review and critique of theories for piezoelectric laminates. *Smart Materials and Structures*, 9:24–48, 2000.

[162] Wang S.Y. A finite element model for the static and dynamic analysis of a piezoelectric bimorph. *International Journal of Solids and Structures*, 41:4075–4096, 2004.

[163] Kim J., Varadan V.V., and Varadan V.K. Finite element modelling of structures including piezoelectric active devices. *International journal for numerical methods in engineering*, 40:817–832, 1997.

[164] Marinkovic D., Koppe H., and Gabbert U. Accurate modeling of the electric field within piezoelectric layers for active composite structures. *Journal of intelligent material systems and structures*, 18:503–513, 2007.

[165] Dong X.J., Peng Z.K., Hua H.X., and Meng G. Modeling of the through-the-thickness electric potentials of a piezoelectric bimorph using the spectral element method. *Sensors*, 14:3477–3492, 2014.

[166] Lloyd J.M. *Electrical porperties of macro-fiber composite actuators and sensors.* 2004.

[167] Nasser H., Deraemaeker A., and Belouettar S. Electric field distribution in macro fiber composite using interdigitated electrodes. *Advanced Materials Research*, 47-50:1173–1176, 2008.

[168] Sirohi J. and Chopra I. Fundamental understanding of piezoelectric strain sensors. *Journal of Intelligent Material Systems and Structures*, 11:246–257, 2000.

[169] Bhalla S. and Soh C.H. Electromechanical impedance modeling for adhesively bonded piezo-transducers. *Journal of Intelligent Material Systems and Structures*, 15:955–972, 2004.

[170] Wait J.R. and Todd M.D. Validation of macro fiber composites as strain sensors. *IMAC-XXV: conference and exposition on structural dynamics, US*, 2007.

[171] Dan C.A., Malinowski P., Kudela P., Opoka S., Radzienski M., Mieloszyk W., and Ostachowicz W. Validation of macro fiber composites for strain measurements in structural health monitoring applications of complex aerospace structures. *Proceedings of the 9th International Conference on Structural Dynamics, EURODYN, Porto, Portugal*, 2014.

[172] Whitney J. *Structural analysis of laminated anisotropic plates.* Technical Publishing Company Inc., 1987.

[173] Barcewell R. *Heaviside's unit step function* $H(x)$ *The Fourier Transform and its applications 3rd edition.* New York: McGraw-Hill, 2000.

[174] Reddy J.N. *Mechanics of laminated composite plates and shells theory and analysis.* CRC Press, New York, 2004.

[175] Craig R.R. Coupling of substructures for dynamic analysis: an overview. *in AIAA/ASME/ASCE/AHS/ASC 41st Structures, Structural Dynamics, and Materials Conference, Atlanta, GA*, pages 3–17, 2000.

[176] Perera R. and Ruiz A. A multistage fe updating procedure for damage identification in large-scale structures based on multiobjective envolutionary optimization. *Mechanical System and Signal Processing*, 22:970–991, 2008.

[177] Weng S., Xia Y., Y.L. Xu, and H.P. Zhu. Substructure based approach to finite element model updating. *Computers and Structures*, 89:772–782, 2011.

[178] Xia Y. and Liu R.M. Improvement on the iterated irs method for structural eigensolutions. *Journal of Sound and Vibration*, 22:713–727, 2004.

[179] Xia Y. and Liu R.M. A new iterative order reduction (ior) method for eigensolutions of large structures. *International Journal for Numerical Methods in Engineering*, 22:713–727, 2004.

[180] Qu Z.Q. An iterative method for dynamic condensation of structural matrices. *Mechanical System and Signal Processing*, 14:667–678, 2000.

[181] Lu X., Zhong W., and Lin J. Dynamic superelements substructure method in forced vibration analysis. *Computers and Structures*, 37:737–741, 1990.

[182] Smart Material Corp. Mfc bonding process. `https://www.smart-material.com/FAQ-all.html`. Accessed on 2017-07-12.

[183] 3M Industrial Adhesives and Tapes Division. 3M Scotch-Weld epoxy adhesives DP460 off-white and DP460NS. *Technical data sheet*, 2017.

[184] Hensel S., Drossel W.G., Nestler M., and Muller R. Modeling of the performance reduction of macro fiber composites for use in numerical forming simulation of piezoceramic-metal-compounds. *CIRP Journal of Manufacturing Science and Technology*, 7:129–138, 2014.

[185] Schwarz B.J. and Richardson M.H. Experimental modal analysis. *CSI Reliability Week*, 1999.

[186] Siemens N.v. FRF estimator. `https://community.plm.automation.siemens.com/t5/Testing-Knowledge-Base/What-is-a-Frequency-Response-Function-FRF/ta-p/354778`. Accessed on 2017-08-01.

[187] Siemens N.v. Aliasing. `https://community.plm.automation.siemens.com/t5/Testing-Knowledge-Base/Aliasing/ta-p/367750`. Accessed on 2017-08-01.

[188] Peeters B., Van der Auweraer H., Guillaume P., and Leuridan J. The polymax frequency-domain method: a new standard for modal parameter estimation? *Shock and Vibration*, 11:395–409, 2004.

[189] Allemang R.J. The modal assurance criterion - twenty years of use and abuse. *Journal of Sound and Vibration*, 37:15–21, 2003.

[190] Matt H.M. and di Scalea F.L. Macro-fiber composite piezoelectric rosettes for acoustic source localization in complex structures. *Smart Materials and Structures*, 16:1489–1499, 2007.

[191] Lee S. and White R.M. Piezoelectric cantilever acoustic transducer. *Journal of Micromechanics and Microengineering*, 8:230–238, 1998.

[192] Fu Y.Q., Luo J.K., Nguyen N.T., Walton A.J., Flewitt A.J., Zu X.T., Li Y., McHale G., Matthews A., Iborra E., Du H., and Milne W.I. Advances in piezoelectric thin films for acoustic biosensors, acousticfluidics and lab-on-chip applications. *Progress in Materials Science*, 89:31–91, 2017.

[193] Zhang L., Yalcinkaya H., and Ozevin D. Numerical approach to absolute calibration of piezoelectric acoustic emission sensors using multiphysics simulations. *Sensors and Actuators A: Physical*, 256:12–23, 2017.

[194] Albuquerque de Castro B., de Melo Brunini D., Batista F.G., and Andreoli A.L. Assessment of macro fiber composite sensors for measurement of acoustic partial discharge signals in power transformer. *IEEE Sensor Journal*, 17:6090–6099, 2017.

[195] Holeczek K., Starke E., Winkler A., Dannemann M., and Modler N. Numerical and experimental characterization of fiber-reinforced thermoplastic composite structures with embedded piezoelectric sensor-actuator arrays for ultrasonic applications. *Applied sciences*, 6:13, 2016.

[196] Li J., Wang C., Ren W., and Ma J. Zno thin film piezoelectric micromachined microphone with symmetric composite vibrating diaphragm. *Smart Materials and Structures*, 26:10pp, 2017.

[197] Smart Material. Macro-fiber composite. `https://www.smart-material.com/MFC-product-main.html`, 2018.

[198] Vivolo M. *Vibro-acoustic characterization of lightweight panels by using small cabin.* KU Leuven PhD thesis, 2013.

[199] Wyckaert K., Augusztinovicz F., and Sas P. Vibro-acoustic modal analysis: Reciprocity, model symmetry and model validation. *Journal of the Acoustical Society of America*, 100:3172–3181, 1996.

[200] Comsol. Acoustic module. `https://www.comsol.fr/acoustics-module`, 2018.

[201] van de Walle A., Naets F., Deckers E., and Desmet W. Stability-preserving model order reduction for time-domain simulation fo vibro-acoustic fe models. *International Journal for Numerical Methods in Engineering*, 109:889–912, 2016.

[202] Beltzinger K.U., Bischoff M., and Ramm E. A unified approach for shear-locking free triangular and rectangular shell finite elements. *Computers and Structures*, 75:321–334, 2000.

[203] Siemens N.v. Differential input. `https://community.plm.automation.siemens.com/t5/Testing-Knowledge-Base/Single-Ended-vs-Differential-Inputs/ta-p/355022`. Accessed on 2017-08-01.

[204] PiezoDrive Pty. Ltd. Td250-6 channel 250v amplifier manual and specification. `https://www.piezodrive.com/wp-content/uploads/2017/07/TD250Manual.pdf`. Accessed on 2017-07-12.

Curriculum Vitae

ZhongZhe DONG
2 May 1986 in Shandong, China

Education

2014–present

PhD at Katholieke Universiteit Leuven, Department of Mechanical Engineering, PMA, (Belgium)

PhD at Czech Technical University in Prague, Department of Control Engineering, FEL, (Czech Republic)

Title: "Dynamic modeling of macro-fiber composite transducers integrated into composite structures"
Founded by:

1 Marie Curie FP7-PEOPLE "ARRAYCON (GA 605087)-Application of distributed control on smart structures" supported by the European Commission (2014-2017)

2 Research Fund KU Leuven (2017-2018)

2011–2013

Engineering diploma in Institut Supérieur de l'Aéronautique et de l'Espace (ISAE-SUPAERO, France)

2011–2013

M.Sc. in Institut Supérieur de l'Aéronautique et de l'Espace (ISAE-SUPAERO, France)

2010–2011

1st year of M.Sc. in Université Lille-I (France)

2007–2010

Bachelor in Université Lille-I (France)

Professional Experience

May 2017 to Present

PhD Researcher in Noise and Vibration Research Group, KU Leuven (Belgium)

Member of DSSM lab, Flanders Make, (Belgium)

Visiting researcher in RTD group, Engineering Service, Siemens Software Industry (Belgium)

May 2014 to April 2017

Research Engineer in RTD group, Engineering Service, Siemens Software Industry (Belgium)

Intern **April 2013 to September 2013**

Institut Supérieur de l'Aéronautique et de l'Espace (France)
Topic: Using the fluid-structure interaction theory to optimize the design of the high-altitude balloons by numerical simulations

List of publications

Articles in impacted journals

1. Z.Z. Dong, C. Faria, M. Hromčík, B. Pluymers, M. Šebek and W. Desmet. “Equivalent force modeling of macro fiber composite actuators integrated into non-homogeneous composite plates for dynamic applications" *Smart Materials and Structure*, 26, 090540, 2017.
   Available at: http://iopscience.iop.org/article/10.1088/1361-665X/aa7bd0

2. Z.Z. Dong, C. Faria, M. Hromčík, B. Pluymers, M. Šebek and W. Desmet. "Structure-preserving low-order modeling approach of laminated composite plates integrated with macro-fiber composite transducers for dynamic applications" *Composite structures*, 208, pp287-297, 2019.
   Available at: https://www.sciencedirect.com/science/article/pii/S0263822318306184

Articles in international peer-reviewed journals

3. X. Zhang, Z.Z. Dong, C. Faria, M. Hromčík, K. Hengster-Movric, W. Desmet and H. Van Der Auweraer, “Reduced-order robust controller design for vibration reduction”, SAE Technical Paper, SAE International, June 2016.

Articles in international conference proceedings

4. C. Faria, Z.Z. Dong, X. Zhang "On the decentralized observer/controller strategy for disturbance rejection" *SPIE 10172, A Tribute Conference Honoring Daniel Inman, 101720J*, Portland US, 2017.

5. Z.Z. Dong, C. Faria, M. Hromčík, W. Desmet. "Modeling and experimental test study of a multilayer piezoelectric actuator" *Proceedings of IMAC34 - Model Validation and Uncertainty Quantification, IMAC XXXIV A Conference and Exposition on Structural Dynamics*, Orlando US, 2016.

6. X. Zhang, Z.Z. Dong, C. Faria, K. Hengster-Movric, W. Desmet. "Observer-based distributed controllers design for a cantilever beam." *Proceedings of IMAC34 - Model Validation and Uncertainty Quantification, IMAC XXXIV A Conference and Exposition on Structural Dynamics*, Orlando US, 2016.

7. Z.Z. Dong, W. Desmet, C. Faria "Equivalent force actuation modeling of laminated composites with piezoelectric actuators for vibration suppression" *ISMA conference on Noise and Vibration Engineering*, Leuven Belgium, 2016.

8. X. Zhang, W. Desmet, C. Faria, Z.Z. Dong, M. Šebek. "Decentralized/distributed output feedback H-infinity controller design for vibration reduction of smart structures" *ISMA conference on Noise and Vibration Engineering*, Leuven Belgium, 2016.

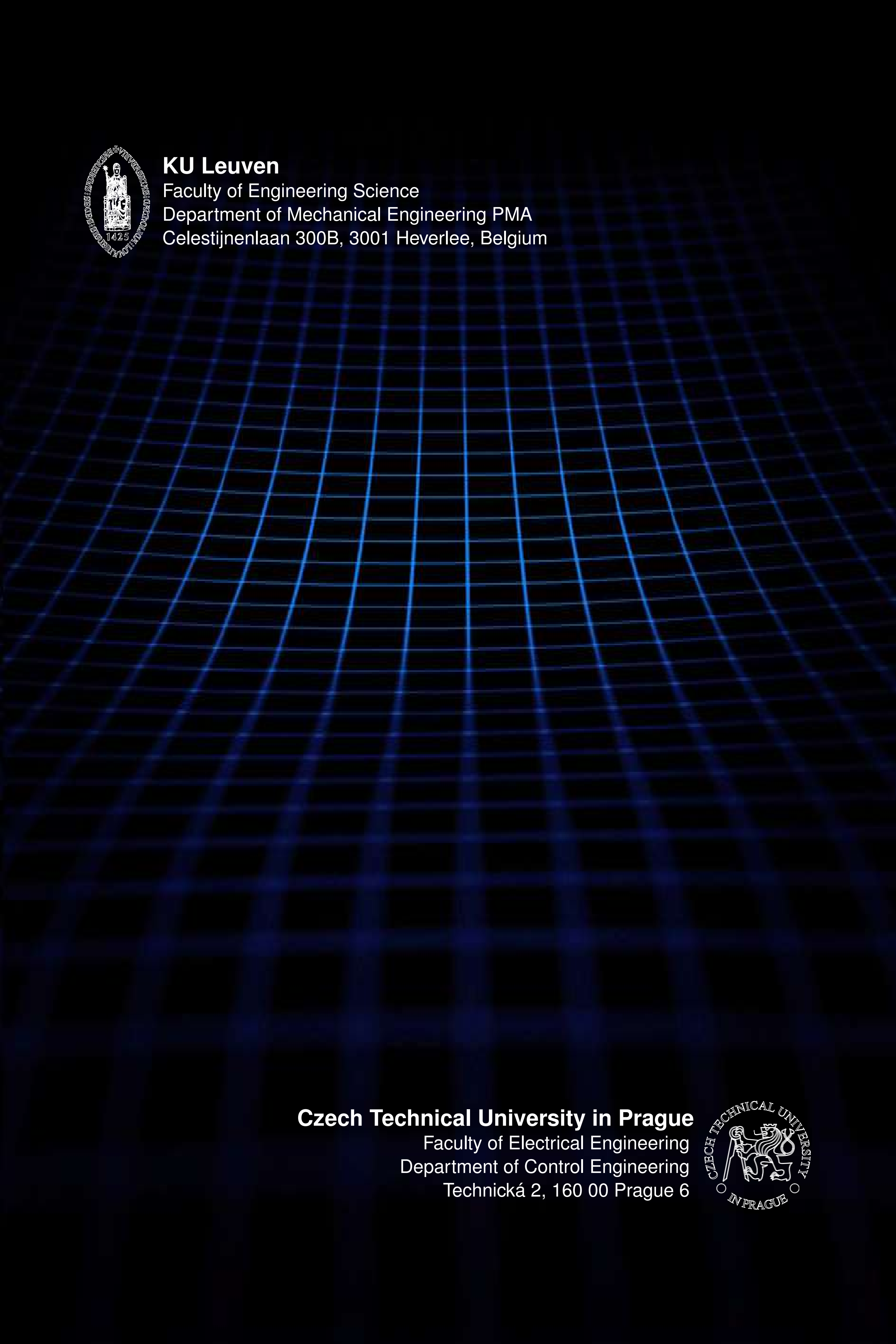

KU Leuven
Faculty of Engineering Science
Department of Mechanical Engineering PMA
Celestijnenlaan 300B, 3001 Heverlee, Belgium

Czech Technical University in Prague
Faculty of Electrical Engineering
Department of Control Engineering
Technická 2, 160 00 Prague 6